L. F. Greimann R. E. Abendroth D. E. Johnson P. B. Ebner

Final Report

Pile Design and Tests for Integral Abutment Bridges

Sponsored by the Iowa Department of Transportation, Highway Division, and the Iowa Highway Research Board

December 1987

Iowa DOT Project HR-273, ERI Project 1780, ISU-ERI-Ames-88060

Final Report

Greimann, Johnson, Abendroth, Ebner

Iowa Department of Transportation

report

College of Engineering
Iowa State University

L. F. Greimann R. E. Abendroth D. E. Johnson P. B. Ebner

Final Report

Pile Design and Tests for Integral Abutment Bridges

December 1987

Submitted to the Highway Division,
Iowa Department of Transportation

Iowa DOT Project HR-273
ERI Project 1780
ISU-ERI-Ames-88060

DEPARTMENT OF CIVIL ENGINEERING
ENGINEERING RESEARCH INSTITUTE
IOWA STATE UNIVERSITY, AMES

The opinions, findings, and conclusions expressed in this publication are those of the authors and not necessarily those of the Highway Division of the Iowa Department of Transportation.

TABLE OF CONTENTS

	Page
LIST OF FIGURES	vii
LIST OF TABLES	xvii
ABSTRACT	xix
NOMENCLATURE	xxi
1. INTRODUCTION	1
2. PREVIOUS WORK WITH INTEGRAL ABUTMENT BRIDGES	5
2.1. State Policies on Integral Abutment Bridges	5
2.2. Soil Characterization	6
2.3. Finite Element Pile Model	16
2.4. Simplified Method	18
3. FIELD TESTS	25
3.1. Objective and Scope	25
3.2. Field Test Program	26
3.2.1. Test Site	26
3.2.2. Test Framework	26
3.2.3. Instrumentation Framework	27
3.2.4. Test Pile Descriptions	27
3.2.5. Vertical Load Test	28
3.2.6. Lateral Load Test	29
3.2.7. Combined Load Test	30
3.2.8. Field Test Comparisons	31
3.3. Test Comparisons with IAB2D	31
3.3.1. Reasons for Comparisons	31
3.3.2. Vertical Load Test and IAB2D	33
3.3.3. Lateral Load Test and IAB2D	39
3.3.4. Combined Load Test and IAB2D	40
3.3.5. Summary of IAB2D/Field Test Correlation	50

Page

4. MODEL TESTS 51

4.1. Objective and Scope 51

4.2. Model Test Program 52

4.3. Model Test Comparisons with IAB2D 53

4.3.1. Reasons for Comparisons 53
4.3.2. Vertical Load Tests and IAB2D 53
4.3.3. Lateral Load Tests and IAB2D 59
4.3.4. Combined Load Tests and IAB2D 62
4.3.5. Summary of IAB2D and Model Test Correlations 83

5. DESIGN RECOMMENDATIONS 85

5.1. AASHTO Design Specification 85

5.2. Case A, Capacity as a Structural Member 89

5.2.1. Equivalent Cantilever Idealization 90
5.2.2. Pile Behavior 93
5.2.3. Design Alternatives 96
5.2.3.1. Alternative One 97
5.2.3.2. Alternative Two 99
5.2.3.3. Comparison with Finite Element 101
5.2.4. Recommendation 108

5.3. Case B, Capacity to Transfer Load to Ground 109

5.4. Case C, Capacity of Ground to Support Load 113

6. DESIGN EXAMPLES 115

6.1. Friction Pile 115

6.1.1. Case A Capacity 127
6.1.1.1. Alternative One 133
6.1.1.2. Alternative Two 135
6.1.2. Case B Capacity 144
6.1.3. Case C Capacity 145
6.1.4. Summary of Friction Pile Design Example 145

6.2. End-Bearing Pile 145

6.2.1. Case A Capacity 147
6.2.2. Case B Capacity 147
6.2.3. Case C Capacity 147
6.2.4. Summary of Bearing Pile Design Example 147

Page

7. SUMMARY, CONCLUSIONS, DESIGN RECOMMENDATIONS, AND RECOMMENDATIONS FOR FURTHER WORK 149

7.1. Summary 149

7.1.1. Overview 149
7.1.2. Field Tests 149
7.1.3. Model Tests 151
7.1.4. Finite Element Model, IAB2D 152
7.1.5. Pile Design Requirements 152

7.2. Conclusions 154

7.2.1. Field Tests 154
7.2.2. Model Tests 155
7.2.3. Comparisons Between Experimental and IAB2D Results 155
7.2.4. Comparisons Between Design Alternatives for Case A and IAB2D 156

7.3. Design Recommendations 157

7.4. Recommendations for Further Work 157

8. LIST OF REFERENCES 159

8.1. Cited References 159
8.2. References Not Cited 165

9. ACKNOWLEDGMENTS 171

10. APPENDIX A: FULL-SCALE PILE TESTS AND DATA REDUCTION 173

10.1. Development 173

10.1.1. Site Description 173
10.1.2. Testing Frame and Load Systems 176
10.1.3. Instrumentation Framework and Support 184
10.1.4. Test Pile Preparations 185

10.2. Field Test Procedures 190

10.2.1. Vertical Compression Test 190
10.2.2. Lateral Load Test 191
10.2.3. Combined Load Test 193

Page

10.3. Field Test Data Reduction and Development of Soil Characteristics 194

10.3.1. Experimental Pile Strains 194
10.3.2. Experimental f-z Curves 199
10.3.3. Experimental q'-z' Curves 207
10.3.4. Experimental p-y Curves 210

11. APPENDIX B: MODEL PILE DEVELOPMENT AND TEST PROGRAM 225

11.1. Development 225

11.1.1. Model Scale and Components 225
11.1.2. Framework 233
11.1.3. Pile Instrumentation 236

11.2. Model Test Procedures 239

11.2.1. General Description 239
11.2.2. Vertical Compression Tests 241
11.2.3. Lateral Load Tests 245
11.2.4. Combined Load Tests 249

11.3. Model Test Data Reduction and Development of Soil Characteristics 252

11.3.1. Experimental Pile Strains 252
11.3.2. Experimental f-z Curves 253
11.3.3. Experimental q-z Curves 258
11.3.4. Experimental p-y Curves 261

12. APPENDIX C: DEVELOPMENT OF EQUIVALENT LENGTH 269

12.1. Fixed-Head Pile in a Uniform Soil 269

12.2. Pinned-Head Pile in a Uniform Soil 278

12.3. Piles in a Nonuniform Soil 282

13. APPENDIX D: MOMENT AMPLIFICATION IN EQUIVALENT CANTILEVERS 289

13.1. Initially Straight Columns 289

13.2. Initially Curved Columns 298

LIST OF FIGURES

		Page
Figure 1.1.	Bridge abutment types: (a) bridge with expansion joints (b) bridge with integral abutments.	2
Figure 2.1.	Design model of soil-pile system.	8
Figure 2.2.	Typical p-y curve.	10
Figure 2.3	Nondimensional form of the modified Ramberg-Osgood equation.	10
Figure 2.4.	Reduction factor α [1].	15
Figure 2.5.	Example illustrating lateral mechanism: (a) schematic drawing of the pile and soil (b) failure modes (c) load-displacement curves for the pile.	20
Figure 2.6.	Comparison of Rankine equation and finite element results [1].	23
Figure 3.1.	IAB2D model for vertical load test.	36
Figure 3.2.	Axial load versus vertical displacement at grade for vertical load test.	38
Figure 3.3.	IAB2D and experimental axial forces for vertical load test.	38
Figure 3.4.	Lateral load versus lateral displacement at grade for lateral load test.	41
Figure 3.5.	IAB2D and experimental bending moments for lateral load test.	41
Figure 3.6.	Lateral load versus lateral displacement at 13 in. above grade for combined load test.	43
Figure 3.7.	Axial load versus vertical displacement at grade for combined load test.	43
Figure 3.8.	Pile strains during lateral load phase of combined load test: (a) at Δ_h = 0.30 in. (H = 4.9 kips) and V = 0 kips (b) at Δ_h = 0.89 in. (H = 13.1 kips) and V = 0 kips (c) at Δ_h = 1.76 in. (H = 20.2 kips) and V = 0 kips.	45

		Page
Figure 3.9.	Pile strains during vertical load phase of combined load test: (a) at Δ_h = 2.04 in. (H = 19.9 kips) and V = 0 kips (b) at Δ_h = 2.07 in. (H = 19.1 kips) and V = 100 kips (c) at Δ_h = 2.16 in. (H = 18.2 kips) and V = 200 kips (d) at Δ_h = 2.40 in. (H = 14.7 kips) and V = 280 kips.	47
Figure 4.1.	Finite element model for model test analyses.	55
Figure 4.2.	Axial load versus vertical displacement at grade for Test Sequence A-1.	56
Figure 4.3.	Axial load versus vertical displacement at grade for Test Sequence D-1.	56
Figure 4.4.	Axial strains for Test Sequence A-1 (V = 88 lb).	58
Figure 4.5.	Axial strains for Test Sequence D-1 (V = 363 lb).	58
Figure 4.6.	Lateral load versus lateral displacement at grade for Test Sequence C-2.	60
Figure 4.7.	Lateral load versus lateral displacement at grade for Test Sequence D-2.	60
Figure 4.8.	Bending strains for Test Sequence C-2 at Δ_h = 0.726 in. (H = 135 lb).	61
Figure 4.9.	Bending strains for Test Sequence D-2 at Δ_h = 0.526 in. (H = 133 lb).	61
Figure 4.10.	Lateral load versus lateral displacement at grade for the lateral phase of Test Sequence A-3.	64
Figure 4.11.	Axial load versus vertical displacement at grade for the vertical load phase of Test Sequence A-3.	64
Figure 4.12.	Total pile strains for the vertical load phase of Test Sequence A-3. (Δ_h = 0.504 in., V = 158 lb).	65
Figure 4.13.	Lateral load versus lateral displacement at grade for the lateral load phase of Test Sequence B-3.	67

		Page
Figure 4.14.	Axial load versus vertical displacement at grade for the vertical load phase of Test Sequence B-3.	67
Figure 4.15.	Total pile strains for the vertical load phase of Test Sequence B-3. (Δ_h = 0.425 in., and V = 701 lb).	68
Figure 4.16.	Lateral load versus lateral displacement at grade for the lateral load phase of Test Sequence C-3.	70
Figure 4.17.	Axial load versus vertical displacement at grade for the vertical load phase of Test Sequence C-3.	70
Figure 4.18.	Total pile strains for the vertical load phase of Test Sequence C-3. (Δ_h = 0.061 in., and V = 139 lb).	71
Figure 4.19.	Lateral load versus lateral displacement at grade for the lateral load phase of Test Sequence D-3.	73
Figure 4.20.	Axial load versus vertical displacement at grade for the vertical load phase of Test Sequence D-3.	73
Figure 4.21.	Total pile strains for the vertical load phase of Test Sequence D-3. (Δ_h = 0.426 in., and V = 406 lb).	74
Figure 4.22.	Lateral load versus lateral displacement at grade for the lateral load of Test Sequence E-3: (a) first cycle (b) second cycle.	76
Figure 4.23.	Axial load versus vertical displacement at grade for the vertical load phase of Test Sequence E-3.	79
Figure 4.24.	Lateral load versus lateral displacement at grade for the lateral phase of Test Sequence F-3.	81
Figure 4.25.	Induced axial compressive force in the pile at 35 in. below soil surface during lateral load phase of Test Sequence F-3.	81

		Page
Figure 4.26.	Axial load versus vertical displacement at grade for the vertical load phase of Test Sequence G-3. (H = 93 lb, and Δ_h = 0.250 in.).	84
Figure 5.1.	Cantilever idealization of the pile: (a) fixed-head condition (b) pinned-head condition.	91
Figure 5.2.	Equivalent cantilevers for fixed-head piles embedded in a uniform soil.	94
Figure 5.3.	Equivalent cantilevers for pinned-head piles embedded in a uniform soil.	94
Figure 5.4.	Equivalent cantilevers: (a) fixed-head conditions (b) pinned-head conditions.	102
Figure 5.5.	Finite element and the design equations for a HP10 × 42 pile with a fixed-head and Δ = 0. (see Table 5.2 for Case identification).	103
Figure 5.6.	Comparison of finite element and the design equations for a HP10 × 42 pile with a pinned-head and Δ = 0. (see Table 5.2 for Case identification).	103
Figure 5.7.	Comparison of finite element and the design equations for a HP10 × 42 pile with a fixed-head and Δ = 1 in. (see Table 5.2 for Case identification).	104
Figure 5.8.	Comparison of finite element and the design equations for a HP10 × 42 pile with a pinned-head and Δ = 1 in. (see Table 5.1 for Case identification).	104
Figure 5.9.	Comparison of finite element and the design equations for a HP10 × 42 pile with a fixed-head and Δ = 2 in. (see Tables 5.1 and 5.2 for Case identification).	105
Figure 5.10.	Comparison of finite element and the design equations for a HP10 × 42 pile with a pinned-head and Δ = 2 in. (see Tables 5.1 and 5.2 for Case identification).	105
Figure 5.11.	Formation of a gap between the pile and the soil because of cyclic horizontal load.	110

		Page
Figure 5.12.	Soil-pile system for determining the friction capacity of the pile.	110
Figure 5.13.	Displacement for a fixed-head pile embedded in a uniform soil.	112
Figure 5.14.	Displacement for a pinned-head pile embedded in a uniform soil.	112
Figure 6.1.	Section through abutment and soil profile.	116
Figure 6.2.	Transverse section through deck.	117
Figure 6.3.	Variation of horizontal soil stiffness with depth.	119
Figure 6.4.	Idealized abutment foundation and girder endspan: (a) approximate structural model (b) free body diagram with passive soil pressure.	123
Figure 6.5.	Alignment chart for effective length of columns in continuous frames, braced against sidesway [28].	129
Figure 6.6.	Inelastic rotation of equivalent cantilever: (a) elastic (b) inelastic (c) idealized moment-rotation relationship.	137
Figure 10.1.	Test framework plan.	179
Figure 10.2.	Elevation of test frame and jacking beam for vertical load test.	180
Figure 10.3.	Elevation of test frame and horizontal girder for vertical load test.	180
Figure 10.4.	Elevation of test framework and horizontal girder for lateral load test.	181
Figure 10.5.	Elevation of test framework and horizontal girder for combined load test.	181
Figure 10.6.	Strain gage locations on test piles.	187
Figure 10.7.	Displacement instrumentation for Test Pile P1: (a) bottom flange of load girder (b) vertical DCDT (c) Test Pile P1 (d) vertical dial gage (e) bracket.	192

		Page
Figure 10.8.	Vertical load pile behavior: (a) forces acting on incremental pile segment (b) unloaded pile (c) loaded pile.	200
Figure 10.9.	Development of f and z at nth node.	203
Figure 10.10.	Axial strain, ε_o, distributions for vertical load test.	204
Figure 10.11.	Skin friction force, f, distributions for vertical load test.	204
Figure 10.12.	Relative vertical displacement, z, versus depth for vertical load test.	205
Figure 10.13.	Modified Ramberg-Osgood f-z curve at 10.5 ft depth.	205
Figure 10.14.	Modified Ramberg-Osgood f-z curve at 19.5 ft depth.	206
Figure 10.15.	Modified Ramberg-Osgood f-z curve at 31.5 ft depth.	206
Figure 10.16.	Maximum skin friction force, f_{max}, versus depth.	208
Figure 10.17.	Initial skin friction stiffness, k_v, versus depth.	208
Figure 10.18.	Modified Ramberg-Osgood q'-z' curve at 34.5 ft depth.	211
Figure 10.19.	Forces acting on a segment of a laterally displaced pile.	212
Figure 10.20.	Bending strain distribution for the lateral load test.	215
Figure 10.21.	Lateral soil resistance, p, distribution for lateral load test.	215
Figure 10.22.	Lateral soil displacement, y, along the pile length for lateral load test.	217
Figure 10.23.	Modified Ramberg-Osgood p-y curve at 3.0 ft depth for lateral load test.	217

		Page
Figure 10.24.	Modified Ramberg-Osgood p-y curve at 4.0 ft depth for lateral load test.	219
Figure 10.25.	Modified Ramberg-Osgood p-y curve at 5.0 ft depth for lateral load test.	219
Figure 10.26.	Ultimate lateral resistance, p_u, versus depth.	220
Figure 10.27.	Initial lateral stiffness, k_h, versus depth.	220
Figure 10.28.	Modified Ramberg-Osgood p-y curve at 3.0 ft depth for combined load test.	223
Figure 10.29.	Modified Ramberg-Osgood p-y curve at 4.5 ft depth for combined load test.	223
Figure 10.30.	Modified Ramberg-Osgood p-y curve at 6.0 ft depth for combined load test.	224
Figure 11.1.	Partical size distribution curve for model pile tests.	229
Figure 11.2.	Model test pile location in the soil bin (a) plan view (b) cross section.	231
Figure 11.3.	Vertical and lateral frameworks for model pile tests.	234
Figure 11.4.	Strain gage locations for the model test piles: (a) gage pattern 1 (b) gage pattern 2 (c) gage pattern 3 (d) gage pattern 4.	237
Figure 11.5.	Pile head configurations for Test Groups A, B, C, D, E, and G: (a) test group A (b) test groups B, C, E, and G (c) test group D.	242
Figure 11.6.	DCDT arrangement for vertical load tests: (a) plan view (b) side elevation (c) back elevation.	243
Figure 11.7.	Pile head configuration for Test Group F: (a) plan view (b) front elevation (c) side elevation.	244
Figure 11.8.	DCDT arrangement for pile test involving an abutment: (a) front elevation (b) side elevation.	246

		Page
Figure 11.9.	DCDT arrangement for lateral load tests: (a) plan view (b) side elevation (c) rear elevation.	248
Figure 11.10.	Experimental axial force in pile for combined load pile tests.	255
Figure 11.11.	Several f-z curves for the vertical load phase of Test Sequence A-3.	257
Figure 11.12.	Modified Ramberg-Osgood f-z curve at 49 in. depth for the vertical load phase of Test Sequence A-3.	257
Figure 11.13.	Maximum skin friction force, f_{max}, versus depth for vertical load tests in loose sand.	259
Figure 11.14.	Initial skin friction stiffness, k_v, versus depth for vertical load tests in loose sand.	259
Figure 11.15.	Maximum skin friction force, f_{max}, versus depth for vertical load tests in dense sand.	260
Figure 11.16.	Initial skin friction stiffness, k_v, versus depth for vertical load tests in dense sand.	260
Figure 11.17.	Modified Ramberg-Osgood q-z curve at 56 in. depth for the vertical load phase of Test Sequence C-3.	262
Figure 11.18.	Ultimate lateral resistance, p_u, versus depth for lateral load tests in loose sand.	266
Figure 11.19.	Initial lateral stiffness, k_h, versus depth for lateral load tests in loose sand.	266
Figure 11.20.	Ultimate lateral resistance, p_u, versus depth for lateral load tests in dense sand.	267
Figure 11.21.	Initial lateral stiffness, k_h, versus depth for lateral load tests in dense sand.	267
Figure 12.1.	Winkler model of soil-pile system with applied horizontal load, H, and moment, M.	271
Figure 12.2.	Piles in nonuniform soil: (a) actual variation of stiffness (b) equivalent uniform stiffness (c) assumed displaced shape.	271

		Page
Figure 12.3.	Second moment of area about line A - A.	287
Figure 12.4.	Layered soil system for example of determining k_e.	287
Figure 13.1.	Initially straight fixed-head column: (a) displaced location (stressed in this position before the vertical load is applied) (b) free body diagram for determining the differential equation.	290
Figure 13.2.	Initially straight pinned-head column: (a) displaced location (stressed in this position before the vertical load is applied) (b) free body diagram for determining the differential equation.	291
Figure 13.3.	Moment amplification for an initially straight fixed-head column with a horizontal head displacement, Δ.	294
Figure 13.4.	Moment amplification for an initially straight pinned-head column with a horizontal head displacement, Δ.	294
Figure 13.5.	Moment amplification for an initially curved fixed-head column with a horizontal head displacement, Δ.	300
Figure 13.6.	Moment amplification for an initially curved pinned-head column with a horizontal head displacement, Δ.	300

LIST OF TABLES

		Page
Table 2.1.	Parameters for p-y curve.	11
Table 2.2.	Parameters for f-z curve.	12
Table 2.3.	Parameters for q-z curve.	12
Table 2.4.	Soil properties and curve parameters for an HP10 × 42 pile in clay.	13
Table 2.5.	Typical soil properties and curve parameters for an HP10 × 42 pile in sand.	14
Table 3.1.	Field testing summary.	32
Table 5.1.	Elastic buckling load, P_e, and ultimate load, P, for combined loading of piles in soil [1].	106
Table 5.2.	Elastic buckling load, P_e, and ultimate load, P, for combined loading of columns (Case E).	106
Table 10.1.	Boring No. 1.	174
Table 10.2.	Boring No. 2.	175
Table 10.3.	Blow counts.	177
Table 10.4.	Laboratory test results of soil.	178
Table 10.5.	Experimental axial and bending strains for vertical and combined load tests.	197
Table 10.6.	Experimental bending strains for lateral load test.	198
Table 11.1.	Scaling relationships.	227
Table 11.2.	Test matrix for model piles.	240
Table 11.3.	Summary of soil parameters n, q_{max}, and k_q.	263

ABSTRACT

Expansion joints increase both the initial cost and the maintenance cost of bridges. Integral abutment bridges provide an attractive design alternative because expansion joints are eliminated from the bridge itself. However, the piles in these bridges are subjected to horizontal movement as the bridge expands and contracts during temperature changes. The objective of this research was to develop a method of designing piles for these conditions.

Separate field tests simulating a pile and a bridge girder were conducted for three loading cases: (1) vertical load only, (2) horizontal displacement of pile head only, and (3) combined horizontal displacement of pile head with subsequent vertical load. Both tests (1) and (3) reached the same ultimate vertical load, that is, the horizontal displacement had no effect on the vertical load capacity. Several model tests were conducted in sand with a scale factor of about 1:10. Experimental results from both the field and model tests were used to develop the vertical and horizontal load-displacement properties of the soil. These properties were input into the finite element computer program Integral Abutment Bridge Two-Dimensional (IAB2D), which was developed under a previous research contract. Experimental and analytical results compared well for the test cases.

Two alternative design methods, both based upon the American Association of State Transportation Officials (AASHTO) Specification, were developed. Alternative One is quite conservative relative to IAB2D results and does not permit plastic redistribution of forces. Alternative

Two is also conservative when compared to IAB2D, but plastic redistribution is permitted. To use Alternative Two, the pile cross section must have sufficient inelastic rotation capacity before local buckling occurs. A design example for a friction pile and an end-bearing pile illustrates both alternatives.

NOMENCLATURE

k_h	initial lateral stiffness
p	generalized soil resistance
p_u	ultimate lateral soil resistance
n	shape parameter
y	generalized displacement
f_{max}	maximum shear stress between pile and soil
k_v	initial vertical stiffness
q_{max}	maximum bearing stress at the pile tip
k_q	initial point stiffness
ℓ	embedded length of the pile
A_e	effective pile tip area
A_e	rectangular area formed by the section depth and the flange width
Δ	horizontal displacement
P_e	elastic buckling load
M_{pc}	plastic moment capacity of the pile reduced for axial load
P	ultimate load, sometimes called the inelastic buckling load; also applied axial load
P_e	elastic buckling load
P_p	plastic mechanism load
P_y	yield load
ε_{50}	axial strain at one-half peak stress difference from triaxial test
f	vertical friction force between pile and soil per unit length of pile
z	relative vertical displacement between pile and soil

q	bearing stress on effective tip area
B	pile width
γ	effective unit soil weight
x	depth from soil surface
ϕ	angle of internal friction
k_p, k_a	$\tan^2 (45° \pm \phi/2)$
k_o	$1 - \sin\phi$
α	$\phi/2$ for dense or medium sand, $\phi/3$ for loose sand
β	$45° + \phi/2$
J	200 for loose, 600 for medium, 1500 for dense sand
y_{50}	displacement at one-half ultimate soil reaction: $2.5\ B\varepsilon_{50}$ for soft and stiff clay, $2.0\ B\varepsilon_{50}$ for very stiff
c_u	undrained cohesion of the clay soil, approximately 97N + 114(psf)
c_a	adhesion between soil and pile, αc_u(psf). See Fig. 2.4 for α.
N	average standard penetration blow count
z_c	vertical displacement at maximum force: 0.4 in. for sand, 0.25 in. for clay
N_{corr}	corrected standard penetration test blow count at depth of pile tip; equal to N if $N \leq 15$ or $15 + 0.5(N - 15)$ if $N > 15$
D	dead load
L	live load
T	temperature load
I	impact load
α	superstructure material coefficient of thermal expansion
ΔT	average temperature change
f_a	applied axial stress
f_b	applied bending stress

F_a	allowable axial stress
F_b	allowable bending stress
F'_e	Euler buckling load divided by a factor of safety
C_m	equivalent moment factor = $0.6 + 0.4\ (M_1/M_2) \geq 0.4$; where M_1 and M_2 are the smaller and larger end moments, respectively, of a column with no lateral load or joint translation. The ratio M_1/M_2 is positive for single curvature and negative for reverse curvature
M	applied moment
A_s	cross-sectional area
F_y	yield stress of the steel
F_{cr}	critical buckling stress
F_e	Euler buckling stress
M_u	ultimte moment
M_p	full plastic moment
C	C_m
ℓ	length of the actual pile embedded in the ground
ℓ_e	equivalent embedded length, depth from the soil surface to the fixed base of the equivalent cantilever
L	total length of the equivalent cantilever, length ℓ_u plus ℓ_e
ℓ_c	critical length
Δ	horizontal displacement
K	effective length factor
H	horizontal force
$P\Delta$	overturning moment
P_y	yield load
ℓ_u	length of pile above the ground
ℓ_n	length deducted for lateral displacement

F_y	yield strength
θ_{iD}	inelastic rotation demand
C_i	inelastic rotation capacity reduction factor
θ_p	elastic rotation within the plastic hinge location
ℓ_p	length of the plastic hinge
ϕ_p	beam curvature corresponding to M_p
M_y	yield moment
Δ_i	allowable total displacement consistent with the inelastic rotation capacity
Δ_p	horizontal displacement at pile head corresponding to the formation of a plastic mechanism
θ_{iC}	inelastic rotation capacity

1. INTRODUCTION

Traditionally, a system of expansion joints, roller supports, and other structural releases has been provided on bridges to prevent damage caused by thermal expansion and contraction of the superstructure with annual temperature variations (Fig. 1.1a). Expansion joints within the superstructure increase the initial cost of a bridge and often do not function properly after years of service unless they are extensively maintained. Thus, integral abutment bridges, which have no expansion joints within the span or at supports (Fig. 1.1b), provide a design alternative that potentially offers lower initial costs and lower maintenance costs. However, the piles in an integral abutment bridge are subjected to horizontal movements as the bridge expands and contracts [1].

The objective of this research was to develop a rational method to design piles suitable for integral abutments, that is, for pile head movements caused by the expansion or contraction of the superstructure. Integral abutments have been used for some time, but their design is often based on intuitive arguments or arguments like "How does it function? We can't say for certain--but it works!" [2]. The design method presented in Section 5 was verified with the Integral Abutment Bridge Two-Dimensional (IAB2D) finite element program. This finite element program was developed specifically for this problem, and its results were compared to experimental results by others [1]. The design method, formulated for use by practicing bridge engineers, is shown to give conservative results when compared to the finite element solutions.

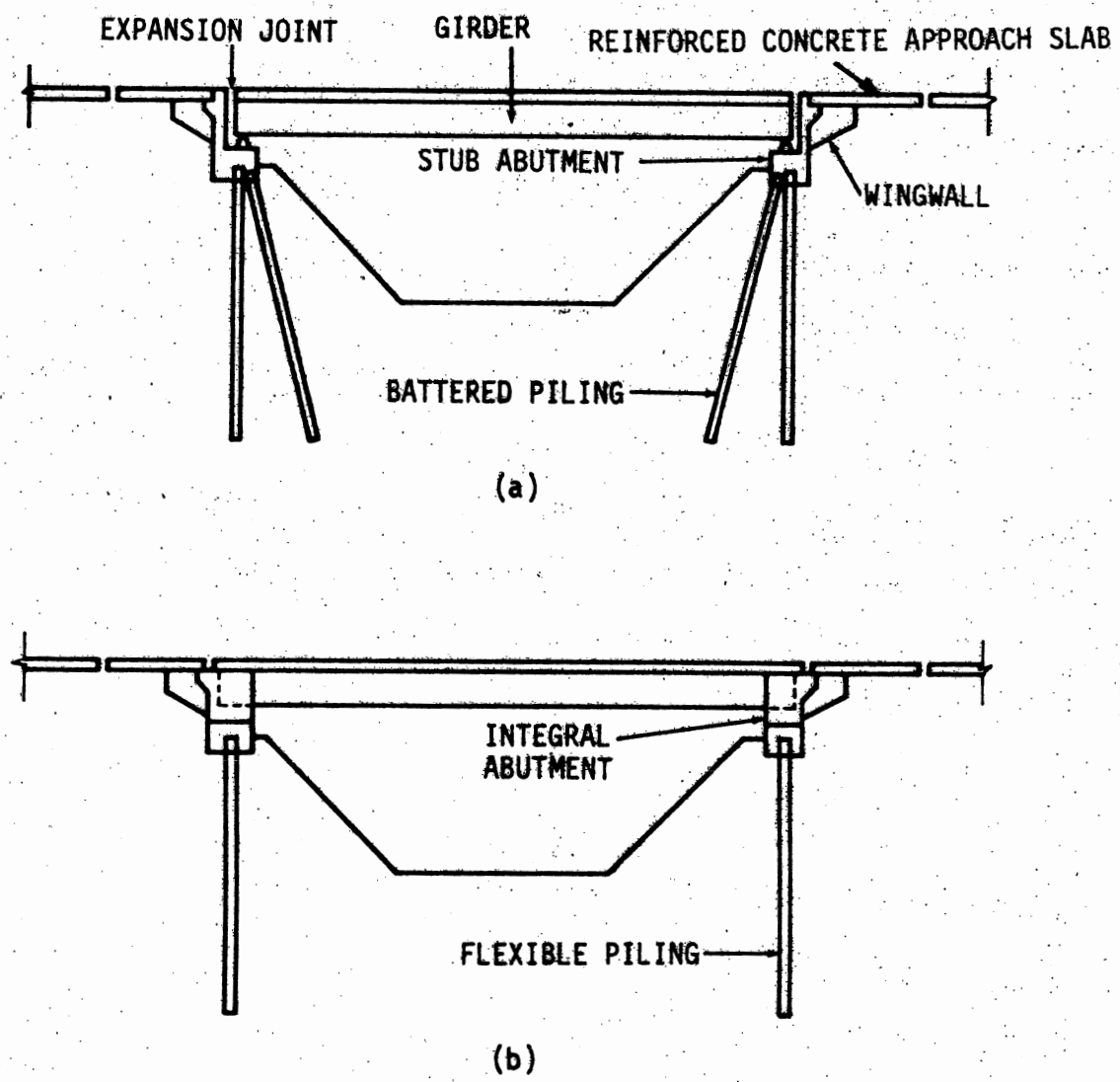

Figure 1.1. Bridge abutment types: (a) bridge with expansion joints (b) bridge with integral abutments.

The program has been further verified by experiments conducted under this program. Specifically, correlations with three full-scale field tests and eleven 1/10-scale model tests are reported in Sections 3 and 4, respectively.

Other factors to be considered in determining the allowable length for integral abutment bridges include (1) the axial stresses induced in the superstructure that are caused by the partially restrained abutment and (2) the effects of the abutment movement on the integrity of the approach slab and backfill. With the proposed design method the forces induced in the superstructure by the horizontal restraint of the pile can now be determined; however, the forces induced by the soil pressure against the abutment were not investigated, nor was the behavior of the approach slab.

2. PREVIOUS WORK WITH INTEGRAL ABUTMENT BRIDGES

2.1. State Policies on Integral Abutment Bridges

The use of integral abutments in bridge design has, so far, been accepted by 28 state highway departments and the District Construction Office of the Federal Highway Administration (FHWA), Region 15. This section summarizes their theory and practice in integral abutment design as reflected in the resuls of a 1983 survey. Responses to this survey and others concerning the use of integral abutments [3,4] have indicated that most state highway departments have their own limitations and criteria in designing integral abutments. The bases of these limitations and criteria are primarily empirical.

Of the 28 states and the FHWA, only Iowa, South Dakota, and FHWA, Region 15, indicated that piling stresses due to horizontal movement are calculated for integral abutment bridges. Alaska and Idaho indicated that such calculations are warranted only for integral abutment bridges that involve some unique feature. The remaining states essentially neglect piling stresses due to horizontal movement, although some states (e.g., California) require some type of mitigating construction detail, such as driving the piles into predrilled holes.

Construction details also vary widely from state to state. Pile head conditions may be of the hinge, fixed, or partially restrained type. Pile caps may or may not be used. In some states, approach slabs are tied to the abutment with dowels, causing these slabs to move back and forth with the superstructure, while in other states, an expansion joint between approach slab and bridge slab is considered

necessary to prevent possible maintenance problems. While granular material is the material most widely used as backfill, some states (e.g., New Mexico) no longer use specified backfill. Wingwalls may be in-line or flared. Some states (e.g., New York) do not allow U-walls because of design uncertainty, backfill compaction difficulty, and the additional design details that require attention for the joint between the wingwalls and approach slab. New York recommends avoiding wingwall lengths in excess of 10 ft. Tennessee requires the designer to use a comprehensive analysis if wingwall lengths greater than 12 ft are to be used.

Length limitations for integral abutment bridges have been set, for the most part, on the basis of experience and engineering judgment. Many of the states (e.g., Tennessee [2]) have been progressively increasing length limitations over the past 30 years, primarily as a result of observed satisfactory performance in actual installations. As of 1983, the length limitations for nonskewed integral abutment bridges were steel: 150 ft to 400 ft; concrete: 150 ft to 800 ft; and prestressed concrete: 200 ft to 800 ft. Most states use the same length limitations for skewed integral abutment bridges.

2.2. Soil Characterization

The Winkler soil model is used for the analysis of the soil pile interaction [5,6]. The model assumes that the soil can be represented as a series of vertical and lateral springs along the length of the

pile as shown in Fig. 2.1. Also, the model assumes that there is no interaction between the different soil springs as the pile is displaced.

The soil characteristics of each of three types of springs can be described by soil resistance and displacement curves: (1) p-y curves, which describe the relationship between the lateral soil pressure (horizontal force per unit length of pile) and the corresponding lateral pile displacement; (2) f-z curves, which describe the relationship between skin friction (vertical force per unit length of pile) and the relative vertical displacement between the pile and the soil; and (3) q-z curves, which describe the relationship between the bearing stress (vertical force on effective pile tip area) at the pile tip and the pile tip settlement. All three types of curves assume the soil behavior to be nonlinear. Again, the Winkler model assumes that these springs are uncoupled, that is, that motion at one spring does not affect another.

The modified Ramberg-Osgood model [7] is used to approximate the p-y, f-z, and q-z soil resistance and displacement curves for use in the finite element solution:

$$p = \frac{k_h y}{\left[1 + \left|\frac{y}{y_u}\right|^n\right]^{1/n}} \tag{2.1}$$

$$y_u = \frac{p_u}{k_h} \tag{2.2}$$

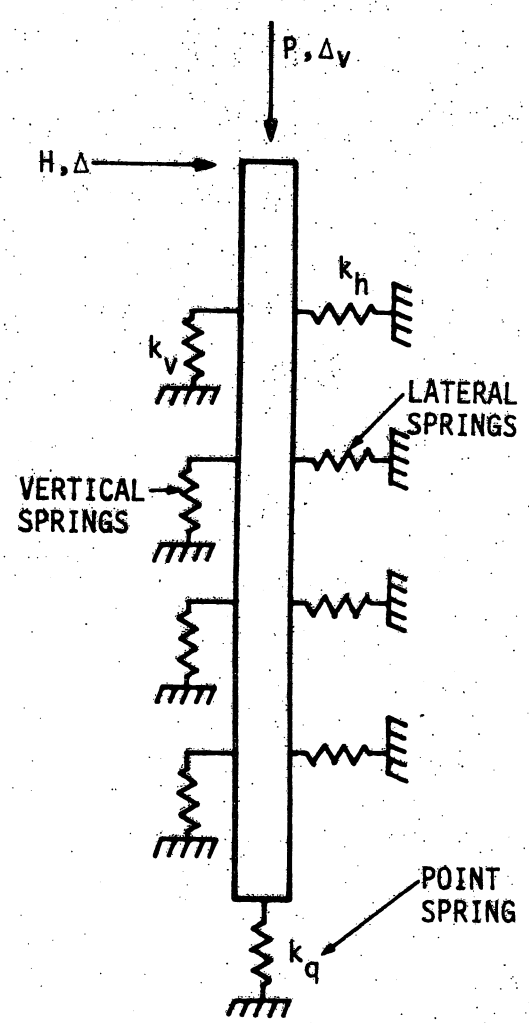

(a)

Figure 2.1. Design model of soil-pile system.

in which

k_h = initial stiffness

p = generalized soil resistance

p_u = ultimate soil resistance

n = shape parameter

y = generalized displacement

Nonlinear behavior models for symmetrical or periodic loadings have been presented by a number of workers [8-13]. Figure 2.2 and Eq. (2.1) show the modified Ramberg-Osgood curve for a typical p-y curve. Similar equations for a typical f-z curve (with f_{max}, the maximum shear stress developed between the pile and soil, and k_v, the initial vertical stiffness) or a typical q-z curve (with q_{max}, the maximum bearing stress at the pile tip, and k_q, the initial point stiffness) will be used. Figure 2.3 shows the effect of the shape parameter, n, on the soil resistance and displacement behavior. The constants needed in Eq. (2.1) can be empirically determined from basic soil properties as presented in Ref. [1] and repeated here as Tables 2.1, 2.2, and 2.3 [6,14-17]. Typical values are listed for clay and sand in Tables 2.4 and 2.5, respectively, for an HP10 × 42 steel pile.

For the design method developed herein a simplified elastic, perfectly plastic behavior will be assumed. This behavior for a typical p-y curve is shown in Fig. 2.2. The only soil spring properties needed for the design method are the ultimate resistance and the initial stiffness. Typical soil parameter values for the design method can also be found in Tables 2.4 and 2.5.

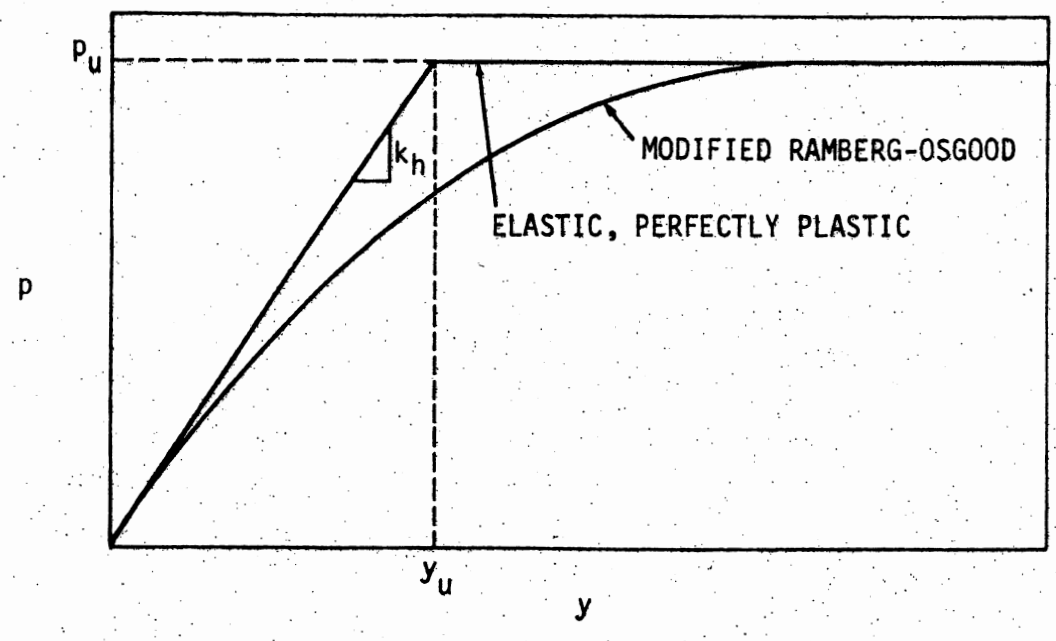

Figure 2.2. Typical p-y curve.

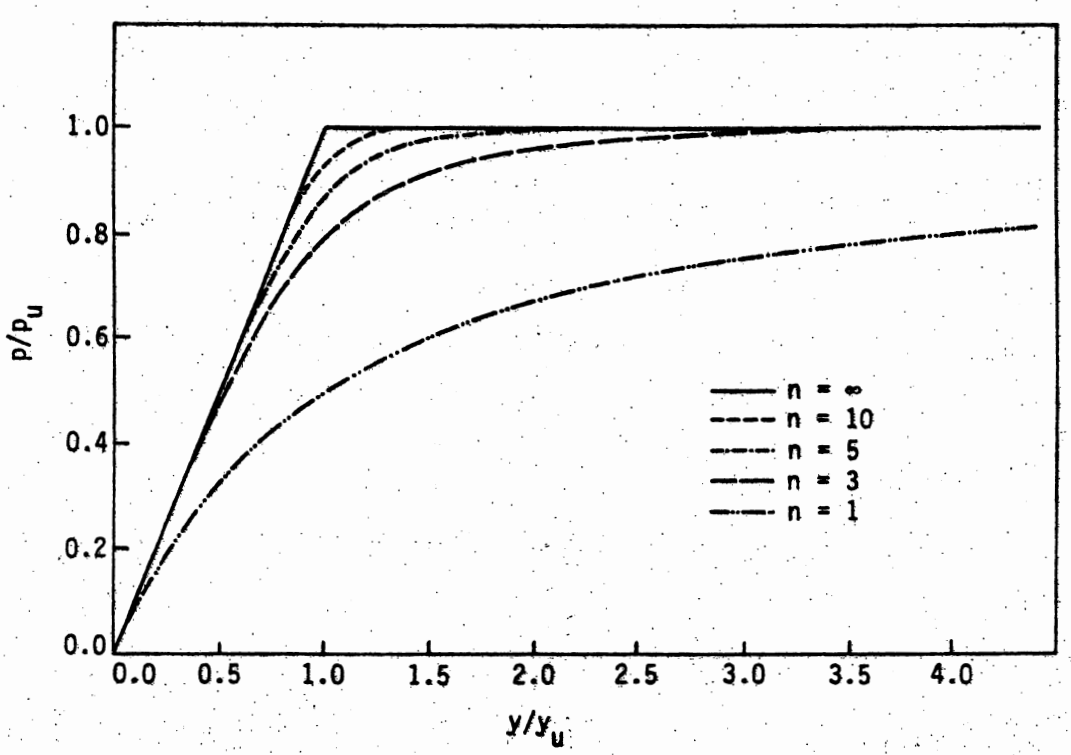

Figure 2.3 Nondimensional form of the modified Ramberg-Osgood equation.

Table 2.1. Parameters for p-y curve.

Case	n	p_u (use lesser value)	k_h
Soft clay and stiff clay	1.0	$p_u = 9c_uB$	
		$p_u = 3 + \frac{\gamma}{c_u}x + \frac{0.5}{B}x \quad c_uB$	$\frac{p_u}{y_{50}}$
Very stiff clay	2.0	$p_u = 9c_uB$	
		$p_u = 3 + \frac{\gamma}{c_u}x + \frac{2.0}{B}x \quad c_uB$	$\frac{p_u}{2y_{50}}$
Sand	3.0	$p_u = \gamma x[B(k_p - k_a) + xk_p\tan\alpha\tan\beta$	$\frac{J\gamma x}{1.35}$
		$+ xk_o\tan\beta(\tan\phi - \tan\alpha)]$	
		$p_u = \gamma x \quad k_p^3 + 2k_p^2k_o\tan\phi - k_a \quad B$	

ε_{50} Axial strain at one-half peak stress difference from triaxial text; or use 0.02 for soft clay, 0.01 for stiff clay, or 0.005 for very stiff clay.

c_u Cohesion from an unconsolidated, undrained test

B Pile width

γ Effective unit soil weight

x Depth from soil surface

ϕ Angle of internal friction

k_p, k_a $= \tan^2 (45° \pm \phi/2)$

k_o $= 1 - \sin\phi$

α $= \phi/2$ for dense or medium sand, $\phi/3$ for loose sand

β $= 45° + \phi/2$

J = 200 for loose sand, 600 for medium sand, 1500 for dense sand

y_{50} Displacement at one-half ultimate soil reaction: $2.5\ B\varepsilon_{50}$ for soft and stiff clay, $2.0\ B\varepsilon_{50}$ for very stiff clay.

Table 2.2. Parameters for f-z curve.

Case	n	f_{max} H Piles	f_{max} Others	k_v
Clay	1.0	The least of: $2(d + b_f)c_u$ $2(d + 2b_f)c_a$ $2(dc_u + b_f c_a)$	The lesser of c_u or c_a times pile perimeter	$\frac{10f_{max}}{z_c}$
Sand	1.0	$0.02N(2(d + 2b_f))$ (klf)	0.04N times pile perimeter (klf)	$\frac{10f_{max}}{z_c}$

c_u = Undrained cohesion of the clay soil, approximately 97N + 114 (psf)

c_a = Adhesion between soil and pile, ηc_u(psf). See Fig. 2.4 for η.

N = Average standard penetration blow count

z_c = Displacement at maximum force: 0.4 in. for sand, 0.25 in. for clay

d, b_f = Depth and flange width, respectively, of H shape.

Table 2.3. Parameters for q-z curve.

Case	n	q_{max}	k_q
Clay	1.0	$9c_u$	$\frac{10q_{max}}{z_c}$
Sand	1.0	$8N_{corr}$ (ksf)	$\frac{10q_{max}}{z_c}$

N_{corr} = Corrected standard penetration test blow count at depth of pile tip; equal to N if $N \leq 15$ or $15 + 0.5(N - 15)$ if $N > 15$.

Table 2.4. Soil properties and curve parameters for an HP10 × 42 pile in clay.

	Soft	Stiff	Very Stiff
Soil Properties:			
Blow count, N	3	15	40
Effective unit weight, γ (pcf)	50	60	65
Undrained cohesion, c_u (psf)	400	1,600	5,000
p-y Curve Parameters:			
n	1.0	1.0	2.0
p_u (klf) (use lesser value)	3.0 or 1.0 + 0.24x	12 or 3.9 + 0.85x	37 or 12.5 + 10.1x
k_h (ksf) (use lesser value)	72 or 24 + 5.8x	580 or 190 + 41x	2,200 or 750 + 610x
f-z Curve Parameters:			
n	1.0	1.0	1.0
f_{max} (klf)	1.3	3.6	6.22
k_v (ksf)	620	1,700	2,960
q-z Curve Parameters:			
n	1.0	1.0	1.0
q_{max} (ksf)	3.6	14	45
k_q (kcf)	1,700	6,700	21,000

Table 2.5. Typical soil properties and curve parameters for an HP10 × 42 pile in sand.

	Loose	Medium	Dense
Soil Properties:			
Blow count, N	5	15	30
Effective unit weight, γ (pcf)	55	60	65
Angle of friction, ϕ	30°	35°	40°
p-y Curve Parameters:			
n	3.0	3.0	3.0
p_u (klf)	$0.070x^2 + 0.12x$ for $x \leq 20$	$0.15x^2 + 0.17x$ for $x \leq 18$	$0.26x^2 + 0.24x$ for $x \leq 22$
	$1.5x$ for $x > 20$	$2.9x$ for $x > 18$	$5.9x$ for $x > 22$
k_h (ksf)	8.0x	27x	72x
f-z Curve Parameters:			
n	1.0	1.0	1.0
f_{max} (klf)	0.5	1.5	3.0
k_v (ksf)	150	450	900
q-z Curve Parameters:			
n	1.0	1.0	1.0
q_{max} (ksf)	40	120	180
k_q (kcf)	12,000	36,000	55,000

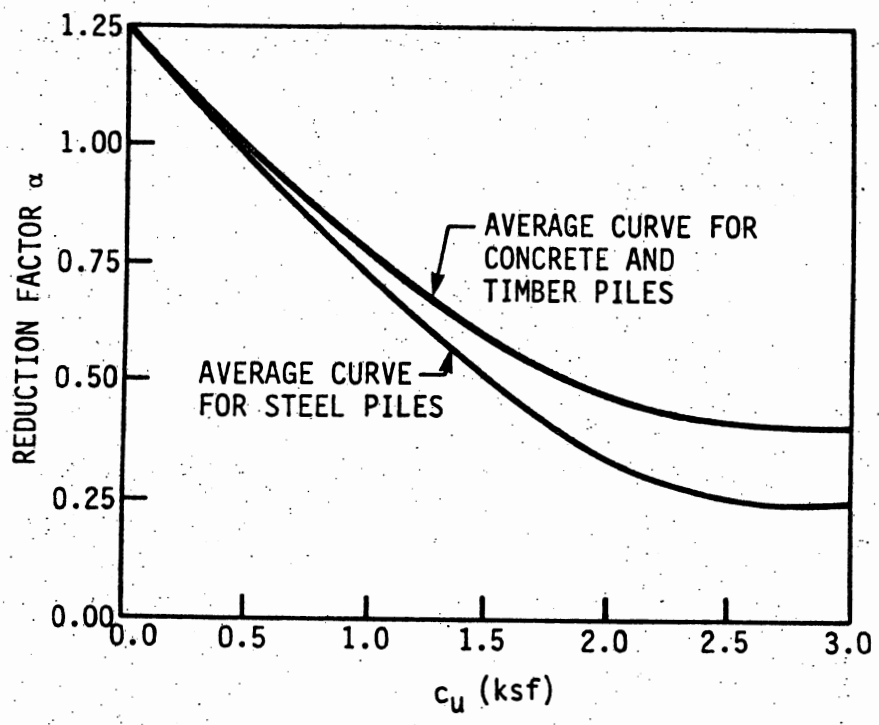

Figure 2.4. Reduction factor α [1].

For practical purposes, k_h is often assumed to be constant or to vary linearly with depth. Uncertainty in estimating soil behavior from standard soil tests will usually be consistent with the errors introduced by the use of such a simple soil modulus versus depth function [13]. For the parameters presented in Tables 2.1 through 2.5, the subgrade-reaction modules for clay soils are assumed to be constant within a soil layer and to vary linearly for granular soils. (The pile test reported herein did not use these assumptions because a more accurate variation was determined.)

2.3. Finite Element Pile Model

To better understand the behavior of the piles in an integral abutment bridge, a two-dimensional, nonlinear, finite element program (IAB2D) has been written previously [1]. It is a nonlinear finite element program with materially and geometrically nonlinear, two-dimensional beam elements and a nonlinear Winkler soil model for the vertical, horizontal, and pile tip springs (Fig. 2.1). The program assumes that the soil resistance and displacement relationships and the pile stress-strain relationship are in the form of Ramberg-Osgood curves. The program allows general variations in soil and pile properties with depth. Any combination of specified loads and displacements can be assumed. Load and displacement boundary conditions can be varied during an analysis. Output from the program consists of nodal displacements, element forces at each load and displacement increment, and final reactions. A three-dimensional version, IAB3D, was also developed.

Guidelines for using this program were developed on the basis of the experience gained during the previous work. In the region of high curvature gradients, a finer mesh is necessary to obtain satisfactory solutions. For inelastic problems, high curvature gradients occur in the region of a plastic hinge and a finer mesh is required to achieve comparable accuracy. Also, the mesh must be sufficiently fine to model changing soil and pile properties.

Several numerical example problems were solved by using the computer program IAB2D. As mentioned in a previous report [17], a beam-column problem and a short, thick column problem were first used to check geometric and material nonlinearity, respectively. Additional problems were introduced: (1) a snap-through problem, (2) a Williams' toggle problem, (3) a two-dimensional frame problem, (4) a thermal problem, and (5) a soil problem. The solutions from the finite element program compare very well with the theoretical solutions.

The results from four experimental pile tests by others were also compared to results from the IAB2D program. The experimental tests consisted of an axial load test on a point-bearing H-pile, lateral load tests on drilled concrete piers and on timber piles, and axial and combined load tests on a timber pile [18]. In general, the results of the finite element program were close to the experimental results. An exception to this was for the lateral load tests on instrumented timber piles. The main reason for the discrepancy was the inability to model the soil adequately; this problem was described in quite general terms in the original paper [19].

As outlined in Section 1, this project includes full-scale and 1/10-scale (model) tests. These test results and their comparison to the IAB2D results are reported in Sections 3 and 4.

2.4. Simplified Method

A simplified method for analyzing piles in integral abutment bridges was presented in Ref. [1]. The model was developed from previous analytical models and observations of pile behavior. The soil was idealized as illustrated in Fig. 2.2 and described in Section 2.2. The two failure modes examined for a pile were the slip mechanism, where the pile slips through the soil, and the lateral mechanism, where the pile deflects laterally. Equations for determining the ultimate load for the pile for each mechanism were obtained. The simplified model was compared to results from the finite element program and was shown to be conservative.

For the slip mechanism, the load capacity, P, of the pile is equal to the sum of the maximum load carried by skin friction along the length of the pile and the maximum load carried by bearing at the pile tip. This load can be calculated from

$$P = \Sigma f_{max} \ell + q_{max} A_e \tag{2.3}$$

where ℓ is the embedded length of the pile and A_e is the effective pile tip area. For an H-pile, A_e is the rectangular area formed by the section depth and the flange width.

Failure of the soil and pile system can also be associated with lateral movement of the pile. This movement activates the lateral soil springs. As an example, consider the pile in Fig. 2.5a. (Note: the slip mechanism has been eliminated by the bottom support.) This pile has lateral restraint, representing the abutment, at the pile head. The pile is given a horizontal displacement, Δ, to simulate the expansion or contraction of the superstructure. If the movement is sufficiently large, a plastic hinge may form near the top of the pile. An axial load, P, representing the live load on the bridge, is then applied to the pile. If geometric instability were the only collapse consideration; that is, if the material does not yield, the ultimate load would equal the elastic buckling load, P_e. This is the perfectly elastic case illustrated on the left in Fig. 2.5b. (The elastic buckling load for an initially bent column is equal to the elastic buckling load for a straight column provided the initial imperfections are relatively small [20]). On the other hand, if collapse were due only to material yielding, that is, no geometric instability, the plastic mechanism load, P_p, would occur when a sufficient number of plastic hinges form to produce a plastic mechanism. The rigid, perfectly plastic case on the right of Fig. 2.5b illustrates this situation. For pinned-head piles, the plastic mechanism load is

$$P_p = \frac{2M_{pc}}{\Delta} \tag{2.4}$$

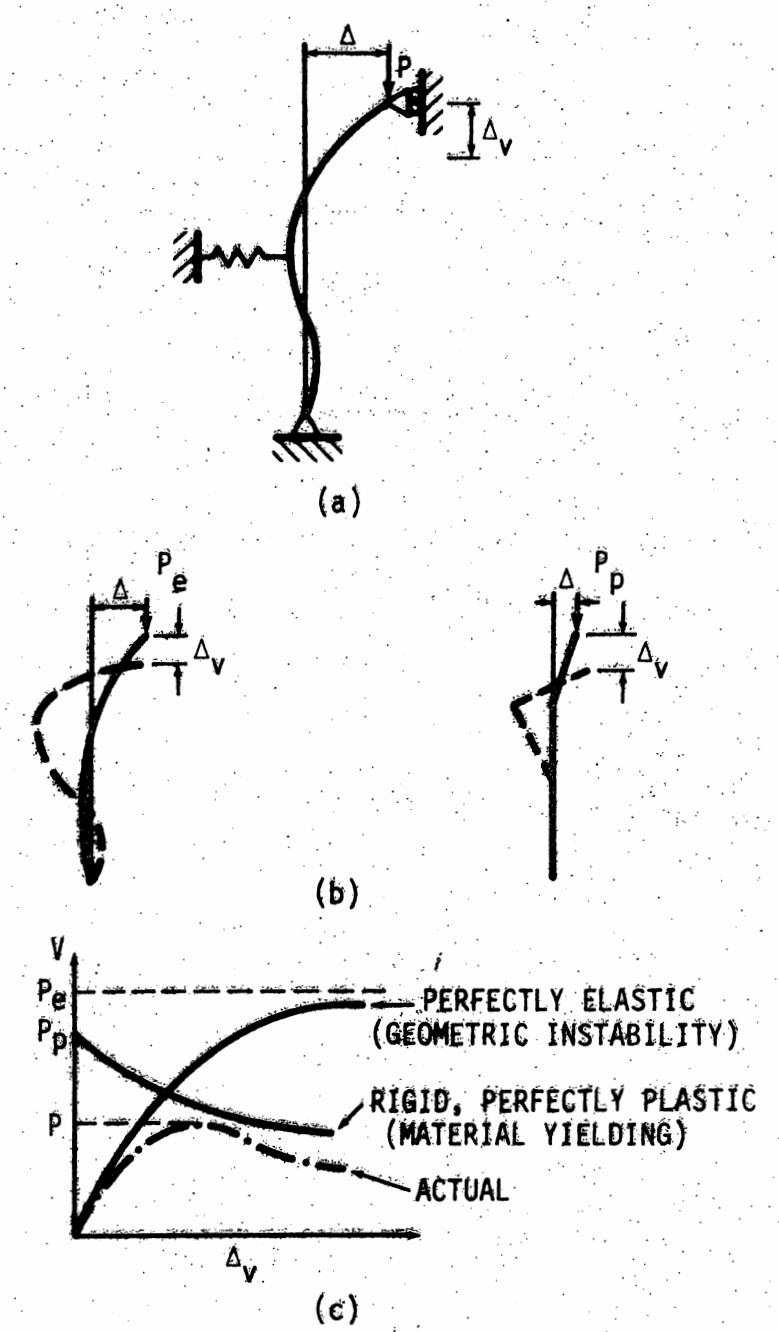

Figure 2.5. Example illustrating lateral mechanism: (a) schematic drawing of the pile and soil (b) failure modes (c) load-displacement curves for the pile.

and for all fixed-head piles, it is

$$P_p = \frac{4M_{pc}}{\Delta} \tag{2.5}$$

where M_{pc} is the plastic moment capacity of the pile reduced for axial load [21]. For example, for a rectangular cross section this relationship is

$$\frac{M_{pc}}{M_p} = 1 - \left(\frac{P}{P_y}\right)^2 \tag{2.6}$$

where M_p is the full moment capacity and P_y is the yield load. Load-displacement curves for each extreme case, namely geometric and material instability, are illustrated in Fig. 2.5c.

In general, both geometric and material effects interact such that the actual load versus displacement behavior, as observed from IAB2D and experimental results, is similar to that illustrated in Fig. 2.5c. The actual curve is bounded by the curves for P_p and P_e. The resulting ultimate load, P, sometimes called the inelastic buckling load, is lower than either the elastic buckling load, P_e, or the plastic mechanism load, P_p. The design method was not intended to predict this complete curve. However, a conservative estimate of the ultimate load, P, was obtained by using the Rankine equation [6,20].

$$\frac{P}{P_e} + \frac{P}{P_p} = 1.0 \tag{2.7}$$

This equation combines both geometric and material instabilities.

The results obtained when using the Rankine equation are compared with those obtained using the finite element program (IAB2D) in Fig. 2.6 [1]. For all the examples an HP10 × 42 pile was used. The pile was bent about the weak axis and had a modulus of elasticity of 29,000 ksi and a yield stress of 50 ksi. Even though the soil types with parameters equal to 1/5 of the values for soft clay are unrealistic, these parameters were used to check the Rankine equation for a greater range of soil parameters. Because of conservative approximations made in determining Eqs. (2.4) and (2.5), the plastic mechanism load, P_p, is conservative (see points near the ordinate in the figure). The figure also shows that plasticity effects tend to dominate the behavior of piles in realistic soil types and that elastic buckling is unlikely to occur; that is, the points tend to be in the upper left corner of the figure.

One reason for the development of the design method to be presented in Section 5 is that the Rankine equation (Eq. (2.7)) is too conservative, particularly for small horizontal displacements. For example, for a column with Δ equal to zero, the mechanism load, P_p, is equal to the yield load, P_y. (To see this, multiply Eq. (2.4) by Δ. If Δ is equal to zero, M_{pc} must be equal to zero. The quantity M_{pc} will equal zero only if the axial load is equal to the yield load.) Equation (2.7) can then be restated in the following form:

$$\frac{P}{P_y} = \frac{1}{1 + \frac{P_y}{P_e}} \tag{2.8}$$

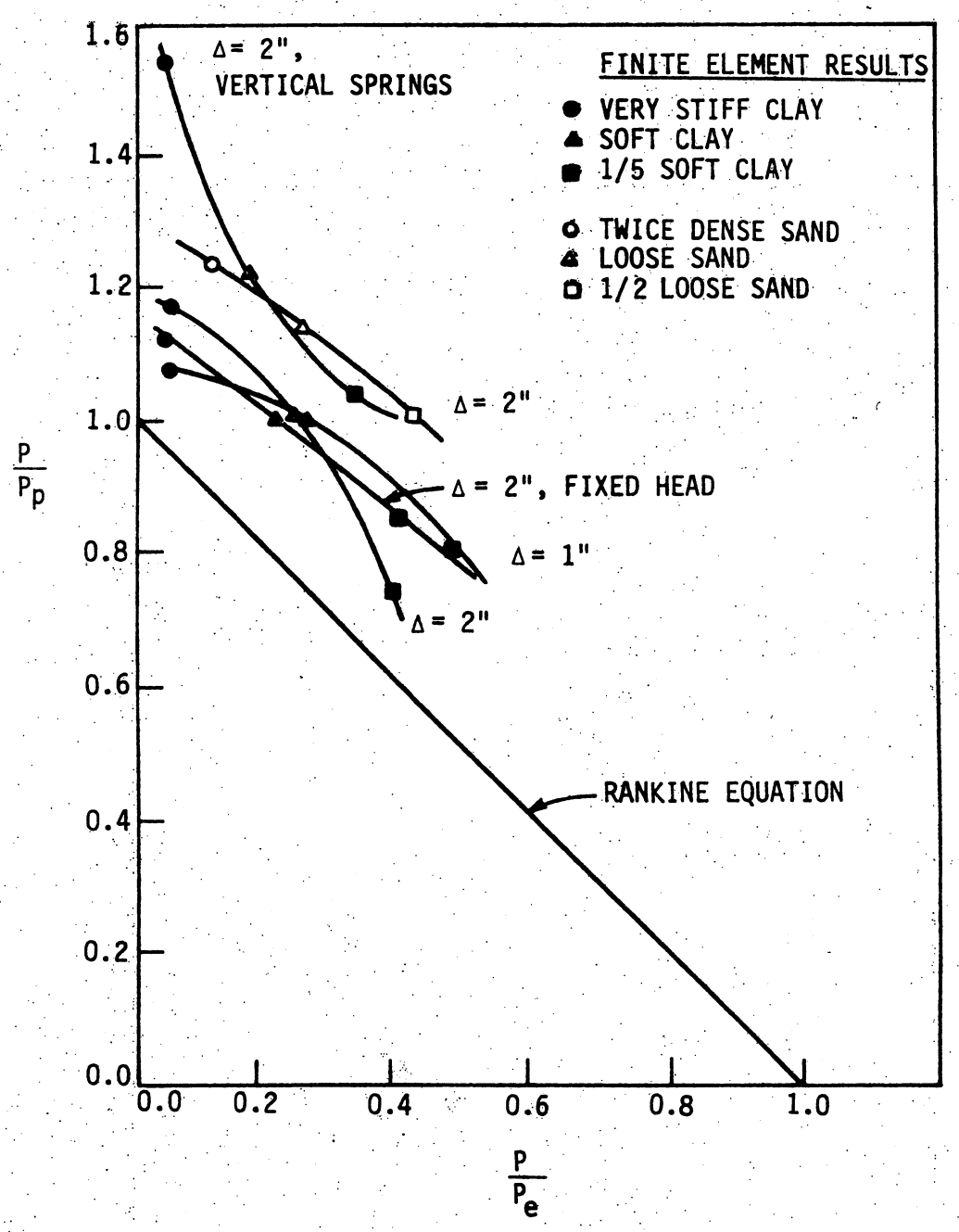

Figure 2.6. Comparison of Rankine equation and finite element results [1].

On the other hand, the AASHTO Specification Eq. (10-151) [22] for short and intermediate length columns can be rewritten, without a factor of safety, as

$$\frac{P}{P_y} = \left(1 - \frac{P_y}{4P_e}\right) \tag{2.9}$$

For P_y/P_e equal to 1.0, the values of P/P_y from Eqs. (2.8) and (2.9) are 0.5 and 0.75, respectively. Hence, for this case the result from the Rankine equation (Eq. (2.8)) is 33% more conservative than that from the AASHTO equation.

3. FIELD TESTS

3.1. Objective and Scope

A full-scale field testing program was established for isolated steel HP-shaped friction piles to determine whether the longitudinal expansion and contraction of the bridge superstructure affects the vertical load capacity of the abutment piling. The experimental testing was also developed to substantiate pile behavior predicted by analytical modeling involving finite element techniques. Three independent loading conditions were applied to instrumented test piles. First, a vertical load test was performed to determine pile behavior and to establish modified Ramberg-Osgood soil response characteristics involving skin friction and vertical displacement (f-z curves) and bearing and tip displacement (q-z curves) relationships. A second field test consisted of applying a horizontal load on another steel test pile to establish pile behavior for lateral loads and to establish modified Ramberg-Osgood soil response characteristics involving lateral resistance and lateral displacement (p-y curves) relationships. A third field test involving a vertical load test on a horizontally displaced pile was conducted to compare experimentally and analytically derived pile displacements and internal pile forces. Also, the combined load test provided a direct experimental comparison with the vertical load test, since both tests were performed on the same test pile.

3.2. Field Test Program

3.2.1. Test Site

The site for the pile field tests was located adjacent to the Structural Engineering Laboratory on the northwest corner of the Iowa State University campus. A subsurface soil investigation was conducted by drilling two 50-ft-deep borings to obtain Shelby tube samples for laboratory testing, to perform standard penetration tests by split spoon sampling, to determine general soil classification, to determine the depth to the water table, and to confirm that bedrock did not occur within 10 feet below the bottom of the test piles. The boring records along with the laboratory soil test results and a more detailed site description can be found in Section 10.1.1 of Appendix A. The substrata consisted of weathered and unweathered glacial till, which was composed of silt and clay with sand and gravel inclusions that had a stiff to hard consistency.

3.2.2. Test Framework

An elaborate test framework consisting of anchor beams, girders, and spreader beams, as shown in Figs. 10.1-10.5, was designed to accommodate the three field tests conducted on two HP10 × 42 test piles (Piles P1 and P6). The frame was designed to resist uplift forces of up to 400 kips and lateral thrust forces of up to 50 kips. The applied vertical loads for the first and the third field tests were resisted by a 200-ton-capacity jacking beam, provided by the Iowa DOT, that transferred the uplift forces to four HP10 × 42 vertical reaction piles. The applied horizontal loads for the second field test of another

HP10 × 42 test pile were resisted by the weak-axis bending strength of the same four vertical reaction piles. For the third field test involving combined loading on the first test pile, the applied lateral loads were resisted by the strong-axis bending strength of the second test pile. The locations for the test and reaction piles were established to comply with the spacing requirements specified by the ASTM standards for vertical load tests [23] and lateral load tests [24]. A more detailed description of the testing frame and load system can be found in Section 10.1.2 of Appendix A.

3.2.3. Instrumentation Framework

The instrumentation required to monitor the displacements of the two test piles was mounted on steel beams spanning between short HP10 × 42 steel piling. The support piles were located beyond the recognized zone of influence of the test and reaction piling for both vertical [23] and lateral loading [24] to minimize any detectable movement of the instrumentation framework, which would introduce errors into the measured displacements. Also, the instrumentation beams were positioned within a covered trench to prevent extreme temperature variations that would significantly change the length of the instrumentation beam and to protect the beam from wind-induced lateral displacements or oscillations during the testing. Section 10.1.3 in Appendix A provides additional information on the instrumentation framework and supports.

3.2.4. Test Pile Descriptions

The two 50-ft-long HP10 × 42 test piles had electrical resistance strain gages mounted along their length. To protect the gages and the wire leads, embossed sheet metal cover plates and conduits were fabricated

and welded to the test piles after waterproof coatings had been applied to the gages and wire lead connections. The wires were fastened to the pile within the length of the conduits and near the top of the pile within a sheet metal enclosure. The elaborate protection system for the strain gages and wire leads was required to minimize damage caused by the pile driving operations. Specific details of the test pile preparation is given in Section 10.1.4 of Appendix A.

The test piles were driven with a 5700-lb gravity hammer that produced a hammer energy of 19.95 ft-tons from a drop height of 7 ft. A pile driving log was made by personnel from the Materials Division of the Iowa DOT to obtain a bearing capacity for the piles at various penetration depths. At the selected 40-ft embedment depth for each test pile, the calculated allowable pile bearing capacities were 38.7 tons and 39.7 tons for Test Piles P1 and P6, respectively. The pile formula [25] used to determine these bearing loads is given by Eq. (3.1).

$$P = \left[\frac{3WH}{S + 0.35}\right]\left[\frac{W}{W + M}\right] \tag{3.1}$$

where P is the safe bearing load (tons), W is the weight of the hammer (tons), H is the hammer freefall height (ft), S is the average penetration of the pile for the last five blows (in./blow), and M is the pile weight plus the pile cap weight (tons).

3.2.5. Vertical Load Test

The axial compression test of Test Pile P1 was conducted on October 3, 1986, approximately 16 weeks after the piles were driven. The testing procedure and measurement techniques discussed in Section

10.2.1 of Appendix A are similar to the Standard Loading Procedure of the ASTM Standard [23]. The axial load was applied in increments of 20 kips by a 300-kip hydraulic ram. At each load level, a convergence settlement rate of 0.01 in./hr was satisfied, while the applied load was maintained, before the load was considered to be resisted successfully. Throughout the test, pile strains and displacements were monitored. The ultimate axial load was 280 kips, approximately 3.5 times the safe bearing capacity evaluated from the pile formula (Eq. (3.1)). An attempt to increase the test pile load to 290 kips resulted in a pile settlement of over 2.5 in. The entire vertical load test took 17 hours to complete.

3.2.6. Lateral Load Test

On October 16, 1986, approximately 18 weeks after the piles were driven, a lateral load test was performed on Test Pile P6. Section 10.2.2 of Appendix A contains a description of the test procedure. The test was conducted with displacement control, since pile response for a given lateral displacement was desired. Therefore, for each displacement increment the horizontal load was adjusted to maintain the specified total horizontal movement. This method of testing was quite sensitive to soil deformations, especially the relaxation of lateral soil pressures. Additionally, since the lateral load mechanism (see Section 10.1.2 of Appendix A) was attached to a horizontal girder, any changes in the girder length due to temperature fluctuations required adjustment of the lateral load to maintain the specified lateral displacement.

Before conducting the test, the maximum lateral displacement was established at approximately 2 in. This magnitude of movement was

considered to be comparable to the amount of expansion or contraction anticipated at one end of a long integral abutment bridge. The experimental results revealed that a horizontal force of 25 kips located 20.5 in. above the ground level caused the HP10 × 42 test pile to displace 2.06 in. laterally at the ground surface. The complete lateral load test lasted about 30 hours.

3.2.7. Combined Load Test

A vertical load test on a laterally displaced pile (Test Pile P1) was performed November 19-21, 1986. This test involved the testing procedures and instrumentation associated with the first two field tests. (Additional comments are in Section 10.2.3 of Appendix A.) The lateral loading portion of the test was conducted with displacement control, while the vertical load phase was performed with load control.

A light snowfall during the application of lateral displacements kept the air temperature constant; therefore, this portion of the test proceeded without any delays. However, during the process of changing from lateral load to vertical load, a test malfunction caused a complete loss of the lateral load. The lateral displacement was reapplied in approximately four equal amounts. An applied lateral load of 19.9 kips induced a lateral pile displacement of 1.93 in. at the ground surface.

As the vertical load was applied to the test pile, the lateral displacement increased slightly. At the ultimate vertical load of 280 kips, which was the same maximum load resisted when only a vertical load was applied to the test pile, the lateral pile displacement increased to 2.40 in. and the horizontal load decreased to 14.7 kips. The unloading of the test pile was accomplished in the reverse order

of the load application, following the same unloading sequences specified for the vertical and lateral load tests. The combined load test took approximately 48 hours to complete.

3.2.8. Field Test Comparisons

A summary of the three field tests is given in Table 3.1. The most significant observation involves the magnitude of the experimentally determined ultimate vertical load capacity for the friction test pile. The 2-in.-lateral displacement did not appear to affect the vertical pile capacity. Both the vertical load test and the combined load test, conducted on the same test pile, reached an ultimate vertical load capacity of 280 kips.

Strain gage and displacement reductions for analytical comparisons are discussed in the following sections.

3.3. Test Comparisons with IAB2D

3.3.1. Reasons for Comparisons

The computer program IAB2D was written during a previous phase of integral abutment bridge research to provide an analytical method that describes the behavior of a pile subjected to vertical and lateral loads. As discussed in Section 2, the soil medium was idealized by isolated, nonlinear springs located at the pile element nodes. The vertical and horizontal springs along the pile and the vertical spring at the pile tip represent the skin friction and lateral load resistances and the end-bearing resistance, respectively. The behavior for each

Table 3.1. Field testing summary.

	Vertical Test Pile P1	Lateral Test Pile P6	Combined Test Pile P1
Pile orientation	N.A.*	Strong-axis	Weak-axis
Head condition	Pinned horizontally	Free	Continuity with horizontal girder
Test control	Load	Displacement	Vert. load and hor. displacement
Max. vertical load	280 kips	N.A.	280 kips
Vertical disp.	0.44 in.	N.A.	0.93 in.
Max. horizontal load	N.A.	25.0 kips	19.9 kips to 14.7 kips
Horiz. disp.	N.A.	2.06 in.	2.04 in. to 2.40 in.

*N.A. = not applicable.

of the three types of soil springs was assumed to be uncoupled and described by a modified Ramberg-Osgood equation.

The finite element model has been confirmed previously by solving both theoretical and experimental problems [1]. To further substantiate the validity of the IAB2D computer model, comparisons have been made between the results from the three field tests conducted during this phase of research and the predicted behavior obtained from IAB2D. In Section 4 similar comparisons have been presented between the scale-model pile tests and the computer solutions.

3.3.2. Vertical Load Test and IAB2D

The axial compressive load capacity of a vertical friction pile is provided by skin friction along the pile length and end-bearing resistance at the pile tip. The relationship between the skin friction resistance, f, and the relative vertical displacement, z, is represented mathematically by the modified Ramberg-Osgood expression given in Eq. (3.2).

$$f = \frac{k_v z}{\left[1 + \left|\frac{z}{z_u}\right|^n\right]^{1/n}} \tag{3.2}$$

where

$$z_u = \frac{f_{max}}{k_v} \tag{3.3}$$

The three parameters establishing the soil response are the initial vertical stiffness, k_v; the maximum friction force, f_{max}; and the shape

factor, n. These design parameters are required to model the nonlinear, vertical soil springs along the pile length in IAB2D. Curves of the modified Ramberg-Osgood equation expressing the f-z soil relationship at three soil depths with n equal to unity and the variation in k_v and f_{max} along the length for Test Pile P1 were developed and are discussed in Section 10.3.2 of Appendix A.

To mathematically model the soil behavior at the pile tip, the bearing stress, q, and the tip settlement, z, relationship was represented by the modified Ramberg-Osgood expression

$$q = \frac{k_q z}{\left[1 + \left|\frac{z}{z_n}\right|^n\right]^{1/n}} \tag{3.4}$$

where

$$z_u = \frac{q_{max}}{k_q} \tag{3.5}$$

The three parameters that establish the stress and displacement relationship are the initial point stiffness, k_q, the maximum bearing stress, q_{max}, and the shape factor, n. The soil response at the pile tip was revised as discussed in Section 10.3.3 of Appendix A because the axial load at the bottom of the pile was unavailable. A revised soil bearing stress, q', that includes the skin friction resistance for the bottom 5.5 ft of the pile in addition to the tip bearing stress was developed. The revised pile displacement corresponding to q' is z', which is the

pile displacement at 5.5 ft from the pile bottom. With these revisions, Eqs. (3.4) and (3.5) become

$$q' = \frac{k'_q z'}{\left[1 + \left|\frac{z'}{z'_u}\right|^n\right]^{1/n}} \tag{3.6}$$

and

$$z'_u = \frac{q'_{max}}{k'_q} \tag{3.7}$$

The three parameters describing the modified soil spring at a point 5.5 ft above the actual pile tip are the initial modified point stiffness, k'_q, the maximum modified bearing stress, q'_{max}, and the shape factor, n. From the curve fit of the modified Ramberg-Osgood equation (Eq. (3.6) with n equal to unity) to the q'-z' data (Fig. 10.19), the values for k'_q and q'_{max} were established at 20.4 k/in.^{3} and 135 ksf, respectively.

The finite element model shown in Fig. 3.1 was used to analyze the test pile in the vertical load field test. Since the same element mesh was used to model the pile for the first and third field tests, shorter element lengths were required in the upper portion of the pile where the bending strains were greatest in the third field test. A supplemental study on the effect of mesh size was performed by comparing analytical results using the 32-element mesh shown in Fig. 3.1 to results obtained by eliminating every other node. A slight variation existed between the two solutions; therefore, the finer mesh was selected.

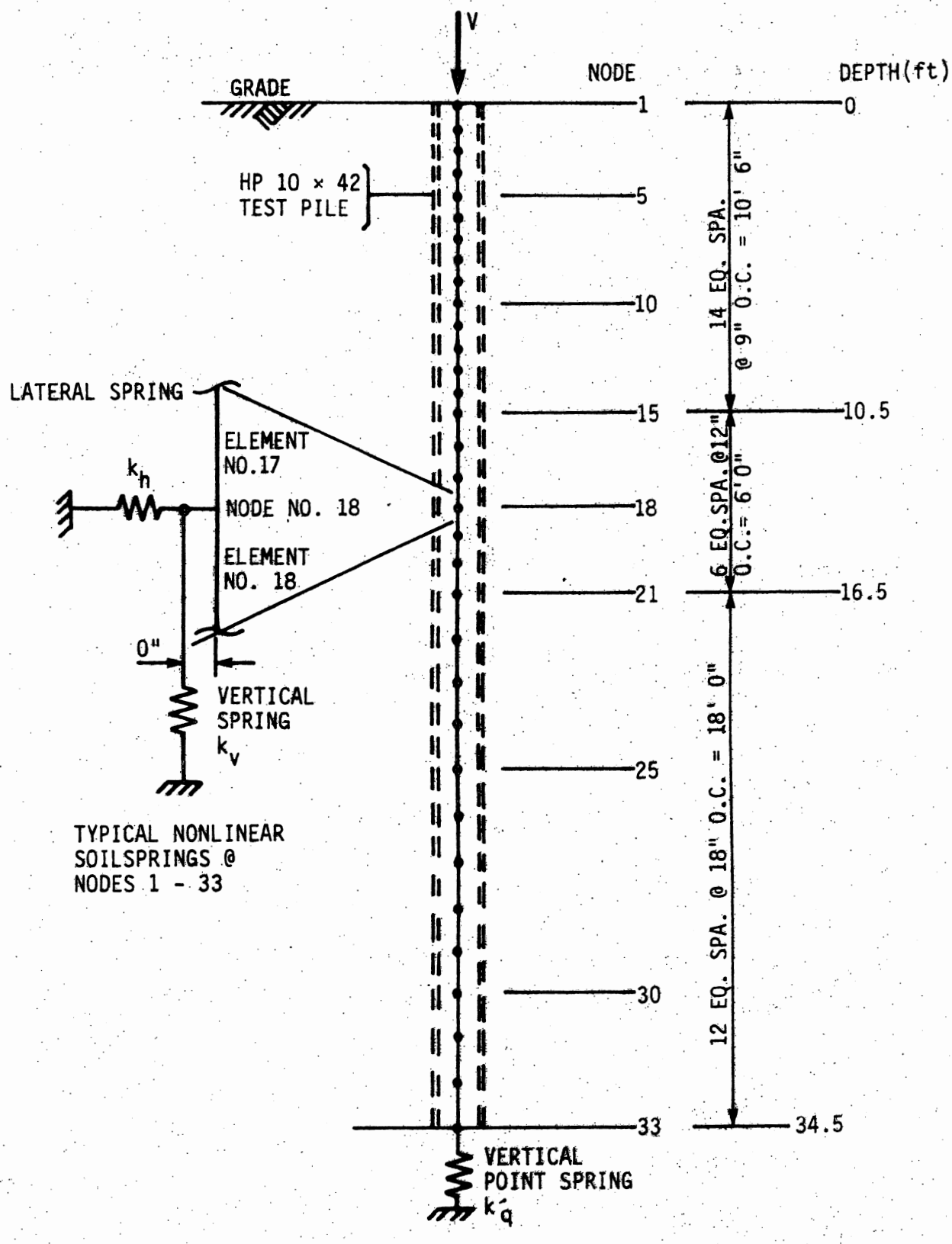

Figure 3.1. IAB2D model for vertical load test.

The soil behavior was modeled by three types of nonlinear springs attached at the pile nodes, as shown in Fig. 3.1. For the vertical springs, corresponding to the skin friction resistance, the soil parameters f_{max} and k_v were obtained from Appendix A, Figs. 10.16 and 10.17, respectively. Soil parameters p_u and k_h for the lateral springs, representing the lateral resistance of the soil, were obtained from the lateral load phase of the combined load test (Figs. 10.26 and 10.27) on Test Pile P1. The vertical point spring at the bottom of the pile was characterized by soil parameters q'_{max} and k'_q discussed in Eqs. (3.6) and (3.7).

Figure 3.2 shows a graph of applied axial compressive load versus vertical displacement of the pile at the ground surface that was generated by IAB2D with increasing magnitudes of applied vertical load at the top of the pile. Close correlation exists between the analytical solutions and the experimental results. The ultimate load predicted by IAB2D was about 278 kips as found by the method described in Ref. [26]; while the maximum load obtained during the vertical load field test was 280 kips.

Analytical and experimental axial pile forces along the length of the pile are compared for three magnitudes of applied vertical load in Fig. 3.3. The experimental axial force at the strain gage locations were computed by multiplying the axial strains (Fig. 10.10) by the axial rigidity of the pile, AE. The composite cross-sectional area of the test pile included the sheet metal conduits. Considering the load versus displacement and the axial load distribution results, the

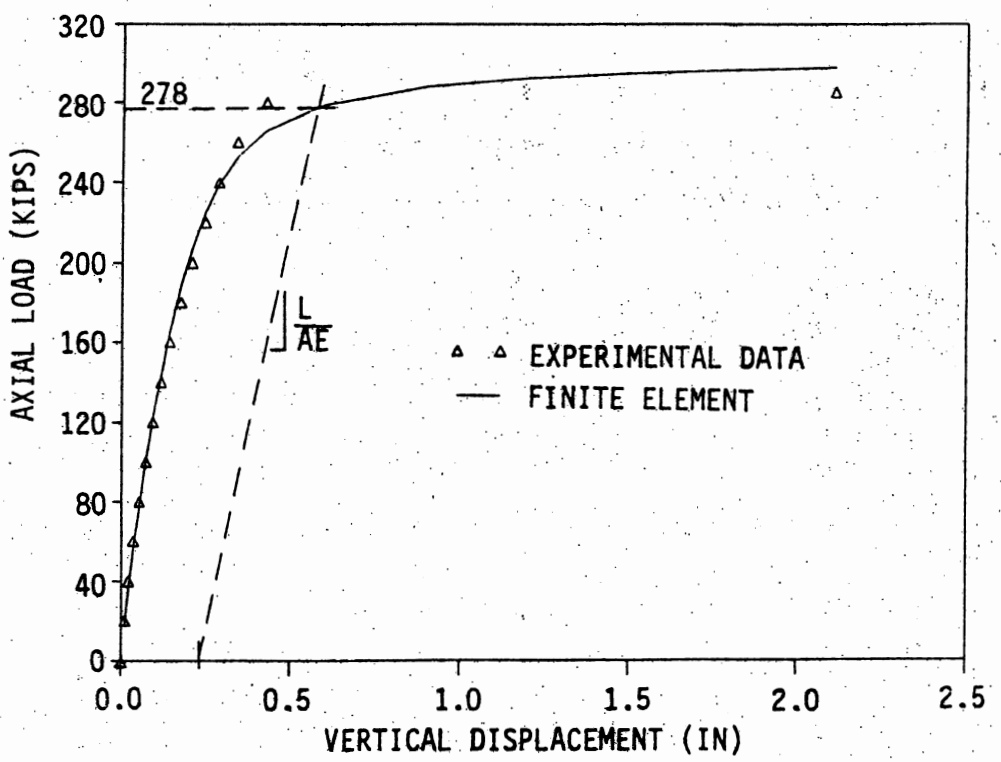

Figure 3.2. Axial load versus vertical displacement at grade for vertical load test.

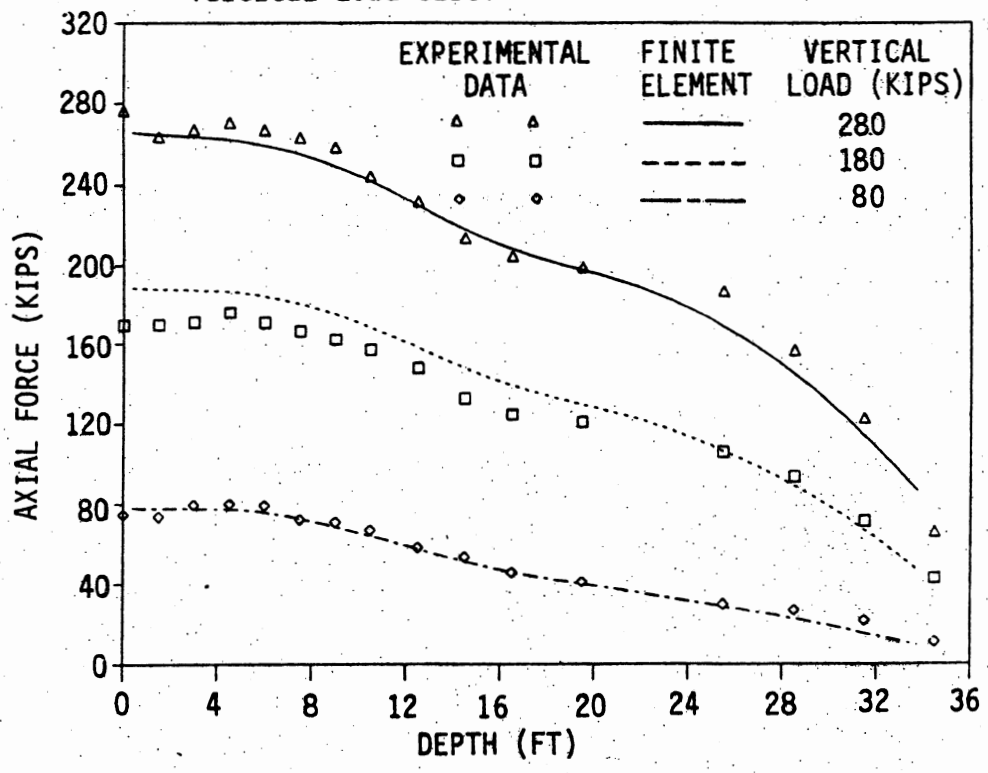

Figure 3.3. IAB2D and experimental axial forces for vertical load test.

computer program IAB2D provided an accurate representation of the test pile behavior for the vertical load field test.

3.3.3. Lateral Load Test and IAB2D

The lateral load capacity of a pile is provided by the flexural strength of the pile and the resistance of the soil to lateral displacement. To analytically model the lateral resistance, p, and corresponding lateral displacement, y, of the soil, the modified Ramberg-Osgood expression, given by Eq. (3.8), was selected to represent the nonlinear soil behavior.

$$p = \frac{k_h y}{\left[1 + \left|\frac{y}{y_u}\right|^n\right]^{1/n}} \tag{3.8}$$

where

$$y_u = \frac{p_u}{k_h} \tag{3.9}$$

This lateral soil response is characterized by three parameters. They are the initial lateral stiffness, k_h, the ultimate lateral resistance, p_u, and the shape factor, n. The modified Ramberg-Osgood equation parameters, p_u and k_h, needed to express the p-y soil relationship at any depth for Test Pile P2 were developed with n equal to two and are discussed in Section 10.3.4 of Appendix A, Figs. 10.26 and 10.27.

The analytical study of the lateral load test was performed with a finite element model that was similar to the model shown in Fig. 3.1. The element lengths were modified to locate every other node at a strain

gage station on the test pile. The vertical soil behavior, f-z and q'-z', was assumed to be the same as the vertical load test. To provide for application of the lateral load, the analytical pile model was extended 25 in. above the ground surface to match the load location for the field test pile. The bottom of the pile model was 34.5-ft deep, corresponding to the modified point spring location used in the model for the first field test.

Figure 3.4 shows the lateral load and displacement relationship for both the experimental and analytical studies of the second field test. The lateral displacement was at the ground surface. As shown in the figure, the analytical results closely match the measured experimental values.

The distributions for the pile bending moment at three magnitudes of lateral load are shown in Fig. 3.5. Both the analytical and experimental results showed that the maximum moment occurred at a depth of approximately 6 ft below the ground surface. The difference between the IAB2D and the test results in the bending moment at a particular depth were considered to be acceptable. Since reasonable agreement existed between the analytical study and the actual test results, the computer program IAB2D provided an accurate representation of the test pile behavior for the lateral load field test.

3.3.4. Combined Load Test and IAB2D

The IAB2D pile soil model for the vertical load test described in Section 3.3.2 was modified to analyze the pile during the combined load test. The majority of the finite element mesh spacing for the pile was kept the same as shown in Fig. 3.1; however, since the combined

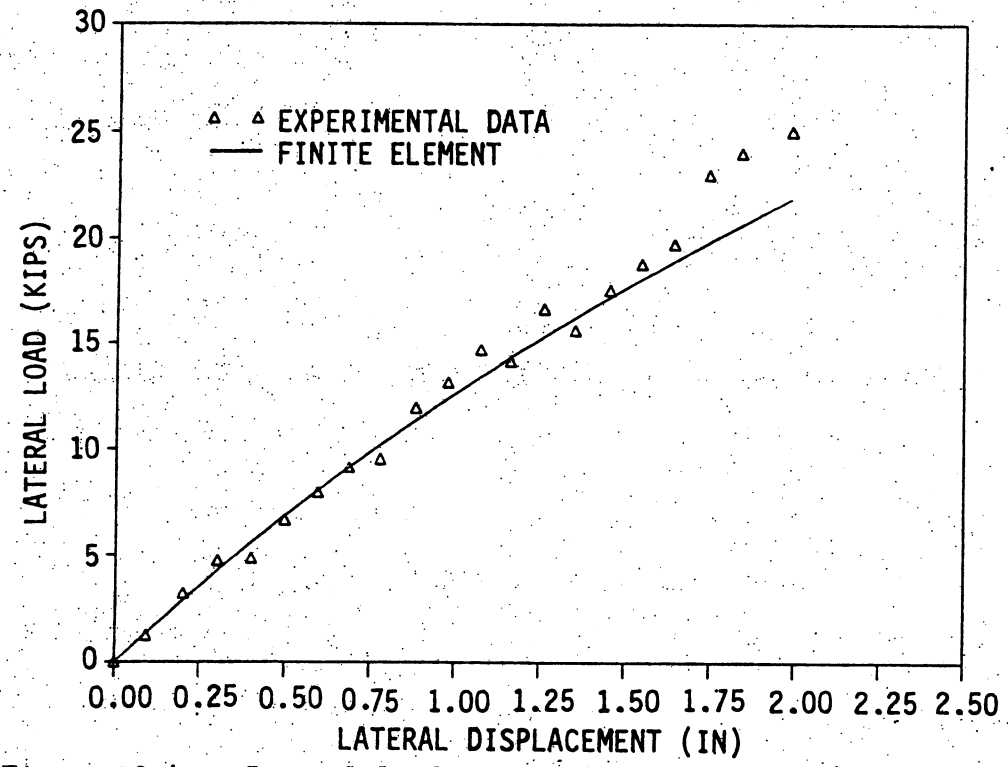

Figure 3.4. Lateral load versus lateral displacement at grade for lateral load test.

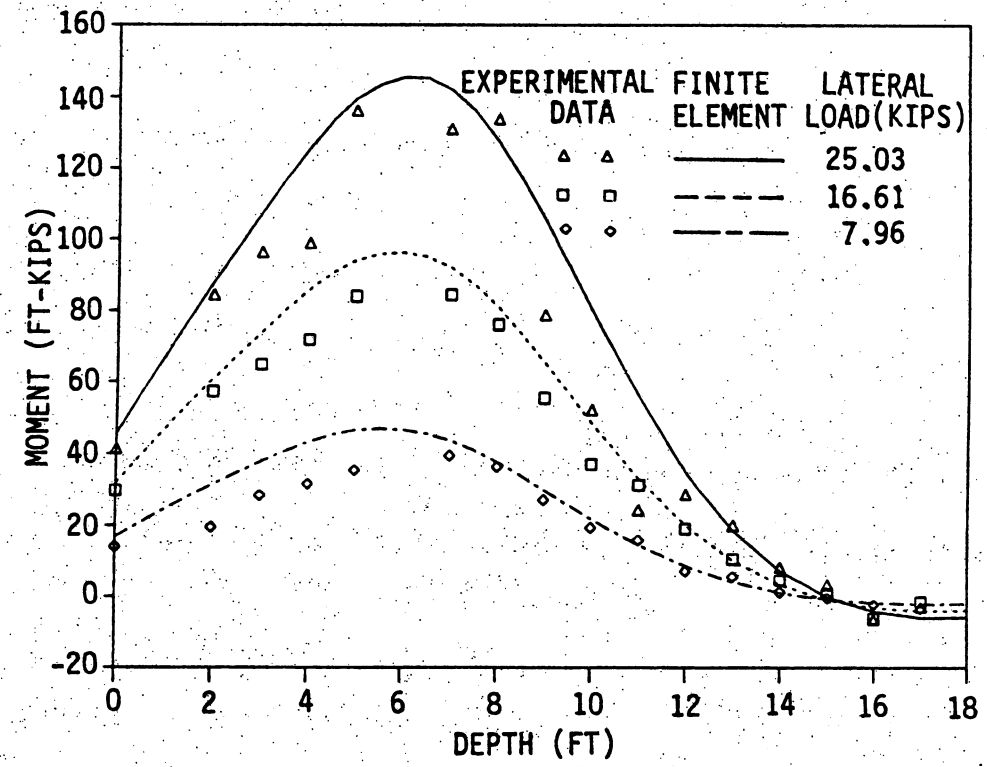

Figure 3.5. IAB2D and experimental bending moments for lateral load test.

load test involved restraint at the top of the pile, several elements were added to the pile above the soil surface and the two I-shaped bridge beams that were bolted to the test pile flanges at the top of the pile (Fig. 10.5) were included in the finite element model. The vertical soil springs describing the soil behavior for the f-z (Figs. 10.16 and 10.17) and q-z (Fig. 10.18) responses were identical with those used for the vertical load pile test analysis. The lateral soil springs were modeled by the p-y (Figs. 10.26 and 10.27) behavior established during the lateral load phase of the combined load test.

The load program for the IAB2D model followed the experimental load program. That is, the node at the west end of the horizontal girder was moved horizontally an amount equal to the experimentally applied lateral displacement. To simulate the second phase of the combined load test, a downward vertical force was applied to the node at the top pile. During the modeling of the vertical load phase of the combined load test, the analytical horizontal displacement was adjusted to match the measured experimental values.

The horizontal load versus horizontal displacement relationship is shown in Fig. 3.6 for both the experimental and IAB2D results. Good correlation occurred between the measured and analytical results, including the portion on the right where the horizontal force decreased as the displacements became greater than 2 in. This region represents the second phase of the test where the vertical loading was applied. The experimental data points and analytical vertical load versus displacement curve for the second phase of the combined load test is presented in Fig. 3.7. Again, the agreement between the measured and

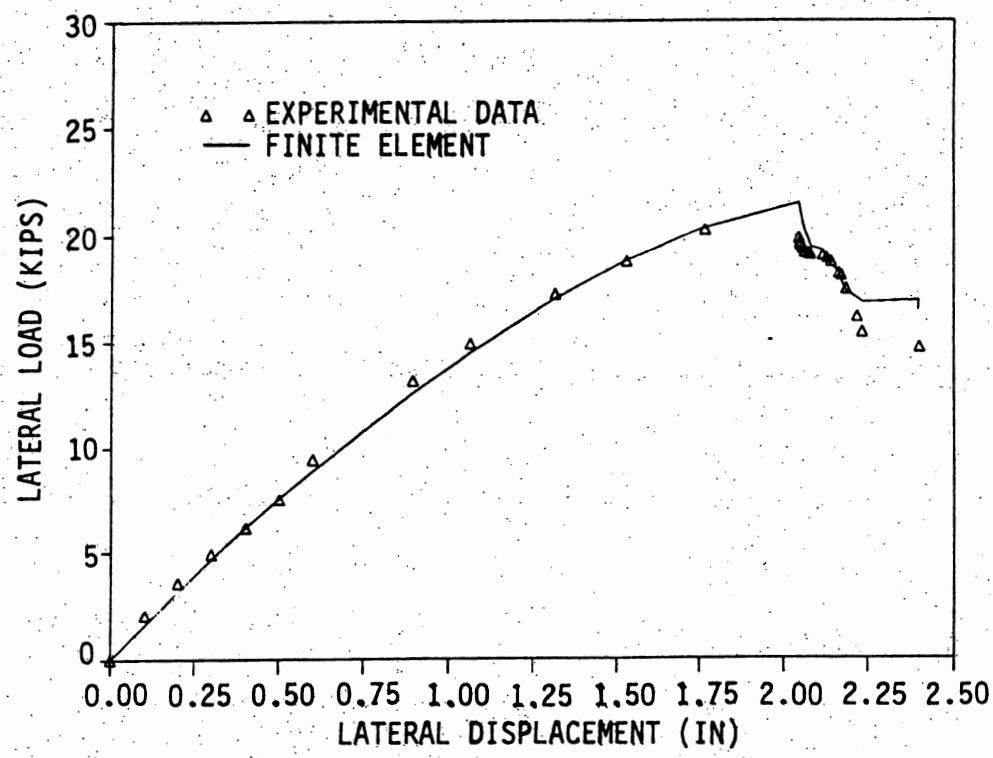

Figure 3.6. Lateral load versus lateral displacement at 13 in. above grade for combined load test.

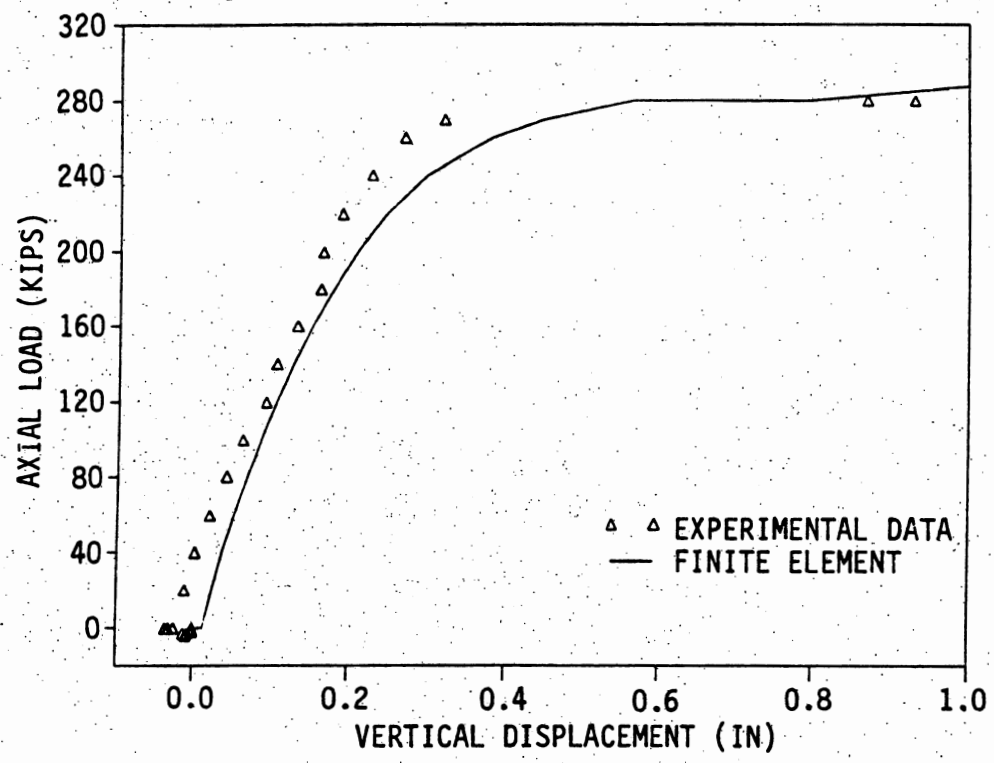

Figure 3.7. Axial load versus vertical displacement at grade for combined load test.

computed behavior is quite good. As shown in the figure, there is a slight initial offset to the experimental data and the analytical curve. The measured vertical displacements indicated that the test pile moved upward during the lateral load phase of the combined load test, while the analytical study predicted that the test pile would displace downward. This apparent discrepancy in the vertical displacement is attributed to the rapid loss of lateral load as discussed in Section 3.2.7. The experimental and analytical ultimate loads compare very well and, as mentioned in Section 3.2.8, are very close to the results for the first test with vertical load only.

The experimental and analytical strains in the pile flanges at the strain gage locations for several loading cases are illustrated in Fig. 3.8 for the lateral load phase and in Fig. 3.9 for the vertical load phase of the combined load test. These figures show the total strains in the east and west flange of Test Pile P1. In the lateral load phase (Fig. 3.8), IAB2D tends to underestimate the pile strain by 10% to 20%. On the other hand, IAB2D tends to overestimate the pile strains near the end of the vertical load phase (Fig. 3.9(d)). IAB2D seems to exaggerate the secondary bending moments that are associated with beam-column behavior (combined axial load and lateral displacement). The experimental test results showed little evidence of increased bending strains with the application of axial load. The experimental bending strains, obtained as the difference between the east and west total flange strains in Fig. 3.9(a) through Fig. 3.9(d) are about equal for all values of the vertical load.

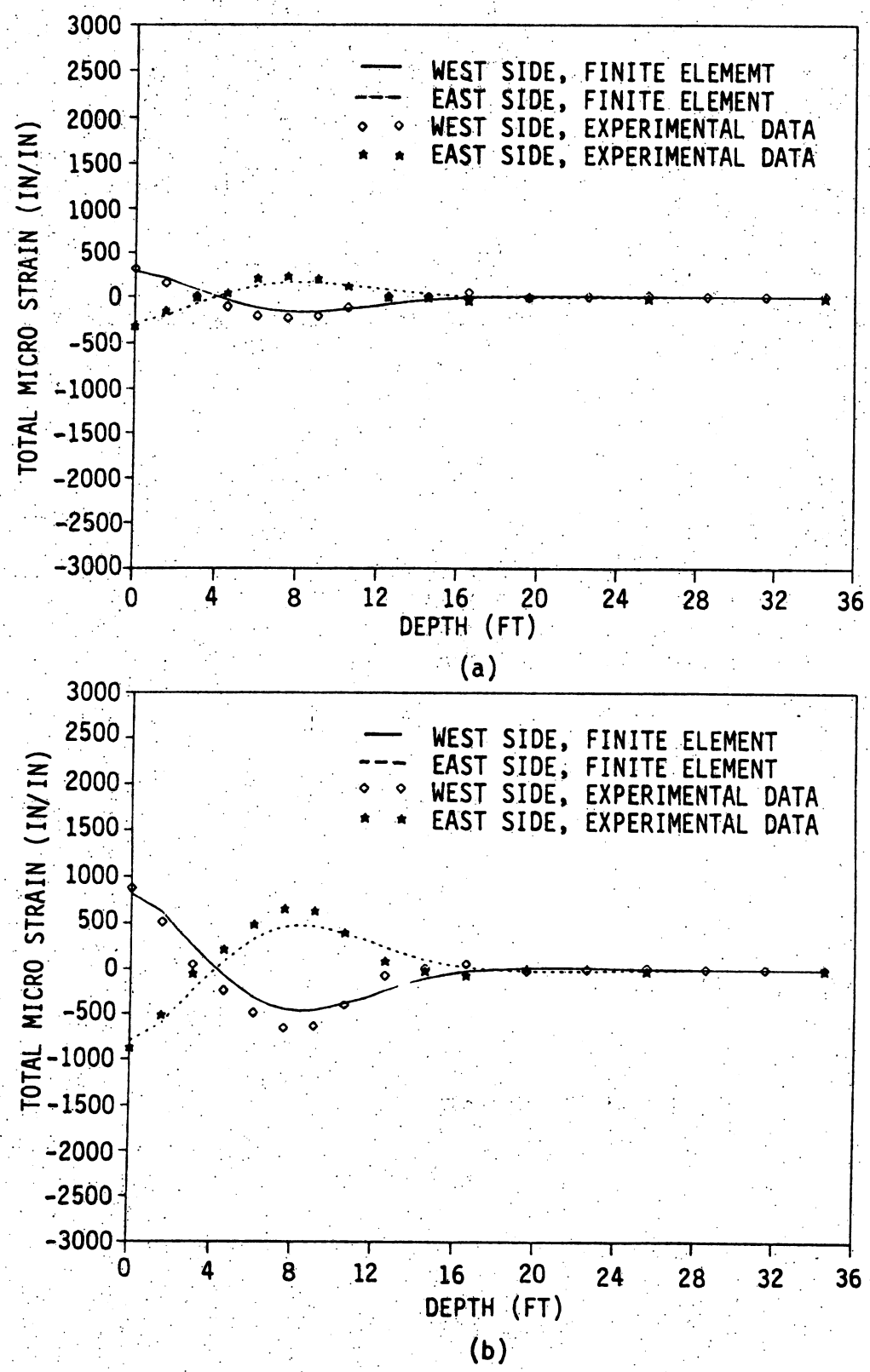

Figure 3.8. Pile strains during lateral load phase of combined load test: (a) at Δ_h = 0.30 in. (H = 4.9 kips) and V = 0 kips (b) at Δ_h = 0.89 in. (H = 13.1 kips) and V = 0 kips (c) at Δ_h = 1.76 in. (H = 20.2 kips) and V = 0 kips.

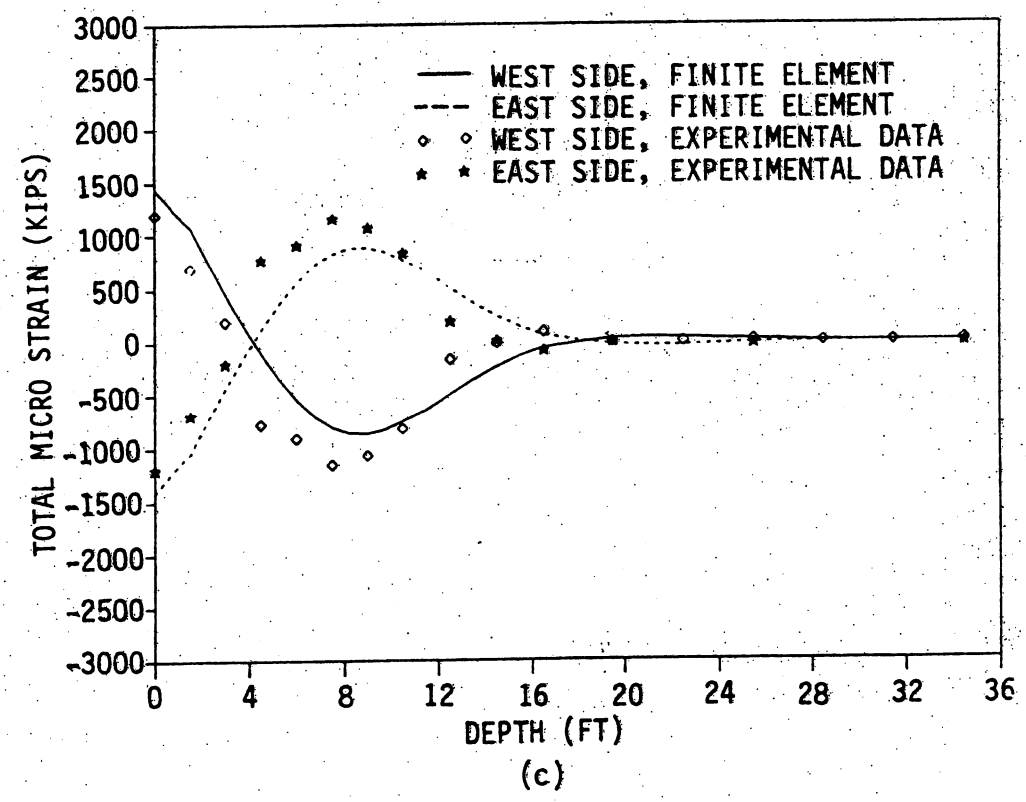

(c)

Figure 3.8. Continued.

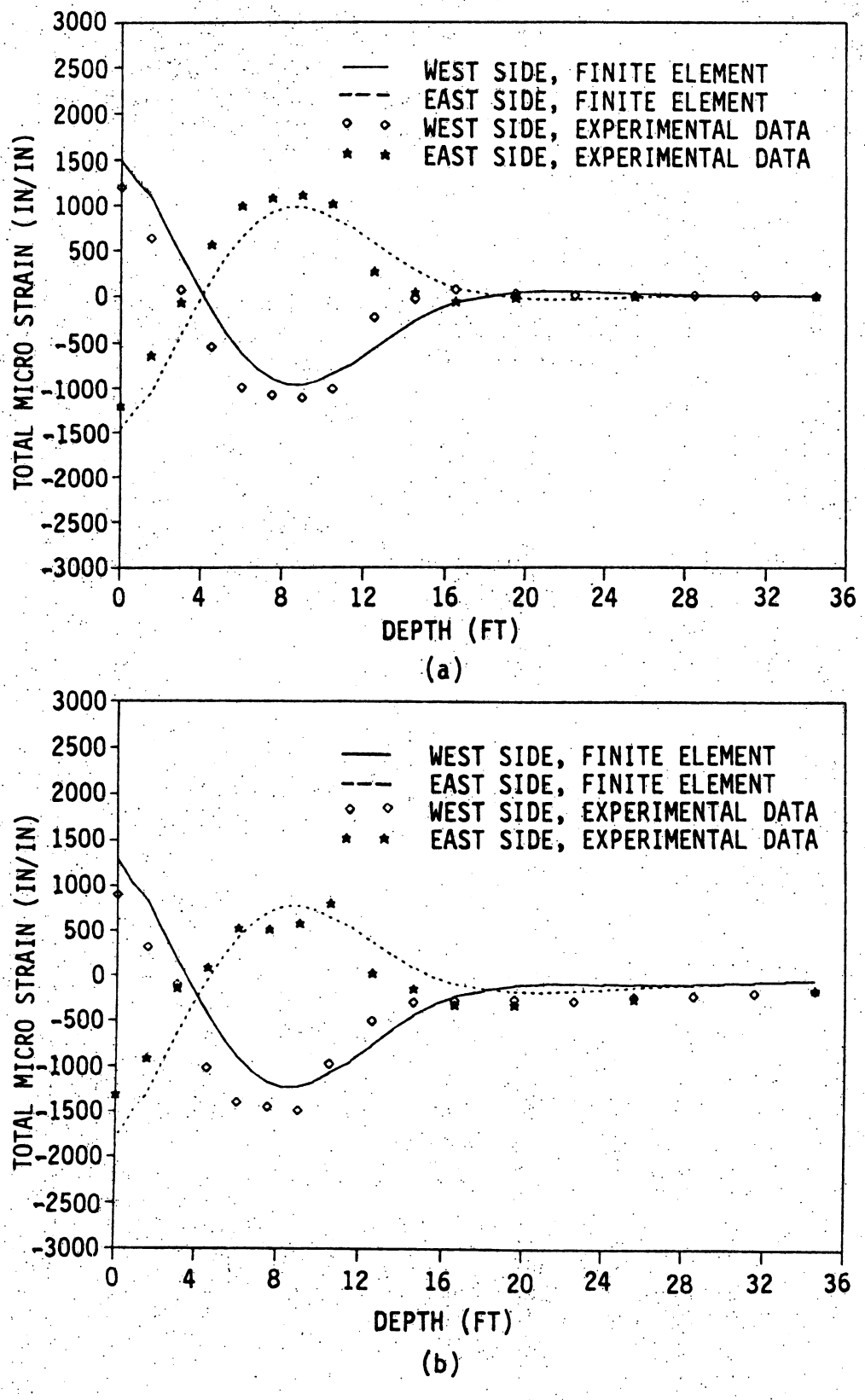

Figure 3.9. Pile strains during vertical load phase of combined load test: (a) at Δ_h = 2.04 in. (H = 19.9 kips) and V = 0 kips (b) at Δ_h = 2.07 in. (H = 19.1 kips) and V = 100 kips (c) at Δ_h = 2.16 in. (H = 18.2 kips) and V = 200 kips (d) at Δ_h = 2.40 in. (H = 14.7 kips) and V = 280 kips.

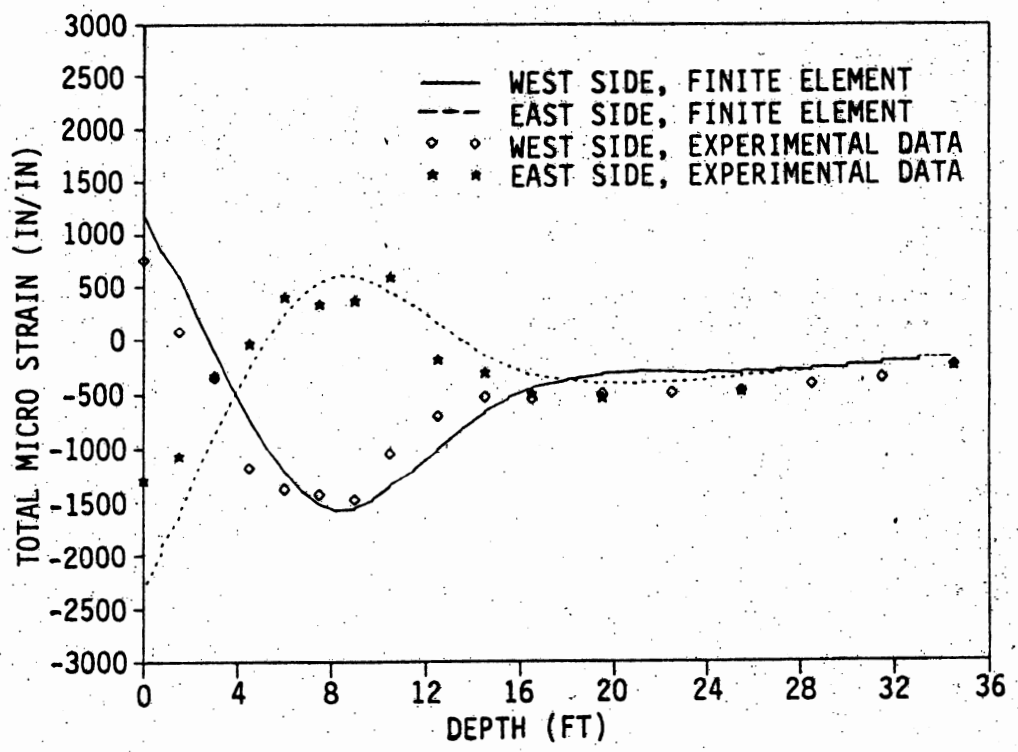

(c)

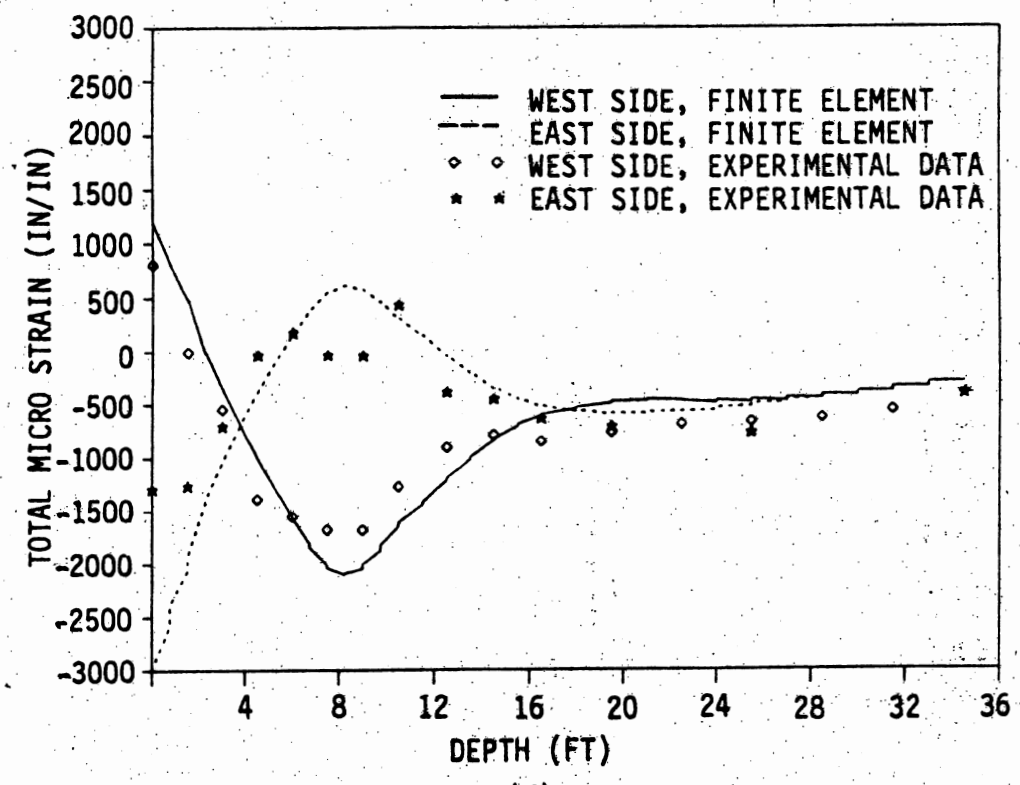

(d)

Figure 3.9. Continued.

The analysis of the pile behavior in the combined load test was sensitive to the lateral soil resistance and displacement relationship. Variations between the experimental and analytical total pile strains resulted when the p-y soil behavior from Test Pile P6 (Figs. 10.26 and 10.27) was applied to the analytical model for Test Pile P1. Correlation between the experimental and analytical results for Pile P1 was achieved only when the p-y soil behavior obtained from the lateral load phase of the combined test was incorporated into the analytical model. As discussed in Appendix A, the differences in the p-y soil behavior for Pile P1 and P6 were attributed to the lateral bearing surfaces of the pile against the soil, that is, flange face (Pile P6) bearing versus flange edge (Pile P1) bearing.

According to the IAB2D results, yielding of the steel occurred over a significant pile length at the top of the pile where it was rigidly attached to the horizontal girder. Strain gages were not mounted at this location on Pile P1 to confirm experimentally this state of stress. If such yielding occurred, a plastic hinge was partially or completely formed at the pile head. Since there was no experimental evidence of local flange buckling or hinge rotation, the HP10 × 42 had sufficient inelastic rotation capacity to maintain its full plastic moment.

Although one test is insufficient to draw firm conclusions, the strains in the lower portion of the pile (Fig. 3.9) illustrate that a possible coupling exists between the horizontal and vertical resistance of the soil. In the lower portion of the pile, the strains on both flanges were about equal; therefore, primarily axial load was present.

The experimental strains were consistently larger than the analytical strains, indicating that the lower portion of the pile carried more axial load than IAB2D predicted. From another viewpoint, the upper portion of the pile carried less axial load than predicted. This could suggest that the vertical frictional resistance in the upper portion of the pile embeddment has been degraded by the lateral displacement. IAB2D does not consider coupling of the soil resistance. Insofar as pile design is concerned, the degraded frictional soil resistance is discussed again in Section 5.3.

3.3.5. Summary of IAB2D/Field Test Correlation

In summary, IAB2D satisfactorily predicted the pile strains in the field tests, and the pile behavior results are sensitive to the experimental soil properties.

4. MODEL TESTS

4.1. Objective and Scope

A scale model testing program was developed to study the effects different pile head, load, and soil conditions had on the behavior of a single pile subjected to vertical, lateral, and combined loads. The laboratory testing program was performed to substantiate the underlying assumptions of pile and soil interaction used in the development of the analytical model, IAB2D. The pile strains at various locations along the pile length were measured to establish the soil response characteristics (f-z, q-z, and p-y), as described in Section 3, for the two sand densities in the model tests. The test program contained seven test groups involving from one test to three tests each. The applied load at the pile head was either a vertical, lateral, or combined load. Each particular test sequence was performed to examine experimentally pile behavior related to a particular test parameter. The test parameters that were considered were classified into four areas: (1) pile types (friction and end-bearing), (2) pile head types (pinned, fixed, abutment, and predrilled hole), (3) load types (vertical, lateral, combined, and lateral cyclic), and (4) soil types (loose sand and dense sand). In total, 40 laboratory model tests were conducted to establish testing procedures, calibration of equipment, sensitivity characteristics, and pile and soil behavior. Eleven of these tests were analyzed by the finite element computer model, IAB2D. A test matrix for these 11 laboratory tests is given in Table 11.2. A more

detailed description of the model tests can be found in Section 11.2.1 of Appendix B.

4.2. Model Test Program

A scaling factor equal to 1/10 was selected for the development of the scale model pile test program. As discussed in Section 11.1.1, complete similitude between a prototype system and a scale model was not required. The primary model components are the pile and soil medium. To model the HP10 × 42 pile that was used in the full-scale field tests (Sections 3 and 10), a 1-in.-square by 60-in.-long steel tube was selected. The vertical load tests, which were performed to determine vertical soil characteristics involving skin friction and vertical displacement (f-z curves) and tip bearing and tip displacement (q-z curves), require a small cross-sectional area to improve the sensitivity of the axial pile strains when vertical loads were applied at the pile head. The lateral load tests, which were conducted to determine lateral soil resistance and displacement (p-y curves) relationships, require a large bending stiffness characterized by a relatively thick wall thickness. As a compromise, a wall thickness of 0.032 in. was used for subsequent vertical, lateral, and combined loaded tests.

A fine, uniformly graded, dry, masonry sand was used for the model soil. The sand, obtained from a local supplier, was analyzed by laboratory tests as noted in Section 11.1.1 of Appendix B. A soil bin measuring

18-in. wide by 36-in. long by 72-in. high was used to contain the soil during tests.

The tests were constructed by positioning the pile in the soil bin and placing the soil around the pile. A soil placement technique was developed to produce soil structures that would be relatively consistent among similar tests. The placement technique was based upon the raining technique described by Monzoori et al. [27]. In-situ soil densities were calculated by measuring the volume of the known weight of each soil lift placed in the soil bin.

Additional discussion of the scale model components and a description of the test framework and pile instrumentation is contained in Sections 11.1.1, 11.1.2, and 11.1.3, respectively.

4.3. Model Test Comparisons with IAB2D

4.3.1. Reasons for Comparisons

To further substantiate the validity of the computer model, IAB2D, comparisons have been made between the experimental results for the model tests and the predicted behavior obtained from IAB2D. The laboratory model tests involved pile conditions that were not present in the full-scale field tests.

4.3.2. Vertical Load Tests and IAB2D

Two model pile tests with vertical compressive loads applied to the top of the test pile are reported herein. These laboratory tests included Test Sequences A-1 and D-1, which are described in Sections 11.2.1 and 11.2.2. The pile strains from these tests were analyzed to

determine characteristic soil parameters (f_{max} and k_v for Eq. (3.2) and q_{max} and k_q for Eq. (3.4)) according to the procedure described in Sections 11.3.2 and 11.3.3. These parameters along with the corresponding shape parameters, n, were used in the analytical model IAB2D to define the behavior of the nonlinear vertical soil springs along the length of the pile and at the pile tip.

The finite element models for the tests are shown in Fig. 4.1. For the vertical soil springs, corresponding to the skin friction resistance, the soil parameters f_{max} and k_v were obtained from Figs. 11.13 and 11.14 for loose sand and Figs. 11.15 and 11.16 for dense sand, respectively. To provide lateral stability at the nodes below the sand surface, horizontal soil springs that represent the lateral soil resistance were incorporated into the analytical pile model. The soil parameters p_u and k_h for these lateral soil springs were obtained from the results for Test No. 3 of the corresponding test group, shown in Figs. 11.18 and 11.19 for loose sand and Figs. 11.20 and 11.21 for dense sand, respectively (i.e., the p-y relationship for Test Sequence A-1 was obtained from the results for Test Sequence A-3). The vertical point spring at the bottom of the analytical pile model, which is characterized by the soil parameters q_{max} and k_q given in Table 11.3, was obtained from figures similar to Fig. 11.17. The horizontal load beam shown in Fig. 4.1 was attached to the test pile during the laboratory tests, to provide lateral stability during loading; therefore, this beam was included in the analytical model.

Figures 4.2 and 4.3 show the vertical load versus vertical displacement at the soil surface for a model test pile in loose (Test Sequence

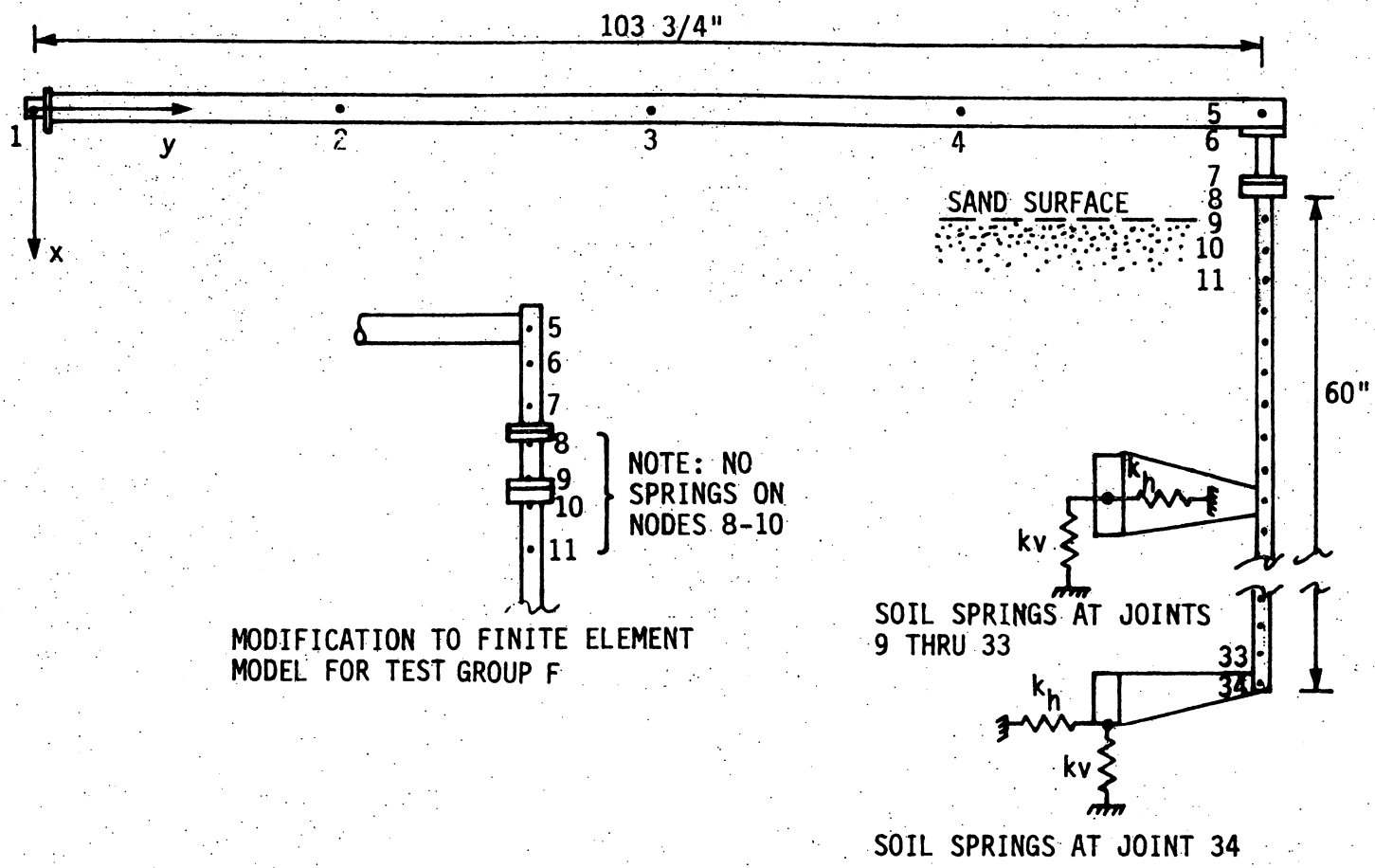

Figure 4.1. Finite element model for model test analyses.

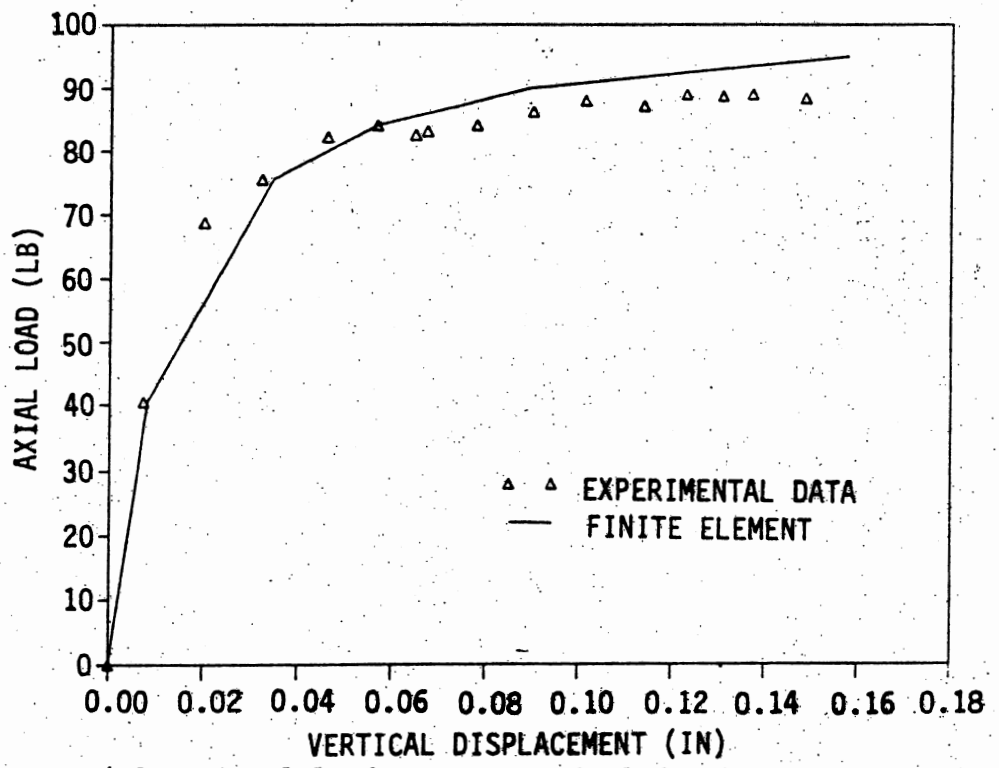

Figure 4.2. Axial load versus vertical displacement at grade for Test Sequence A-1.

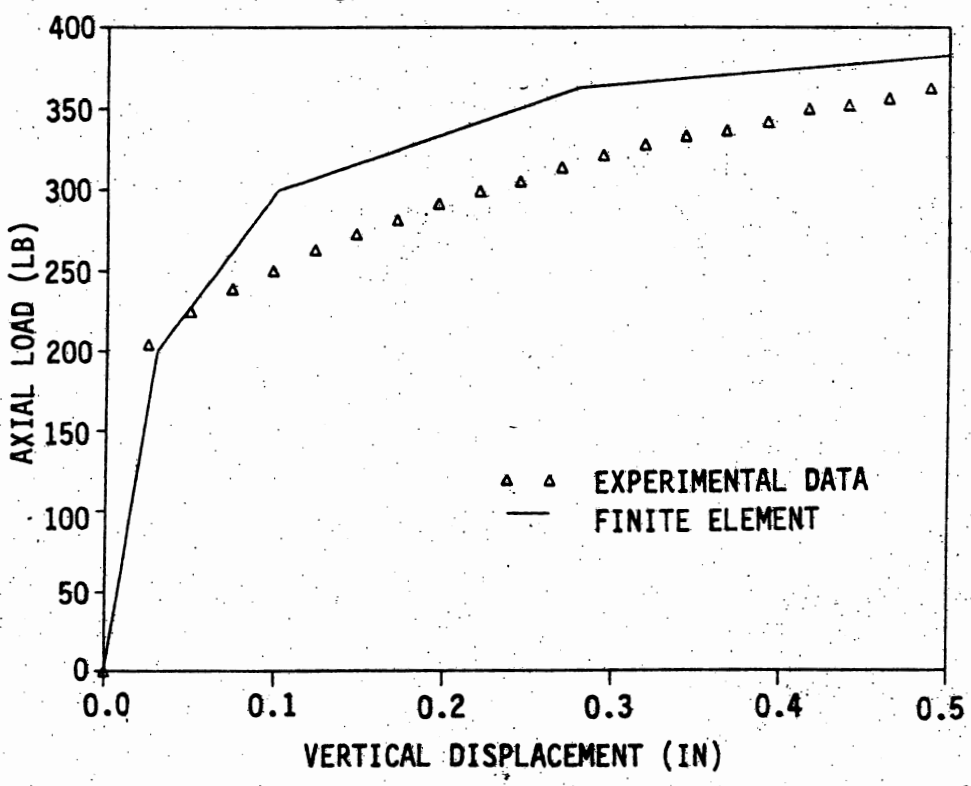

Figure 4.3. Axial load versus vertical displacement at grade for Test Sequence D-1.

A-1) and dense sand (Test Sequence D-1), respectively. The analytical solutions from IAB2D involved computer analyses for increasing magnitudes of vertical load. Close correlation occurred between the experimental and analytical results for the pinned-head, model test pile in loose sand, while the computer solution overestimated the vertical load capacity of the fixed-head, predrilled hole, model test pile in dense sand.

Both the laboratory test and analytical study of a friction pile in loose sand revealed that the vertical slippage failure occurred at approximately 90 lb of applied vertical load. This small compressive load induced small axial pile strains throughout the length of the pile, as shown in Fig. 4.4. The fluctuation in the axial strain can be attributed to the normal scatter associated with strain gage measurements having small magnitudes. Figure 4.5 shows axial strain versus depth for the fixed-head pile with a predrilled hole in dense sand. The increase in the experimental axial strains between the bottom of the predrilled hole and a depth of 14 in. implies negative frictional resistance that physically should not have occurred. Since the test pile head was essentially fixed against rotation, vertical displacement of the pile head induced bending strains in the top of the pile. As discussed in Section 11.3.2, the sensitivity of the strain measurements did not provide the accuracy necessary to separate the axial strain from the total measured strains in regions of high bending moment. As seen in Figs. 4.4 and 4.5, the analytical solution adequately predicted the model test pile behavior, considering the scatter associated with the experimental testing program.

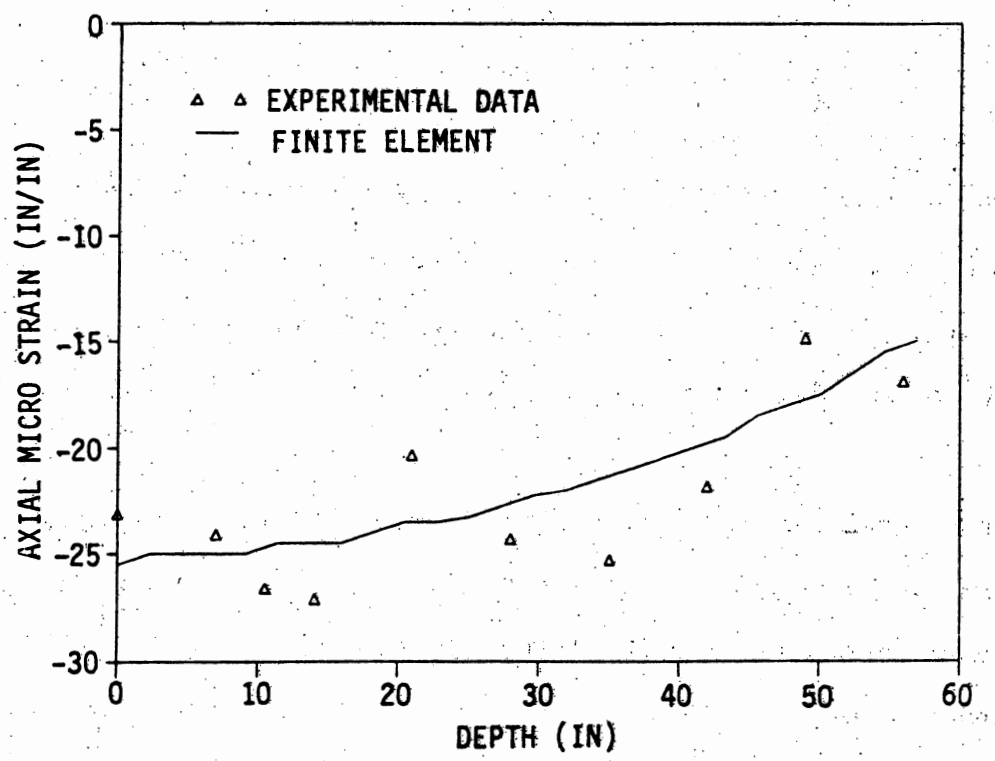

Figure 4.4. Axial strains for Test Sequence A-1 (V = 88 lb).

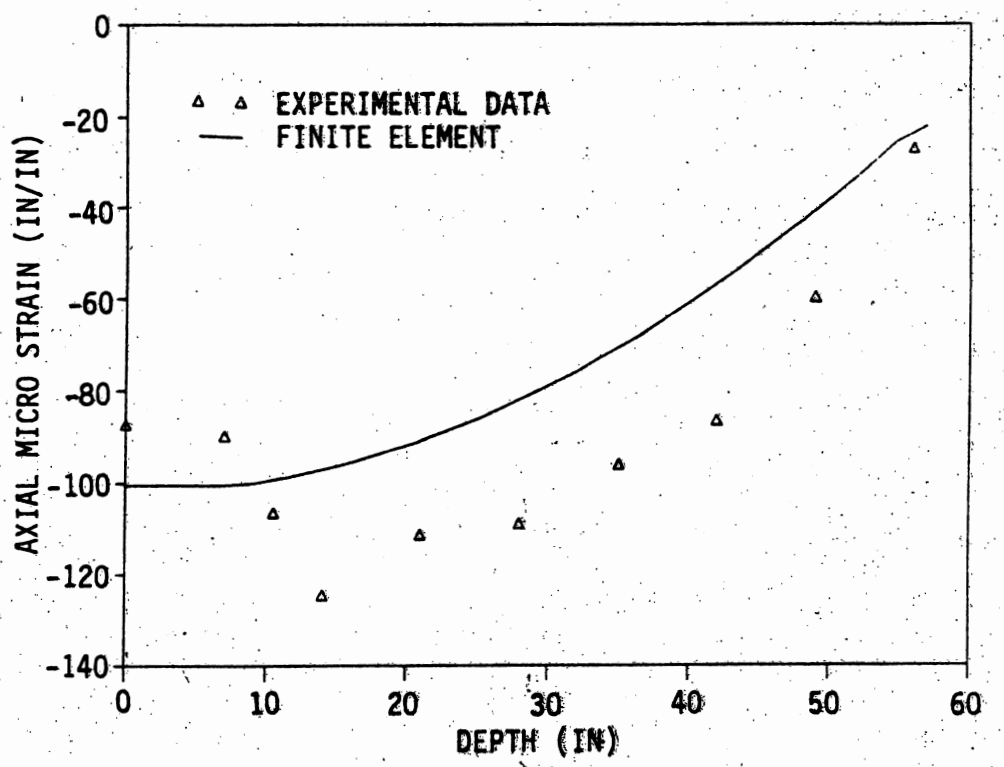

Figure 4.5. Axial strains for Test Sequence D-1 (V = 363 lb).

4.3.3. Lateral Load Tests and IAB2D

Two model pile tests (Test Sequences C-2 and D-2) are reported here to establish lateral (p-y) soil behavior. The modified Ramberg-Osgood expression (Eq. (3.8)) was used to describe the stiffness of the lateral soil springs for the finite element model (Fig. 4.1). The characteristic soil parameters for the maximum lateral resistance, p_u, and initial lateral stiffness, k_h, (Figs. 11.20 and 11.21) were developed in Section 11.3.4 of Appendix B for loose and dense sand. The two sand densities produced two shape parameter values (n = 1 for loose sand and n = 1/3 for dense sand) from a visual curve fit of the modified Ramberg-Osgood equation. To complete the analytical model, the vertical soil behavior along the pile length and at the pile tip was represented by the f-z and q-z relationships, respectively, that were established from the results for the vertical load phase of Test No. 3 of the corresponding test group (Test Sequences C-3 or D-3). The magnitudes for the maximum friction force, f_{max}, and initial vertical stiffness, k_v, were obtained from Figs. 11.13 and 11.14 or Figs. 11.15 and 11.16, respectively; while the values for the maximum bearing stress, q_{max}, and initial point stiffness, k_q, were obtained from Table 11.3.

Test Sequences C-2 and D-2 involved lateral loads on a fixed-head friction pile in loose sand and dense sand, respectively. The latter test contained a predrilled hole for the upper 8 in. of pile length. Comparisons between the experimental and analytical results for these tests are shown graphically in Figs. 4.6 through 4.9. Figures 4.6 and 4.7 show the lateral load and the corresponding lateral displacement at the soil surface for each test. IAB2D consistently underestimated

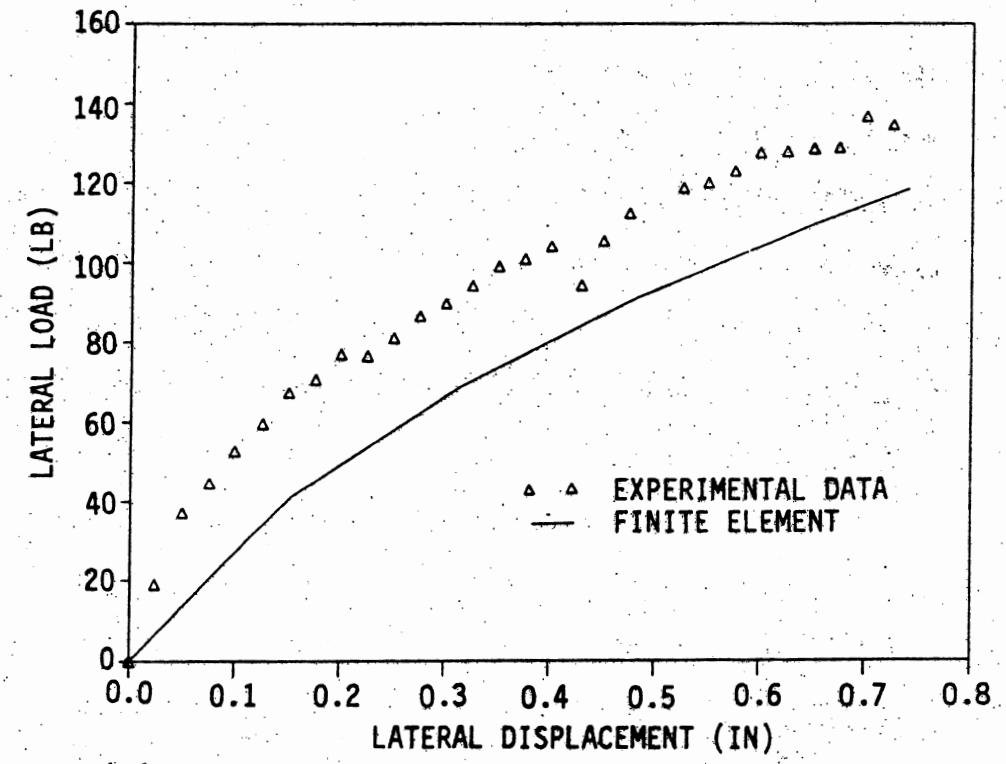

Figure 4.6. Lateral load versus lateral displacement at grade for Test Sequence C-2.

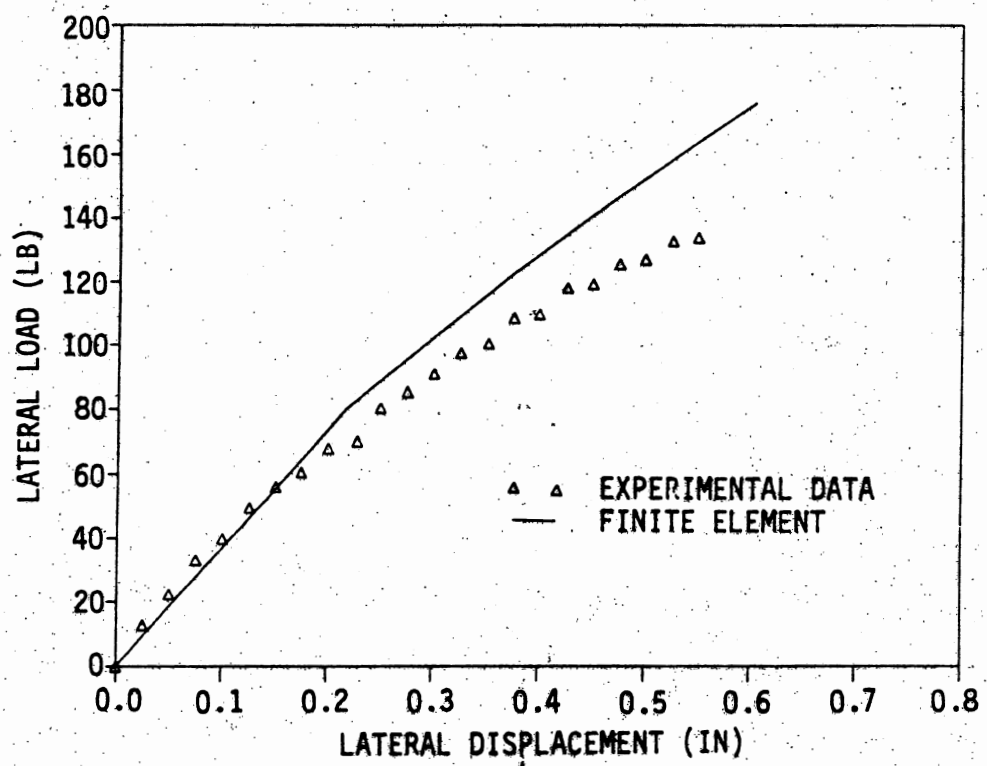

Figure 4.7. Lateral load versus lateral displacement at grade for Test Sequence D-2.

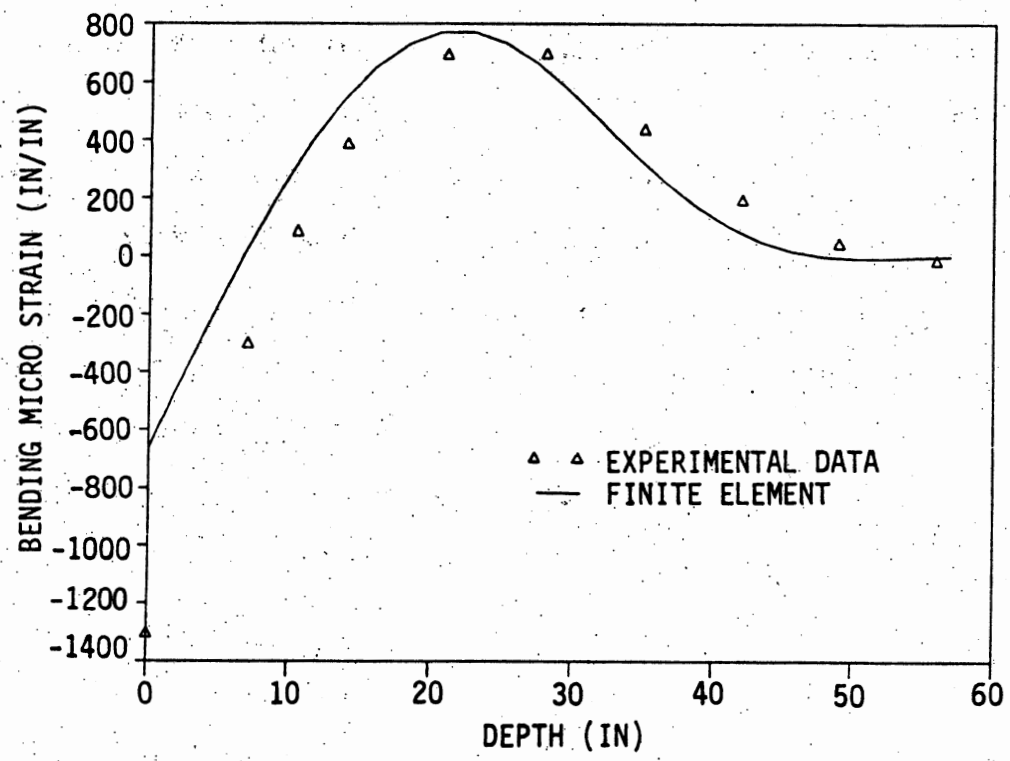

Figure 4.8. Bending strains for Test Sequence C-2 at Δ_h = 0.726 in. (H = 135 lb).

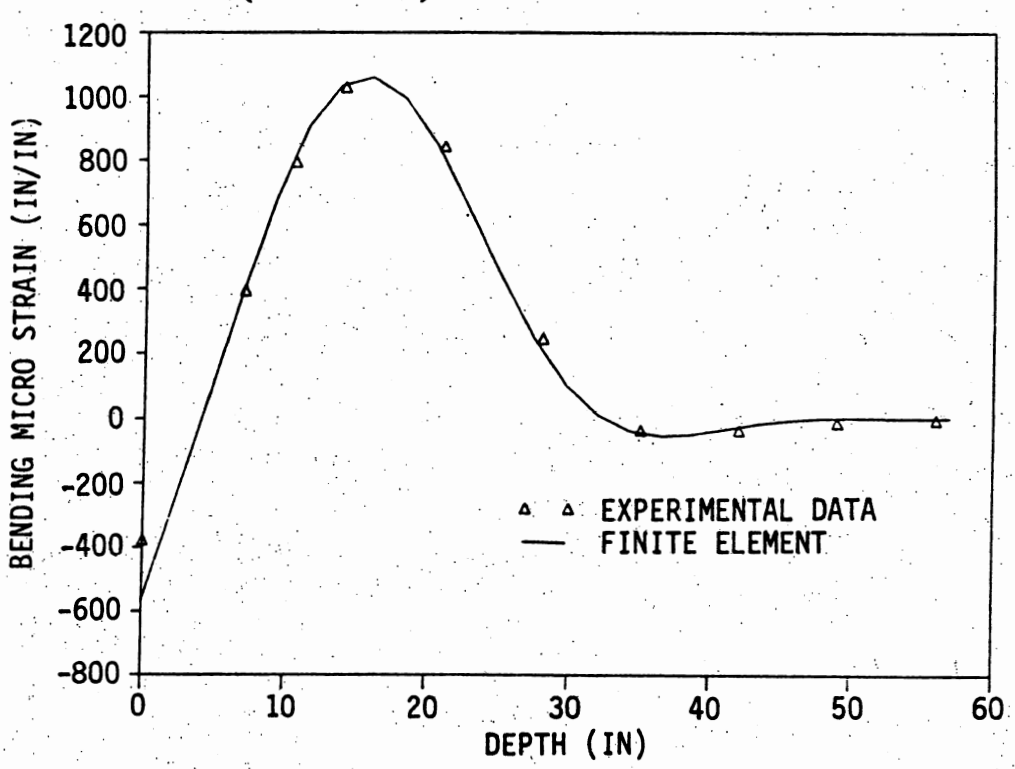

Figure 4.9. Bending strains for Test Sequence D-2 at Δ_h = 0.526 in. (H = 133 lb).

lateral load for a given lateral displacement (or overestimated the lateral displacement for a given magnitude of lateral load) for the pile in loose sand (Fig. 4.6), while the analytical solution more closely matched the experimental behavior for the pile in dense sand (Fig. 4.7). The maximum lateral displacement of the pile, which was measured at the soil surface, was approximately 3/4 in. and 1/2 in. for Test Sequences C-2 and D-2, respectively.

The pile strains obtained from the laboratory measurements and from IAB2D are compared for the two lateral load tests, with an applied horizontal force of 135 lb for each test, in Figs. 4.8 and 4.9. The maximum bending strain that was predicted by the analytical solution closely matched the experimental results for both tests. The results for the lateral load pile test in dense sand (Fig. 4.9) show excellent correlation between the measured and theoretical bending strains throughout the pile length.

4.3.4. Combined Load Tests and IAB2D

Comparisons between the experimental and analytical results for the seven model tests involving combined loads (Test Sequences A-3 through G-3) were made to provide additional evidence that substantiated the accuracy of the analytical model, IAB2D. The pile strains and displacement measurements obtained during the lateral displacement phase of each test group (Table 11.2) were used to develop the lateral soil behavior (p-y relationships). The technique for establishing the maximum lateral resistance, p_u, and initial lateral stiffness, k_h, are described in Section 11.3.4. These parameters were obtained from

Figs. 11.18 and 11.19 for loose sand conditions (n equal unity) or from Figs. 11.20 and 11.21 for dense sand conditions (n equal to 1/3).

The pile strains and displacement measurements obtained during the vertical load phase of the combined load tests were used to develop the vertical soil behavior along the pile length (f-z relationships) and at the pile tip (q-z relationship). The methods that establish the maximum friction force, f_{max}, and initial vertical stiffness, k_v, are discussed in Section 11.3.2; and the approach used to develop the maximum bearing stress, q_{max}, and initial point stiffness, k_q, is presented in Section 11.3.3 of Appendix B. The values of f_{max} and k_v were obtained from Figs. 11.13 and 11.14, respectively, for loose sand, or from Figs. 11.15 and 11.16, respectively, for dense sand, to represent the analytical vertical soil springs along the pile length. The vertical support condition at the pile tip for the friction piles was described by the soil parameters n, q_{max}, and k_q obtained from Table 11-2. For the end-bearing pile in Test Sequence G-3, the vertical restraint at the pile tip was modeled as a stiff spring to simulate the bottom of the test bin.

Test Sequence A-3 involved combined loading on a friction pile in loose sand. The pile head was not significantly restrained against rotation by the small lateral load beam; therefore, the pile head was essentially pinned. Figures 4.10 through 4.12 show comparisons between the experimental and analytical results for this test. The lateral load and corresponding lateral displacement relationship during the lateral displacement phase and the vertical load and corresponding vertical displacement during the vertical load phase of the combined

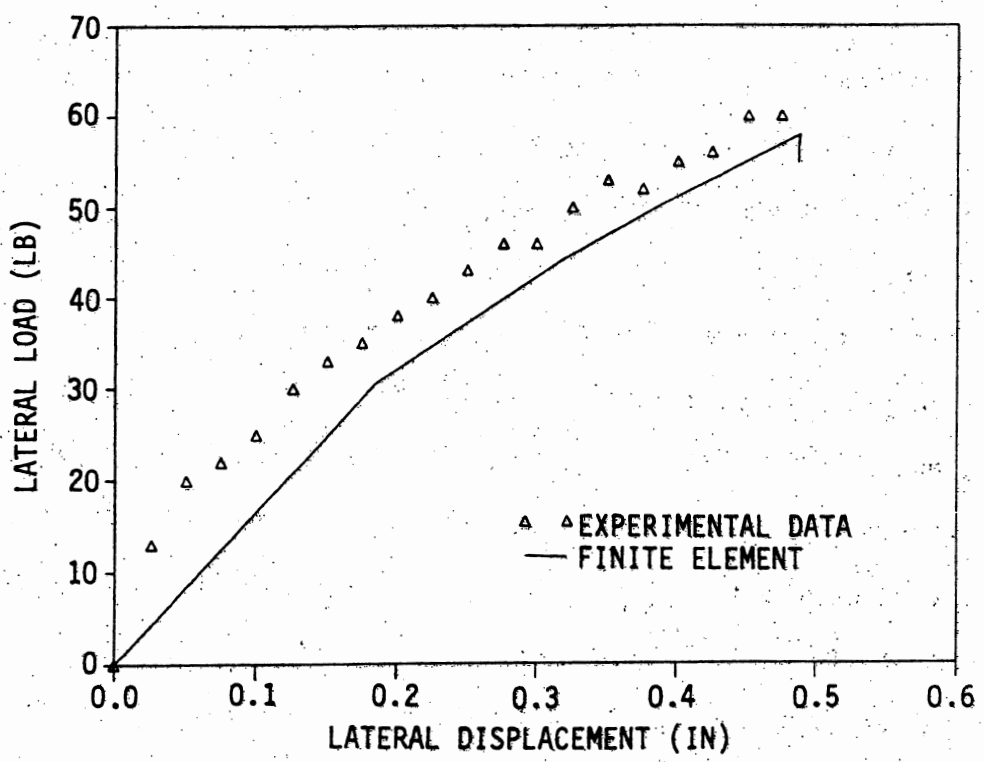

Figure 4.10. Lateral load versus lateral displacement at grade for the lateral phase of Test Sequence A-3.

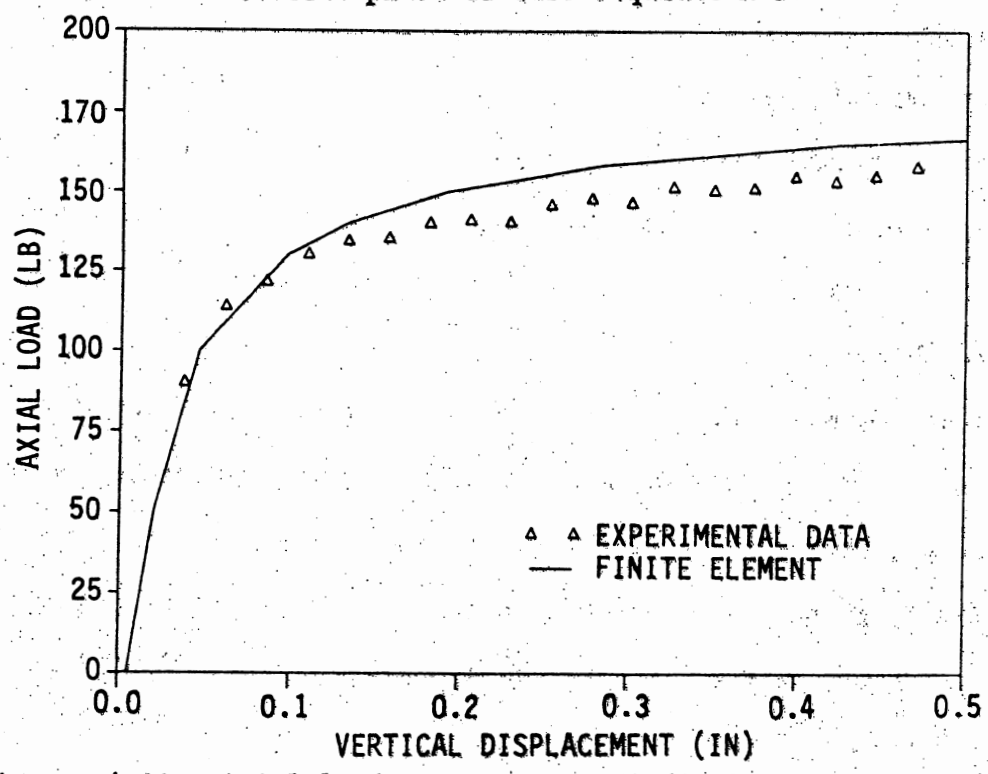

Figure 4.11. Axial load versus vertical displacement at grade for the vertical load phase of Test Sequence A-3.

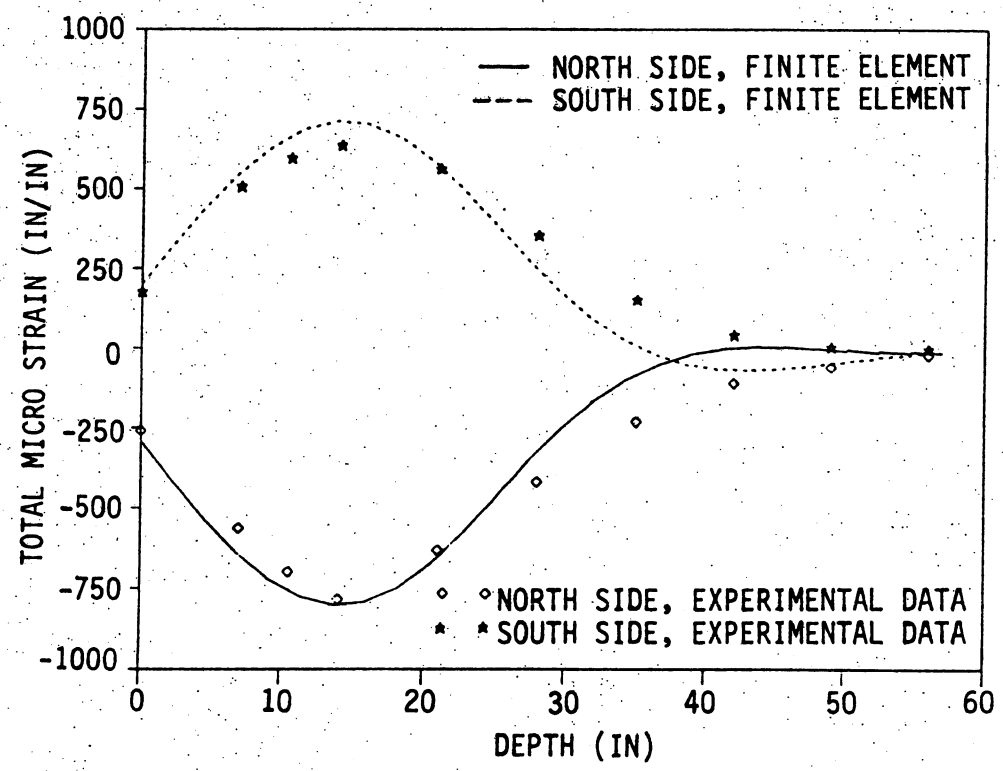

Figure 4.12. Total pile strains for the vertical load phase of Test Sequence A-3. (Δ_h = 0.504 in., V = 158 lb).

load test, both determined at the soil surface, are shown in Fig. 4.10 and 4.11, respectively. Both figures show good correlation between experimental values and predict analytical values, with IAB2D slightly underestimating lateral stiffness of the soil (Fig. 4.10) and overestimating vertical pile capacity (Fig. 4.11). Comparisons of the experimental and analytical total pile strains with a vertical load of 158 lb are shown in Fig. 4.12. IAB2D accurately predicts the pile behavior along the upper portion of the pile, where the total strain values are relatively large. The experimental strain shown at a depth of approximately 3 in. from the soil surface on the north face of the pile is in error due to an erratic gage behavior at this load point. The analytical solution indicates that an inflection point should occur at a depth of approximately 37 in.; however, the experimental results did not substantiate this behavior. This variation between the results is not of significant concern, since the small total pile strains in the lower portions of the pile length do not affect the pile design.

Test Sequence B-3 involved combined loading on a friction pile in dense sand. The pile head rotation in the plane of lateral displacement was essentially fixed by the large lateral load beam. Figures 4.13 through 4.15 show displacement and pile strain results for both the laboratory model test and IAB2D. The pile response at the soil surface is illustrated by the lateral load and corresponding lateral displacement relationship (Fig. 4.13) and by the vertical load and corresponding vertical displacement relationship (Fig. 4.14). The experimental results shown in Fig. 4.14 indicate that the vertical load resistance of the model test pile appeared to experience an increase in axial stiffness

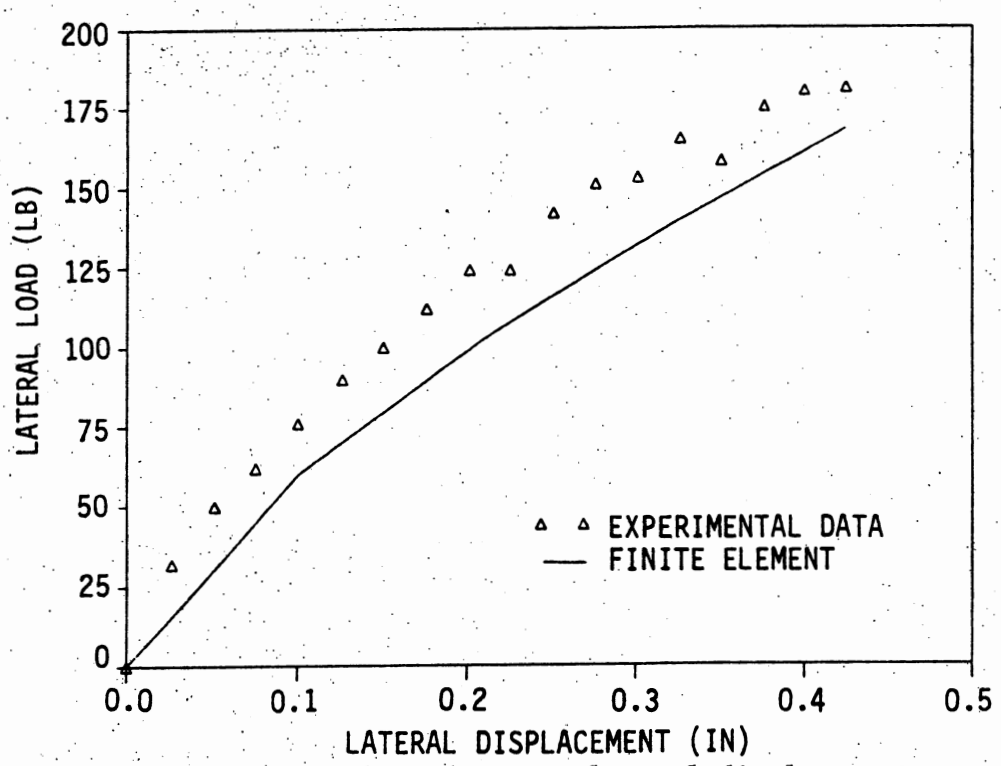

Figure 4.13. Lateral load versus lateral displacement at grade for the lateral load phase of Test Sequence B-3.

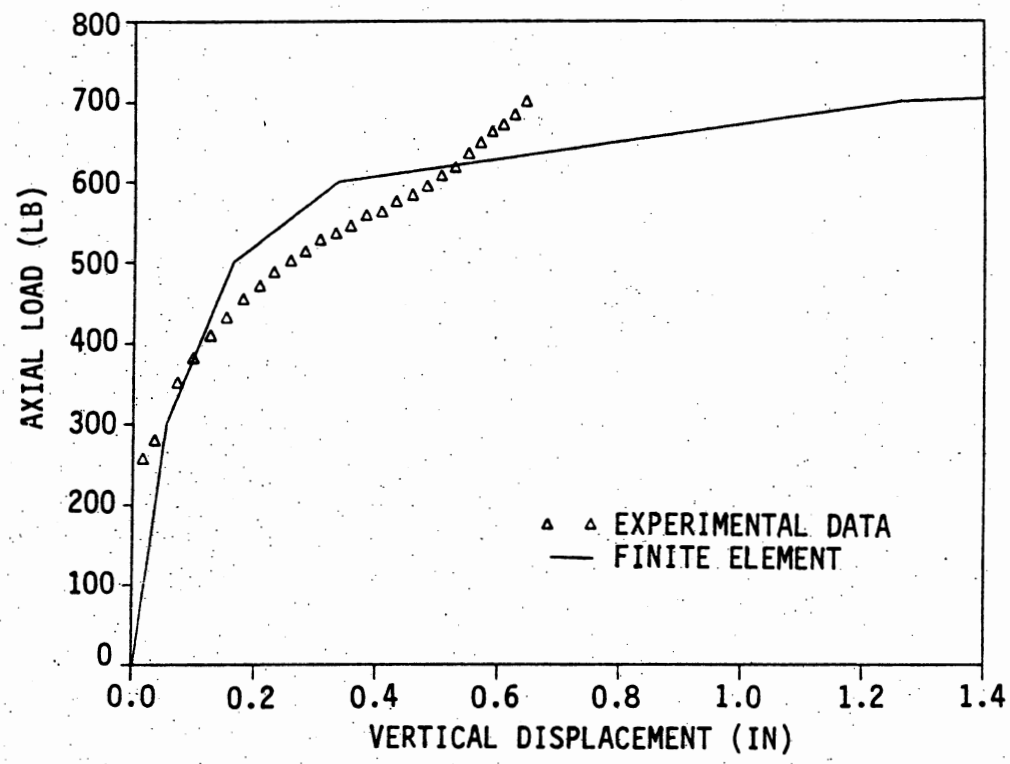

Figure 4.14. Axial load versus vertical displacement at grade for the vertical load phase of Test Sequence B-3.

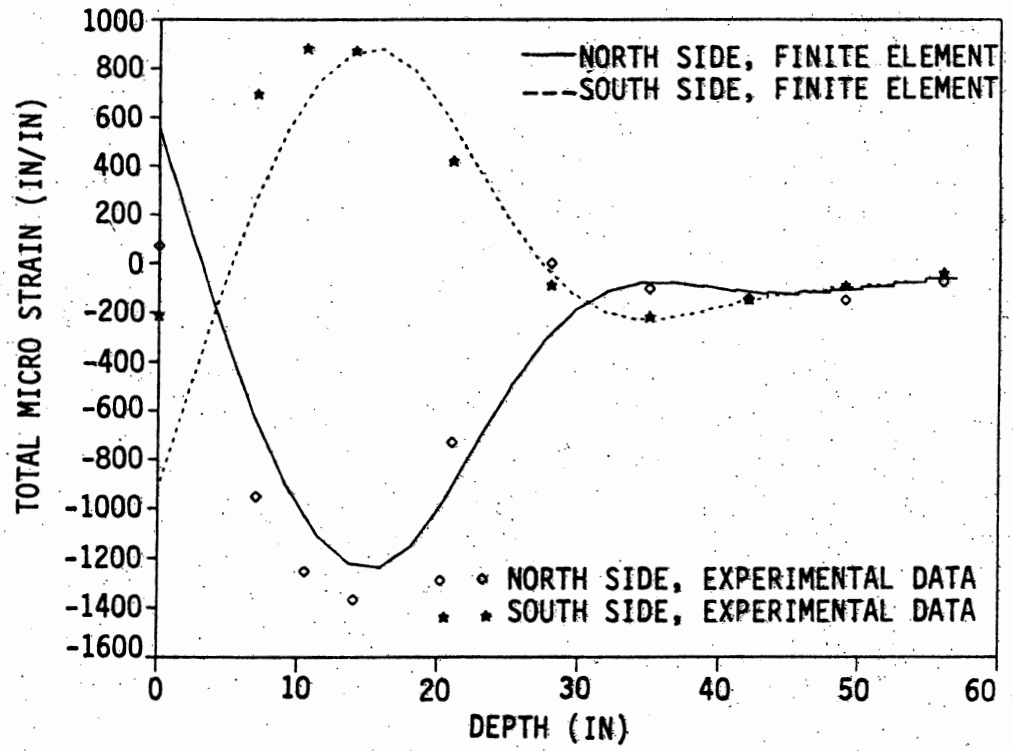

Figure 4.15. Total pile strains for the vertical load phase of Test Sequence B-3. (Δ_h = 0.425 in., and V = 701 lb).

after a vertical displacement of approximately 0.5 in. This behavior is unexplained. Figures 4.13 and 4.14 reveal that IAB2D slightly underestimated the lateral soil resistance and slightly overestimated the vertical load capacity of the model test pile. Figure 4.15 shows measured and calculated total pile strains along the pile length with an applied 701-lb vertical load. Some irregularities in the measured experimental strains occurred in the north face of the pile at the soil surface. IAB2D accurately predicted the magnitude of the maximum total pile strain; however, the location was about 4 in. below the location indicated by the experimental results. The location where the maximum bending strain occurs and the depths to points of reverse curvature (inflection points) are sensitive to the soil properties (p-y relationship). Soils that exhibit relatively stiff lateral resistance will cause the maximum pile strain location and the inflection point locations to occur closer to the top of the pile than soils that exhibit flexible lateral resistance. As discussed in Section 11.3.4, the p-y soil behavior developed from the experimental pile strains were slightly underestimated. Therefore, the IAB2D results (Fig. 4.15) for the total pile strain were shifted toward the pile tip when compared to the experimentally measured strains. As shown in Fig. 4.15, IAB2D confirmed the experimental result that three inflection points would occur along the pile length.

Test Sequence C-3 involved a fixed-head friction pile in loose sand. The experimental and analytical results for this combined load test are illustrated in the load versus displacement and total pile strain relationships given in Figs. 4.16 through 4.18. These figures

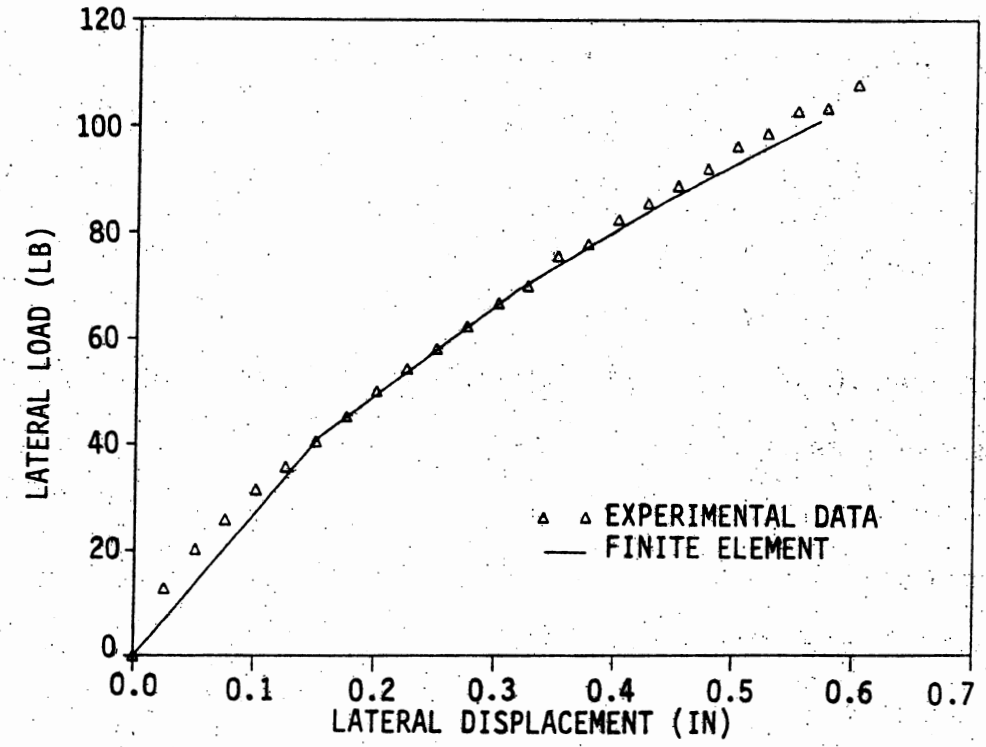

Figure 4.16. Lateral load versus lateral displacement at grade for the lateral load phase of Test Sequence C-3.

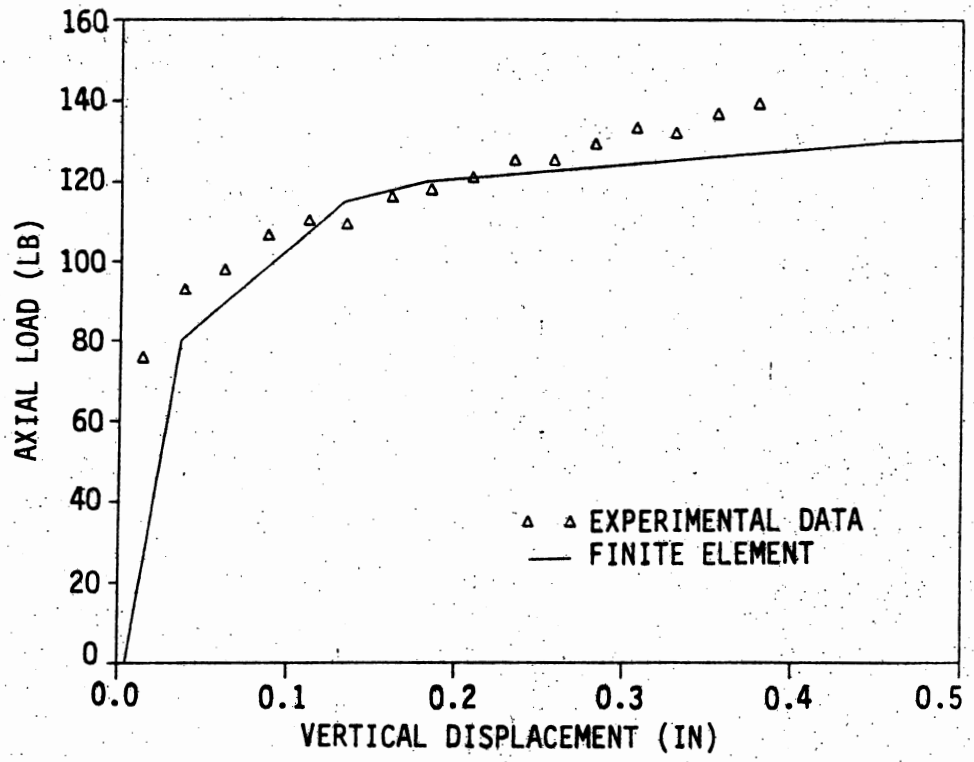

Figure 4.17. Axial load versus vertical displacement at grade for the vertical load phase of Test Sequence C-3.

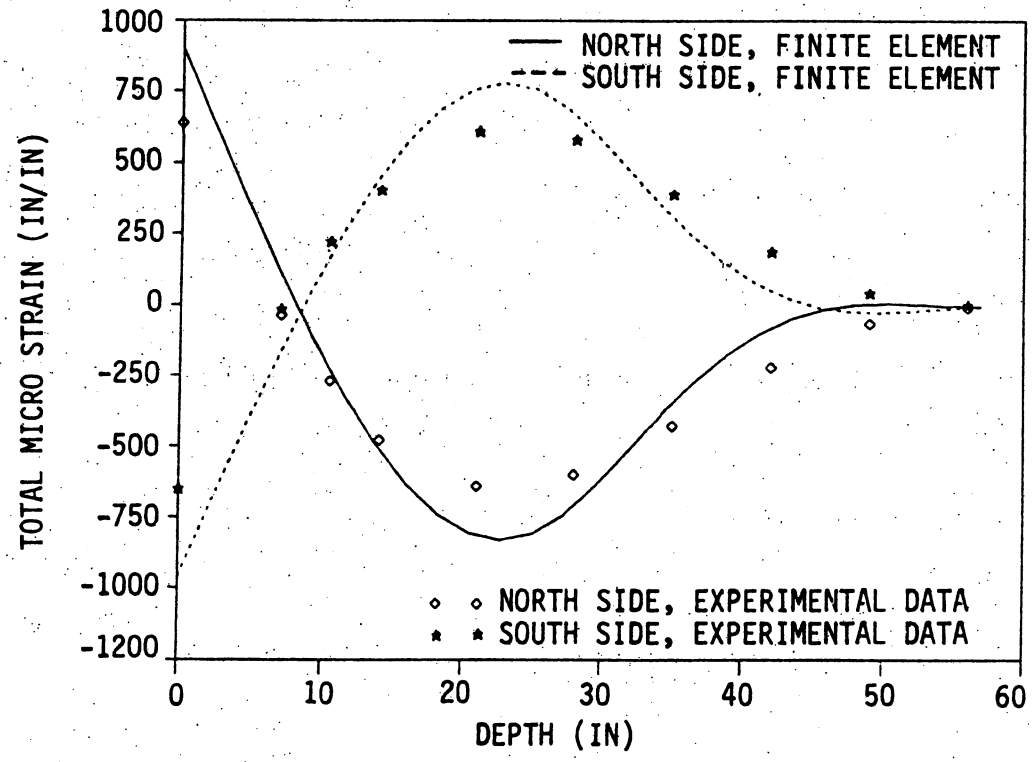

Figure 4.18. Total pile strains for the vertical load phase of Test Sequence C-3. (Δ_h = 0.061 in., and V = 139 lb).

show that the finite element model IAB2D adequately predicted the pile displacement and strain behavior.

A comparison of the test results for a fixed-head friction pile in dense and loose sands (Test Sequences B-3 and C-3, respectively) reveals some of the effects that soil stiffness has on pile behavior. As expected, the lateral and vertical pile displacements at the soil surface, for the same magnitude of applied force at the pile head, are substantially smaller for a pile in dense sand (Figs. 4.13 and 4.14) than for a pile in loose sand (Figs. 4.16 and 4.17). Considering pile strains, the locations of the point of maximum total strain and inflection points are closer to the top of the pile for the dense sand medium (Fig. 4.15) than for the loose sand medium (Fig. 4.18).

Test Sequence D-3 was conducted on a fixed-head friction pile in dense sand. A predrilled hole in the soil provided greater flexibility for the top of the model pile. Figures 4.19 through 4.21 show close correlation between the experimental and IAB2D results regarding load versus displacement and total pile strain versus depth relationships.

The soil placement techniques produced similar sand densities for the three laboratory tests of Test Group D (Test Sequences D-1, D-2, and D-3); therefore, some general comparisons can be made between these tests. A comparison of the lateral load behavior for the lateral load phase of Test Sequence D-3 (Fig. 4.19) with Test Sequence D-2 (Fig. 4.7) reveals that the pile behavior is essentially identical for the two tests. Observations of the pile strains for the combined load test (Fig. 4.21) and lateral load test (Fig. 4.9) show that the inflection points occur at approximately 5 in. and 32 in. below the soil surface

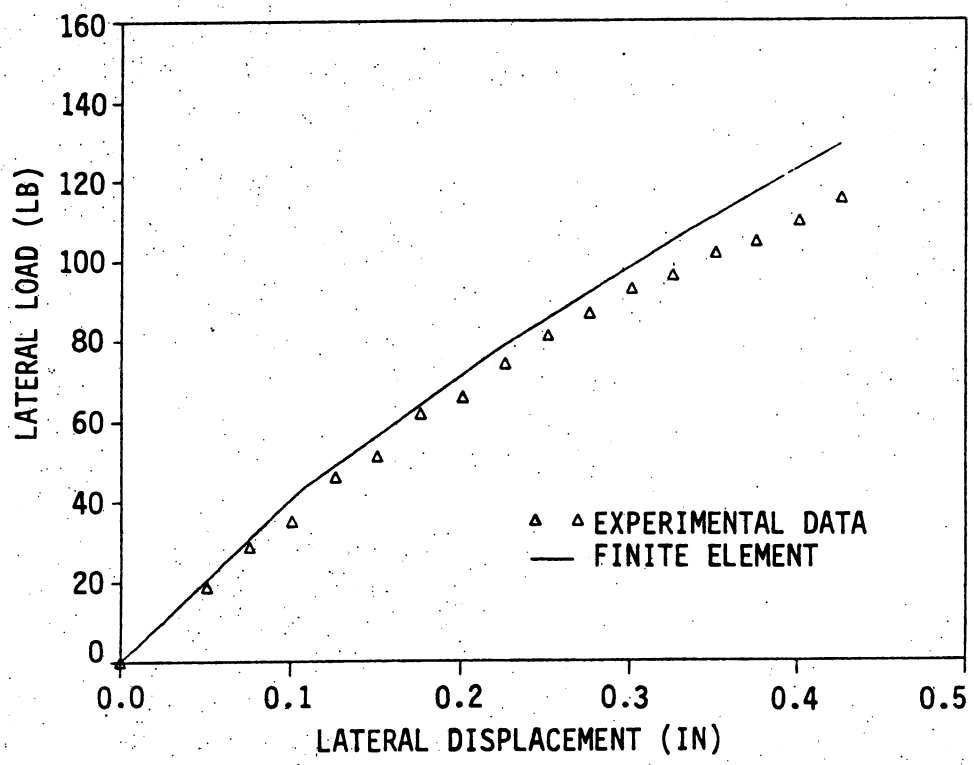

Figure 4.19. Lateral load versus lateral displacement at grade for the lateral load phase of Test Sequence D-3.

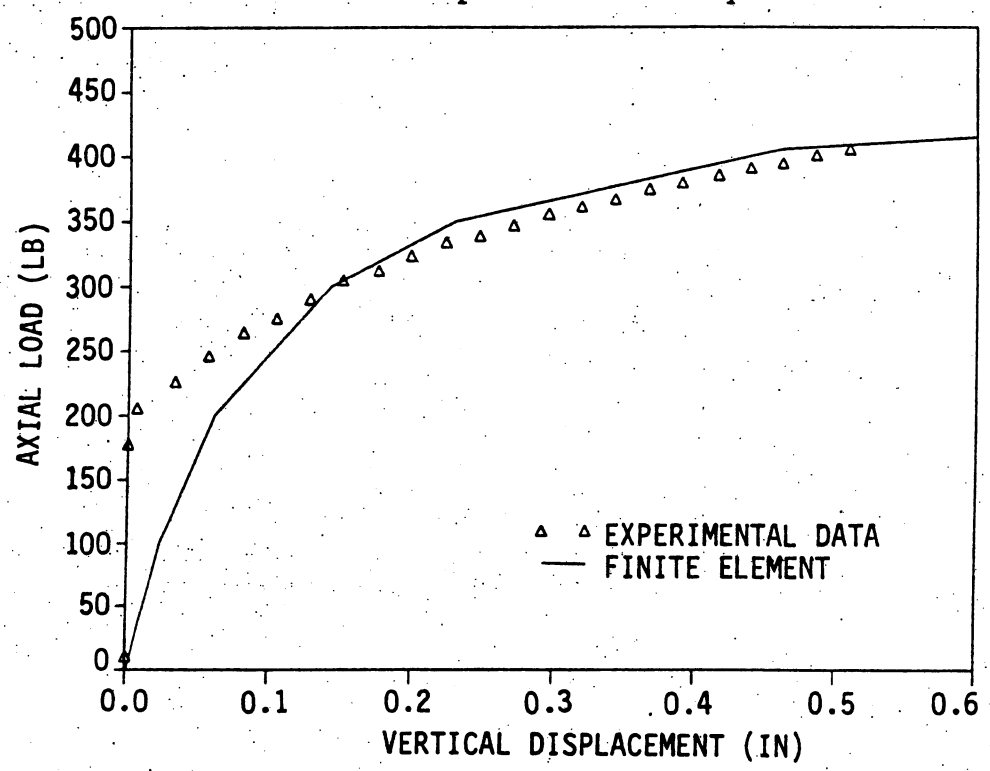

Figure 4.20. Axial load versus vertical displacement at grade for the vertical load phase of Test Sequence D-3.

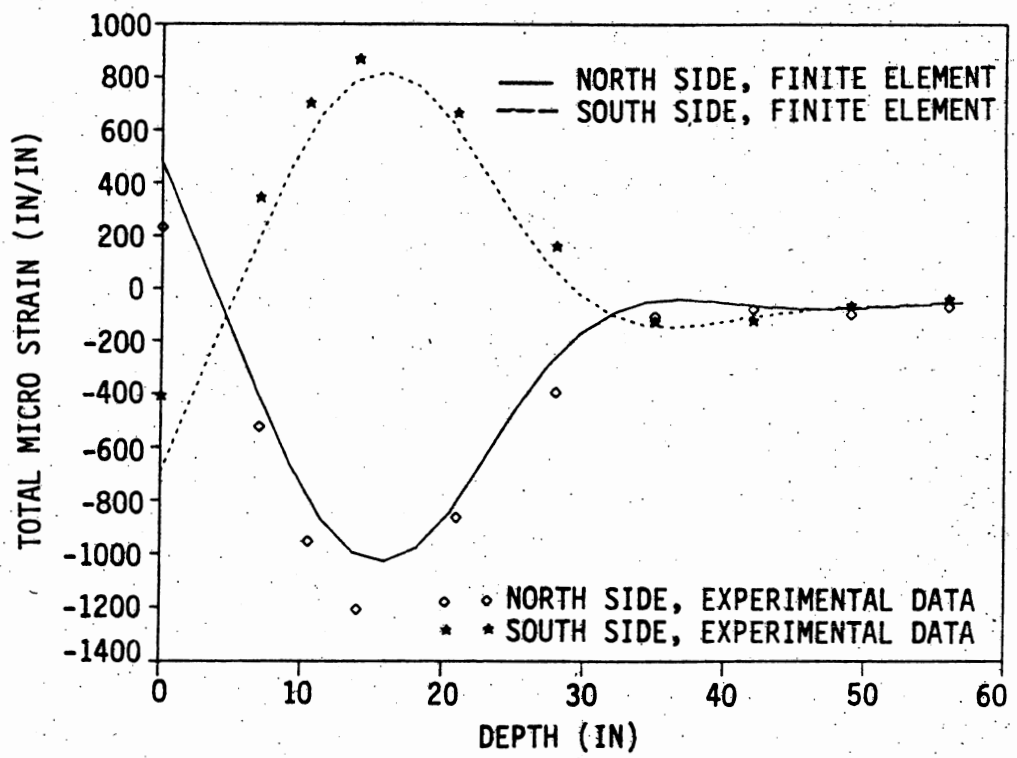

Figure 4.21. Total pile strains for the vertical load phase of Test Sequence D-3. (Δ_h = 0.426 in., and V = 406 lb).

in both instances, indicating very similar lateral behavior for the soil for Test Sequence D-3 and D-2. The experimentally measured vertical load and corresponding vertical displacement relationship for the vertical load phase of Test Sequence D-3 (Fig. 4.20) is quite similar to the behavior obtained for Test Sequence D-1 (Fig. 4.3). The vertical load capacity for a given vertical displacement was approximately the same for each test. Therefore, the lateral displacement of the pile head in the combined load test (Test Sequence D-3) did not significantly affect the vertical load resistance for the model pile when compared to the resistance provided by the pile in Test Sequence D-1, which did not involve a lateral displacement of the pile head. The full-scale field tests reported in Section 3.3.4 illustrated a similar vertical load behavior.

Test Sequence E-3 investigated the effects of cyclic lateral loads on the behavior of a fixed-head friction pile in dense sand. Figure 4.22 shows the experimental and analytical results for the lateral load and corresponding lateral displacement for the first two hysteresis loops. The measured total pile strains induced during the initial application of lateral load for the first load cycle (Fig. 4.22a) were used to establish the lateral soil resistance, p-y, relationships. These p-y relationships were assumed to be applicable for the entire cyclic response modeled by IAB2D. The analytical model has an algorithm to account for cyclic p-y soil behavior. Instead of using the modified Ramberg-Osgood expression (Eq. (3.8)) a modified Ramberg-Osgood cyclic model [1] given by Eq. (4.1) was incorporated into the analytical solution.

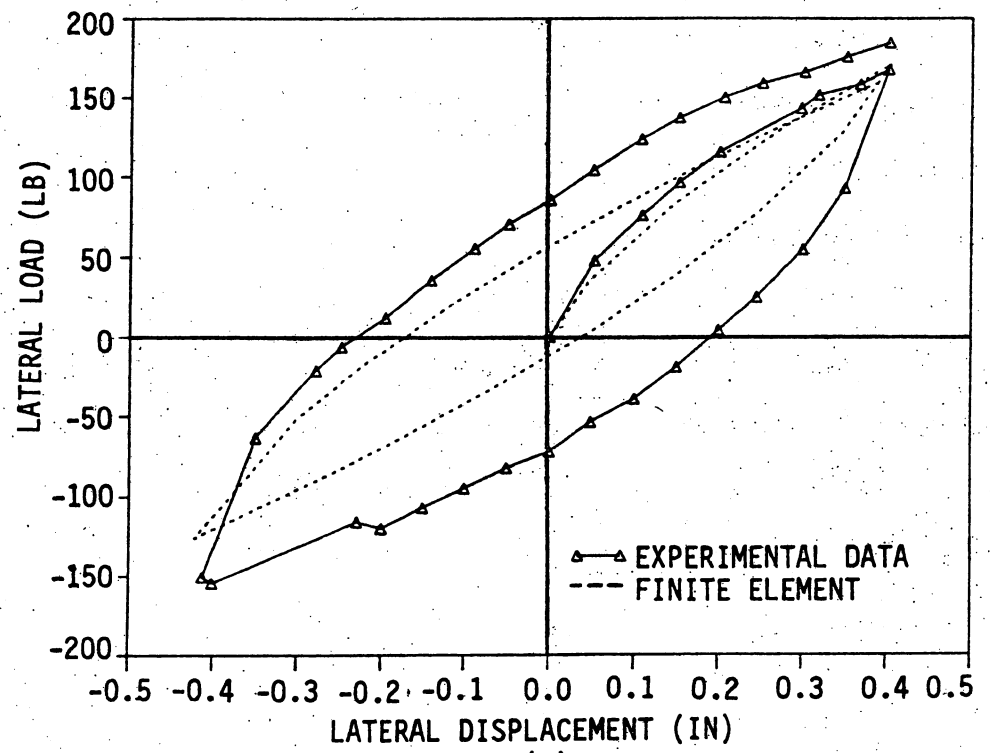

(a)

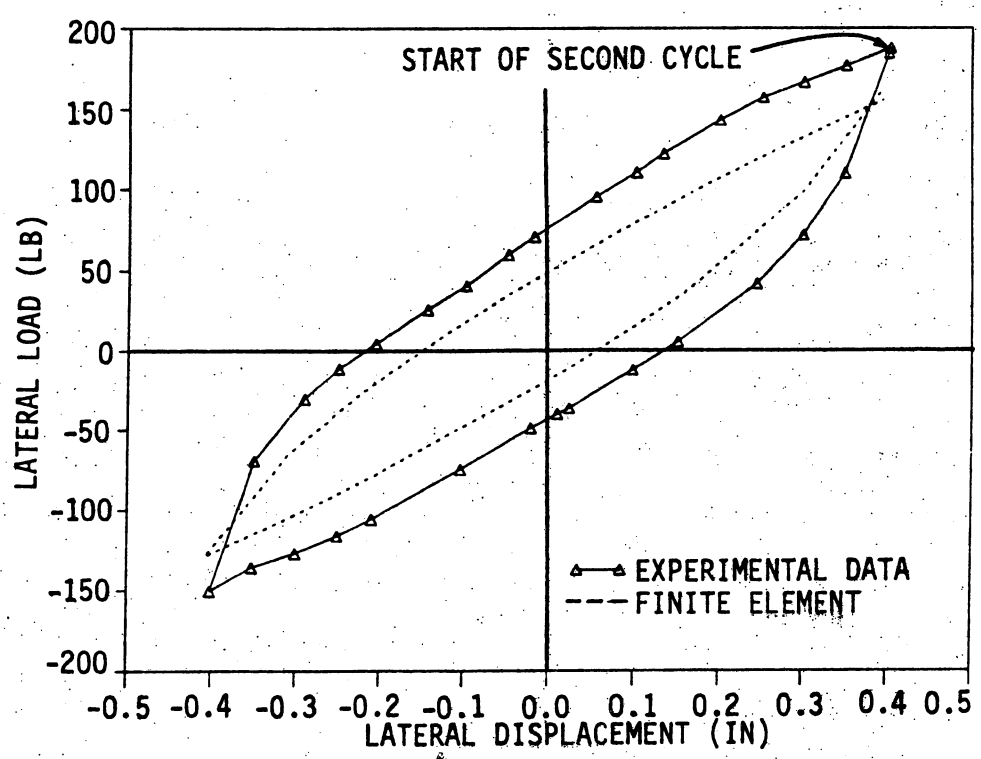

(b)

Figure 4.22. Lateral load versus lateral displacement at grade for the lateral load of Test Sequence E-3: (a) first cycle (b) second cycle.

$$p = p_c + \frac{k_h(y - y_c)}{\left[1 + \left(\frac{1}{C}\left|\frac{y - y_c}{y_n}\right|\right)^n\right]^{1/n}} \tag{4.1}$$

where

$$C = \left|\pm 1 - \frac{p_c}{p_u}\right| \tag{4.2}$$

in which p_c and y_c are the soil resistance and displacement at the last reversal, respectively, and the parameters p_u, k_h, and n are the same as those in the noncyclic model. The hysteresis loops were analytically established by applying two rules presented by Pyke [12]. First, the tangent modulus for each load reversal was set equal to the initial tangent modulus for the previously completed load application. Second, the shape of an unloading or reloading curve was essentially the same as the initial loading curve, except that the new curve has been enlarged in scale by the factor C. The first term in Eq. (4.2) is positive for reloading and negative for unloading. The maximum and minimum values for p and y are bounded by p_u and y_u. Comparing the analytical and experimental results presented in Fig. 4.22, reveals that IAB2D accurately predicted the model pile behavior for the initial loading stage of the first load cycle and provided reasonable correlation with the experimental behavior for the remaining portions of the lateral load versus lateral displacement relationship. After the lateral cyclic loading had completed two cycles, the model pile was displaced laterally for the last time and vertical loading was applied to the top of the

test pile. Figure 4.23 shows the vertical load and corresponding vertical displacement results for the laboratory test and for the finite element solution. IAB2D accurately predicted the vertical load capacity and provided reasonable agreement with the experimental results throughout the entire range of load versus displacement.

Test Sequence F-3 was conducted on a fixed-head friction pile that had a model abutment mounted above the top of the model pile. The pile installation procedure, described in Section 11.1.1, produced a dense soil medium for the volume of sand below the first strain gage station on the pile and a loose soil medium for the sand backfill. This test was conducted to investigate pile and abutment behavior due to passive soil pressure exerted on the abutment and backwall by the backfill material as the model bridge superstructure expanded. Since more complex soil behavior occurs with the abutment, wingwall and pile system, the experimental pile strains measured in this test sequence were not used to obtain the soil parameters required in the analytical model. Instead, soil parameters derived from Test Sequence D-3 were used for the dense sand around the pile, and soil parameters derived from Test Sequence C-3 were used for the loose sand behind the abutment, backwall, and wingwalls.

The analytical model shown in Fig. 4.1 was used to analyze the experimental model. Since pieces of foam rubber were inserted around the load cell and under the pile cap plate to reduce the bearing capacity of these areas, vertical and lateral soil springs were not included in the finite element model at Nodes 8 through 10. As shown in Fig. 4.24, the analytical model provided an accurate representation of the

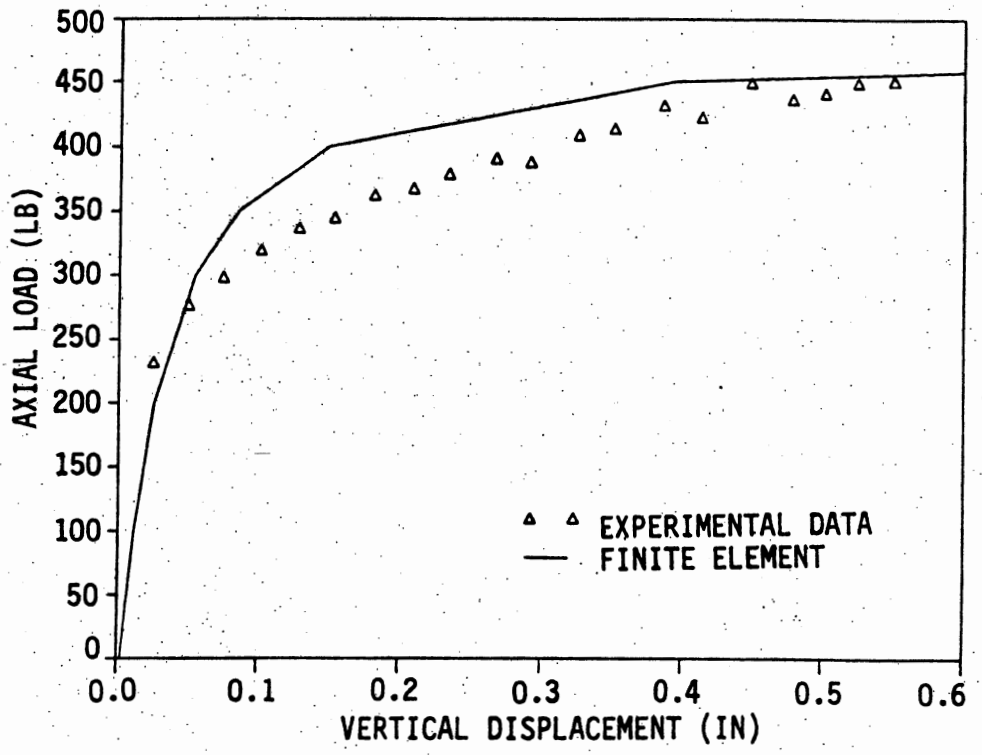

Figure 4.23. Axial load versus vertical displacement at grade for the vertical load phase of Test Sequence E-3.

experimental lateral load versus lateral displacement pile behavior for the combined load test. The lateral displacement was measured at the top of the abutment. The lateral load, which was applied by the horizontal load beam, caused the abutment to be pushed against the backfill. This movement created passive soil pressures against the abutment, backwall, and wingwalls. The location of the resultant horizontal soil pressure was below the center of gravity for the horizontal load beam (model bridge girder). The eccentricity between the compressive force in the horizontal load beam and the resultant passive soil pressure force induced a moment that was resisted by a vertical force couple that consisted of an upward end reaction on the horizontal load beam and a downward or an axial compressive force in the abutment pile. This behavior was predicted in an earlier study [1]. Figure 4.25 shows this induced axial compression force in the model pile versus horizontal displacement of the abutment. The analytical model underestimated the magnitude of the experimental pile force. The discrepancy was attributed to the fact that the soil parameters used in IAB2D for the soil pressure on the abutment were derived from other model pile tests, which had no abutment. The existence of an induced pile axial load, which was caused by horizontal abutment movement, is clearly evident in both the experimental and analytical results.

Test Sequence G-3 involved a combined load test of an end-bearing pile in loose sand. The model test pile head was essentially fixed with respect to bending in the plane formed by the pile and the stiff horizontal load beam. The model pile was effectively pinned in the

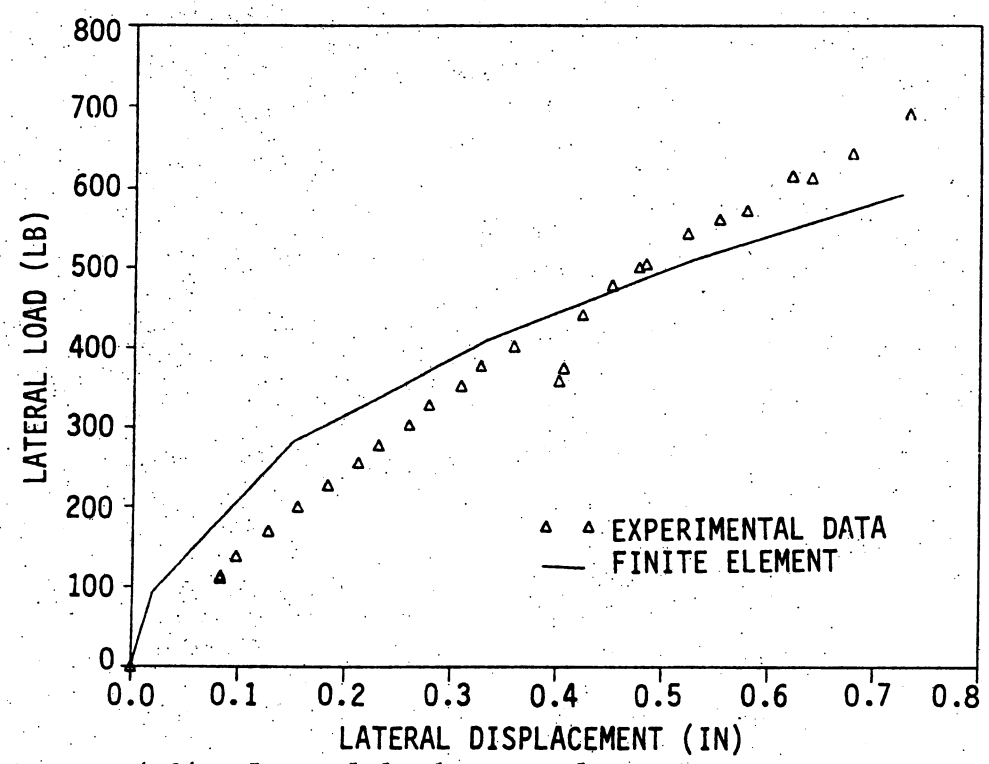

Figure 4.24. Lateral load versus lateral displacement at grade for the lateral phase of Test Sequence F-3.

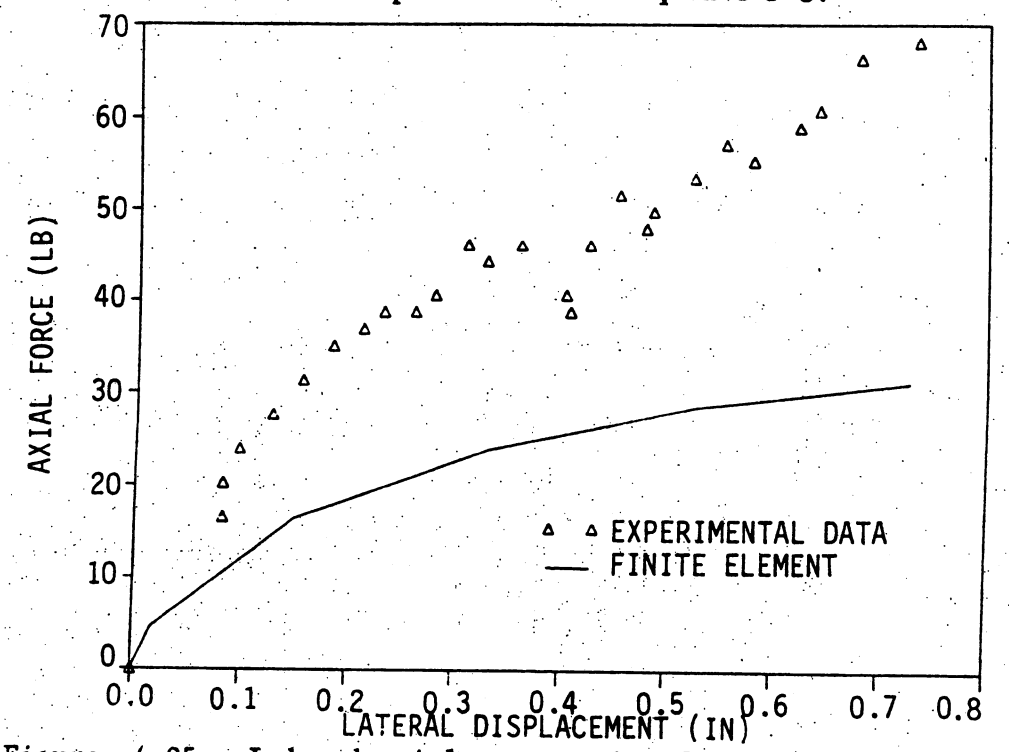

Figure 4.25. Induced axial compressive force in the pile at 35 in. below soil surface during lateral load phase of Test Sequence F-3.

transverse direction, since the pile was guided by vertical rollers that restrained only transverse displacement of the pile head.

The analytical investigation of this experimental test required establishing geometric conditions and soil characteristics that reasonably represented the laboratory test. An inspection of the testing apparatus and the model test pile revealed that the axial load was slightly misaligned from the center of gravity of the pile and that the test pile had a slight camber prior to testing. These imperfections can significantly affect the behavior of end-bearing piles; therefore, they were both accounted for in the analytical model by applying the vertical load with a 1-in. eccentricity. As described in Section 11.2.2, the pile tip was placed against a steel spacer that was supported by the soil test bin floor. Since the floor of the bin displaced vertically during application of the vertical load, the vertical point spring stiffness in the analytical model was adjusted to account for the flexibility of the bin and test fixture. The soil parameters for the vertical friction resistance were assumed to be the same as those determined for Test Sequence C-3, which also involved a loose sand density. The maximum friction force, f_{max}, and initial vertical stiffness, k_v, could not be experimentally determined for Test Sequence G-3, since the relative vertical pile displacements are extremely small for an end-bearing pile. The soil parameters for the lateral resistance were computed for Test Sequence G-3 by the same techniques discussed for the other model tests involving lateral loads.

The ultimate vertical load capacity of this combined load test was obtained when the model pile buckled transverse to the plane of

lateral displacement at a vertical load of about 2600 lb. Failure was evidenced by a bending failure of the tube section at the soil surface. Since the two-dimensional computer model IAB2D can only predict pile behavior in one plane, the pile was analyzed in the transverse plane. The head condition was considered pinned for that direction. Figure 4.26 shows the vertical load and corresponding vertical displacement relationship for both the experimental and analytical investigations. The pile behavior predicted by the finite element model reasonably matched the experimental results. IAB2D overestimated the vertical pile displacement; however, the analytical failure load was only slightly smaller than the experimental load.

4.3.5. Summary of IAB2D and Model Test Correlations

In summary, IAB2D satisfactorily predicted the model pile behavior for all 11 experimental laboratory tests that were analyzed. Reasonable correlation existed between the load and displacement relationships and between the pile strains for the vertical, lateral, and combined load tests.

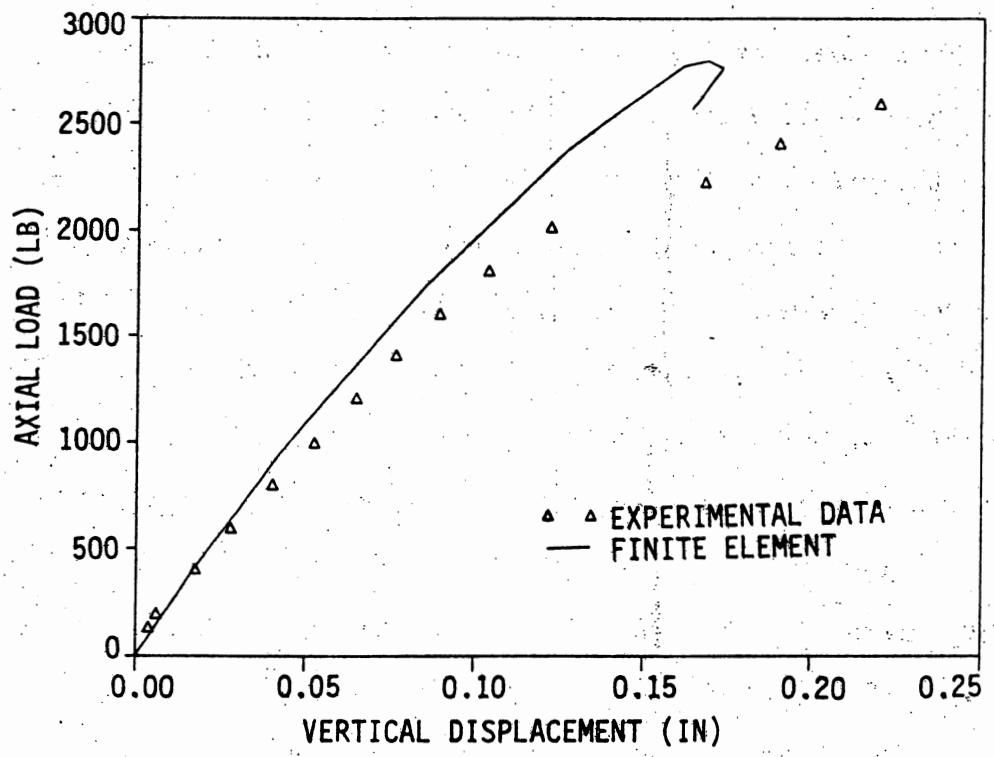

Figure 4.26. Axial load versus vertical displacement at grade for the vertical load phase of Test Sequence G-3. (H = 93 lb, and Δ_h = 0.250 in.).

5. DESIGN RECOMMENDATIONS

5.1. AASHTO Design Specification

This section summarizes the provisions of the AASHTO Standard Specifications for Highway Bridges [22] that affect the design of the piling for an integral abutment bridge. These provisions will be used as a basis for the design method. Articles referenced in this Section are from the AASHTO Specification.

The Specification (Art. 3.16) requires that stresses or movements due to temperature variations be taken into account in design. In an integral abutment bridge any change in bridge length that is due to temperature changes introduces forces into the piling and the superstructure. AASHTO (Art. 3.22) provides three loading groups that include temperature: Group IV, Group V, and Group VI. For this research the terms of interest include dead load (D), live load (L), and temperature (T). Load Group IV gives the smallest basic unit stress for service load design and the largest load factor for load factor design:

Service Load Design, Group IV

$$D + (L + I) + T \text{ at } 125\% \text{ of allowable stress}$$

Load Factor Design, Group IV

$$1.3\ [D + (L + I) + T]$$

Live load stresses produced from H or HS loading must include impact, I. The impact is required for portions of steel pile above the ground line that are rigidly connected to the superstructure as in a frame or continuous structure (Art. 3.8.1). The following values for the

superstructure material coefficient of thermal expansion, α, and the average temperature change, ΔT (Art. 3.16), are given by the Specification:

α	= 0.000006 /°F	normal weight concrete
	= 0.0000065 /°F	structural steel
ΔT_{ave}	= 60°F	moderate climate, metal structures
	= 75°F	cold climate, metal structures
	= 35°F	moderate climate, concrete structures
	= 40°F	cold climate, concrete structures

The design load for a pile is controlled by the minimum of the following cases (Art. 4.3.4.1):

Case A: Capacity of the pile as a structural member.

Case B: Capacity of the pile to transfer load to ground.

Case C: Capacity of the ground to support the load.

The Load Factor Design method is to be used only for proportioning structural members and not for designing foundations (soil pressure, pile loads, etc.) (Art. 3.22.3). Therefore, the capacity of Case B and Case C cannot be determined by using this design method.

The capacity of the pile as a structural member, Case A, is determined as that of a column (Art. 4.3.12.4). It includes any length of pile, whether in air, water, or soil, that is not capable of providing significant lateral support (Art. 4.3.4.2). For this case the provisions for compression members apply; for example, provisions in AASHTO Chapter

10 apply for structural steel. For Service Load Design, the interaction equations for a beam-column with bending about one axis are (Art. 10.36)

$$\frac{f_a}{F_a} + \frac{C_m f_b}{\left(1 - \frac{f_a}{F'_e}\right)F_b} \leq 1.0 \qquad (5.1)$$

and

$$\frac{f_a}{0.472\ F_y} + \frac{f_b}{F_b} \leq 1.0 \qquad (5.2)$$

where

f_a = applied axial stress

f_b = applied bending stress

F_y = yield stress of the steel

F_a = allowable axial stress

F_b = allowable bending stress

F'_e = Euler buckling load divided by a factor of safety

C_m = equivalent moment factor = $0.6 + 0.4\ (M_1/M_2) \geq 0.4$; where M_1 and M_2 are the smaller and larger end moments, respectively, of a column with no lateral load or joint translation. The ratio M_1/M_2 is positive for single curvature and negative for reverse curvature.

For Load Factor Design, the interaction equations for a beam-column are (Art. 10.54.2)

$$\frac{P}{0.85\ A_s\ F_{cr}} + \frac{CM}{M_u\left(1 - \frac{P}{A_s F_e}\right)} \leq 1.0 \qquad (5.3)$$

and

$$\frac{P}{0.85\ A_s\ F_y} + \frac{M}{M_p} \leq 1.0 \qquad (5.4)$$

where

P = applied axial load

M = applied moment

A_s = cross-sectional area

F_y = yield stress of the steel

F_{cr} = critical buckling stress

F_e = Euler buckling stress

M_u = ultimate moment

M_p = full plastic moment

C = C_m

Equations (5.1) and (5.3) are often referred to as the stability equations and Eqs. (5.2) and (5.4) as the yield equations [28].

The capacity of the pile to transfer the load to the soil, Case B, is subdivided into two categories: point-bearing and friction piles. Point-bearing piles transfer the load through direct bearing at the tip of the pile. The pile must be driven into material capable of developing this bearing capacity. For steel H-piles the bearing stress must not exceed 9000 psi over the cross-sectional area of the pile tip (Art. 4.3.4.3.1). Friction piles transfer the load along the length

of the pile through friction between the pile and surrounding soil and by point bearing. The capacity of a friction pile must be determined by one of the following methods (Art. 4.3.4.3.2):

1. Driving and load testing piles (Art. 3.6.1).
2. Pile-driving experience in the vicinity.
3. Adequate tests of the soil strata through which the pile is to be driven.

The capacity of the ground to support the load, Case C, is determined by load testing or a subgrade investigation. For point-bearing piles, group action should be considered and the capacity reduced when the pile rests on a thin stratum of hard material over a thick stratum of soft or yielding material. For friction piles borings must be carried well below the tip of the piles and soil mechanics methods must be used to determine the capacity of the material below the tip. A single row of friction piles is not considered to act as a group provided the center-to-center spacing is more than 2-1/2 times the nominal dimension of the piles (Art. 4.3.4.4).

5.2. Case A, Capacity as a Structural Member

In the following sections, a method is developed to analyze the pile in an integral abutment bridge as a structural member. Two alternative design criteria, both based on the beam-column interaction equations, are presented in the following sections. The first of these alternatives accounts for the stresses produced by the horizontal thermal displacement. The second alternative neglects the stresses produced

from thermal expansion or contraction of the superstructure but accounts for the thermal displacement at the head. Both alternatives are compared with the IAB2D finite element program.

The deformation of a pile, due to the displacement of the abutment, will generally be confined to the upper portion of the pile and will seldom exceed a length of ten pile diameters below the soil surface [5]. This has led to the idealization of the pile as an equivalent cantilever of some effective length with boundary conditions at the head being the same as those for the actual system. The length of this equivalent cantilever will be developed. The Winkler soil model is used to represent the soil. Typical values for the soil parameters are given in Tables 2.4 and 2.5.

5.2.1. Equivalent Cantilever Idealization

Embedded piles can be represented, using the equivalent cantilever method, as a column with a base fixed at some distance below the ground surface (Fig. 5.1). The notation is the same for both the fixed and pinned-head conditions. The length of the actual pile embedded in the ground is represented as ℓ, and the length above the ground is ℓ_u. The equivalent embedded length, ℓ_e, is the depth from the soil surface to the fixed base of the equivalent cantilever. The total length of the equivalent cantilever is the length ℓ_u plus ℓ_e, represented by L. For a long pile embedded in soil, there is a depth below which the horizontal displacements at the pile head have negligible effects. A critical length, ℓ_c, which represents this depth, can be calculated. Beyond this length, lateral displacements and bending moments are a small percentage (about 4%) of those at the pile head. If a pile is

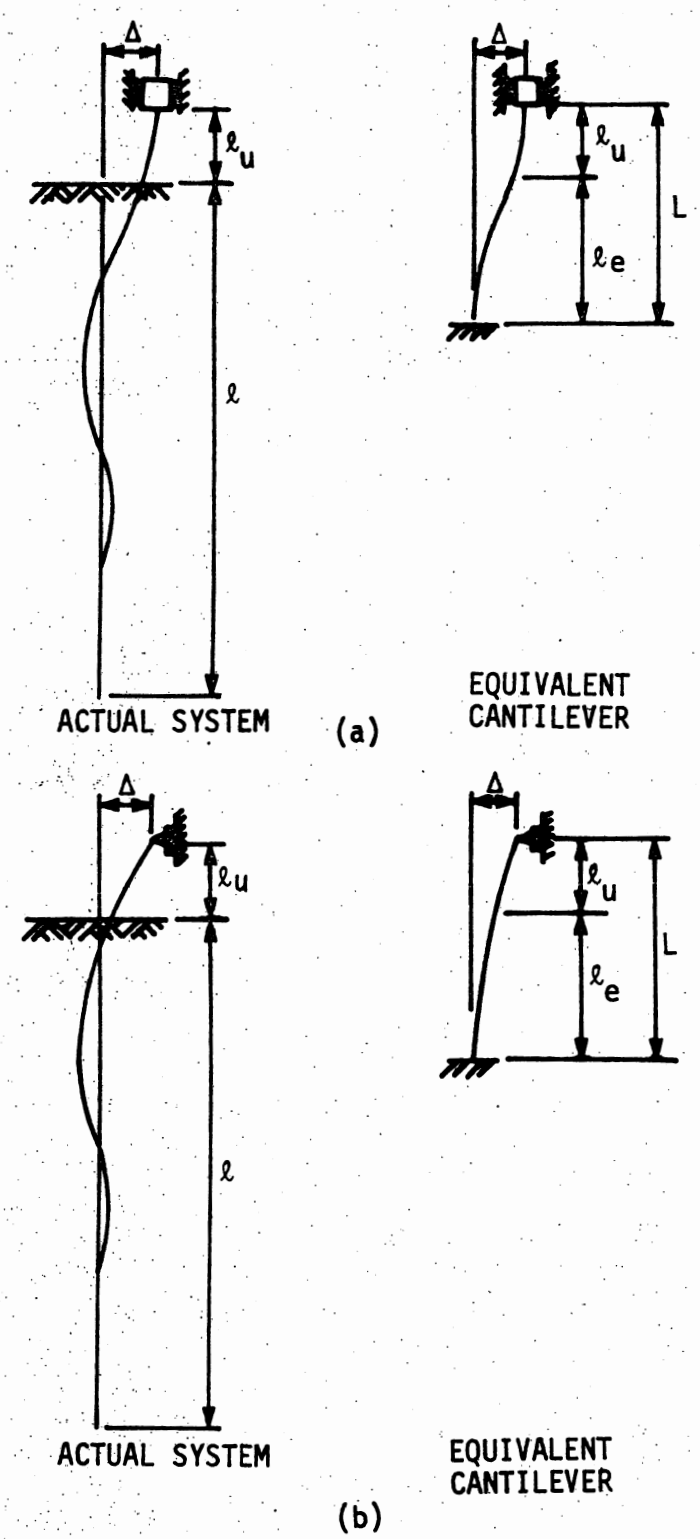

Figure 5.1. Cantilever idealization of the pile: (a) fixed-head condition (b) pinned-head condition.

longer than ℓ_c, the pile behaves as if it is infinitely long. For a soil with a uniform subgrade-reaction modulus, the critical length [5,6,29] is selected as

$$\ell_c = 4R \tag{5.5}$$

in which the relative stiffness factor R is

$$R = \sqrt[4]{\frac{EI}{k_h}} \tag{5.6}$$

Most piles used in practice are longer than their critical length and behave as "flexible" piles. Note that ℓ_c is a parameter of the pile and soil system and is not a physically identifiable length.

Equivalent cantilevers can be used to calculate the forces in the pile and the bridge superstructure [30]. For example, an equivalent cantilever can be determined such that its maximum moment would be equal to the maximum moment in real pile. However, the complete moment diagram below the ground surface could not be determined with the same equivalent cantilever. Three different equivalencies were considered in the development of the design method. They are based on (1) the horizontal stiffness of the soil-pile system, (2) the maximum moment in the pile, and (3) the elastic buckling load of the pile. For each equivalency, the boundary condition at the pile head was either fixed (no rotation) or pinned (no moment). The horizontal displacement, Δ, at the top of the equivalent system corresponds to the longitudinal expansion or contraction of the bridge superstructure at the integral abutment (Fig. 5.1).

The development of the equations for determining the equivalent embedded length are found in Section 12 (Appendix C). These equations are plotted in a nondimensional form for fixed-head and pinned-head piles embedded in a uniform soil in Figs. 5.2 and 5.3, respectively. The horizontal axis is the ratio of the length of pile above the ground, ℓ_u, to the critical length of the soil-pile system, ℓ_c, Eq. (5.5). The vertical axis is the ratio of the equivalent embedded length, ℓ_e, to the critical length. The equivalent embedded length, determined from Figs. 5.2 and 5.3 (or the equations in Appendix C), are added to the length of pile above the surface to obtain the total length of the equivalent cantilever. As can be seen from Fig. 5.2 and 5.3, an unfilled predrilled hole significantly reduces the equivalent embedded length until the hole is approximately ℓ_c deep, that is, ℓ_u/ℓ_c equals approximately one. Below that depth, the effective length remains essentially constant over the range used for most integral abutment bridges.

For piles embedded in a non-uniform soil, the equivalent soil stiffness developed in Section 12 is used with Figs. 5.2 and 5.3 to determine the equivalent cantilevers.

5.2.2. Pile Behavior

The behavior of the equivalent cantilever is governed by a complex interaction of material and geometric instabilities often called inelastic buckling. For explanation purposes, it is usually described by considering the two extreme cases of material instability (plastic collapse) and geometric instability (elastic buckling). (See Section 2.4 and Fig. 2.5.)

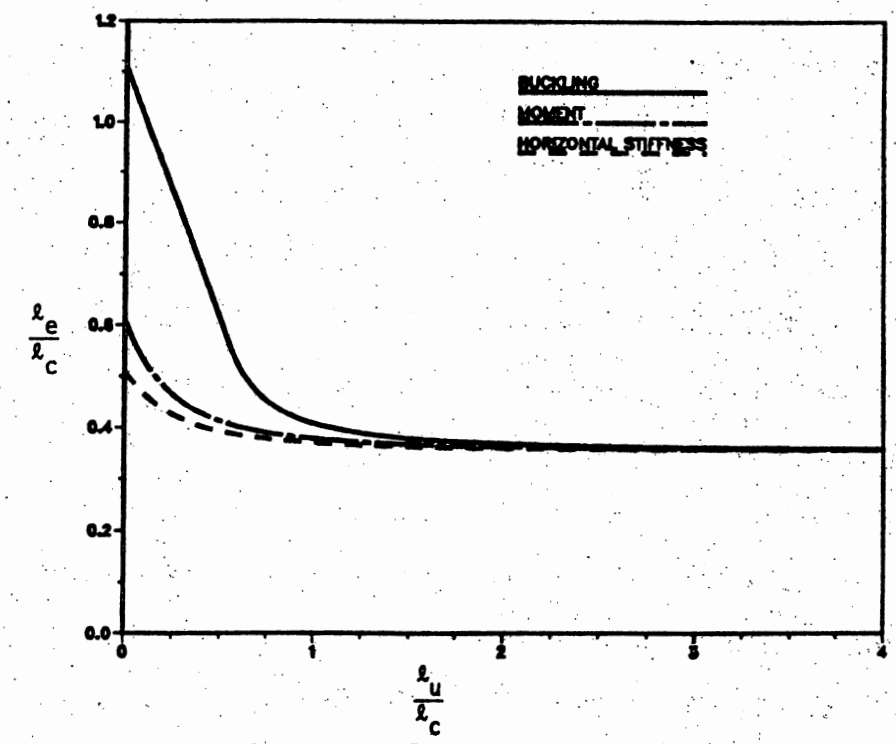

Figure 5.2. Equivalent cantilevers for fixed-head piles embedded in a uniform soil.

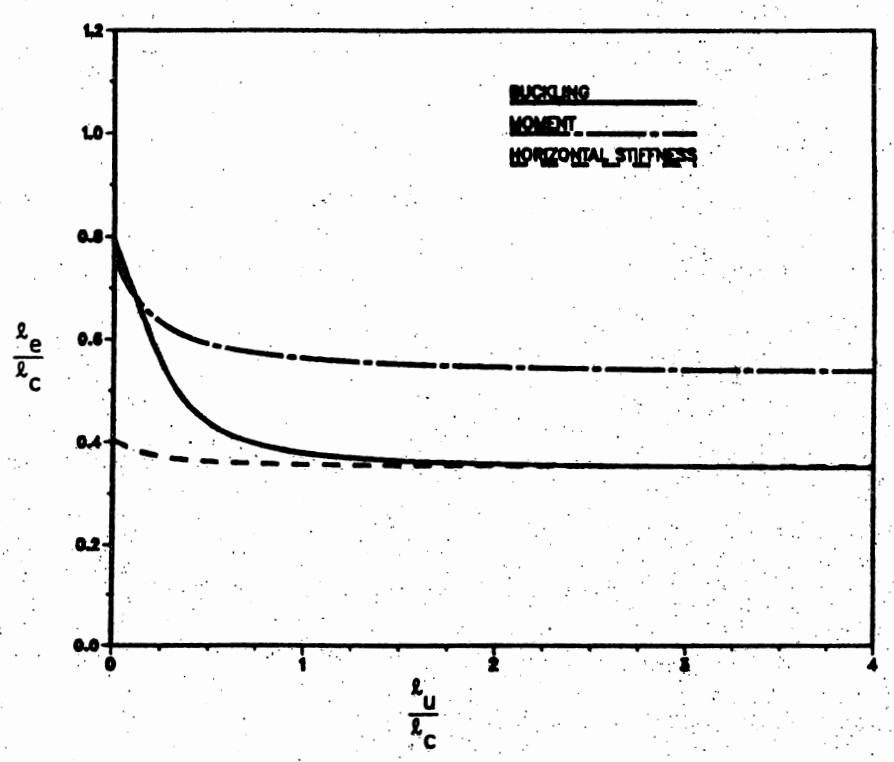

Figure 5.3. Equivalent cantilevers for pinned-head piles embedded in a uniform soil.

During plastic collapse, a plastic mechanism is formed as the material yields in a sufficient number of locations. For a complete mechanism, sufficient ductility must be present to permit a full redistribution of force, that is, sufficient rotation capacity must exist at plastic hinge locations. For example, local and lateral buckling must be prevented in steel HP sections. For a perfectly straight column, plastic collapse would occur when the axial load reaches the yield load:

$$P_y = F_y A \tag{5.7}$$

In first-order plastic theory involving small displacements, the plastic collapse load is not affected by residual stress, thermal stress, imperfect fit or, as in this case, support movement [31,32]. Hence, the first-order plastic collapse load for the equivalent cantilever is not reduced by the horizontal motion at its head.

At the other extreme, the elastic buckling strength of a column is also not affected by residual stress or support motion. Hence, the elastic buckling strength of the equivalent cantilever with a given horizontal displacement is the same as an initially straight column, that is,

$$P_e = \frac{\pi^2 EI}{(KL)^2} \tag{5.8}$$

where K is the effective length factor. (The discussion in Section 13 (Appendix D) verifies this.)

However, between these two extremes, inelastic buckling occurs and the buckling strength is affected by support motion and residual stresses. Within this regime, geometric and material instabilities interact to produce failure of the column. Typically, the complex behavior in this region is approximated by some sort of transition curve between plastic collapse and elastic buckling [22,31,33], such as Eq. (2.8) (Rankine) or Eq. (2.9). As described in Section 2.4, the Rankine equation is a conservative method for representing this transition. The finite element analysis, summarized in Section 2.3 and verified by the experimental work, adequately predicts this complex behavior and will be used to evaluate the design equations.

5.2.3. Design Alternatives

As stated in the summary of the AASHTO Specification (Section 5.1), the capacity of a pile as a structural member, Case A, is to be determined using the beam-column interaction equations, Eqs. (5.1) thru (5.4). To compare these equations with the finite element solution, the factors of safety will be removed from the interaction equations. Additionally, lateral-torsional buckling and local buckling of the compression elements, which must be considered in design, will not be considered now. However, these factors will be incorporated into the actual design equations. Equations (5.1) and (5.3) are modified to become

$$\frac{P}{P_{cr}} + \frac{CM}{M_p\left(1 - \frac{P}{P_e}\right)} \leq 1.0 \qquad (5.9)$$

and Eqs. (5.2) and (5.4) become

$$\frac{P}{P_y} + \frac{M}{M_p} \leq 1.0 \tag{5.10}$$

The expression for P_{cr} is found in the AASHTO Specification [22] (Eqs. (10-151) thru (10-154))

for

$$\frac{KL}{r} \leq C_c = \sqrt{\frac{2\pi^2 E}{F_y}}$$

$$P_{cr} = F_y A \left[1 - \frac{F_y}{4\pi^2 E} \left(\frac{KL}{r} \right)^2 \right] \tag{5.11}$$

for

$$\frac{KL}{r} > C_c$$

$$P_{cr} = \frac{\pi^2 EA}{\left(\frac{KL}{r} \right)^2} \tag{5.12}$$

Equation (5.11) corresponds to Eq. (2.9) and Eq. (5.12) corresponds to Eq. (5.8). In the following sections two alternatives for the applied moment, M, are considered and compared with the finite element solution.

5.2.3.1. Alternative One

Alternative One accounts for the first-order stresses induced in the pile caused by thermal expansion or contraction of the superstructure. The pile is considered an equivalent cantilever with a horizontal

pile-head displacement, Δ, as described in Section 5.2.1. This displacement produces first-order elastic moments that do not take into account any plastic redistribution of internal forces. For a fixed-head pile the maximum moment is

$$M = \frac{6EI\Delta}{L^2} \tag{5.13}$$

and for a pinned-head pile is

$$M = \frac{3EI\Delta}{L^2} \tag{5.14}$$

Ductility of the pile material is not taken into account; therefore, failure is assumed to occur when the internal forces reach their yield values. Hence, unlike the plastic collapse theory where support movements do not affect member strength, Alternative One can be expected to show a drastic reduction in the pile capacity caused by the horizontal displacement, Δ.

The differential equation solution in Section 13 (Appendix D) shows that the elastic buckling load, which will be used in the moment amplification term of Eq. (5.9), can be taken as

$$P_e = \frac{\pi^2 EI}{(0.5L)^2} \tag{5.15}$$

or

$$P_e = \frac{\pi^2 EI}{(0.7L)^2} \tag{5.16}$$

for the fixed-head and pinned-head piles, respectively. The corresponding values of the moment gradient factor, C, for the equivalent cantilevers in Eq. (5.9) are 0.4 and 0.6. The recommended effective length factor, K, for design purposes are 0.65 and 0.8 for the fixed-head and pinned-head piles, respectively.

5.2.3.2. Alternative Two

Alternative Two assumes that the stresses in the pile due to the longitudinal displacement of the superstructure have no significant effect on the pile capacity; however, this alternate accounts for the secondary PΔ effect. As stated in Section 2.1, 28 states and the Federal Highway Administration, Region 15, have used integral abutment bridges. Of these, 26 states neglect stresses due to the longitudinal displacement, although 2 of these states do calculate stresses if the bridge has some type of unique feature. The effect of essentially neglecting these stresses will be studied by comparing the results of Alternative Two to the finite element results.

Discussion in Section 5.2.2 points out another motivation for Alternative Two, that is, support movement and thermal stresses do not affect either the plastic collapse load or the elastic buckling load. However, the system must have sufficient ductility to develop a mechanism with the associated plastic hinge rotations. For example, steel sections must be sufficiently compact (AASHTO Art. 10.48.1) and sufficiently braced to prevent both local and lateral buckling as the plastic hinge undergoes inelastic rotation.

For an equivalent cantilever with a horizontal head displacement, Δ, (Fig. 5.4), the combined effects of moment, M, and shear, H, balance the overturning moment, $P\Delta$ [34]. For the fixed-head pile,

$$P\Delta = HL + 2M \tag{5.17}$$

and for the pinned-head pile,

$$P\Delta = HL + M \tag{5.18}$$

For our case, one useful and conservative bound will be to assume that the $P\Delta$ effects are resisted entirely by the moment, that is,

$$M = \frac{P\Delta}{2} \tag{5.19}$$

and

$$M = P\Delta \tag{5.20}$$

for the fixed-head pile and pinned-head pile, respectively.

By using Eqs. (5.19) and (5.20) the moments associated with Alternative One (Eqs. (5.13) and (5.14)) are neglected. This amounts to assuming the pile to be in a stress-free state after the thermal movement of the superstructure.

As with Alternative One, Section 13 shows that the elastic buckling load to be used in the amplification of Eq. (5.9) is the same as is given in Eqs. (5.15) and (5.16) for the fixed and pinned-head conditions, and the corresponding values of C in Eq. (5.9) are 0.4 and 0.6.

5.2.3.3. Comparison with Finite Element

Design Alternative One and Alternative Two will be compared with the results from the finite element program. Three columns or equivalent cantilevers, of length 10, 20, and 30 ft were analyzed (Fig. 5.4). The column is an HP10 × 42 pile (F_y of 36 ksi) bending about its weak axis. For the finite element analysis, the column material stress-strain curve was approximated by the modified Ramberg-Osgood equation using a shape factor, n, of five to simulate the effects of residual stresses [35]. The initially straight column was given a specified horizontal head displacement and then displaced vertically until its peak axial compressive load was reached. This peak load was compared with the design equation results without safety factors, local buckling, or lateral-torsional buckling (Eqs. (5.9) and (5.10)).

Figures 5.5 through 5.10 compare the finite element results and results to the design equations using the two design alternatives for fixed or pinned-head columns. Also, finite element results were presented in Ref. [1] for piles totally embedded in different soils. The tabulated values for the finite element results are presented in Tables 5.1 and 5.2 for the embedded piles and columns, respectively. Case A, B, C, D, and E are defined in the tables to identify Figs. 5.5 through 5.10. The vertical axis is the ratio of the ultimate axial load, P, to the yield load, P_y. The horizontal axis is the ratio of the yield load to the elastic buckling load, P_e, Eq. (5.8). Hence, the horizontal axis is proportional to the square of the slenderness of the column (KL/r).

Figures 5.5 and 5.6 show the results for a pile that is not horizontally displaced. Since there is no moment from lateral loading,

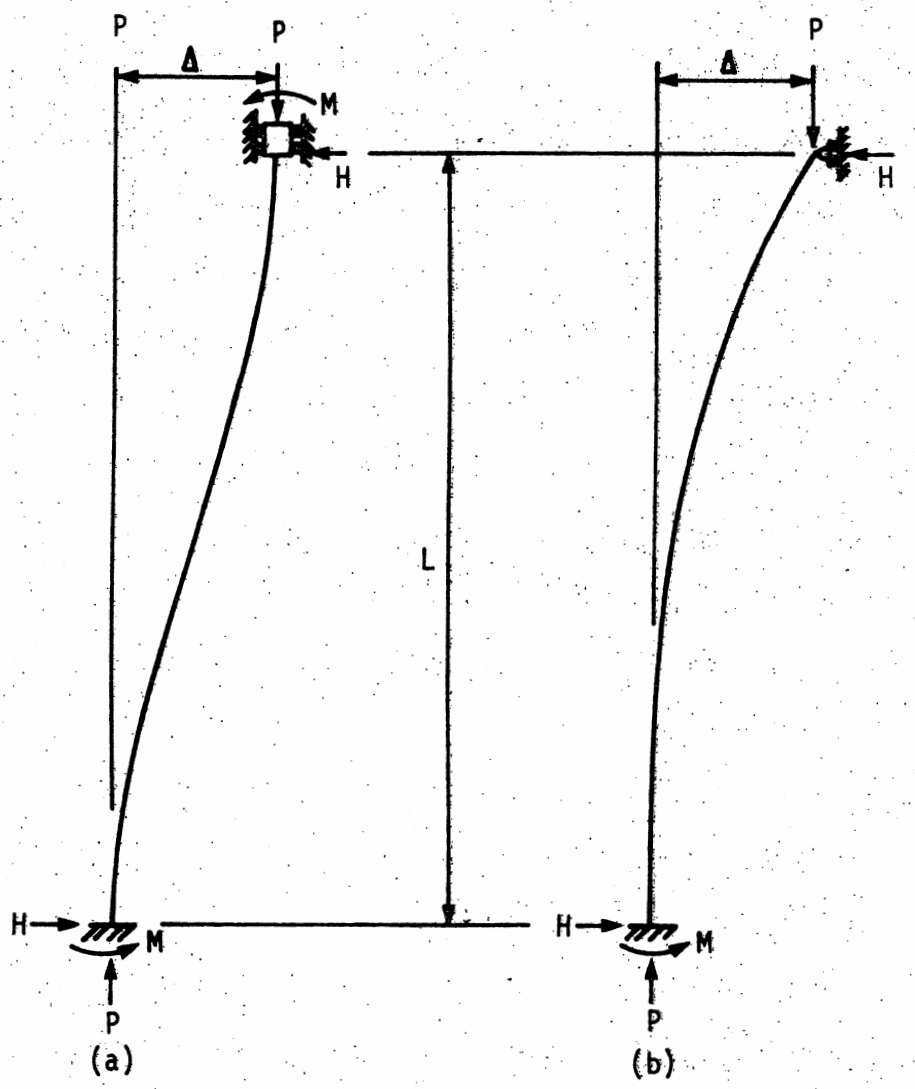

Figure 5.4. Equivalent cantilevers: (a) fixed-head conditions (b) pinned-head conditions.

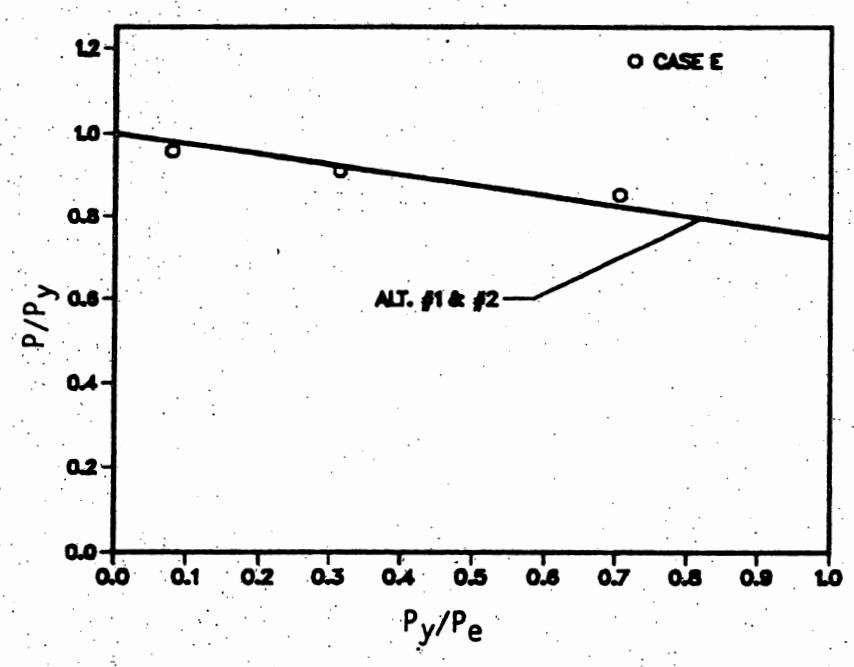

Figure 5.5. Finite element and the design equations for a HP10 × 42 pile with a fixed-head and Δ = 0. (see Table 5.2 for Case identification).

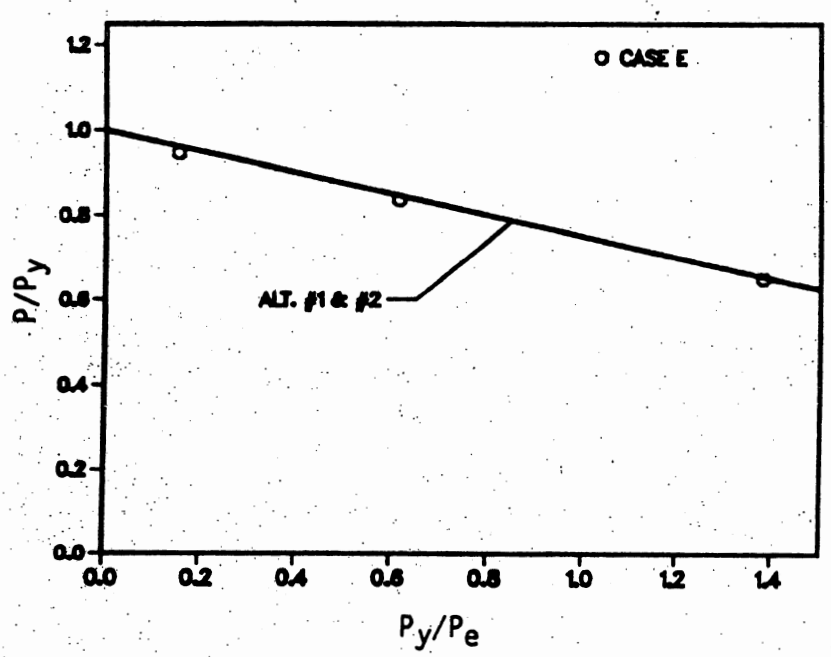

Figure 5.6. Comparison of finite element and the design equations for a HP10 × 42 pile with a pinned-head and Δ = 0. (see Table 5.2 for Case identification).

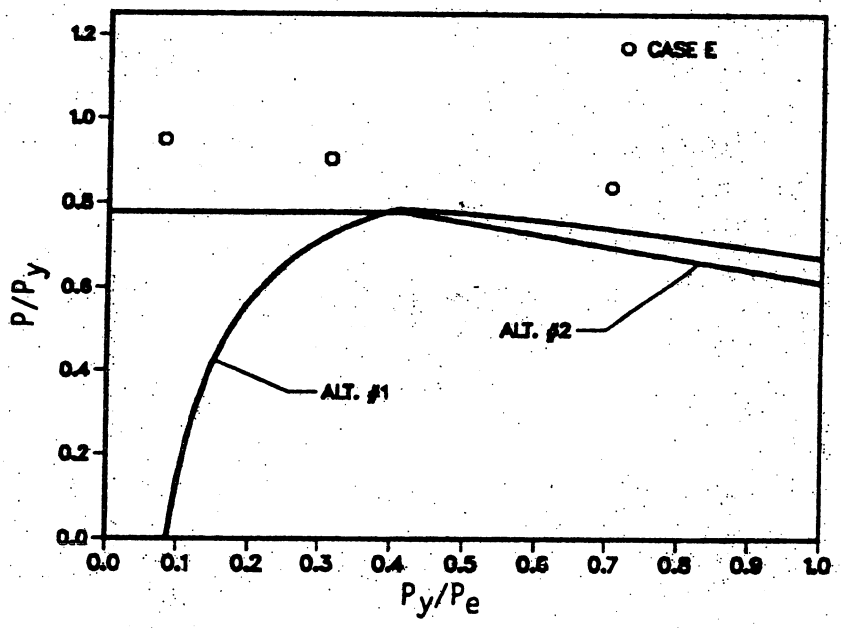

Figure 5.7. Comparison of finite element and the design equations for a HP10 × 42 pile with a fixed-head and Δ = 1 in. (see Table 5.2 for Case identification).

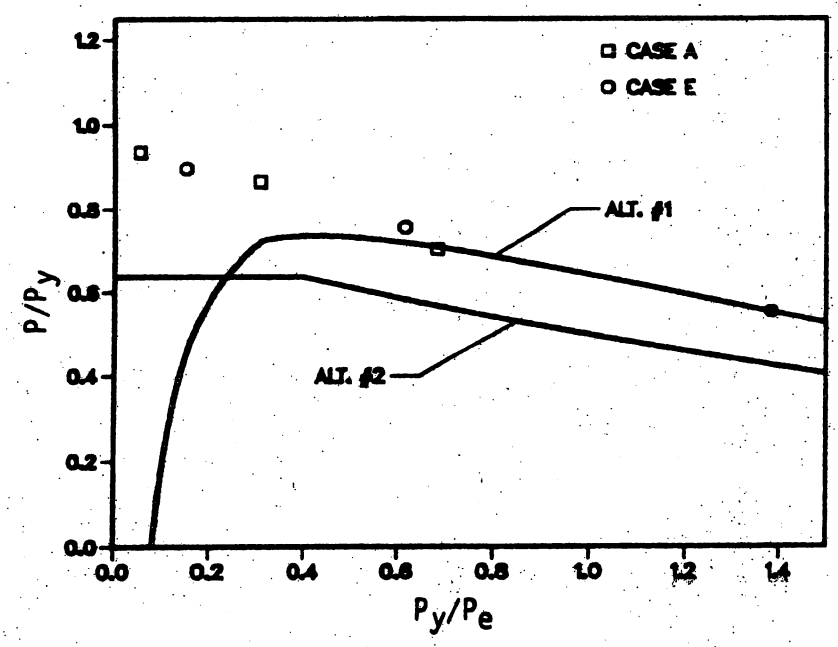

Figure 5.8. Comparison of finite element and the design equations for a HP10 × 42 pile with a pinned-head and Δ = 1 in. (see Table 5.1 for Case identification).

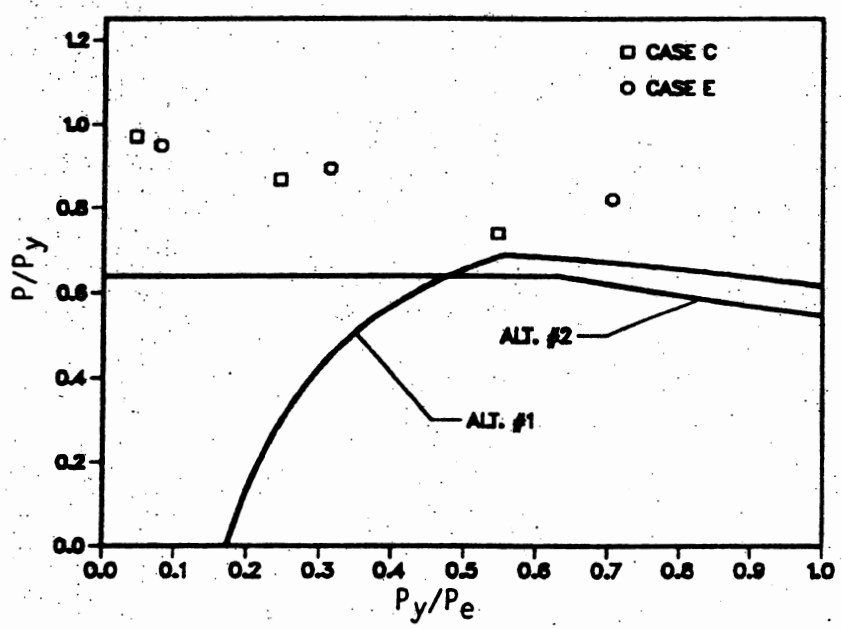

Figure 5.9. Comparison of finite element and the design equations for a HP10 × 42 pile with a fixed-head and Δ = 2 in. (see Tables 5.1 and 5.2 for Case identification).

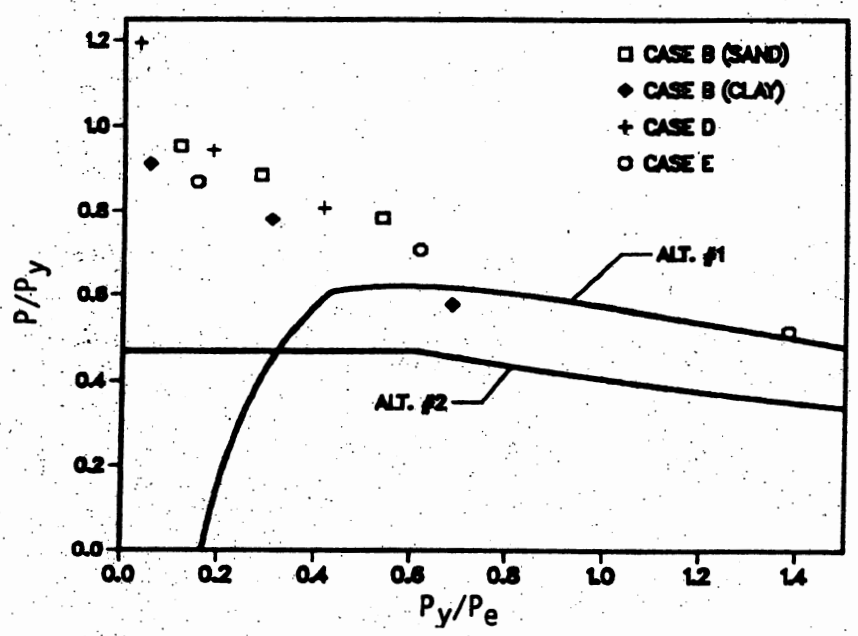

Figure 5.10. Comparison of finite element and the design equations for a HP10 × 42 pile with a pinned-head and Δ = 2 in. (see Tables 5.1 and 5.2 for Case identification).

Table 5.1. Elastic buckling load, P_e, and ultimate load, P, for combined loading of piles in soil [1].

Case	Soil Types	P_e (kips)	P (kips) (finite element)
A			
Δ = 1 in. (Pinned-head, pinned support at pile tip)	very stiff clay	11352	580
	soft clay	2036	537
	1/5 soft clay	909	437
B	very stiff clay	11352	564
Δ = 2 in. (Pinned-head, pinned support at pile tip)	soft clay	2036	483
	1/5 soft clay	909	357
	twice dense sand	5260	590
	medium sand	2201	548
	1/2 loose sand	1156	485
C			
Δ = 2 in. (Fixed-head, pinned support at pile tip)	very stiff clay	14190	602
	soft clay	2545	538
	1/5 soft clay	1136	458
D			
Δ = 2 in. (Pinned-head, w/vertical springs, no support at pile tip)	very stiff clay	18787	740
	soft clay	3370	584
	1/5 soft clay	1504	500

Table 5.2. Elastic buckling load, P_e, and ultimate load, P, for combined loading of columns (Case E).

Head Conditions	Length (ft)	P_e (kips)	P (kips) (finite element)		
			Δ = 0	Δ = 1 in.	Δ = 2 in.
Fixed	10	5696	427	424	424
	20	1424	406	404	399
	30	633	380	374	366
Pinned	10	2906	422	400	387
	20	726	373	338	316
	30	323	290	247	229

both design alternatives give the same result, that is, Eqs. (5.11) or (5.12) predict the column will fail at P_{cr}. Additionally, the finite element results compare well with the design equations, demonstrating that the shape factor of five in the modified Ramberg-Osgood equation adequately accounts for residual stresses and other imperfections.

Figures 5.7, 5.8, 5.9, and 5.10 compare piles with various horizontal head displacements. Both alternatives give conservative estimates of the finite element results, except for a single point for a very long pinned-head column with a 2-in. horizontal displacement, which falls only slightly below the Alternative One design equation. This case corresponds to a pile with a small elastic buckling load in a very flexible soil.

The ascending portion of the Alternative One design equation (on the left in the figures) is controlled by the strength equation Eq. (5.10). As mentioned in Section 5.2.3.1, this alternative predicts that the horizontal displacement causes a drastic reduction in the capacity because there is no allowance for plastic redistribution. Yielding occurs in bending for a small horizontal motion and no elastic reserve is available for the axial load. The finite element results indicate significant redistribution occurs.

Alternative Two is conservative for all of the finite element results. The yield equation, Eq. (5.10), again controls the horizontal portion of the curve to the left in the figures, but the reduction in this region is not nearly as drastic as Alternative One, since the stresses due to temperature have been essentially neglected. In effect,

Alternative Two recognizes that some plastic redistribution of internal forces can occur, as indicated by the finite element solution.

Both alternatives are somewhat conservative on the right in the figures where the stability equation controls. As shown in Section 13 (Appendix D), the conservation occurs because, in this case, the amplification factor in the stability equation is a conservative approximation to the actual amplification factor.

5.2.4. Recommendation

Equations (5.1) and (5.2) or (5.3) and (5.4) are required when the capacity of a pile as a structural member (Case A) governs the design. Alternative One moments, from Eq. (5.13) or (5.14), are recommended for use in the design equations for piles that have little ductility and where plastic redistribution cannot occur. Noncompact steel sections, which do not have the required plastic hinge rotation capacity, should use Alternative One. Although not studied here, the design of certain timber and nonductile concrete sections should be limited to Alternative One. Alternative Two moments (Eq. (5.19) or (5.20)) are recommended for use when the pile is sufficiently ductile to ensure adequate plastic hinge rotation capacity and to allow redistribution of forces. A compact steel section (AASHTO Art. 10.48.1) or a ductile reinforced concrete section fit this category. The design example in Section 6 illustrates that a HP10 × 42 pile, though not compact, does have sufficient ductility for that particular example. Alternative Two is a rational alternative to the design basis mentioned in Section 1 ("...it works").

5.3. Case B, Capacity to Transfer Load to Ground

Case B considers the transfer of load through the interface between the pile and the soil. There are two mechanism that transfer load: skin friction (cohesion and adhesion) along the length of the pile and bearing at the pile tip (see Section 2.4). For a pile embedded in a layered soil, the friction capacity will be the sum of the friction capacity in each layer. The capacity of the frictional interface can be affected by horizontal motion [5]. As seen in Fig. 5.11, a gap may form between the pile and the soil near the ground surface, particularly, during cyclic loading. This gap would certainly destroy the frictional capacity of the soil near the surface. Even if no visible gap develops, the frictional capacity could be reduced near the top. Although not conclusively proven, an indication of this phenomenon was present in the third field test, Sec. 3.3.4. The reduced friction capacity near the top of the pile reduces the length of the pile that is effective in transferring the load from the pile to the soil through friction.

A pile displacement, y_{max}, which represents the maximum lateral displacement below which the friction capacity is unaffected, will be determined. At lateral displacements above y_{max}, the frictional capacity is assumed to be zero. Factors that affect the depth at which y_{max} occurs include (1) boundary condition at the pile head, (2) soil-pile relative stiffness, (3) number of horizontal load cycles, and (4) magnitude of the horizontal displacement at the pile head. Since the horizontal displacement of the pile head is an annual occurrence, the number of load cycles will be relatively small.

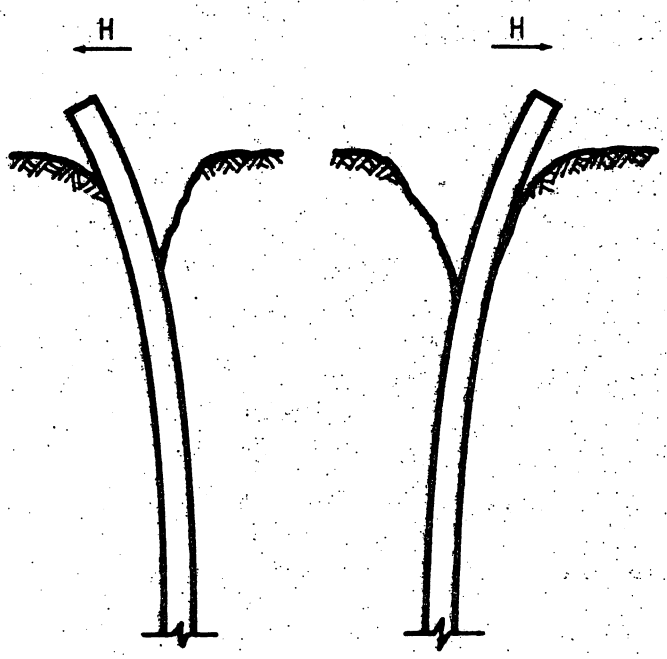

Figure 5.11. Formation of a gap between the pile and the soil because of cyclic horizontal load.

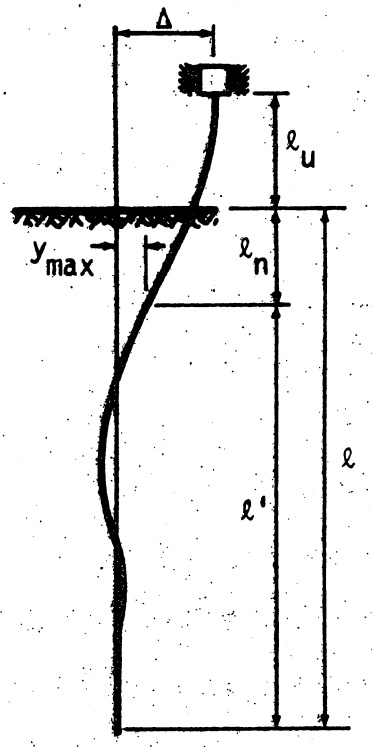

Figure 5.12. Soil-pile system for determining the friction capacity of the pile.

The development of equations for determining the length that should be neglected for friction capacity is presented in Section 12 (Appendix C). These equations were developed for the system shown in Fig. 5.12; the notation is the same for both fixed and pinned-head piles. The length of pile remaining to resist the vertical load by friction, ℓ', is

$$\ell' = \ell - \ell_n \tag{5.21}$$

in which ℓ_n is the length of pile that is taken to be ineffective for friction.

Figures 5.13 and 5.14 are plots developed in Section 12 for fixed-head and pinned-head piles embedded in a uniform soil. The horizontal axis is the ratio of the length of pile above the ground, ℓ_u, to the critical length of the soil and pile system, ℓ_c, Eq. (5.5). The vertical axis is the ratio of the length, ℓ_n, to the critical length. The length ℓ_n can be determined from Fig. 5.13 or 5.14 for a selected value of y_{max}/Δ. Two percent of the pile diameter is suggested in Ref. [5] for y_{max}. This amount corresponds to a horizontal displacement of approximately 0.2 inches for an HP10 × 42 pile. If Δ is 1 inch, there will be little, if any, effect on the vertical capacity for a pile in an unfilled predrilled hole with ℓ_u/ℓ_c greater than one, since ℓ_n/ℓ_c equals zero when y_{max}/Δ equals 0.2.

For piles embedded in a nonuniform soil, the equivalent soil stiffness developed in Section 12 is used with Figs. 5.13 and 5.14 to determine the length, ℓ_n.

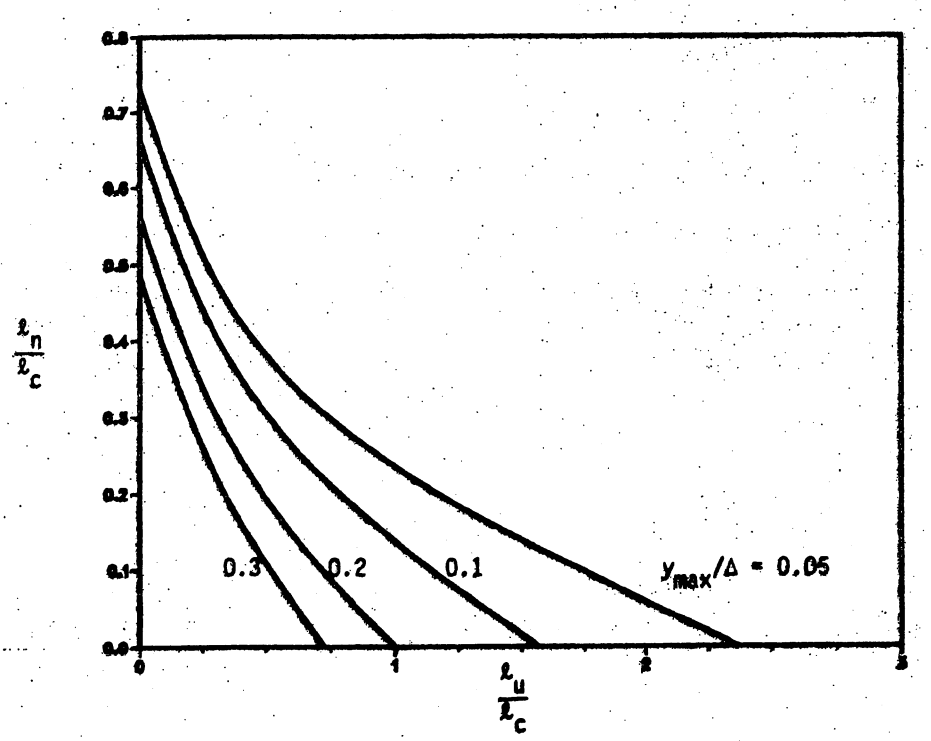

Figure 5.13. Displacement for a fixed-head pile embedded in a uniform soil

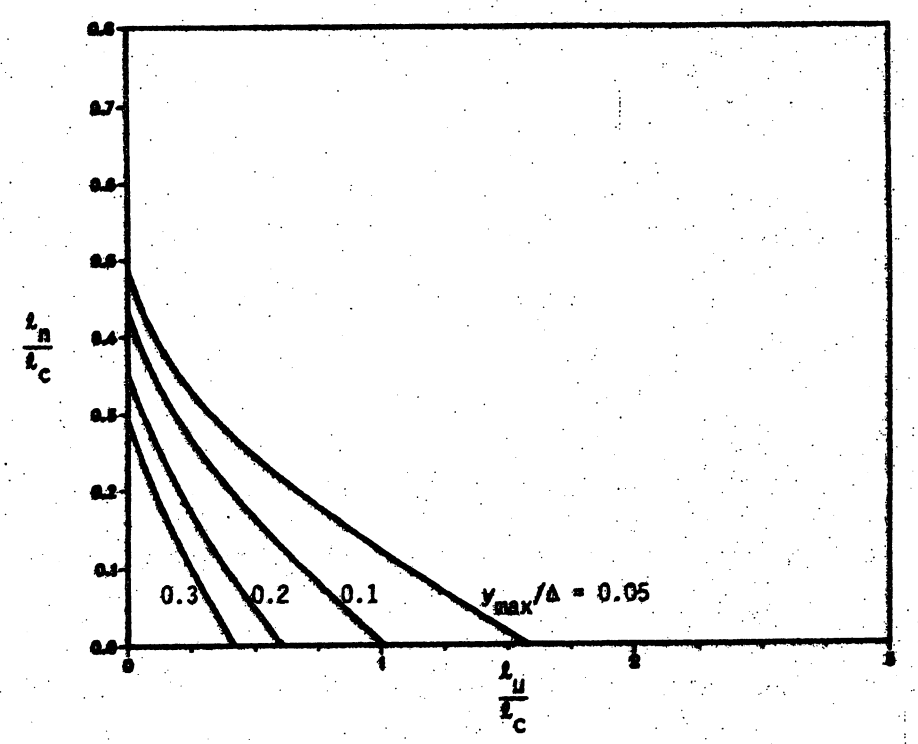

Figure 5.14. Displacement for a pinned-head pile embedded in a uniform soil

End bearing piles are not affected by the gap described above. For steel H-piles involving Case B design, the AASHTO Specification [22] limits the pile stress to 9000 psi over the cross-sectional area of the pile tip.

5.4. Case C, Capacity of Ground to Support Load

Case C deals with the capacity of the soil around and below the pile to support the load. The capacity of a pile in a group may be reduced from the capacity of a single isolated pile. Instead of the piles failing individually, they fail as a group. This type of failure is generally associated with a close spacing of the piles.

For friction piles, the group failure is associated with the soil between the piles displacing with the piles. The AASHTO Specification [22] states that for friction piles the group effect for vertical capacity can be neglected as long as the piles are spaced, center-to-center, at least 2-1/2 times their nominal diameter or dimension (Section 5.1). If the piles are spaced closer than the above limit, the specification recommends decreasing the efficiency of the piles. A method is provided in the AASHTO Specification (Art. 4.3.4.7) for determining the reduction for a single pile capacity when used in a group. A center-to-center spacing of three times the nominal diameter or dimension is sufficient to neglect group effects for horizontal loading [36].

For point-bearing piles the material below the tip of the piles must be able to develop the point-bearing forces from the group of

piles. The AASHTO Specification requires sufficient borings to determine the quality and thickness of the stratum in which the point bearing is to be developed.

Although horizontal movement may affect the transfer of load from the pile to the soil, Case B, the authors assume that it does not affect group action. Therefore, the capacity of a pile group, Case C, should be determined in the same manner as if the horizontal movement was not present.

6. DESIGN EXAMPLES

To illustrate the design procedure described in Section 5, a pile will be designed to support a 50-kip load (D + L + I) for the case shown in Fig. 6.1. The pile is an HP10 × 42 with a yield strength, F_y, of 36 ksi. There are eight piles per abutment, as shown in Fig. 6.2, spaced 6 ft-4 in. center-to-center. The piles were driven in an 8-ft-deep predrilled, oversized hole that was filled with loose sand. The existing soil consists of an initial 12 ft of stiff clay underlain by very stiff clay. The integral abutment bridge is a seven-girder, five-span structure (60-80-80-80-60 ft) having a total length of 360 ft. The end spans are 60-ft long with AASHTO Type III bridge girders.

6.1. Friction Pile

First, a preliminary design is performed to determine what length is required to carry the vertical load as a friction pile. The allowable design, vertical load for the pile is 50 kips or 25 tons. Then, the effect of the horizontal abutment displacement on the pile will be checked. Both Alternative One and Two are considered.

- Perform preliminary design:

  The estimated allowable resistance value for the steel friction pile will be taken as 0.8 tons/ft and 1.2 tons/ft for the stiff and very stiff clay, respectively. These values correspond to "Firm silty glacial clay" and "Firm-very firm glacial clay" from the Iowa D.O.T. Foundation Soils Information chart, revised June 1976. AASHTO Load

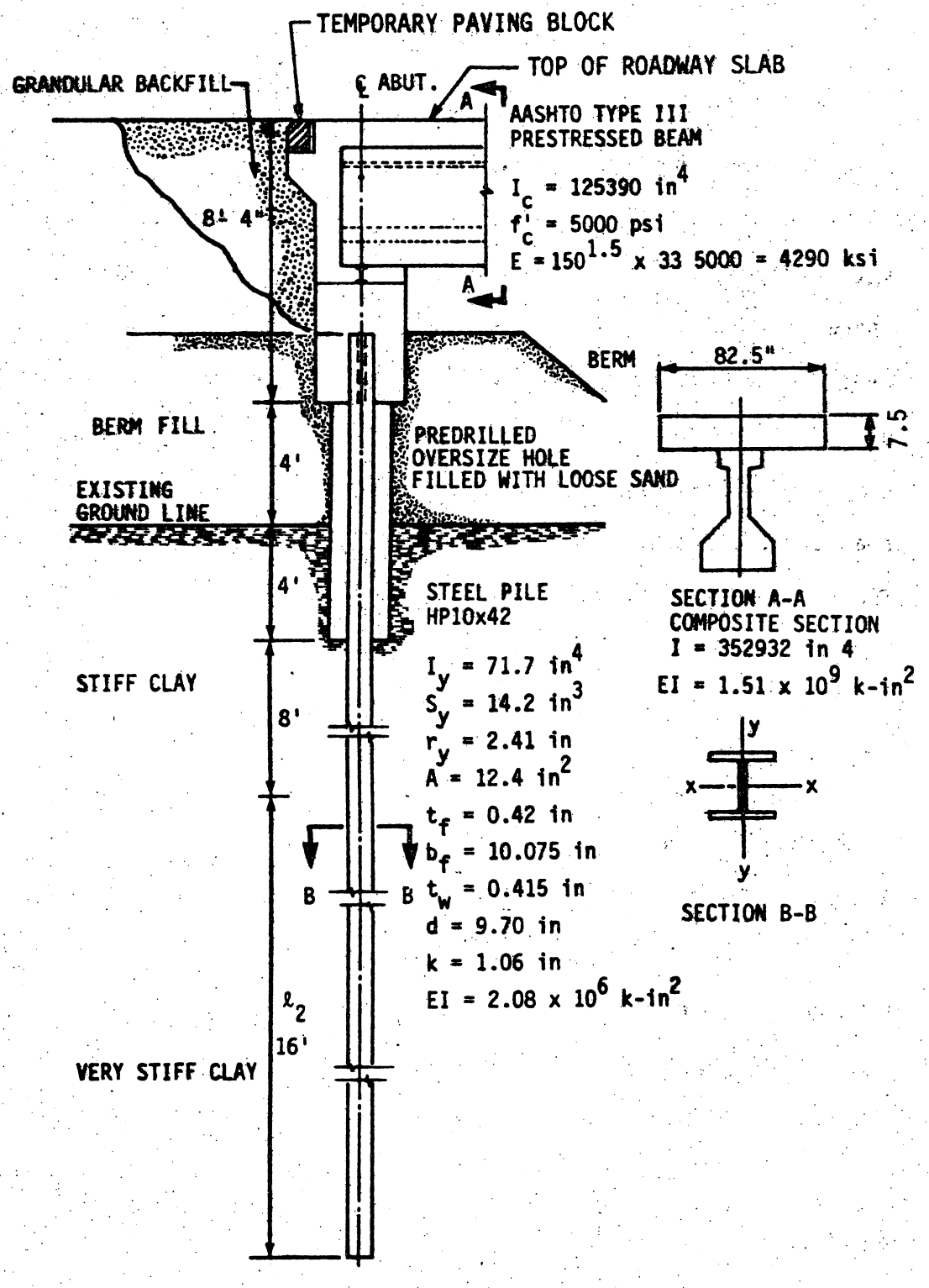

Figure 6.1. Section through abutment and soil profile.

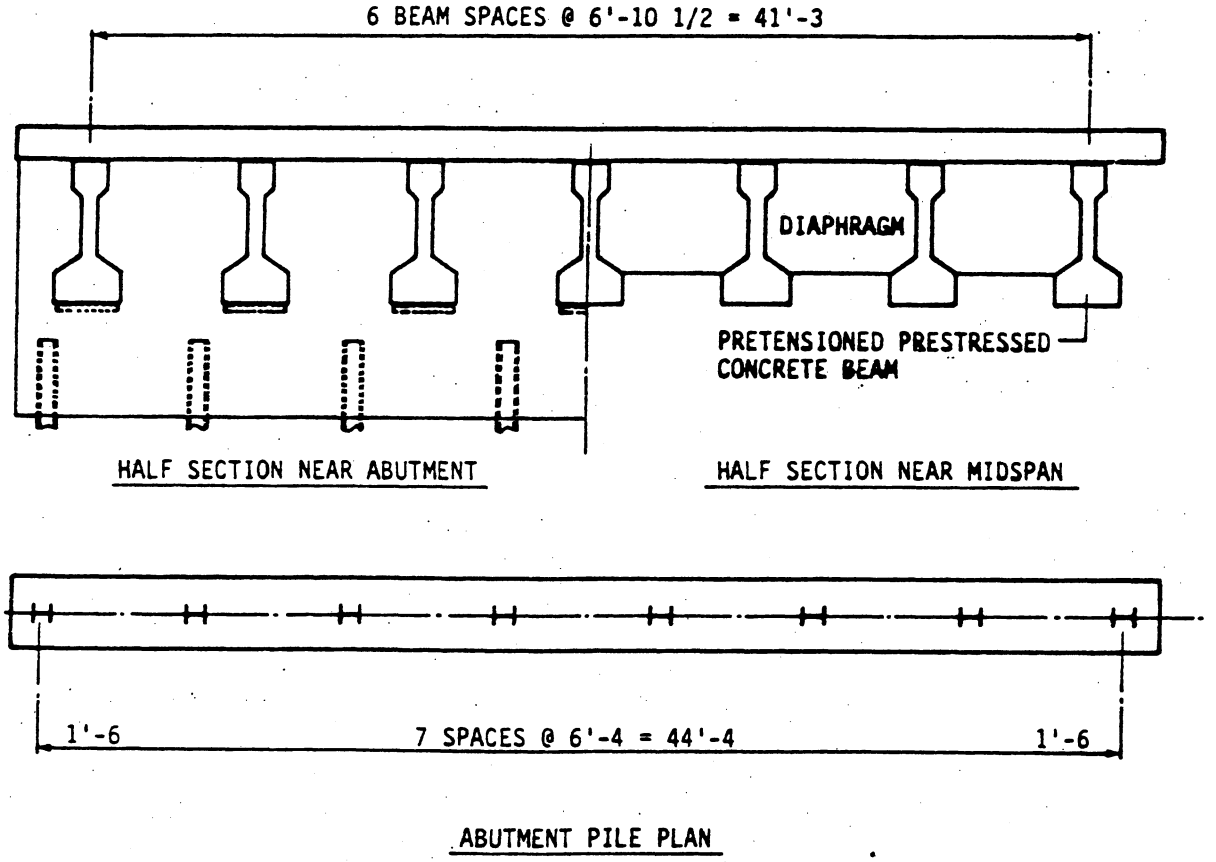

Figure 6.2. Transverse section through deck.

Group I, Case B is assumed to control for this preliminary design. The length of the embeddment, ℓ_2, into the very stiff clay can be found from

$$0.8 \text{ tons/ft } (8 \text{ ft}) + 1.2 \text{ tons/ft } (\ell_2) = 25 \text{ tons} \tag{6.1}$$

solving,

$$\ell_2 = 15.5 \text{ ft} \tag{6.2}$$

Rounding up this length to 16 ft, the total embedded length below the bottom of the predrilled hole becomes 24 ft. The contribution of the sand in the predrilled hole has been neglected, including possible negative skin friction effects.

- Determine the equivalent uniform stiffness, k_e, of the soil:

  The top eight feet of pile is surrounded by loose sand in a predrilled hole, which has been bored in the granular backfill and stiff clay. The lateral soil stiffness is difficult to estimate in this region. It is not as flexible as loose sand because the predrilled hole has only a 2-foot diameter and the zone of influence of the pile is up to six pile diameters, about 5 ft. The stiffness will be assumed as shown in Fig. 6.3, which corresponds to loose-medium sand in Table 2.5. The value of stiff clay in Table 2.4 will be used to approximate the existing soil stiffness. Following the procedure in Section 12

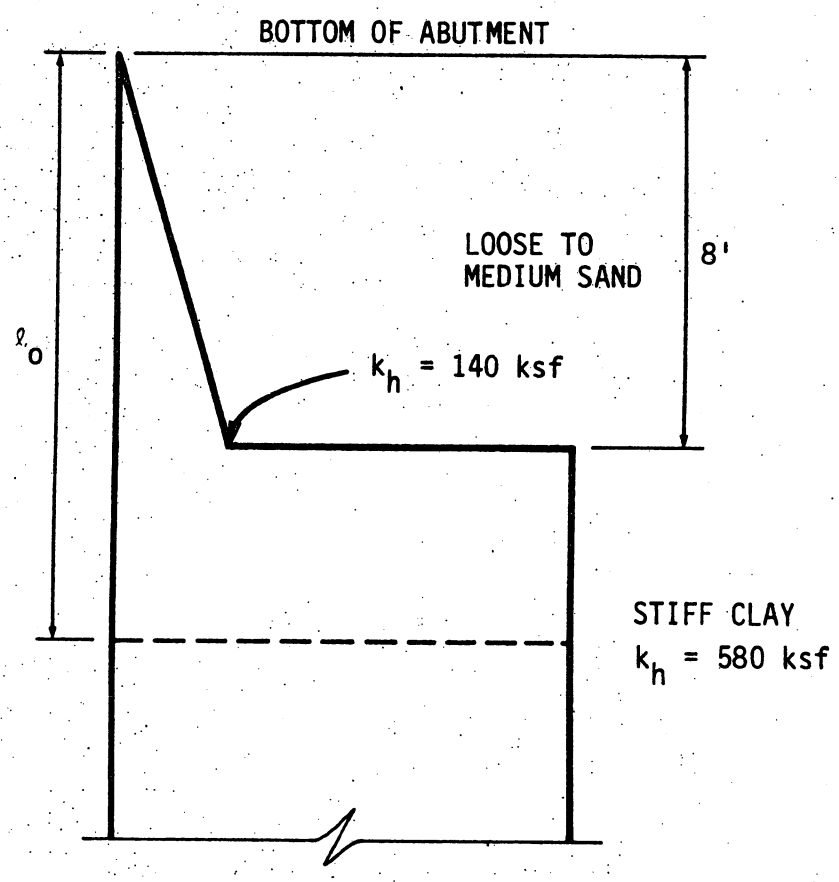

Figure 6.3. Variation of horizontal soil stiffness with depth.

(Appendix C), k_e is assumed to be equal to 40 ksf (Step 1). Now, establish the active length, ℓ_o, of the pile in bending from Eq. (12.40) (Step 2)

$$\ell_o = 2\sqrt[4]{\frac{(2.08)(10^6)\text{k-in.}^2}{40\ \text{ksf}(144\ \text{in.}^2/\text{ft}^2)}} = 8.72\ \text{ft} \qquad (6.3)$$

The integral I_k (Eq. (12.44)) is found using Fig. 12.3 (Step 3) as

$$I_k = 140\ \text{ksf}\left[\frac{(8\ \text{ft})^3}{36} + \frac{8\ \text{ft}}{2}\left(\frac{8\ \text{ft}}{3} + 0.72\ \text{ft}\right)^2\right]$$

$$+ 580\ \text{ksf}\ \frac{(0.72\ \text{ft})^3}{3} = 8486\ \text{kft} \qquad (6.4)$$

Establish a new k_e value (Step 4) as

$$k_e = \frac{3(8486\ \text{k-ft})}{(8.72\ \text{ft})^3} = 38.4\ \text{ksf} \qquad (6.5)$$

The next series of iterations converges to

$$k_e = 38.8\ \text{ksf} \qquad (6.6)$$

From Eqs. (5.5) and (5.6), the critical length parameter, ℓ_c, is

$$\ell_c = 4\sqrt[4]{\frac{(2.08)(10^6)\text{k-in.}^2}{(38.8\ \text{ksf})(144\ \text{in.}^2/\text{ft}^2)}} = 17.6\ \text{ft} \qquad (6.7)$$

(As discussed in Section 5.2.1, the critical length parameter, ℓ_c, is the length beyond which the pile can be considered flexible.)

- Determine the length of the equivalent cantilever:

  From Fig. 5.2, assuming the pile head is fixed against rotation and taking ℓ_u/ℓ_c equal zero,

$$\ell_e = \begin{cases} 0.5\ \ell_c = 0.5\ (17.6) = 8.8 \text{ ft (stiffness)} \\ 0.6\ \ell_c = 0.6\ (17.6) = 10.6 \text{ ft (moment)} \\ 1.1\ \ell_c = 1.1\ (17.6) = 19.4 \text{ ft (buckling)} \end{cases} \tag{6.8}$$

  Since ℓ_u equals zero, the total equivalent cantilever length, L, equals ℓ_e. A different effective length is required to calculate stiffness, moment, and buckling. Now, if the loose sand in the predrilled hole is completely neglected, the equivalent soil stiffness in the stiff clay is 580 ksf. The critical length, ℓ_c, is 8.9 ft. From Fig. 5.2, with ℓ_u/ℓ_c equal to 8 ft/8.9 ft or 0.9, one obtains an equivalent embedded length, ℓ_e, of 3.6 ft. The total equivalent cantilever length, L, would become 11.6 ft. In this case, the cantilever length, L, is about the same for stiffness, moment, and buckling. The equivalent cantilever for the pile in loose sand should not be reasonably longer than this. Hence, the following total equivalent lengths will be used:

$$L = \begin{cases} 8.8 \text{ ft or } 106 \text{ in. (stiffness)} \\ 10.6 \text{ ft or } 127 \text{ in. (moment)} \\ 11.6 \text{ ft or } 139 \text{ in. (buckling)} \end{cases} \tag{6.9}$$

Since soil parameters can seldom be established with certainty, a designer may reasonably choose to estimate upper and lower bounds of the parameters and check the pile design for both bounds.

- Perform structural analysis of bridge/pile/soil system for live and dead load:

  An idealized structural model is shown in Fig. 6.4a. Since the composite bending stiffness of the seven girders is at least 100 times the bending stiffness of the eight piles, the rotational restraint provided by the piles is negligible. Even though the bridge superstructure is continuous at the first pier, this continuity can be conservatively neglected when the girder rotation at the abutment is being considered. Therefore, the girder span can be assumed to be simply supported at both ends. For a uniformly distributed load, the total girder load, W, corresponding to the 50-kip pile load (D + L + I) is

$$W = \frac{8 \text{ pile } (50 \text{ kip})2}{7 \text{ girder}} = 114 \text{ kip} \qquad (6.10)$$

For this loading, the rotation, θ_W, at the left end is

$$\theta_W = \frac{WL^2}{24\ EI}$$

$$= \frac{(114 \text{ k})(60 \text{ ft})^2(12 \text{ in/ft})^2}{24(4290 \text{ ksi})(352{,}932 \text{ in.}^4)} = 0.00163 \text{ rad} \qquad (6.11)$$

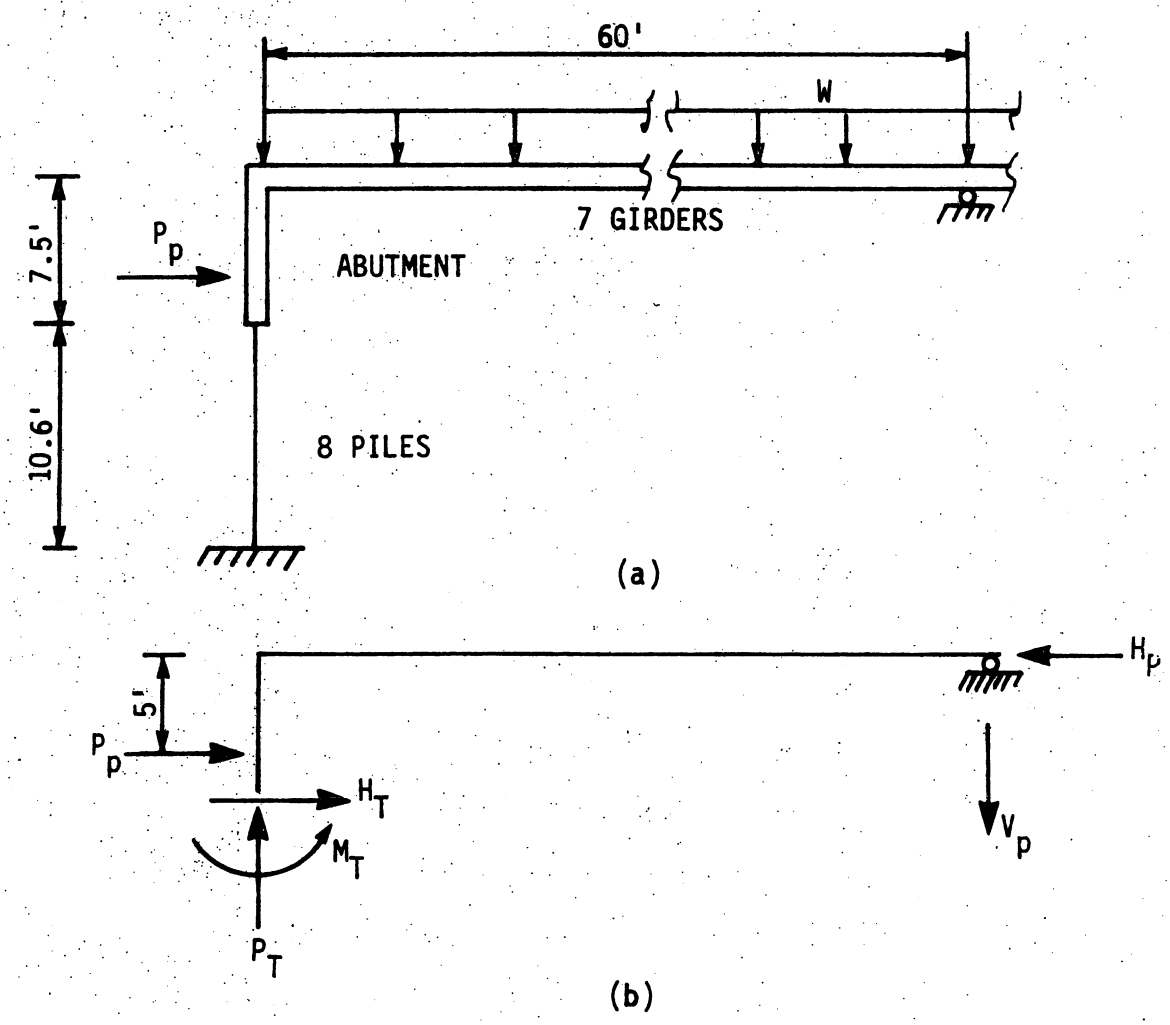

Figure 6.4. Idealized abutment foundation and girder endspan: (a) approximate structural model (b) free body diagram with passive soil pressure.

Since the top of the pile is rigidly connected to the integral abutment, the pile head will rotate by θ_W. Then, the induced moment, M_W, in the equivalent cantilever due to vertical load is

$$M_W = \frac{4\ EI}{L}\ \theta_W$$

$$= \frac{4(29000\ \text{ksi})(71.7\ \text{in.}^4)}{(10.6\ \text{ft})(12\ \text{in./ft})}\ (0.00163\ \text{rad.}) = 107\ \text{k-in} \tag{6.12}$$

The above analysis is approximate and can be improved in several ways. For example, it is possible that only a portion of the dead load and all of the live load not the entire total load will cause pile rotation. Also the assumption of a simple support at the right end need not be made in a more complete analysis involving girder continuity. However, this analysis will serve for this example.

- Perform a structural analysis for the thermal expansion:

  The horizontal displacement at each abutment is

$$\Delta = \frac{1}{2}\ \alpha\ \Delta T_{ave}\ L_b \tag{6.13}$$

where the bridge length, L_b, equals 360 ft. From Sec. 5.1., the coefficient of thermal expansion for a concrete superstructure is

$$\alpha = 0.000006\ /^{\circ}F \tag{6.14a}$$

Assuming that the bridge is constructed in the middle of the 80° F temperature range, one-half of the total anticipated change in temperature is

$$\Delta T = 40°F \tag{6.14b}$$

Substituting these terms into the expression (Eq. (6.13)) for the horizontal displacement at each abutment,

$$\Delta = \frac{1}{2}\,(0.000006\ /°F)\ (40°F)[(360\ ft)(12\ in./ft)]$$

$$= 0.52\ in. \tag{6.15}$$

(Note: Research funded by the Iowa Department of Transportation is currently underway at Iowa State University to measure the actual movement of two bridges: a prestressed concrete superstructure and a steel superstructure. Preliminary indications are that α may be as low as 0.000004 /°F. Predicted horizontal motions will be refined in that research.)

The moment, M_T, (Eq. (5.13)) induced by the lateral displacement of 0.52 in. at the top of the pile is

$$M_T = \frac{6(29000\ ksi)(71.7\ in.^4)(0.52\ in.)}{(127\ in.)^2} = 402\ k\text{-}in. \tag{6.16}$$

where the equivalent length for the moment (Eq. 6.9) has

been used. The corresponding horizontal force, H_T, (Eq. (12.7)) at the top of the pile is

$$H_T = \frac{12(29000 \text{ ksi})(71.7 \text{ in.}^4)(0.52 \text{ in.})}{(106 \text{ in.})^3} = 10.9 \text{ kip} \tag{6.17}$$

where the equivalent length for the horizontal stiffness (Eq. 6.9) has been used. The total moment and axial force in the seven bridge girders will be eight times the M_T and H_T values. (Note that M_T cannot exceed the plastic moment capacity of the pile nor can H_T exceed the value associated with a plastic mechanism.)

As verified by the laboratory scale model tests involving model Test Sequence F-3 (Section 4) and by computations with IAB2D, a horizontal force on the back side of the abutment occurs as the bridge expands. This force can be estimated conservatively as the passive resistance of the soil behind the abutment, P_p. Using an elementary soil model for a grandular material [37],

$$P_P = \frac{1}{2} \gamma H^2 \left(\frac{1 + \sin\phi}{1 - \sin\phi} \right) \tag{6.18}$$

where γ is the unit soil weight, H is the abutment height, and ϕ is the soil friction angle. For this example, the passive soil pressure along an abutment length equal to the pile spacing is

$$P_P = \frac{1}{2}\,(130\ \text{lb/ft}^3)(7.5\ \text{ft})^2(6.33\ \text{ft})\left(\frac{1 + \sin 35°}{1 - \sin 35°}\right)$$

$$= 85.4\ \text{kip} \tag{6.19}$$

where the pile spacing (Fig. 6.2) is 6.33 ft. Again, assuming that the bridge girder end span is simply supported, the axial force in the pile, P_T, is found by summing moments about the right end in the free body diagram of Fig. 6.4(b).

$$P_T = \frac{P_P(5.0\ \text{ft}) + H_T(7.5\ \text{ft}) + M_T}{60\ \text{ft}} \tag{6.20}$$

Substituting values for M_T, H_T, and P_P from Eq. 6.16, 6.17, and 6.19, respectively, the induced axial compression force in the pile is

$$P_T = 9.04\ \text{kip} \tag{6.21}$$

As with the previous analysis for the girder load, the analysis for thermal expansion is approximate; however, it serves the purposes of this example.

6.1.1. Case A Capacity

Determine the capacity of the pile as a structural member using Service Load Design as expressed by Eqs. (5.1) and (5.2).

- Determine the effective length factor, K, for buckling of the equivalent cantilever:

  Even though horizontal movement at the pile bend was cased by the expansion or contraction of the bridge superstructure further lateral displacement at the top of the piles is

prevented. Therefore, the top of the equivalent cantilever is considered braced against the sidesway. For Fig. 6.5, the nomograph designation for end conditions is expressed as

$$G = \frac{\Sigma\ (EI/L)_{columns}}{\Sigma\ (EI/L)_{girders}} \tag{6.22}$$

At the head of the equivalent cantilever, the composite flexural rigidity, EI, for the seven bridge girders and the flexural rigidity for the eight piles (Fig. 6.1) is applied in Eq. (6.22).

$$G = \frac{\left(\frac{2.08 \times 10^6\ \text{k-in.}^2}{127\ \text{in.}}\right)(8\ \text{piles})}{\left(\frac{1.51 \times 10^9\ \text{k-in.}^2}{720\ \text{in.}}\right)(7\ \text{girders})} = 0.009 \tag{6.23}$$

At the base of the equivalent cantilever, since it is theoretically fixed (by definition of the equivalent cantilever), G = 0. From reading the nomograph, the effective length factor is

$$K \cong 0.5 \tag{6.24}$$

Therefore, the assumption of a fixed-head pile used in determining ℓ_e and in the approximate structural analyses is valid. The value of K is increased to 0.65 for design (AASHTO, Table C-1).

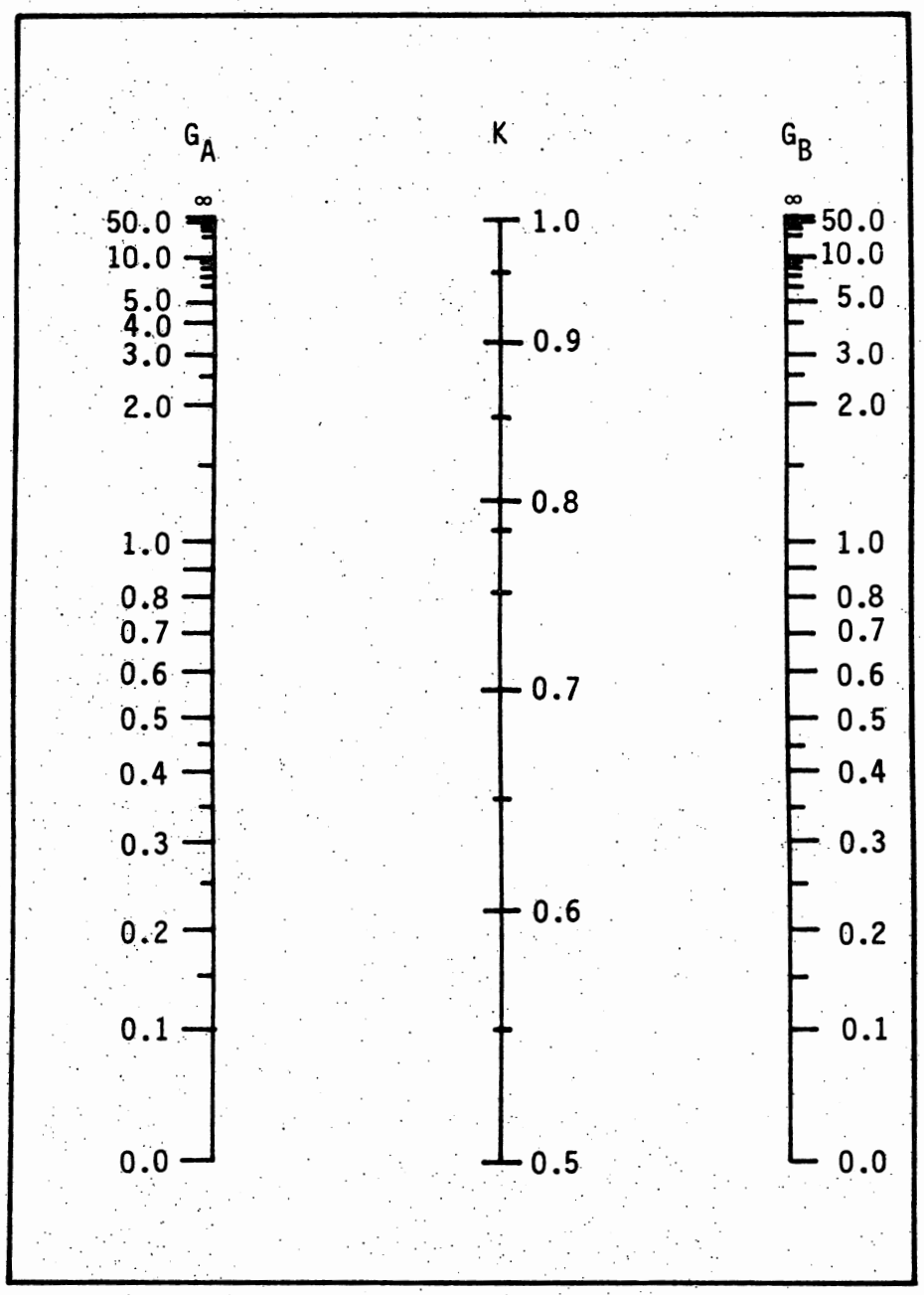

Figure 6.5. Alignment chart for effective length of columns in continuous frames, braced against sidesway [28].

- Determine allowable axial stress:

  The governing slenderness ratio is

$$\left(\frac{KL}{r_y}\right) = \frac{(0.65)(139\text{ in.})}{2.41\text{ in.}} = 37.5 \qquad (6.25)$$

  Now, following AASHTO Table 10.32.1A

$$C_c = 126.1 > 37.5$$

  Therefore, inelastic column buckling governs the allowable axial stress

$$F_a = \frac{36\text{ ksi}}{2.12}\left[1 - \frac{(37.5)^2(36\text{ ksi})}{4\pi^2(29000\text{ ksi})}\right] 1.25 = 20.3\text{ ksi} \qquad (6.26)$$

  Where, the 1.25 factor represents the allowable stress increase for AASHTO Group IV loading.

- Determine the elastic buckling stress (AASHTO Eq. (10-43)):

$$F_e' = \frac{\pi^2(29000\text{ ksi})(1.25)}{(37.5)^2(2.12)} = 120.0\text{ ksi} \qquad (6.27)$$

  Note that the elastic buckling stress was also increased for Group IV loading.

- Determine the allowable bending stress:

  Table 10.32.1A of the AASHTO Specification lists an allowable bending stress of 0.55 F_y. No mention is made specifically to weak axis bending. The AISC Allowable Stress Design (ASD) Specification Article 1.5.1.4.1 [33] recommends an allowable bending stress of 0.66 F_y for strong axis bending

of compact sections. For weak axis bending of compact sections, the AISC Specification Article 1.5.1.4.3 permits an increase in the allowable bending stress to 0.75 F_y because of the larger percentage of increase in the plastic moment capacity over the yield moment capacity for bending about this axis. AASHTO also does not explicitly address local buckling of the flange for weak axis bending, that is, flange compactness. According to the AISC Specification, the flange is considered to be compact for weak axis bending if the width-thickness ratio, $b_f/2t_f$, of the unstiffened flange element is equal to or less than $65/\sqrt{F_y}$. The dimensions b_f and t_f are the flange width and thickness, respectively. If $b_f/2t_f$ is greater than this limit but less than $95/\sqrt{F_y}$, the flange is considered to be partially compact and the AISC Eq. (1.5-5b) applies. The AISC Load and Resistance Factor Design (LRFD) Specification and Commentary, Section B.5 [38], uses the term noncompact rather than partially compact. Decreasing the AISC allowable bending stresses in AISC Article 1.5.1.4.3 by the ratio of 0.55 to 0.66 produces the following allowable bending stress for weak axis bending

$$F_b = 0.625\ F_y \tag{6.28}$$

when

$$\frac{b_f}{2t_f} \leq \frac{65}{\sqrt{F_y}}$$

and

$$F_b = F_y \left[0.896 - 0.0042 \left(\frac{b_f}{2t_f} \right) \sqrt{F_y} \right] \tag{6.29}$$

when

$$\frac{65}{\sqrt{F_y}} \leq \frac{b_f}{2t_f} \leq \frac{95}{\sqrt{F_y}}$$

For an HP10 × 42 pile, the width-thickness ratio for the flange is

$$\frac{b_f}{2t_f} = \frac{10.025 \text{ in.}}{2(0.42 \text{ in.})} = 12.0 \tag{6.30}$$

For A36 steel (F_y = 36 ksi), the limitations on the width-thickness ratios become

$$\frac{65}{\sqrt{F_y}} = \frac{65}{\sqrt{36}} = 10.83 \tag{6.31}$$

and

$$\frac{95}{\sqrt{F_y}} = \frac{95}{\sqrt{36}} = 15.8 \tag{6.32}$$

Therefore, the HP10 × 42 shape is not compact with respect to the flange. Applying Eq. (6.29) and including the

allowable stress increase permitted for AASHTO Group IV loading, the allowable bending stress becomes

$$F_b = 36 \text{ ksi}[0.896 - 0.0042(12.0)\sqrt{36}](1.25) = 26.7 \text{ ksi} \tag{6.33}$$

Note that lateral bracing is not required since bending occurs about the weak axis (AISC Commentary Article 1.5.1.4).

- Determine the applied axial stress:

The sum of the axial force due to the vertical load of 50 kip and the thermal expansion (Eq. 6.21) is

$$P = 50 \text{ kip} + 9.04 \text{ kip} = 59.0 \text{ kip} \tag{6.34}$$

The corresponding axial stress is

$$f_a = \frac{59.0 \text{ kips}}{12.4 \text{ in.}^2} = 4.76 \text{ ksi} \tag{6.35}$$

6.1.1.1. Alternative One

- Determine the applied bending stress:

The moment at the top of the pile for Alternative One is the sum of the moment due to vertical load (Eq. 6.12) and thermal expansion (Eq. 6.16)

$$M = 107 \text{ k-in} + 402 \text{ k-in} = 509 \text{ k-in} \tag{6.36}$$

The resulting extreme fiber flexural stress is

$$f_b = \frac{509 \text{ k-in.}}{14.2 \text{ in.}^3} = 35.8 \text{ ksi} \tag{6.37}$$

which is just below the minimum specified yield stress of the steel.

- Check the stability equation

  For the equivalent fixed-ended beam-column, the moment gradient factor, C_m, equals 0.40 (See C_m definition with Eq. 5.1). Since the real pile is subjected to transverse loads (soil pressures), one could argue conservatively that a C_m value of 0.85 may be more appropriate (AISC Commentary Article Sec. 1.6.1). Substituting the appropriate terms into Eq. (5.1),

$$\frac{4.76 \text{ ksi}}{20.3 \text{ ksi}} + \frac{0.85(35.8 \text{ ksi})}{\left(1 - \frac{4.76 \text{ ksi}}{120.0 \text{ ksi}}\right)(26.7 \text{ ksi})} = 1.42 > 1 \tag{6.38}$$

  Therefore, the stability criteria is not satisfied. The intent of the moment amplification term $(C_m/(1 - f_a/F_e'))$ is not to permit the primary bending stress, f_b, to exceed the allowable bending stress, F_b (AISC Commentary Article 1.6.1).

- Check the yield equation:

  Substituting the appropriate stresses into Eq. (5.2) and increasing the allowable axial stress by 25% for AASHTO Group IV loading,

$$\frac{4.76 \text{ ksi}}{0.472(36 \text{ ksi})(1.25)} + \frac{35.8 \text{ ksi}}{26.7 \text{ ksi}} = 1.56 > 1 \qquad (6.39)$$

  As expected, strength is not adequate, since f_b is greater than F_b. Therefore, an HP10 × 42 pile cannot be used in this bridge with an integral abutment according to Alternative One. However, if the bridge were shorter or if deeper pre-bored holes were used, Alternative One might provide an acceptable design.

6.1.1.2. Alternative Two

- Find the applied bending stress:

  For Alternative Two, the moment due to thermal expansion is equal to $P\Delta/2$ (Eq. (5.19)). Consistent with the arguments made for Alternative Two, that is, redistribution of forces through inelastic rotation, the stresses introduced into the pile by both the horizontal motion and by the rotation of the girder under vertical load are neglected. Therefore, the extreme fiber bending stress becomes

$$f_b = \frac{59 \text{ kips}(0.52 \text{ in.})}{2(14.2 \text{ in.}^3)} = 1.08 \text{ ksi} \qquad (6.40)$$

- Check the stability equation, Eq. (5.1):

$$\frac{4.76\ \text{ksi}}{20.3\ \text{ksi}} + \frac{0.85(1.08\ \text{ksi})}{\left(1 - \frac{4.76\ \text{ksi}}{120.0\ \text{ksi}}\right)(26.7\ \text{ksi})} = 0.27 < 1 \tag{6.41}$$

Stability is adequate.

- Check the yield equation, Eq. (5.2):

$$\frac{4.76\ \text{ksi}}{0.472(36\ \text{ksi})(1.25)} + \frac{1.08\ \text{ksi}}{26.7\ \text{ksi}} = 0.26 < 1 \tag{6.42}$$

Strength is adequate.

- Determine plastic hinge rotation demand:

Alternative Two requires sufficient plastic hinge rotation capacity of the pile. The inelastic rotation demand, θ_{iD}, that will be required of the pile as its head is displaced laterally must be less than the inelastic rotation capacity of the section, θ_{iC}. Figure 6.6 will be used to calculate the inelastic rotation demand. The idealized equivalent cantilever, involving a perfectly elastic-plastic material, behaves elastically until the end moments reach the plastic moment capacity, M_p. A mechanism is formed (Fig. 6.6b) and the moments remain constant as an unrestrained rotation, θ_i, occurs at each plastic hinge location. Substituting the values from Fig. 6.6b into the basic slope-deflection equation [32] gives

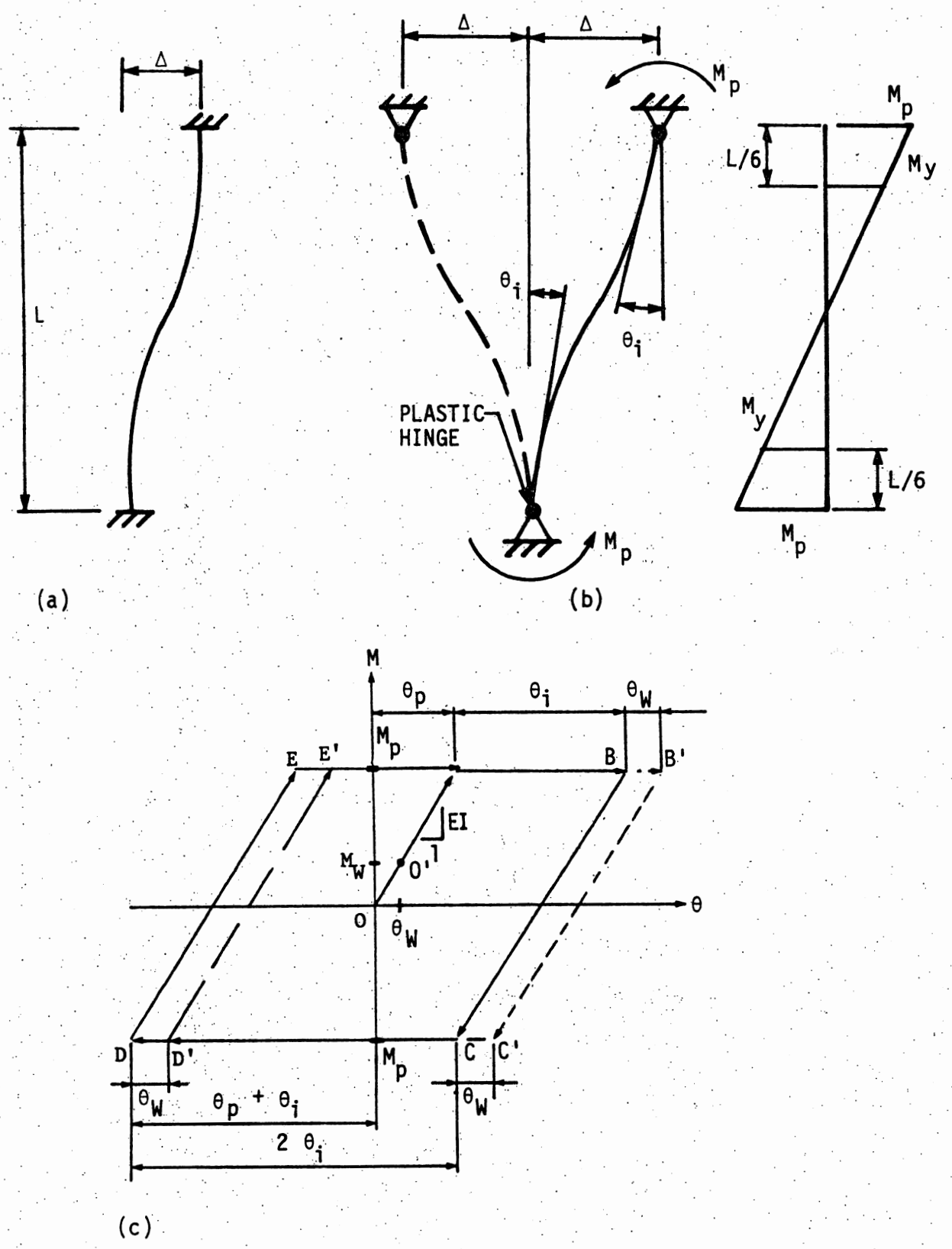

Figure 6.6. Inelastic rotation of equivalent cantilever: (a) elastic (b) inelastic (c) idealized moment-rotation relationship.

$$M_p = \frac{2EI}{L}(-2\theta_i - \theta_i + 3\Delta/L) \tag{6.43}$$

where Δ is the lateral displcement at the pile head. Solving for the inelastic rotation during the first portion of the displacement cycle,

$$\theta_i = \frac{\Delta}{L} - \frac{M_p L}{6EI} \tag{6.44}$$

The relationship between the moment and rotation is shown in Fig. 6.6(c). The limit of elastic behavior is indicated as Point A where the elastic rotation within the length of the plastic hinge is θ_p. For an idealized moment-curvature relationship,

$$\theta_p = \frac{M_p}{EI}\ell p \tag{6.45}$$

where ℓ_p is the length of the plastic hinge, which is approximately equal to the length within which the moment is greater than the yield moment. For weak axis bending of an HP-shape, M_p is about 1.5 times the yield moment. Since the moment diagram in Fig. 6.5b is linear, the plastic hinge length is equal to L/6. Substituting this length into Eq. (6.45),

$$\theta_p = \frac{M_p}{EI}\left(\frac{L}{6}\right) \tag{6.46}$$

The inelastic rotation from Eq. (6.44) is represented by Point B. As the bridge cycles into another season of the year, the temperature change is a -40° F (Eq. (6.14b)). During this period, the pile moves to the left of its original position by a displacement Δ (Fig. 6.6(b)). The pile first unloads elastically from Point B to C in Fig. 6.6(c) and, then, inelastically to Point D. During continued seasonal temperature changes, the pile will follow the path D to E to B to C and back to D again. The rotation from C to D and from E to B represent the total ineastic rotation demand of the plastic hinge. For this example,

$$\theta_{iD} = 2\theta_i \tag{6.47}$$

Substituting Eq. (6.44) into Eq. (6.47),

$$\theta_{iD} = 2\left(\frac{\Delta}{L} - \frac{M_p L}{6EI}\right) \tag{6.48}$$

If Δ was not the same in both directions, in other words, the displacement to the left, Δ_L, is not the same as the displacement to the right, Δ_R, the inelastic rotation demand for the thermal movements would be

$$\theta_{iD} = \frac{\Delta_L}{L} + \frac{\Delta_R}{L} - \frac{M_p L}{3EI} \tag{6.49}$$

Note that the end rotation of the girder due to vertical load induces an additional rotation θ_W (Eq. (6.11)) at the pile head, represented by Point O' in Fig. 6.6(c). The rotation θ_W will add to the rotation demand during the first portion of the displacement cycle. Therefore, Point B will move to the right (to point B') by the amount θ_W. During the first thermal loading, the rotation demand will be equal to θ_W plus θ_i. Also, Points C and D will move an equal amount to the right (to Points C' and D', respectively). Therefore, the total rotation capacity will still be equal to 2 θ_i, unless θ_W is greater than θ_i, in which case

$$\theta_{iD} = \theta_i + \theta_W \tag{6.50}$$

In summary, the rotation demand will be given by the larger of Eq. (6.49) and Eq. (6.50). If Δ_L and Δ_R are equal, Eq. (6.48) replaces Eq. (6.49).

- Determine plastic hinge rotation capacity:

  According to the commentary in the AISC LRFD Specification and Commentary Section B.5 [38], compact sections with a $b_f/2t_f$ ratio equal to $65/\sqrt{F_y}$ have a inelastic rotation capacity of three, that is, θ_{iC} equal to $3\theta_p$. Noncompact sections with a $b_f/2t_f$ ratio equal to $95/\sqrt{F_y}$ have no inelastic rotation capacity. (Note that the limit $95/\sqrt{F_y}$ is given in AISC LRFD Table B5.1 for pure compression loading. Larger limits are given for pure flexure.)

Between the two limits of $65/\sqrt{F_y}$ and $95/\sqrt{F_y}$, the inelastic rotation capacity, θ_{iC}, can be assumed to vary linearly, following the same reasoning used for Eq. (6.29), that is

$$\theta_{iC} = 3\theta_p C_i \tag{6.51}$$

in which an inelastic rotation capacity reduction factor, C_i, is expressed as

$$C_i = \frac{19}{6} - \frac{b_f/2t_f}{30/\sqrt{F_y}} \tag{6.52}$$

When $b_f/2t_f$ equals $65/\sqrt{F_y}$, C_i equals unity; and when $b_f/2t_f$ equals $95/\sqrt{F_y}$, C_i equals zero.

Combining Eq. (6.46) and (6.51), the inelastic rotation capacity can be expressed as

$$\theta_{iC} = \frac{M_p L}{2EI} \; C_i \tag{6.53}$$

- Check plastic hinge rotation:

  Sufficient plastic hinge rotation capacity will be present if

$$\theta_{iC} \geq \theta_{iD} \tag{6.54}$$

In the case that θ_W is less than θ_i, Eq. (6.48) applies for θ_{iD}. With Eq. (6.53) the rotation capacity criterion can be written as

$$\Delta \leq \frac{M_p L^2}{6EI}\left(1 + \frac{3}{2} C_i\right) = \Delta_p \left(1 + \frac{3}{2} C_i\right) \tag{6.55}$$

where Δ_p is the lateral displacement at the pile head that corresponds to the formation of a plastic mechanism. Since Service Load Design is being utilized in this example, the service level conditions will be used for the displacement demand Δ and, hence, the rotational capacities must be reduced by the factor of safety. As a Service Load Design criteria, Eq. 6.55 can be rewritten as

$$\Delta \leq \Delta_i \tag{6.56}$$

in which Δ_i is the allowable total lateral displacement consistent with the inelastic rotation capacity of the pile. Dividing Δ_p of Eq. 6.55 by the AASHTO bending factor of safety, Δ_i can be expressed as

$$\Delta_i = \Delta_b \left(1 + \frac{3}{2} C_i\right) \tag{6.57}$$

in which Δ_b is the displacement corresponding to the allowable service load moment, $F_b S_y$. For a fixed-head pile, the lateral displacement Δ_b is

$$\Delta_b = \frac{(F_b S_y) L^2}{6EI} \tag{6.58}$$

Note that a pinned-head pile behaves similar to the lower half of the fixed-head pile; therefore, the corresponding displacement would be

$$\Delta_b = \frac{(F_b S_y)L^2}{3EI} \tag{6.59}$$

For the HP10 × 42 equivalent cantilever in this example, the inelastic rotation capacity reduction factor given by Eq. (6.52) equals

$$C_i = \frac{19}{6} - \frac{12.0}{30/\sqrt{36}} = 0.77 \tag{6.60}$$

The lateral displacement corresponding to the allowable bending stress (Eq. (6.58)) is

$$\Delta_b = \frac{26.7 \text{ ksi}(14.2 \text{ in.})^3(127 \text{ in.})^2}{6(2.08 \times 10^6 \text{k-in.}^2)} = 0.49 \text{ in.} \tag{6.61}$$

Substituting the values for C_i and Δ_b into Eq. (6.57),

$$\Delta_i = 0.49 \left[1 + \frac{3}{2}(0.77)\right] = 1.06 \text{ in.} \tag{6.62}$$

Since the lateral displacement demand Δ due to thermal expansion is only 0.52 in., the HP10 × 42 pile has more than sufficient ductility for this example. (As discussed in Sec. 3.3.4, the HP10 × 42 test pile had sufficient ductility for the combined load field test.)

Therefore, the HP10 × 42 pile satisfies all of the criteria for Alternative Two, Case A. This example demonstrates the proposed design method for piles in an integral abutment bridge. The conservatism of Alternate One, Case A, is illustrated, since the beam-column behavior

is not satisfied by a HP10 × 42 pile. Alternative Two, Case A, which takes stress redistribution into account, is satisfied by an HP10 × 42 pile because sufficient ductility is present.

6.1.2. Case B Capacity

The effect of the horizontal displacement on the capacity of the pile to transfer the load to the ground is now checked to verify the preliminary design.

- Determine length to deduct for frictional contribution:

  As mentioned in Section 5.3, the maximum lateral displacement, y_{max}, below which the frictional capacity is unaffected is approximately 0.2 in. for the HP10 × 42 pile; therefore,

$$\frac{y_{max}}{\Delta} = \frac{0.2 \text{ in.}}{0.52 \text{ in.}} = 0.38 \tag{6.63}$$

  From Fig. 5.13 with ℓ_u/ℓ_c equal to zero, the length of frictional resistance to deduct is about

$$\ell_n = 0.45\ \ell_c \tag{6.64}$$

  or

$$\ell_n = 0.45(17.6 \text{ ft}) = 7.92 \text{ ft} \tag{6.65}$$

  Since 8 ft of frictional contribution has already been neglected because of the predrilled hole, an additional deduction is not necessary. The allowable vertical capacity of the pile for Load Group IV is

$$P = [(0.8 \text{ tons/ft})(8 \text{ ft}) + (1.2 \text{ tons/ft})(16 \text{ ft})]1.25$$
$$= 32 \text{ tons} \qquad (6.66)$$

which is greater than the applied load of 59 kips (Eq. (6.34).

Therefore, the preliminary design is adequate for Case B. Note that Case B is not controlled by the thermal movement of the abutment, Load Group IV, but is controlled by Load Group I, as assumed in the preliminary design.

6.1.3. Case C Capacity

The horizontal displacement does not affect the capacity of the ground to support the load. Since the spacing of the piles (6 ft-4 in. center-to-center) is greater than three times the pile dimension (Section 5.4), Case C capacity is adequate.

6.1.4. Summary of Friction Pile Design Example

For this example, Case B involving AASHTO Group I loading controls the entire pile design, that is, the integral abutment lateral displacement caused by a thermal expansion and contraction of 0.52 in. for the 360-ft bridge did not detract from the strength of the pile. In fact, the lateral displacement of the pile could be as large as 1.06 in. (Eq. (6.62)) before the integral abutment design would detract from the pile allowable load, indicating that the bridge could be about twice as long.

6.2. End-Bearing Pile

The example will now be reexamined assuming that the pile is bearing on rock 15 ft below the existing ground line in Fig. 6.1. Therefore,

the pile is embedded only 11 ft below the bottom of the pre-drilled hole that is filled with loose sand.

- Perform preliminary design:

  For the preliminary design, assume that Case B and AASHTO Load Group I governs. The allowable tip bearing stress is 9000 psi as stated in AASHTO 4.3.4.3.1 and the Iowa D.O.T. Foundation Information Chart, revised June 1976. The applied axial stress is

$$f_a = \frac{50 \text{ kips} + 9.04 \text{ kips}}{12.4 \text{ in.}^2} = 4.76 \text{ ksi} \tag{6.67}$$

  which is less than the allowable bearing stress. The HP10 × 42 pile appears satisfactory for this application.

- Determine the equivalent uniform stiffness, k_e, of the soil:

  The calculations for k_e are identical to those shown for the friction pile example in Section 6.1; therefore, k_e is equal to 38.8 ksf and the critical length, ℓ_c, is equal to 17.6 ft. As stated in Sections 5 and 12, the developed pile behavior in this study relates to piles that are flexible, that is, their length must be longer than the critical length, ℓ_c, given by Eq. (5.5). For this example, the pile embedment length equals 19 ft. The upper 8 ft of this length is in the loose sand of the predrilled hole and the lower 11 ft of the pile was driven through existing soil. Therefore, the pile is considered flexible and the equations

herein apply. The equivalent cantilever lengths, ℓ_e, will be the same for both the end bearing and friction pile examples.

6.2.1. Case A Capacity

All of the calculations presented for Case A for the friction pile example, Section 6.1.1, apply here for this bearing pile example, because the equivalent cantilever is identical. Therefore, for Alternative One, the pile will be overstressed and not acceptable. However, the pile will be acceptable under Alternative Two, since it has sufficient ductility.

6.2.2. Case B Capacity

As described in Section 5.3, end-bearing allowable stresses for Case B are not affected by lateral motion. Therefore, the preliminary design controls, that is, Load Group I, Case B.

6.2.3. Case C Capacity

The Case C capacity is not affected by lateral motion. (The bedrock should be checked for group action of all eight piles that bear on it.)

6.2.4. Summary of Bearing Pile Design Example

As with the friction pile, the pile design is controlled by Load Group I and Case B. The lateral displacement of the integral abutment caused by thermal movements did not reduce the pile strength in this example.

7. SUMMARY, CONCLUSIONS, DESIGN RECOMMENDATIONS, AND RECOMMENDATIONS FOR FURTHER WORK

7.1. Summary

7.1.1. Overview

Integral abutment bridges have been constructed in many states, including Iowa and the District of Columbia. The length limitations and design considerations for these types of bridges vary considerably between the representative agencies responsible for bridge design. Thermal expansion and contraction of the bridge superstructure induces stresses in the abutment piles. By understanding the behavior of these structures, proper design approaches can be formulated.

The objective of this research project was to develop a simplified and rational design method for the abutment piles in integral abutment bridges. To accomplish this task, experimental and analytical studies were conducted to determine the pile and soil responses when vertical, lateral, or combined loads were applied to the top of a pile. The experimental investigations involved both full-scale, field tests and 1/10-scale model, laboratory tests. Analytical investigations of the experimental tests were accomplished with a two-dimensional finite element model, IAB2D, which was developed in a previous research project [1].

7.1.2. Field Tests

The full-scale field test program (Sections 3 and 10) consisted of three tests on HP10 × 42 steel piles. The first test, involving only vertical compressive loads, was conducted to determine the soil behavior due to vertical pile loads and to establish the ultimate vertical capacity

of an isolated friction pile. Pile strains at discrete points along the pile length, applied vertical load, and vertical displacement were recorded. For each magnitude of applied load, axial pile strains were analyzed to determine the variation of soil skin-friction forces, f, and the corresponding relative pile displacement, z. Modified Ramberg-Osgood expressions fit through these data points provide continuous f-z relationships for use in the analytical model, IAB2D.

The soil response at the pile tip could not be determined due to the sensitivity and availability of the pile strain data at the last strain gage station. To represent the pile tip behavior, the strain gage station 5.5 ft above the end of the pile was considered as a modified pile tip location. The skin friction resistance along the bottom 5.5 ft of pile length and the actual end-bearing resistance were combined to form a modified end-bearing soil response. The axial force in the pile at 5.5 ft from the bottom was defined as the modified pile tip resistance, q', and the modified pile tip displacement, z', was obtained from an integration of the axial pile strains. These q'-z' data point pairs established the pile tip soil response that was mathematically represented by a modified Ramberg-Osgood expression.

The second field test involved a lateral displacement test of another test pile. This test defined the lateral load and displacement behavior of the soil and pile. The measured pile strains were analyzed using the conventional beam theory to determine the lateral soil pressures, p, and corresponding lateral soil displacement, y, at the strain gage depths along the pile length. To obtain a continuous p-y relationship, a

modified Ramberg-Osgood expression was curve fit to the p-y data point pairs.

The third field test, involving a combined load test on the test pile used in the vertical load test, was conducted to determine the effects of lateral displacement of the pile on vertical load capacity. The soil responses (p-y curves), induced by the lateral displacement at the pile head during the first portion of the combined load test, were established by the techniques developed for the second field test. The f-z and q'-z' curves established for this pile in the first test were also used in the third test.

7.1.3. Model Tests

The 1/10-scale model test program (Sections 4 and 11) was conducted to investigate experimentally and analytically the pile and soil behavior for a variety of geometric, loading, and soil density conditions. The model piles were steel tubes 1-in. square by 60-in. long with electrical resistance strain gages mounted along their length. A total of 40 scale-model laboratory tests were conducted to establish the test apparatus design, testing procedures, soil and pile responses, and geometric conditions. From these 40 tests, a test matrix was established that included 11 test sequences involving two pinned-head friction piles, eight fixed-head friction piles, and one fixed-head bearing pile. Other test matrix parameters were considered: dense and loose sand, a pre-drilled hole, and an abutment. Four loading conditions at the pile head were considered. The vertical load tests and the vertical load phase of the combined load tests established the soil f-z and q-z relationships; while the lateral load tests and the lateral load phase

of the combined load tests established the soil p-y relationships. A cyclic lateral load with a subsequent vertical load was applied to a model pile to evaluate response for cyclic loading.

The techniques used to obtain the soil behavior parameters for the modified Ramberg-Osgood expressions were essentially the same as for the full-scale field tests.

7.1.4. Finite Element Model, IAB2D

The experimental test results for the 11 1/10-scale model tests, included in the test matrix, and the three full-scale field tests were investigated further by performing an analytical study with a previously developed [1] two-dimensional, nonlinear, finite element model, IAB2D. The analytical model (Sections 2, 3, and 4) represented the lateral and vertical soil resistance by nonlinear Winkler-type springs described by the modified Ramberg-Osgood expressions. The computer solutions provided a method to verify the pile design recommendations.

7.1.5. Pile Design Requirements

The design requirements (Section 5) for the piles in integral abutment bridges are based on the provisions of the AASHTO Specification, which requires that the capacity of the pile be controlled by the minimum of (1) the capacity of the pile as a structural member (Case A), (2) the capacity of the pile to transfer load to ground (Case B), and (3) the capacity of the ground to support the load (Case C). For Case A, the beam-column interaction equations for Service Load Design or Load Factor Design are used, Eqs. (5.1) and (5.2) or (5.3) and (5.4), respectively. To simplify the complex beam-column behavior for the pile, the concept of an equivalent cantilever idealization (Section 12) was presented.

The differential equations for the elastic buckling of four equivalent cantilevers (beam-columns) with different boundary conditions were solved, and the solution compared to those of the finite element model, IAB2D (Section 13).

Two alternatives were presented for determining the capacity of the pile as a structural member (Case A). Alternative One accounts for the stresses produced by the horizontal displacement of the abutment and the stresses induced by the vertical load. Alternative Two neglects stresses produced by the horizontal displacement but considers stresses caused by the vertical load on the displaced pile. Alternative Two relies on the plastic redistribution of forces; therefore, the pile cross section must be ductile and capable of plastic hinge rotation. To make a comparison between the beam-column interaction equations and the finite element solution, the load factors, local element buckling, and lateral torsional buckling considerations were removed from the Load Factor Design equations. The pile capacities obtained from these revised interaction equations for both Alternates One and Two were compared with the pile capacities predicted by IAB2D.

The capacity of the pile to transfer load to the ground (Case B) is subdivided into point-bearing and friction piles. Point-bearing piles are limited to 9000 psi over the cross-sectional area of the pile tip and are unaffected by the horizontal displacement. For friction piles, the ability of the load to be transferred to the soil near the ground surface can be affected by the horizontal movement. This interaction of vertical load resistance and lateral displacement is accounted for in the design procedure by a reduced frictional length.

The capacity of the ground to support the load (Case C) was assumed to be unaffected by the horizontal displacement.

To illustrate the pile design requirements, two design examples were presented (Section 6). For both the friction and end-bearing pile examples, the designs are illustrated for Alternates One and Two. In each example, the design for Alternate One resulted in the pile being significantly overstressed; while for Alternate Two, the pile was understressed and had sufficient inelastic rotation capacity. Therefore, the pile was unacceptable according to Alternate One and acceptable according to Alternate Two.

7.2. Conclusions

7.2.1. Field Tests

The measured ultimate vertical load capacity was 280 kips for both the vertical load and the vertical load phase of the combined load field tests of the same test pile. The lateral displacement of approximately two inches did not appear to affect the vertical resistance of the test pile.

The soil behavior determined from the lateral load test involving strong-axis pile bending was not the same as the soil behavior determined from the lateral load phase of the combined load test involving weak-axis pile bending. For strong-axis bending, the entire flange width develops the passive soil resistance; but, for weak-axis bending, primarily the flange tips bear against the soil. The soil between the flanges of the test pile had been disturbed during the pile driving, such that the web did not develop significant bearing.

7.2.2. Model Tests

The accuracy of the measured pile strains did not permit an accurate evaluation of the axial strains in regions of large bending strains, such as in the upper portion of the piles with lateral load. A small error in the measured total strain caused a small error in the computed bending strain, but unfortunately, a large error in the computed axial strain.

The end-bearing capacity of the model friction piles was sometimes as large as 50% of the total vertical load capacity. In addition, the vertical frictional resistance of the lower portion of the test piles was significantly larger than the upper portion. Therefore, although the lateral displacements of the combined load tests caused a reduction in the friction resistance along the upper portion, the total vertical load capacity of the pile was not significantly affected.

Soil placement for the model pile tests involved an elaborate technique that significantly reduced the amount of variability in sand structure between the various experimental tests. However, a comparison of results for presumably identical tests revealed that the same soil structure could not be repeated with enough consistency to reproduce identical pile responses.

7.2.3. Comparisons Between Experimental and IAB2D Results

A comparison of the experimental and analytical tests results, involving pile strains, axial force and bending moment along the length of the test pile, and load versus displacement relationships at the soil surface for each of the three full-scale field tests and 11 1/10-scale laboratory tests, showed that IAB2D correctly predicted pile

behavior. The accuracy of the analytical results were considered acceptable, considering normal test scatter, sensitivity of measured pile strain data including data sensoring techniques, and sensitivity of mathematically formulated soil response behavior.

During the analytical investigations of both the field and laboratory tests, the pile response predicted by IAB2D was sensitive to the parameters selected to represent the vertical and lateral resistance and displacement relationships for the soil. Therefore, an accurate evaluation of the soil parameters was required to predict pile response adequately.

7.2.4. Comparisons Between Design Alternatives for Case A and IAB2D

When horizontal displacement of the pile head was prevented, Alternatives One and Two design approaches for Case A gave identical results which closely matched the IAB2D results. When the pile head was displaced horizontally, both design alternatives gave conservative results relative to the finite element model. Alternative One results were much more conservative than Alternative Two when a pile had a high elastic buckling load relative to its yield load. Both alternatives and the finite element model predicted a decrease in Case A axial load capacity with an increase in horizontal displacement. The IAB2D analyses demonstrated that plastic redistribution occurred if the pile had sufficient ductility, which is recognized only by the Alternative Two criteria.

The approximate ampliciation factor in the beam-column stability equation overestimates the secondary bending moments (PΔ effects). This conservatism was verified by the finite element model and the differential equation solution that gave essentially the same results. These solutions

have shown that the elastic buckling load is not affected by the horizontal displacement of the pile head.

7.3. Design Recommendations

The use of a predrilled hole is recommended as a pile construction detail to reduce the pile stresses significantly when horizontal displacements of the pile occur.

When the design of an abutment pile in an integral abutment bridge is governed by the capacity of the pile as a structural member (Case A), two alternative design approaches have been proposed. Alternative One is recommended for piles that have a limited amount of ductility, such as timber, concrete, and steel sections having insufficient moment-rotation capacity. Alternative Two is recommended when the piles have a moment-rotation capacity that exceeds the moment-rotation demand at the plastic hinge locations. Steel piles do not have to be classified as compact sections to meet moment-rotation requirement. Alternative Two will permit the safe design of integral abutment bridges that are several times longer than those designed using Alternative One.

7.4. Recommendations for Further Work

Additional research into the behavior of integral abutment bridges could include the following topics:

1. Effects of the horizontal displacement on the approach slab and backfill and the passive soil resistance behind the abutment.

2. Effects of lateral displacement on the friction capacity of the pile, that is, y_{max} (Section 5.3).
3. Ductility capacity of timber and concrete piles.
4. Forces in the bridge superstructure.
5. Design details at the junction of the girders, piles, abutment, and approach slab.

8. LIST OF REFERENCES

8.1. Cited References

1. Greimann, L. F., Yang, P.-S., Edmunds, S. K., and Wolde-Tinsae, A. M. "Design of Piles for Integral Abutment Bridges." Final Report, DOT Project HR-252, ISU-ERI-Ames 84286, August 1984.
2. Wasserman, E. P., "Jointless Bridge Decks," Engineering Journal, Vol. 24, No. 3, American Institute of Steel Construction, 1987, pp. 98.
3. Greimann, L. F., Wolde-Tinsae, A. M., and Yang, P.-S. "Skewed Bridges with Integral Abutments." Transportation Research Record 903. Transportation Research Board, National Academy of Science, Washington, D.C., 1983.
4. Wolde-Tinsae, A. M., Greimann, L. F., and Johnson, B. V. "Performance of Integral Bridge Abutments." Journal of the International Association for Bridge and Structural Engineering, IABSE Proceedings P-58/83 (February 1983) 17-34.
5. Fleming, W. G., Weltman, A. J., Randolp, M. F., and Elson, W. K. Piling Engineering. New York: Halsted Press, 1985.
6. Poulos, H. G., and Davis, E. H. Pile Foundation Analysis and Design. New York: John Wiley and Sons, Inc., 1980.
7. Desai, C. S., and Wu, T. H. "A General Function for Stress-Strain Curves." Proc. 2nd Int. Conf. on Numerical Methods in Geomechanics, 1 (1976), 306-318.

8. Duncan, J. M., and Chang, C.-Y. "Nonlinear Analysis of Stress and Strain in Soils." Proc. Paper 7513. Journal of Soil Mechanics and Foundation Engineering Division, ASCE, 96, No. SM5 (September 1970), 1629-1653.

9. Finn, W. D., Lee, K. W., and Martin, G. R. "An Effective Stress Model for Liquefaction." Proc. Paper 13008. Journal of the Geotechnical Engineering Division, ASCE, 103, No. GT6 (June 1977) 517-533.

10. Martin, P. P. "Nonlinear Methods for Dynamic Analysis of Ground Response." Ph.D. Thesis, University of California at Berkeley, 1975.

11. Streeter, V. L., Wylie, E. B., and Richard, F. E., Jr. "Soil Motions Computations by Characteristic Methods." Proc. Paper 10410 Journal of the Geotechnical Engineering Division, ASCE, 100, No. GT3 (March 1974), 247-263.

12. Pyke, R. "Nonlinear Soil Models for Irregular Cyclic Loadings." Proc. Paper 14642. Journal of the Geotechnical Engineering Division, ASCE, 105, No. GT6 (June 1977), 715-726.

13. Matlock, H., and Reese, L. C. "Generalized Solutions for Laterally Loaded Piles." Journals of the Soil Mechanics and Foundation Division, ASCE, 86, No. SM5 (October 1960), 63-91.

14. Davisson, M. T. "Lateral Load Capacity of Piles." Transportation Research Record 333, 1970.

15. Ha, N. B., and O'Neill, M. W. "Field Study of Pile Group Action (Appendix A)." Final Report. Federal Highway Administration, Washington, D.C., 1981.

16. Highway Structures Design Handbook. Vol. 1. Pittsburgh, Pennsylvania: United States Steel Corp., 1965.

17. Wolde-Tinsae, A. M., Greimann, L. F., and Yang, P.-S. "Nonlinear Pile Behavior in Integral Abutment Bridges." Final Report. DOT Project HR-227, ISU-ERI-Ames 82123, February 1982.

18. Stevens, J. B., Holloway, M. D., Yoshiharu, M., and Demsky, E. C. "Pile Group Response to Axial and Lateral Loading." In Symposium on Deep Foundations, Ed. by F. Fuller. New York: ASCE, 1979, 396-419.

19. Alizadeh, M. "Lateral Load Tests on Instrumented Timber Piles." Performance of Deep Foundations. ASTM STP444. Philadelphia, Pa.: American Society for Testing and Materials, 1969.

20. Chajes, A. Principals of Structural Stability Theory. Englewood Cliffs, N.J.: Prentice-Hall, Inc., 1974.

21. Commentary on Plastic Design in Steel. ASCE Manual of Engineering Practice, No. 41, ASCE, 1961.

22. American Association of State Highway and Transportation Officials. "Standard Specifications for Highway Bridges." 13th Edition. Washington, D.C.: American Association of State Highway and Transportation Officials, 1983.

23. ASTM. "Standard Method of Testing Piles Under Static Axial Compressive Load." American Society for Testing and Materials, ASTM, Vol. 04.08, Designation D 1143-81, Philadelphia, Pa., pp. 237-252.

24. ASTM. "Standard Method of Testing Piles Under Lateral Loads." American Society for Testing and Materials, ASTM, Vol. 04.08, Designation D 3966-81, Philadelphia, Pa., pp. 649-668.

25. Standard Specifications for Highway and Bridge Construction, Iowa Department of Transportation, Series of 1984, pp. 483-484.

26. Peck, R. B., Hanson, W. E., and Thornburn, T. H. Foundation Engineering, John Wiley and Sons, Inc., New York, N.Y. 1974.

27. Ko, H-Y., Atkinson, R. H., Goble, G. G., and Monzoori, M. "Centrifugal Testing of Model Piles and Pile Groups V.I, II, III." (1984), Report to FHWA, No. 84/004, Tumer Fairbank Highway Research Center, 6300 Georgetown Pike, McLean, Va. 22101.

28. Salmon, C. G., and Johnson, J. E. Steel Structures: Design and Behavior. 2nd Edition. New York: Harper and Row Publishers, Inc., 1980.

29. Granholm, H. "On the Elastic Stability of Piles Surrounded by a Suporting Medium." Centraltryckeriet, Stockholm, Sweden, 1929.

30. Davisson, M. T., and Robinson, K. E. "Bending and Buckling of Partially Embedded Piles." Proc. 6th Int. Conf. on Soil Mechanics and Foundation Engineering, 2 (1965), 243-246.

31. Horn, M. R. Plastic Theory of Structures. Cambridge, Mass. M.I.T. Press, 1971.

32. Neal, B. G. The Plastic Methods of Structural Analysis. 2nd Edition. New York: John Wiley & Sons, Inc., 1963.

33. Manual of Steel Construction. 8th ed., Chicago: American Institute of Steel Construction, Inc., 1980.

34. American Iron and Steel Institute. Plastic Design of Braced Multistory Steel Frames. New York: Committee of Structural Steel Producers and Committee of Steel Plate Producers, 1968.

35. Greimann, L. F., Fanous, F., and Bluhm, D. "Sequoyah Equipment Hatch Seal Leakage." U.S. Nuclear Regulatory Commission, NUREG/CR-3952, July 1985.

36. Prakash, S. "Behavior of Pile Groups Subjected to Lateral Loads." Ph.D. Thesis, University of Illinois, Urbana, Ill., 1962.

37. Spangler, M. G., Soil Engineering, 2nd Ed., International Textbook Company, 1960, pg. 335.

38. Manual of Steel Construction: Load and Resistance Factor Design. 1st ed., Chicago: American Institute of Steel Construction, Inc., 1986.

39. ASTM. "Standard Method for Penetration Test and Split-Barrel Sampling of Soils." American Society for Testing and Materials, ASTM, Vol. 04.08, Designation D 1586-84, Philadelphia, Pa., pp. 296-301.

40. ASTM. "Standard Practice for Thin-Walled Tube Sampling of Soils." American Society for Testing and Materials, ASTM, Vol. 04.08, Designation D 1587-83, Philadelphia, Pa., pp. 302-305.

41. Peck, R. B., Davisson, M. T., and Hansen, Y. Discussion of "Soil Modulus for Laterally Loaded Piles," by Bramlette McClelland and John A. Focht, Jr.. (1958), Transactions of the American Society of Civil Engineers, Vol. 123, pp. 1049-1086.

42. Rocha, M. "The Possibility of Solving Soil Mechanics Problems by the Use of Models." (1957), Proc. 4th Inter. Conf. on Soil Mechanics and Foundation Engineering, V. 1, pp. 183-188.

43. Ovensen, N. K. "The Use of Physical Models in Design." (1980), Design Parameters in Geotechnical Engineering, BGS London, England, V. 4.

44. Saglamer, A., and Parry, R. H. G. "Model Study of Laterally Loaded Single Piles." (1979), Proc. 7th European Conference on Soil Mechanics and Foundation Engineering, V. 2, pp. 115-120.

45. Reese, L. C., and Welch, R. C. "Lateral Loading of Deep Foundations in Stiff Clay." (1975), ASCE Journal of Geotechnical Engineering, Vol. 101, pp. 633-649.

46. Alizadem, M., and Davisson, M. T. "Lateral Load Tests on Piles--Arkansas River Project." ASCE Journal of Soil Mechanics and Foundation Engineering Division, V. 96 (1970).

47. McClelland, B., and Focht, J. A. "Soil Modulus for Laterally Loaded Piles." (1956), ASCE Journal of Soil Mechanics and Foundation Engineering Division, V. 82.

48. Hoadley, P. J., Francis, A. J., and Steven, L. K. "Load Testing of Slender Steel Piles in Soft Clays." (1969), Proc. 7th Inter. Conf. on Soil Mechanics and Foundation Engineering, Mexico, p. 123-130.

49. Reddy, A. S., and Valsangkar, A. J. "Buckling of Fully and Partially Embedded Piles." Journal of the Soil Mechanics and Foundation Division, ASCE, 96, No. SM6 (November 1970), 1951-1965.

50. Chen, Wai-Feh, and Zhou, Suiping. "C_m Factor in Load and Resistance Factor Design," Journal of Structural Engineering, ASCE, Vol. 113, No. 8, August 1987, pp. 1738-1754.

8.2. References Not Cited

Akoz, Y., Ontuna, K. A., and Saglamer, A. "A New Approach to the Analysis of Laterally Loaded Piles." (1981), Proc. 10th Inter. Conf. on Soil Mechanics and Foundation Engineering, V. 2, pp. 587-592.

Avgmerinos, P. J., and Schofield, A. N. "Drawdown Failures of Centrifuged Models." Proc. 7th Inter. Conf. on Soil Mechanics and Foundation Engineering, V. 2, 1969, pp. 497-505.

Banerjee, P. K., and Davies, T. G. "The Behavior of Axially and Laterally Loaded Single Piles Embedded in Nonhomogeneous Soils." (1978), Geotechnique, V. 28, N. 3, pp. 309-326.

Chan, S. F. "Load Transfer Characteristics of an Instrumented Steel Pile in a Fill Ground." (1977), Proc. 5th Southeast Asian Confer. on Soil Engineering, pp. 153-163.

Chari, T. R., and Meyerhoff, G. G. "Ultimate Capacity of Rigid Single Piles Under Inclined Loads in Sand." (1983), Canadian Geotechnical Journal, V. 20, pp. 849-854.

Cooke, R. W., Price, G., and Tarr, K. "Jacked Piles in London Clay: A Study of Load Transfer and Settlement Under Working Conditions." (1979) Geotechnique V. 29, No. 2, pp. 113-147.

Davisson, M. T., and Salley, J. R. "Model Study of Laterally Loaded Piles." ASCE Journal of Soil Mechanics and Foundation Division, V. 96, pp. 1605-1627, 9/70.

Dickin, E. A., and Leung, C. F. "Centrifugal Model Tests on Vertical Anchor Plates." (1983), ASCE Journal of Geotechnical Engineering, V. 109, pp. 1503-1525. Discussion (1984): ASCE Journal of Geotechnical Engineering, V. 110, pp. 1693-1696.

Fumagalli, I. E. Statical and Geomechanical Models. (1973), Springer-Verlag/Wien, New York, N.Y.

Georgiadis, M., and Butterfield, R. "Laterally Loaded Pile Behavior." ASCE Journal of Geotechnical Engineering, V. 108, pp. 155-165 (1982).

Greimann, L. F., Wolde-Tinsae, A. M., and Yang, P.-S.. "Skewed Bridges with Integral Abuments." pp. 64-72. Bridges and Culverts. Transportation Research Board 903. Washington, D.C., 1983.

Hoadley, P. J., Barton, Y. D., and Parry, R. H. G. "Cyclic Lateral Load on Model Pile in a Centrifuge." (1981), Proc. 10th Inter. Conf. on Soil Mechanics and Foundation Engineering, V. 1, pp. 621-625.

Jorgenson, J. L. "Behavior of Abutment Piles in an Integral Abutment Bridge." Report, North Dakota State Highway Department, ND(1)-75(B), November 1981.

Jorgenson, J. L. "Behavior of Abutment Piles in an Integral Abutment in Response to Bridge Movement." pp. 72-79. Bridges and Culverts. Transportation Research Board 903. Washington, D.C., 1983.

Lee, H. W., and Sarsam, M. B. "Analysis of Integral Abutment Bridges." Report, South Dakota Department of Transportation M614(70), March 1973.

Lee, K. L. "Buckling of Partially Embedded Piles in Sand." (1968), Journal of Soil Mechanics and Foundation Engineering Division, V. 94, pp. 255-270.

Levacner, D. R., and Sieffert, J. G. "Tests on Model Tension Piles." (1984), ASCE Journal of Geotechnical Engineering, V. 110, pp. 1735-1748.

Long, J. H., and Reese, L. C. "An Investigation of the Behavior of Vertical Piles in Cohesive Soil Subjected to Repetitive Lateral Loads." (1983), Report to Waterways Experiment Station, Department of the Army, Vicksburg, Miss. GR83-7.

Mansur, C. I., and Hunter, A. H. "Pile Tests--Arkansas River Project." ASCE Journal of Soil Mechanics and Foundation Engineerng Division, V. 96, pp. 1545-1581, September 1970.

Matlock, H. "Cyclic Lateral Load Capacity of Piles in Sand." Technology Assessment and Research Program for Offshore Minerals Operations, 1984 Report. Dept. of the Interior Minerals Management Service. OCS Report MMS84-0001, pp. 287-294.

Meyerhoff, G. G., Yalcin, A. S., and Mather, S. K. "Ultimate Pile Capacity for Eccentric Inclined Load." (1983), ASCE Journal of Geotechnical Engineering, V. 109, pp. 408-423.

Moulton, L. K. "Observations of Highway Bridge Movements and Their Effects on Joints and Bearings." pp. 87-95. Bridges and Culverts. Transportation Research Board 903. Washington, D.C., 1983.

O'Neill, M. W., Hawkins, R. A., and Mahar, L. J. Field Study of Pile Group Action, Final Report, No. FHWA/RD-81/002, March 1981.

O'Neill, M. W. "Side Load Transfer in Driven and Drilled Piles." (1983) ASCE Journal of Geotechnical Engineering, Vol. 109, pp. 1259-1266.

Price, G., and Wardle, I. F. "The Deformation of Vertical Piles in London Clay Under Static and Cyclic Horizontal Working Loads." (1980) Recent Developments in the Design and Construction of Piles, pp. 87-94.

Ranuan, G., Ramasamy, G., and Rao, B. G. "Model Study on Time Dependent Deflections of Laterally Loaded Piles in Saturated Clays." (1977), Proc. 5th Southeast Conf. on Soil Engineering, pp. 141-152.

Reese, L. C., Touma, F. T., and O'Neill, M. W. "Behavior of Drilled Piers Under Axial Loading." (1976), ASCE Journal of Geotechnical Engineering, V. 102, pp. 493-509.

Robinson, K. E. "Horizontal Subgrade Reaction Estimated from Lateral Loading Tests on Timber Piles." (1979), Behavior of Deep Foundations, ASTM STP 670, Raymond Lundgren, Ed., pp. 520-536.

Roscoe, K. H. "Soils and Model Tests." Journal of Strain Analysis, V. 3, N. 1, pp. 57-64, 1968.

Schofield, A. N. "General Principals of Centrifuge Model Testing and a Review of Some Testing Facilities." "The Role of Centrifuge Modeling." Offshore Soil Mechanics, pp. 328-350 (1976).

Seed, H. B., and Reese, L. C. "The Action of Soft Clay Along Friction Piles." (1955), Transactions of the American Society of Civil Engineers, ASCE, No. 2882, pp. 731-765.

Steenfelt, J. S., Randolph, M. F., and Wroth, C. P. "Instrumented Model Piles Jacked into Clay." (1981), Proc. 10th Inter. Conf. on Soil Mechanics and Foundation Engineering, V. 2, pp. 857-864.

Timoshenko, S. P., and Gere, J. M. Theory of Elastic Stability. 2nd Edition. New York: McGraw-Hill Book Company, 1961.

9. ACKNOWLEDGMENTS

The study presented in this report was conducted by the Engineering Research Institute of Iowa State University and was sponsored by the Iowa Department of Transportation, Highway Division, through the Iowa Highway Research Board.

The authors wish to extend sincere appreciation to William Lindquist and Henry Gee from the Iowa Department of Transportation for their support of the integral abutment project. Henry Gee, John Harkin, Iowa Department of Transportation, and Darrel Girton, Associate Professor of Civil Engineering at Iowa State University, provided constructive criticism of the design recommendations in Chapter 6. Also, the writers would like to express their appreciation to Dr. Robert A. Lohnes, Professor of Civil Engineering at Iowa State University, for his assistance in the geotechnical investigations and Mr. Kenneth E. Jensen, Construction Technician II at the Ames Construction Division of the Iowa DOT, for his efforts in supervising and recording data for the pile driving operation.

Mr. Xiaohuan Lu, a graduate student in Structural Engineering, reduced the experimental data from the field and model tests and ran IAB2D. In some ways, he deserves to be listed as an author, although he was not with the project from the beginning. Thanks go to Mr. Doug Wood, Structural Laboratory Supervisor, for his help. Undergraduate students Judy Dambowy, Gregory Stonehouse, Randy Tweden, and Scott Werner contributed significantly to the laboratory labor involved with this project.

10. APPENDIX A: FULL-SCALE PILE TESTS AND DATA REDUCTION

10.1. Development

10.1.1. Site Description

The original proposed test site was an actual integral abutment bridge construction site. The specific location in Iowa would have been determined from construction scheduling at various bridge sites. The field tests were relocated to a site adjacent to the Structural Engineering Laboratory located in the Town Engineering Building of Iowa State University to eliminate coordination, accessibility, and flexibility problems associated with a remote bridge construction site.

The selected site was essentially level and free of surface obstructions. A subsurface soil investigation was performed by drilling two 50-ft-deep bore holes with a track-mounted Central Mine Equipment CME-45 drill rig using 4.5-in.-diameter continuous flight augers. Stabilization drilling techniques were not required. Split-spoon soil samples, designated as "D" on the boring logs (Tables 10.1 and 10.2), were taken according to ASTM D1586-67 [39], using a 2.0-in.-O.D. split-spoon sampler. The Shelby tube samples, designated as "U" on the boring logs, were taken according to ASTM D1587-74 [40], using a 3.0-in.-O.D. thin-walled sampler. The split-spoon samples were placed in glass jars, while the Shelby tube samples were extruded into plastic lined cardboard tubes. All samples were then placed in a moist room until the laboratory tests were conducted.

The blow count shown on the boring logs represents the sum of the hammer blow counts needed to drive the split-spoon sampler from a

Table 10.1 Boring No.1

DRILL HOLE NO.	JOB NO.	DATE	ELEVATION	DATUM	DRILLER	INSPECTOR
1	309CA13	4-17-86	964.0	By ISU	R. Freeman	D. Miller

WATER LEVEL OBSERVATIONS				TYPE OF SURFACE	DRILL RIG
WHILE DRILLING	END OF DRILLING	24 HOURS AFTER DRILLING	____ HOURS	Grassy Lawn	CME-45
17½'+/-				DRILLING METHOD: 4¼" Continuous Flight Augers	TOTAL DEPTH: 50.0'

SAMPLE DATA				SAMPLE DESCRIPTION					LABORATORY DATA				
DEPTH, ft	SAMPLE NO. & TYPE	N VALUE BLOWS/ft	RECOVERY, %	COLOR	MOISTURE	CONSISTENCY	BASIC SOIL TYPE	GEOLOGIC DESCRIPTION & OTHER REMARKS	WATER CONTENT, %	DRY DENSITY, pcf	q_u, tsf	CLASSIFICATION SYMBOL	DEPTH, ft
				Black	Moist	Soft	Sandy Clayey Silt	DEVELOPED ZONE OR POSSIBLE TOPSOIL TILL					
5	D-1	7	90	Grayish-Brown w/ Red & Gray Mottles	Moist	Medium Stiff	Sandy, Silty Clay, Trace Small Gravel	WEATHERED GLACIAL TILL (WISCONSIN AGE) Note: Possible undetected sand seams & boulders.					5
	U-1		100	Gray, Brown & Red/Rust Mottled		Stiff							
10	U-2		80		Very Moist	Hard							10
	D-2	34	80										
15	D-3	30	90	Dark Gray	Very Moist	Hard	Sandy Silty Clay, Trace Gravel	UNWEATHERED GLACIAL TILL (WISCONSIN AGE) Note: Possible undetected sand seams & boulders					15
	U-3		50										
	U-4		70		Wet								
20	U-5		95										20
	D-4	26	100										
25						Very Stiff							25
	D-5	22	100										
30													30
	D-6	66	95	Dark Blueish-Gray	Wet	Hard	Silt w/ Trace Clay	UNWEATHERED GLACIAL DEPOSIT (WISONSIN AGE)					
35													35
	D-7	36	100	Dark Blueish-Gray	Wet	Hard	Silt w/ Trace Clay	UNWEATHERED GLACIAL DEPOSIT (WISCONSIN AGE)					
40						Very Stiff							40
	D-8	22	100					Note: Possible undetected sand semas & boulders.					
	U-6		70										
	U-7		40					Note: Few pebbles @ 45.5'.					
45	D-9	27	40										45
						Hard		Note: Trace of small wood fragments from 37.0' to bottom of hole.					
50	D-10	28	90										50
				Bottom of Hole @ 50.0'									

Table 10.2 Boring No. 2

DRILL HOLE NO.	JOB NO.	DATE	ELEVATION	DATUM	DRILLER	INSPECTOR
2	309CA13	4-17-86	964.7+/-	By ISU	R. Freeman	D. Miller

WATER LEVEL OBSERVATIONS				TYPE OF SURFACE	DRILL RIG
WHILE DRILLING	END OF DRILLING	24 HOURS AFTER DRILLING	____ HOURS	Grassy Lawn	CME-45
24.0'+/-				DRILLING METHOD: 4½" Continuous Flight Augers	TOTAL DEPTH: 50.0'

DEPTH ft.	SAMPLE DATA: SAMPLE NO. & TYPE	SAMPLE DATA: N VALUE BLOWS/ft	SAMPLE DATA: RECOVERY, %	SAMPLE DESCRIPTION: COLOR	MOISTURE	CONSISTENCY	BASIC SOIL TYPE	GEOLOGIC DESCRIPTION & OTHER REMARKS	LABORATORY DATA: WATER CONTENT, %	DRY DENSITY, pcf	OIL, ppf	CLASSIFICATION SYMBOL	DEPTH ft.
				Black	Moist	Soft	Sandy Clayey Silt	DEVELOPED ZONE OR POSSIBLE TOPSOIL FILL					
5	U-1		80	Grayish-Brown w/ Red & Gray Mottles	Moist	Medium Stiff	Sandy, Silty Clay, Trace Gravel	WEATHERED GLACIAL TILL (WISONSIN AGE)					5
	D-1	10	80										
	U-2		70	Gray, Brown, and Red Mottled		Stiff		Note: Possible undetected sand seams & boulders					
10	D-2	18	90			Very Stiff							10
	U-3		80										
	U-4		66										
15	D-3	25	70										15
					Very Moist	Hard							
20	D-4	28	80	Dark Gray	Very Moist	Very Stiff	Sandy Silty Clay, Trace Gravel	UNWEATHERED GLACIAL TILL (WISCONSIN AGE)					20
	U-5		0										
	U-6		95					Note: Possible undetected sand seams & boulders					
25	D-5	23	90		Wet								25
	U-7		100										
	D-6	23	90										
30													30
	D-7	42	90	Dark Gray w/ Slight Blue Cast	Wet	Hard	Silt w/ Trace Clay	UNWEATHERED GLACIAL DEPOSIT (WISCONSIN AGE)					
35													35
				Dark Gray w/ Slight Blue Cast	Wet	Stiff	Silt w/ Trace Clay	UNWEATHERED GLACIAL DEPOSIT (WISCONSIN AGE) Note: Trace of small wood & vegetation fragments from 40' to 50'. with greater amount @ 43½-45' Note: Few thin seams sandy silty clay between 34' & 42'					
40	U-8		100										40
	D-8	33	100			Hard							
45	D-9	26	100			Very Stiff		Note: Possible undetected sand seams & boulders.					45
								Note: Trace sand below 45'.					
50	D-10	21	100										50
						Bottom of Hole @ 50.0'							

penetration of 6 in. to 18 in. at the specified depth in the bore hole. Table 10.3 summarizes the results of the standard penetration tests.

The borings revealed that the site contained three major soil strata below the topsoil fill that was approximately 2-ft thick. These strata consisted of weathered and unweathered glacial till with consistencies for the silt and clay soil ranging from stiff to hard. The water level was around 18 ft and 24 ft during drilling for Boring Nos. 1 and 2, respectively. Approximately 24 hours after drilling, the water table had risen to about 8 ft in both bore holes.

Unconsolidated, unconfined, triaxial shear tests for each of the major soil strata were conducted on the Shelby tube samples to obtain unconfined compressive strengths. Atterberg limits, bulk densities, and soil moistures were also measured. The results of these tests are given in Table 10.4.

10.1.2. Testing Frame and Load Systems

The overall dimensions of the test framework, shown in Figs. 10.1-10.5, were established to comply with the minimum pile spacing requirements provided in the ASTM standards [23,24]. For an axial compression test of a vertical pile, the clear distance between the test pile and an anchor pile should not be less than either 5 pile diameters or 7 ft. For a lateral load test of vertically driven piles, the clear distance in the direction of the applied movement between the test and reaction piles should not be less than either 20 pile diameters or 20 ft. These same clearances apply between the piles and the foundations for the beams that support the instrumentation.

Table 10.3. Blow counts.

Boring No.	Sample No.	Depth (ft)	Actual Blow Count	N-Value as Reported on Boring Logs
1	D-1	5.0- 6.5	2- 3- 4	7
1	D-2	9.5-11.0	9-15-19	34
1	D-3	15.0-16.5	8-14-16	30
1	D-4	21.0-22.5	8-10-16	26
1	D-5	26.0-27.5	4- 8-14	22
1	D-6	31.5-33.0	14-28-38	66
1	D-7	36.0-37.5	10-17-19	36
1	D-8	40.0-41.5	7- 8-14	22
1	D-9	44.5-46.0	9-11-16	27
1	D-10	48.5-50.0	9-12-16	28
2	D-1	5.0- 6.5	3- 4- 6	10
2	D-2	8.5-10.0	4- 8-10	18
2	D-3	15.0-16.5	9-11-14	25
2	D-4	20.0-21.5	8-12-16	28
2	D-5	24.5-26.0	6- 9-14	23
2	D-6	27.5-29.0	6-10-13	23
2	D-7	32.5-34.0	15-19-23	42
2	D-8	40.0-41.5	11-16-17	33
2	D-9	43.5-45.0	10-11-15	26
2	D-10	48.5-50.0	8- 9-12	21

Table 10.4. Laboratory test results of soil.

Shelby Tube Sample	q_u (ksf)	c_u (ksf)	γ_d (lb/cf)	Split-Spoon Sample	W%	LL	PL	PI
U1	1.38	0.69	119.0					
				D1	15.6	21.7	14.7	7.0
				D2	14.0	27.9	16.9	11.0
U3	7.74	3.87	120.6					
U4	7.16	3.58	125.0					
				D3	12.6	23.9	16.1	7.8
				D4	16.2			
U6	8.1	4.05	132.6					
				D5	13.8	24.2	5.2	9.0
				D6	19.0	31.0	21.1	9.9
				D7	24.9			
U8	8.36	4.18	111.8					
				D8	25.3	34.4	24.8	9.6
				D9	22.7			
				D10	23.9			

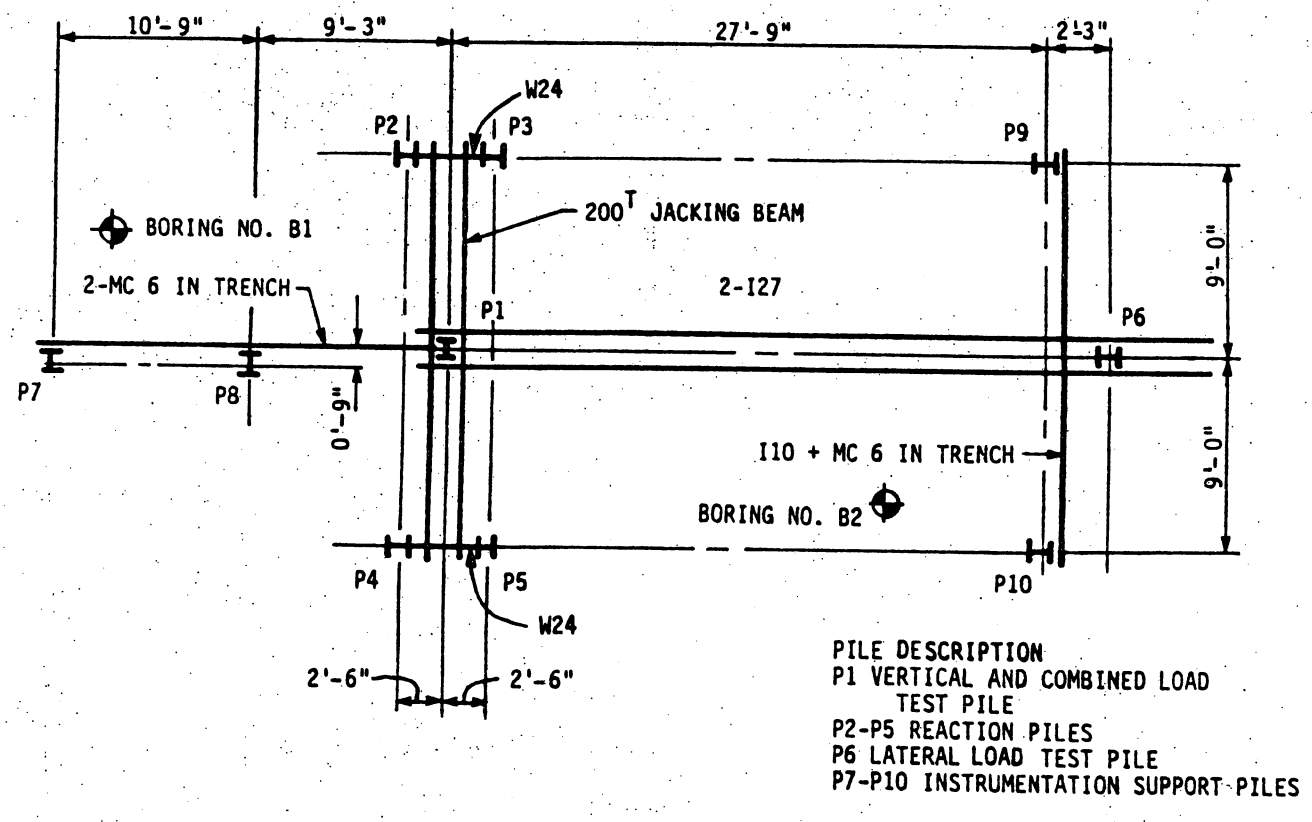

Figure 10.1. Test framework plan.

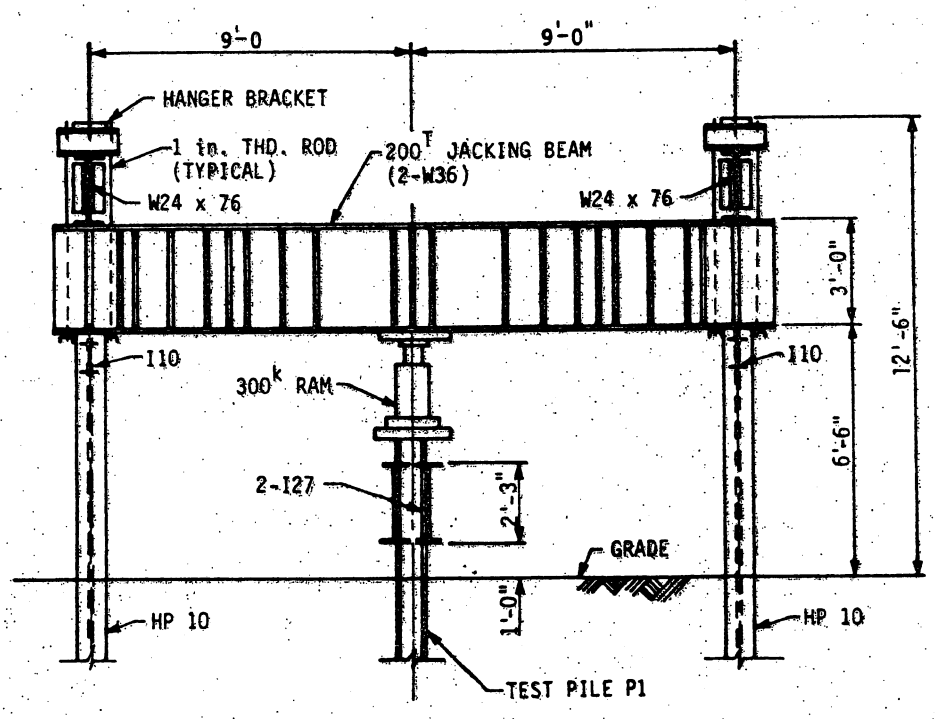

Figure 10.2. Elevation of test frame and jacking beam for vertical load test.

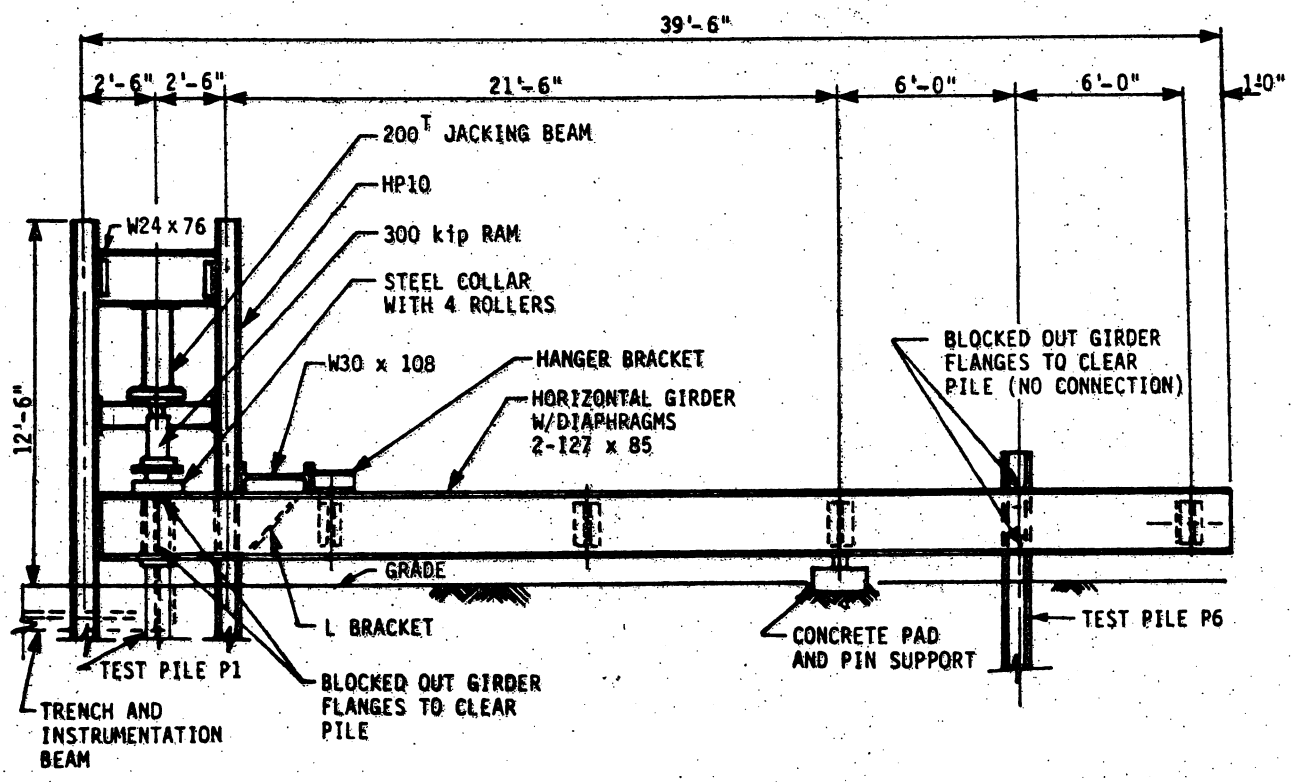

Figure 10.3. Elevation of test frame and horizontal girder for vertical load test.

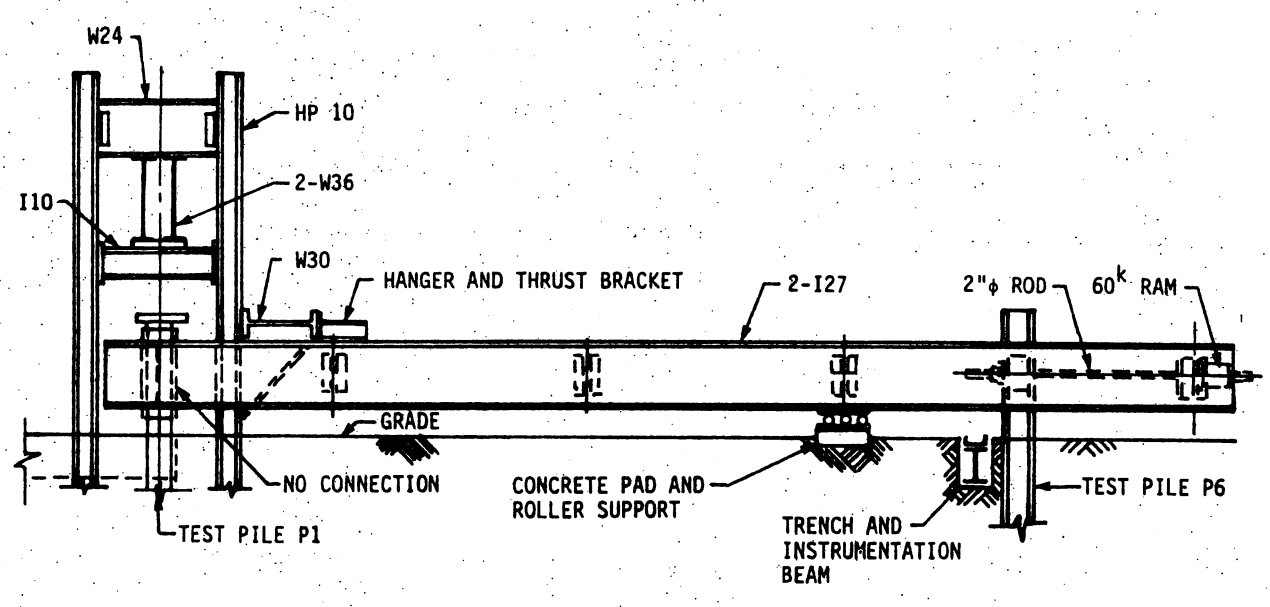

Figure 10.4. Elevation of test framework and horizontal girder for lateral load test.

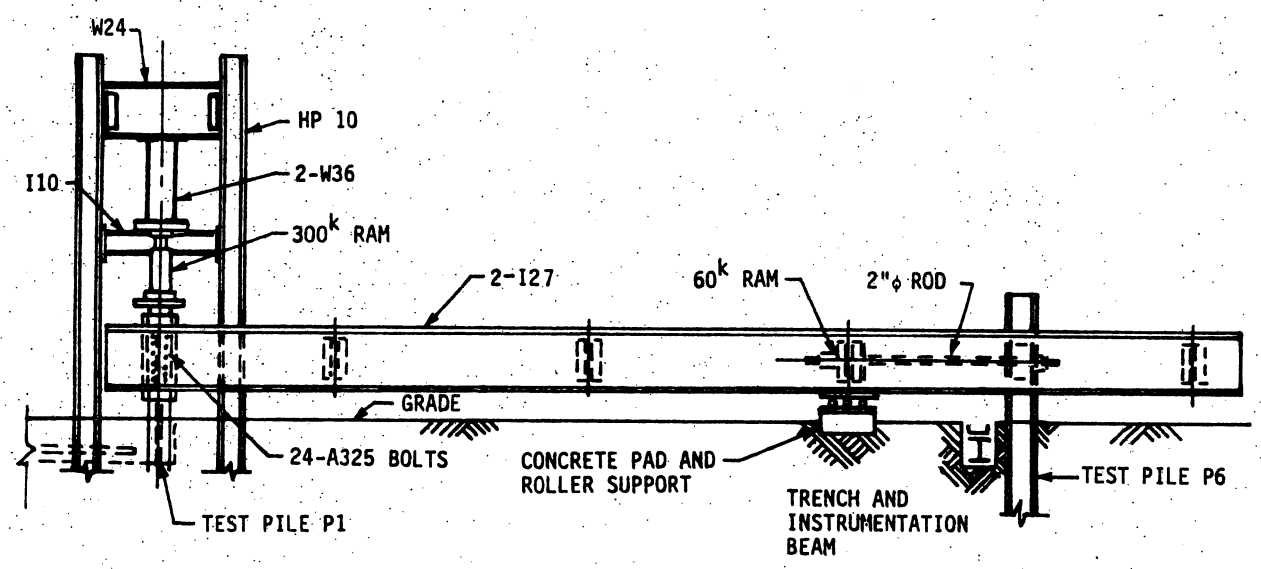

Figure 10.5. Elevation of test framework and horizontal girder for combined load test.

The primary test frame members that resisted the applied vertical load on Test Pile P1, shown in Fig. 10.1, consisted of four 50-ft-long HP10 × 42 vertical reaction piles (Piles P2-P5) that were driven to a depth of 37.5 ft in the corners of a 5-ft by 18-ft rectangle; two W24 × 76 spreader beams spanning 5 ft between the reaction piles; and a 20-ft-long, 200-ton-capacity, Iowa DOT, jacking beam shown in Fig. 10.2. An underground obstruction was struck while driving of the reaction pile P2, causing the pile to twist and displace significantly out of plumb. The plumbness of this misaligned pile was partially corrected by cutting the flanges below grade to within about 1 in. of the web, bending the pile about an axis in the plane of the web, and welding a splice plate to each flange to restore the axial capacity of the pile. Since the twist and offset could not be totally eliminated, a skewed connection at both ends of the W24 × 76 spreader beam had to be designed and field fabricated for attachment to the reaction piles P2 and P3.

A vertical guide system was designed into the test framework to provide lateral stability for the top of the vertical load test pile, which projected approximately 4 ft above grade to accommodate the connection between the test pile and horizontal girder for the combined load test shown in Fig. 10.5. A steel collar with four rollers restraining only lateral movement of the test pile flanges and web was bolted to the top of a horizontal girder consisting of two I27 × 85 beams. As shown in Fig. 10.3, this girder, which was fabricated by blocking out portions of both flanges to straddle the vertical load test pile and the lateral load test pile, was supported by a hanger bracket attached to a W30 × 108 beam that spanned 18 ft between vertical reaction Piles

P3 and P5 and by a concrete pad positioned about 24 ft from the vertical test pile. The horizontal girder did not provide any resistance to the vertical movement of the test pile for the vertical load test.

Vertical loads were applied to the test pile by a 400-kip-capacity hydraulic ram that was positioned between a 2.5-in.-thick pile cap plate that was welded to the top of the test pile and a 2-in.-thick beam bearing plate that was positioned on the underside of the 200-ton capacity jacking beam. Before any loads were applied, the hydraulic ram, a vertical load cell to monitor load, and the jacking beam were centered over the test pile.

For the second field test, a lateral load pile test was conducted on Test Pile P6 located 30 ft west of the vertical load test pile as shown in Figs. 10.1 and 10.4. The primary test frame members that resisted the lateral load were essentially the same members that resisted the vertical load and provided lateral stability to Test Pile P1 used in the vertical load test. However, the steel collar used in the first field test was removed; therefore, lateral movement of the girder would not be resisted by Test Pile P1. The steel framework containing the four vertical reaction piles resisted the lateral force that was applied to Test Pile P6 by a lateral load mechanism consisting of a 2-in.-diameter tension rod, a diaphragm in the horizontal girder, and a 60-kip capacity, hollow core, hydraulic ram. The location of the tension rod and ram for the lateral load test caused the horizontal girder to be subjected to a compression force and the lateral load test pile to displace toward the right in Fig. 10.4.

Since the lateral load test pile was orientated for strong axis bending, the test pile was field fabricated by removing the entire web plate over a specific length and by cutting a hole through the center of both flanges to accommodate the tension rod. Steel plates were welded on and between both flanges to restore the pile shear and flexural strength at the tension rod location.

The same steel frame was used for the third field test, which involved a vertical load test on a horizontally displaced pile. The test pile for the combined loading was Test Pile P1. For this test, the webs of the horizontal girder were bolted to the flanges of the test pile to provide moment continuity, as shown in Fig. 10.5. The vertical and longitudinal support of the girder by the W30 × 108 beam was eliminated; therefore, only the test pile and the concrete pad provided vertical support for the horizontal girder. The rotational restraint, at the top of the test pile provided by the girder, simulated the flexural stiffness of bridge girders in integral abutment bridges.

The location of the hydraulic ram and tension rod that applied the lateral force to Test Pile P1 was changed from the location used in the lateral load test. The new position of the load apparatus shown in Fig. 10.5 caused Test Piles P1 and P6 to be pulled toward each other and induced a tension force in the horizontal girder when a lateral load was applied.

10.1.3. Instrumentation Framework and Support

In order to monitor accurately pile displacements, the dial gages and direct current displacement transducers (DCDTs) must be mounted on a frame that is supported beyond the zone of soil movement due to pile

displacement of both the test and reaction piling. Since both vertical and lateral forces were applied to the test piles, the location of the instrumentation framework supports (Piles P7 - P10 shown in Fig. 10.1) were established to comply with the ASTM Standards [23,24]. Structural steel members were selected for the instrumentation beams and supports to provide adequate flexural rigidity. The supports were short sections of a HP10 × 42 piling embedded approximately 5 ft into the ground.

The instrumentation for the vertical and combined load tests on Test Pile P1 was mounted at the end of the overhang of a 20-ft-long box beam fabricated from two channel shapes. This beam was pinned at Pile P8 and had a longitudinal roller support at Pile P7. The instrumentation beam for the lateral load test of Pile P6 had an 18-ft simple span between the two support piles (Piles P9 and P10 shown in Fig. 10.1). To provide sufficient stiffness, this beam was fabricated from an I-shape and a channel-shape.

The beams were placed below grade in covered trenches to minimize thermal expansion and contraction and wind-induced displacements of the instrumentation beams. Since the temperature within a trench could still vary to some extent during testing, a displacement transducer was installed to measure any change in length of an instrumentation beam. The measured test pile movement was adjusted by any detectable expansion or contraction of the instrumentation beam.

10.1.4. Test Pile Preparations

Two HP10 × 42 test piles, P1 and P6, were instrumented with electrical resistance strain gages to monitor the behavior of the piles below grade. The strain gages were attached on the inside face of the

flanges and were located 1 in. from the corresponding flange tip. Test Pile P1, shown in Fig. 10.1, had 60 strain gages mounted along most of the 40-ft-embedded depth, since the variation in axial force along the length of the pile was to be determined for both the vertical and combined load tests. As shown in Fig. 10.6, the upper 16.5 ft of the Test Pile P1 had four strain gages symmetrically placed on the pile cross section at each particular station along the pile length. Below this depth, two strain gages were mounted symmetrically with respect to the web plate, on one flange for a particular station. The concentration of strain gages within the upper portion of the test pile was required to monitor adequately the bending strains induced during the lateral loading of the pile. To separate axial strains and biaxial bending strains, a minimum of three gages at known locations on the pile cross section are required per station. Four gages were mounted along the length of the pile, which would be subjected to the largest flexural stresses, to provide an additional gage per station if one of the gages malfunctioned. Fewer strain gages were required along the lower portion of the test pile, since the bending strains are minimal at those depths. Even with just two gages per station, axial strains and uniaxial bending strains can be separated.

Test Pile P6, shown in Fig. 10.1, had 36 strain gages mounted along the upper 17 ft of the 40-ft-embedded portion of the pile. As shown in Fig. 10.6, only the top of this test pile was instrumented, since the bending strains induced by lateral loads are minimal in the lower portions of the pile. A close uniform spacing along the pile length was selected for the gage station locations to obtain the bending

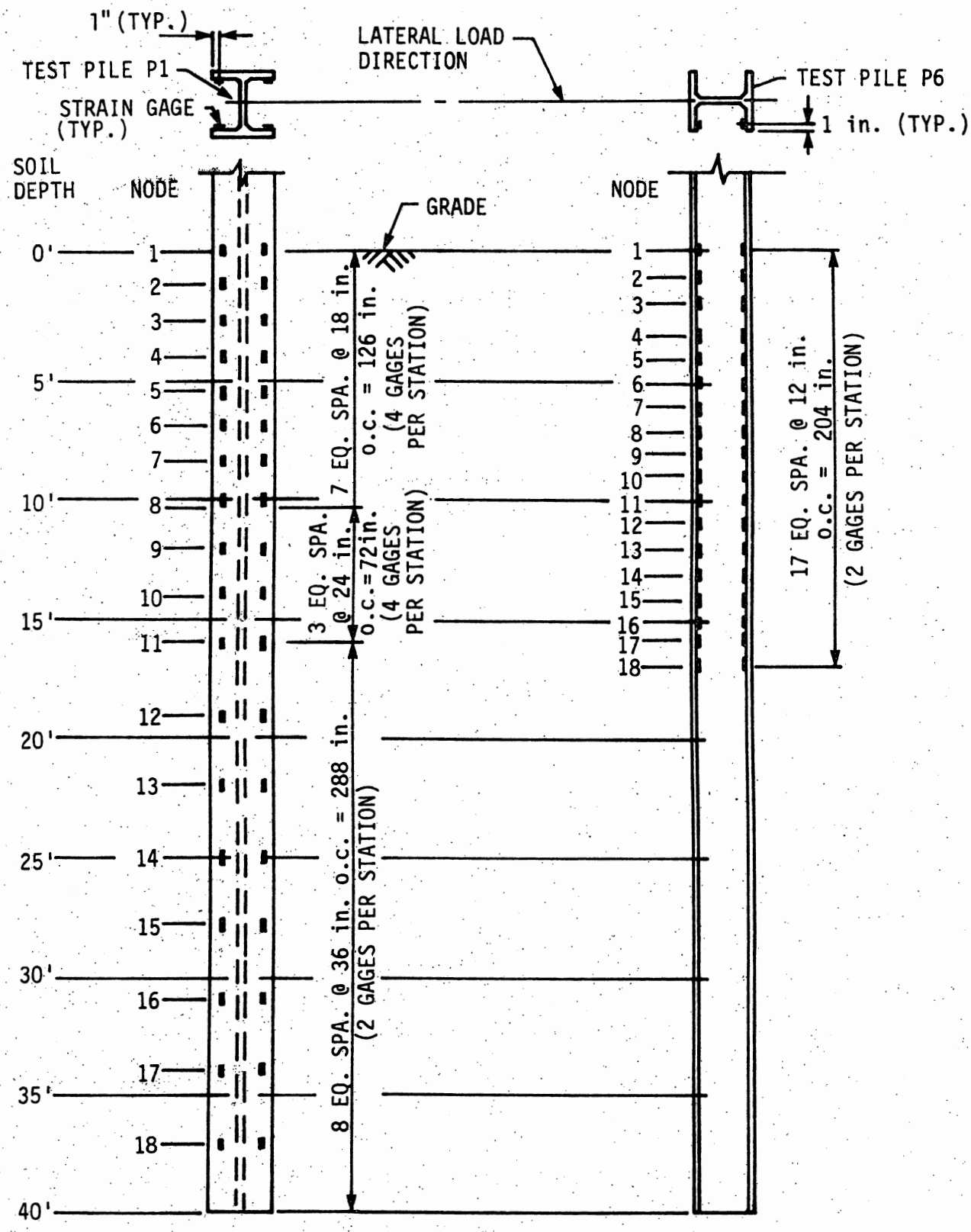

Figure 10.6. Strain gage locations on test piles.

strain distribution. Two strain gages were mounted on opposite flanges on the same side of the web plate at each station to measure the pile strains associated with strong-axis bending of the test pile.

After the electrical resistance strain gages were mounted on the piles and the wire leads were attached to the individual gages, a multi-layered protective covering was placed over each gage. A layer of foil tape was placed over the gages and the connections to the wire leads to reduce electrical interference. Moisture protection was achieved by covering the foil tape with a two-part, polysulfide, liquid polymer. Since the strain gages would be located below the water table after the piles were driven, a silicone gel waterproofing layer was placed over the polymer coating. After the gel had cured, a 16-ga. sheet-metal cover, which had been embossed to match the gage and lead wires, was placed over each gage and welded to the flange of the pile.

The wire leads for the gages, which had waterproof insulation and a waterproof jacket, were bonded intermittently to the pile and each other with a construction adhesive (PL400). These leads were positioned within the corners formed by the web and flange plates. A 16-ga.-bent sheet-metal closure was fabricated to fit diagonally between the pile web and flange, forming a vertical conduit to contain the wire leads. The void spaces within the conduits were filled with an insulation foam to prevent the wires from vibrating during pile driving. At the top of the test piles, the remaining length of the wire leads was wrapped around two foam-rubber-padded threaded rods that were bolted through the web of the pile. The coiled wire was wrapped in foam rubber and

enclosed by a 16-ga. sheet-metal and steel-angle closure assembly that was welded to the pile.

At the bottom of each vertical sheet-metal conduit, a 1-in.-thick triangular plate was welded to the pile flange and web to cover and protect the open end of the conduit. At the bottom of the pile, flat steel bars were welded to the pile flanges in vertical alignment with the sheet-metal strain gage covers. The bars projected just beyond the gage cover embossment height to protect the covers during driving of the pile.

After the piles were driven, several feet of the top of the test piles were removed to accommodate the test framework and to provide a sample of each pile from which tension coupons were taken. The average yield point of the flange steel was determined to be 45.5 ksi and 46.2 ksi for Test Piles P1 and P6, respectively.

Both test piles were reinforced above grade before the individual field tests commenced. The top of Test Pile P1 was reinforced by welding a 3/8 × 12 × 30-in.-long steel cover plate on each flange. These plates strengthened the pile flanges for the bolted connection between the test pile and the horizontal girder for the combined load test. The plates increased the plastic moment capacity of the built-up section to force any possible plastic hinge formation to occur below the girder, rather than within the connection region. The top of Test Pile P6 was modified as described in Section 10.1.2.

10.2. Field Test Procedures

10.2.1. Vertical Compression Test

The procedure for the vertical load test of Test Pile P1 was developed using the Standard Loading Procedure of the ASTM Standard [23] as a guide. Modifications to the standard were made to provide the experimental information needed for the analytical investigations. Axial compressive loads, monitored by a 300-kip-capacity load cell, were applied in increments of 20 kips (approximately 25% of the calculated safe bearing capacity for the pile predicted by Eq. (3.1)). Before the next load increment was applied and while the load was maintained, the rate of vertical displacment for the pile head had to be equal to or less than 0.01 in./hr for the last 5-min. interval between successive data records. Loads were incremented up to the ultimate strength of the pile. Since the test pile was a friction pile, failure was evidenced by excessive settlement of the pile at the ultimate load. For the initial load levels, convergence to the vertical displacement limit occurred within a relatively short time interval; while, for the load levels approaching the pile capacity, several hours would elapse before the settlement rate could be satisfied. After the ultimate capacity of the pile had been obtained and the total vertical settlement had reached at least 15% of the pile diagonal cross-section dimension, the applied vertical load was removed in decrements equal to 25% of the ultimate load. Each successive decrement was not initiated until the settlement rate had stabilized to 0.01 in./hr or less.

The test pile displacements at the ground surface were monitored with direct current displacement transducers (DCDTs), dial gages, and engineering scales, as shown in Fig. 10.7. The DCDTs and the dial gage were calibrated to a 0.001-in. accuracy; while the scales were graduated to 1/50 in. Four DCDTs measured the vertical displacement of the pile near the flange tips, two DCDTs monitored the horizontal displacement parallel to the flanges, and two additional DCDTs recorded the horizontal displacement parallel to the web. A dial gage was mounted off the web plate to provide an immediate visual indication of vertical pile movement. A secondary system to measure pile displacements was accomplished with taut wires, mirrors, and engineering scales. The scales were glued to the mirrors, which were attached to the pile flanges. By aligning a wire with its mirror image, the scale could be read accurately to locate the pile position.

Other information recorded throughout the test included the time, axial load, hydraulic ram pressure (to check the load cell readings), pile strains, ambient air temperature, instrumentation trench air temperature, and vertical movement of the framework reaction piling. The time, load, DCDT displacements, and pile strains were monitored automatically by a data acquisition system (DAS), while the other measurements were recorded manually.

10.2.2. Lateral Load Test

Test Pile P6 was subjected to a lateral load test causing strong axis bending of the HP-shaped cross section. The ASTM Standard [24] was used to establish the testing procedure and instrumentation required to obtain the experimental data. The loading technique was based on

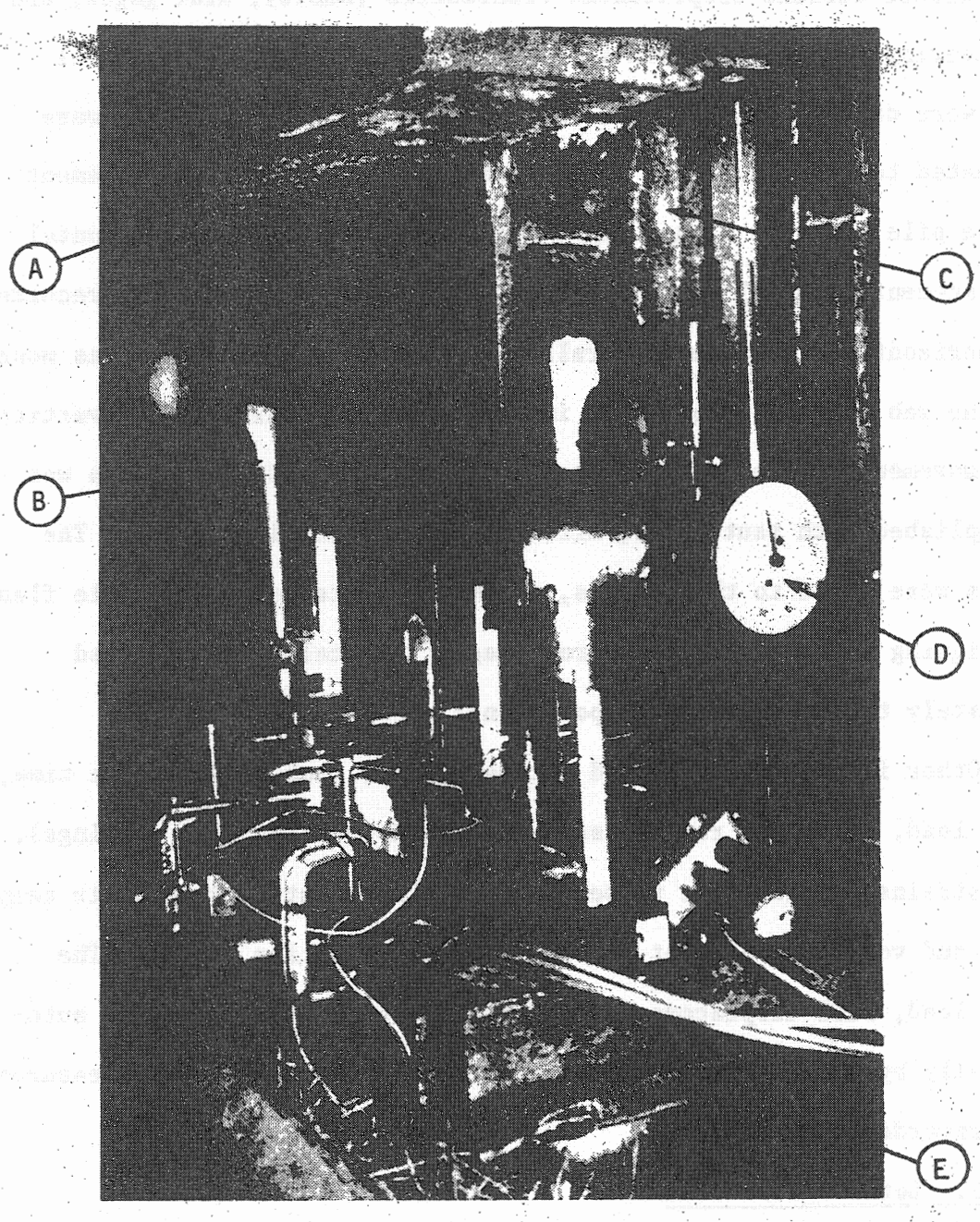

Figure 10.7. Displacement instrumentation for Test Pile P1: (a) bottom flange of load girder (b) vertical DCDT (c) Test Pile P1 (d) vertical dial gage (e) bracket.

displacement control rather than on load control. Lateral displacement increments of 0.10 in. at the ground surface were applied to the test pile until a total displacement of approximately 2 in. was obtained. Before each displacement increment was applied, a lateral load decrement rate of 400 lb/hr, measured over a 5-min. time interval of monitoring, had to be satisfied. This load criteria, established by the precision of the 50-kip load cell that measured the applied lateral load, was satisfied within a relatively short period of time during the initial displacement levels. However, at the larger horizontal movements, several hours elapsed before the load decrement rate was considered acceptable. The unloading of the test pile was accomplished in four equal displacement steps. Each successive decrease in the horizontal displacement was not initiated until the load rate had stabilized to 400 lb/hr or less.

The instrumentation used for the lateral load test was similar to that used for the vertical load test, except that the mirrors and taut wires were replaced by surveying instruments. Measurements of time, lateral load, displacements, and load rate were taken every 5 min. A complete record of all test data was obtained at the beginning and end of each displacement increment.

10.2.3. Combined Load Test

The combined load test for Test Pile P1 was conducted in two stages. First, a 2-in.-lateral displacement, measured at the ground surface, was applied to the pile. The test procedures associated with the first stage of the combined load test were the same as those used for the lateral load test described in the previous section. After the

2-in.-lateral displacement was obtained and the final 0.10-in.-displacement increment satisfied the 400 lb/hr load decrement criteria, vertical loading of the displaced pile commenced. The test procedures for the second stage of the combined load test were the same as those followed for the vertical load test described in Section 10.2.1. Vertical loads were applied in 20-kip increments and the settlement criteria of 0.01 in./hr was satisfied for each load step.

Instrumentation of the test was basically the same as for the previous two field tests. DCDTs and dial gauges measured pile displacements both vertically and horizontally. Load cells monitored the vertical and lateral hydraulically applied loads, and pile strains were determined from the electrical resistance strain gages.

10.3. Field Test Data Reduction and Development of Soil Characteristics

10.3.1. Experimental Pile Strains

The pile strains were monitored by the electrical resistance strain gages at discrete locations on the pile cross section and at specific stations along the pile lengths, as shown in Fig. 10.6. Before a measured strain was accepted as an accurate reading, a data-censoring study was performed. Prior to testing, a general electrical test of the 60 strain gages on Test Pile P1 and 36 strain gages on Test Pile P6 revealed that 49 gages and 23 gages, respectively, were still active. The inactive strain gages may have been damaged by welding the sheet-metal protection devices to the piles, by driving the piles into the ground, or by water leakage into the gage area. Measured strain versus applied load graphs

were drawn to evaluate the acceptability of each active strain gage. When an erratic strain behavior was observed for a particular gage, the gage would be eliminated for the data reduction. The strain-censoring procedure produced acceptable strain measurements from 44, 17, and 45 strain gages for the vertical, lateral, and combined load tests, respectively.

The strain gages measure the total strain, ε, which includes the axial strain, ε_o, induced by the axial load and the bending strains, ε_{by} and ε_{bx}, caused by bending moments about the y-axis and x-axis, respectively. The total strain at any point can be written as

$$\varepsilon = \varepsilon_o \pm \varepsilon_{by} \pm \varepsilon_{bx} \tag{10.1}$$

To determine the axial strain and bending strains at the strain gage locations, the plane section theory was assumed. Therefore, the total strain can be rewritten as

$$\varepsilon = \alpha + \beta x + \gamma y \tag{10.2}$$

where, α = the axial strain, β = the bending moment about the y-axis of the cross section divided by the flexural rigidity with respect to the y-axis, x = the x-coordinate of the point on the cross section where the strain was measured, γ = the bending moment about the x-axis of the cross section divided by the flexural rigidity with respect to the x-axis, and y = the y-coordinate of the point on the cross section where the strain was measured.

The three unknowns in Eq. (10.2) are α, β, and γ. If four gages provide acceptable strain measurements at a pile cross section, a least squares solution provided a method to evaluate the three constants. When three gages function properly at a given station, the three unknowns were determined by solving three simultaneous strain equations. For locations where only two strain gages provide accurate strain measurements, an assumption must be made for one of the bending strain components. A zero bending strain with respect to the strong or weak axis can be assumed, depending upon the gage locations on the cross section and the direction of applied loading to the pile (Test No. 1, 2, or 3). When only one strain gage was available, two strain components had to be assumed. A zero axial and bending strain or zero bending strains were assumed based on the type of pile loading and the depth at which the gage was located. Tables 10.5 and 10.6 list generalized axial and bending strains in terms of the total strain (denoted as a, b, c, or d) measured by gages located in various positions on a cross section. The abbreviations NW, SW, SE, and NE refer to the north-west, south-west, south-east, and north-east flange tips, respectively.

For the first and second field tests, the experimentally measured total pile strains were used directly. The measured strains for the third field test had to be corrected because of an instrumentation malfunction. During the lateral load phase of this combined load test, the recorded strain data implied that a substantial axial load existed, even though vertical loads were not directly applied. Therefore, for the lateral phase of the test, the measured strains were corrected by subtracting the axial strain, ε_o, shown in Table 10.5, such that the

Table 10.5. Experimental axial and bending strains for vertical and combined load tests.

Strain at NW	SW	SE	NE	Test No. 1 & 3 ε_o	Test No. 3 ε_{by}	Remarks
a	b	c	d	- (a + b + c + d)/4	- (a + b - c - d)/4	Least squares solution
a	b	c	--	- (a + c)/2	- (a - c)/2	
a	b	--	d	- (b + d)/2	- (a - d)/2	Simultaneous equation solution
a	--	c	d	- (a + c)/2	- (a - c)/2	
--	b	c	d	- (b + d)/2	Did not occur	
a	b	--	--	- (a + b)/2	Did not occur	Assumes $\varepsilon_{by} = 0$ ($\beta = 0$)
a	--	--	d	- (a + d)/2	- (a - d)/2	Assumes $\varepsilon_{bx} = 0$ ($\gamma = 0$)
--	b	--	d	- (b + d)/2	- (b - d)/2	
a	--	--	--	- a	No solution	Occurred in lower portion of pile. Assumes $\varepsilon_{by} = \varepsilon_{bx} = 0$ ($\beta = \gamma = 0$)

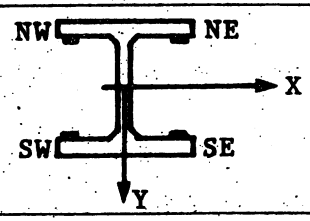

Lateral load for Test No. 3 was applied in the x-z plane along the negative x-direction.

Table 10.6. Experimental bending strains for lateral load test.

Strain at SW	Strain at SE	Test No. 2 ε_{bx}	Remarks
a	b	$-(a-b)/2$	Assumes $\varepsilon_{by} = 0$ ($\beta = 0$)
a	--	-a	Assumes $\varepsilon_o = \varepsilon_{by} = 0$
--	b	+b	($\alpha = \beta = 0$)

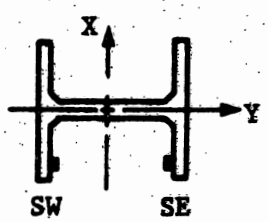

No axial load and the lateral load was applied in the y-z plane along the negative y-direction.

net calculated axial strain at each pile cross section equalled zero. For the vertical phase of the combined load test, the malfunction disappeared. Strains in this phase were adjusted by the axial strain at the beginning of the vertical load phase, when the axial load equalled zero.

10.3.2. Experimental f-z Curves

The first field test, involving only axial compressive loads on Test Pile P1, provided experimental data to establish the relationships for the vertical skin friction force, f, and the relative vertical displacement, z, between the pile and the soil at various points along the pile length. These soil behavioral characteristics, which can be expressed in the form of modified Ramberg-Osgood curves, mathematically describe the soil in contact with the pile along its length.

In order to develop the relationships between the axial strain, vertical skin friction force and the relative vertical displacement, the incremental length, $d\bar{z}$, of pile shown in Fig. 10.8 were considered. Equilibrium of the vertical forces acting on the pile segment requires that

$$\mu s(d\bar{z}) + F - (F + dF) = 0 \qquad (10.3)$$

where, μ = the unit friction force, s = the effective perimeter of the pile, F = the axial compressive force at the bottom of the segment, and dF = the incremental change in the axial force across the length dz. Letting the skin friction force, f, equal μs, Eq. (10.3) becomes

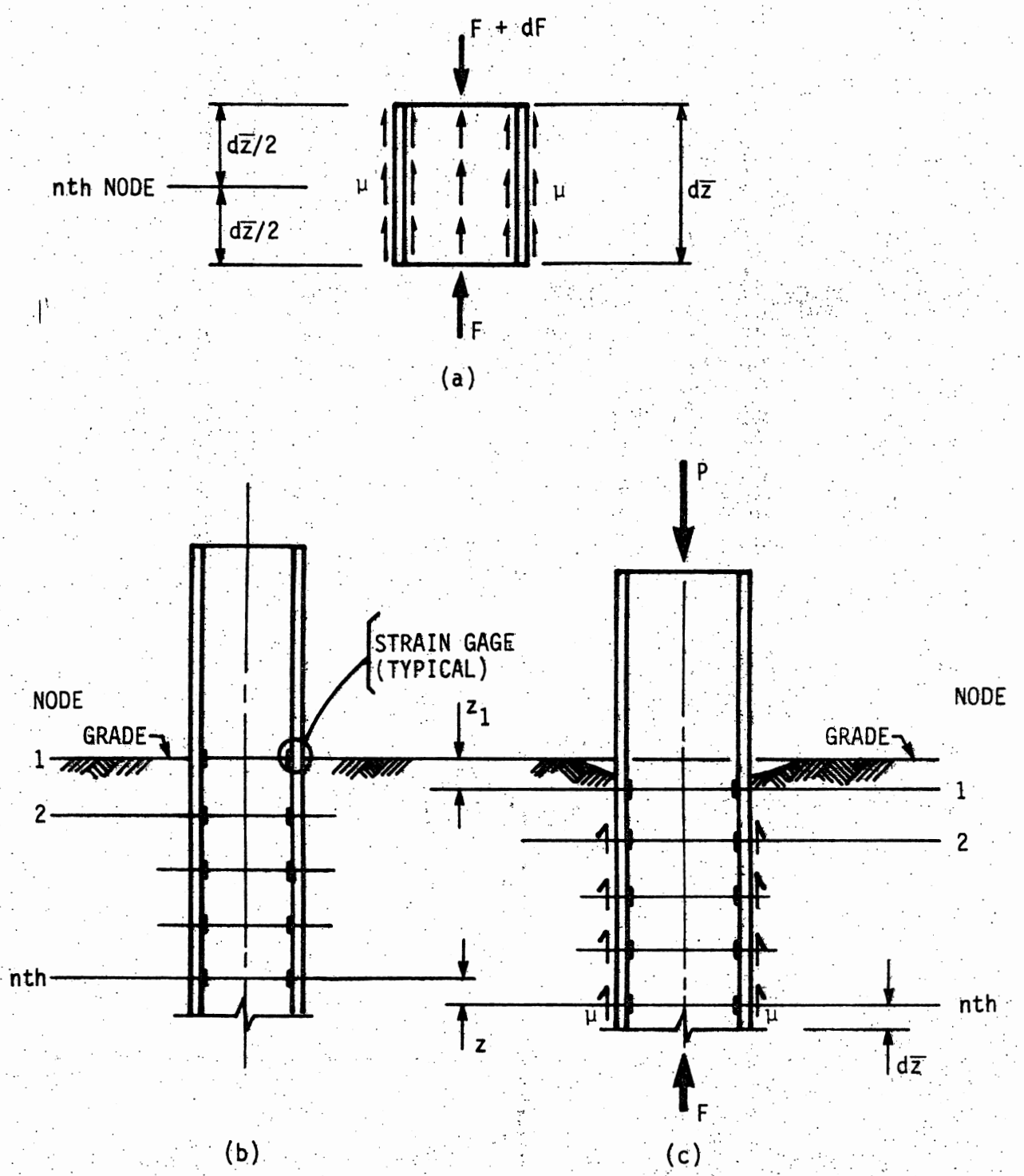

Figure 10.8. Vertical load pile behavior: (a) forces acting on incremental pile segment (b) unloaded pile (c) loaded pile.

$$f = \frac{dF}{d\bar{z}} \tag{10.4}$$

but,

$$dF = EAd\varepsilon_o \tag{10.5}$$

where, E = the modulus of elasticity, A = the cross-sectional area of the pile, and $d\varepsilon_o$ = the incremental pile axial strain. Substituting Eq. (10.5) into Eq. (10.4),

$$f = EA \frac{d\varepsilon_o}{d\bar{z}} \tag{10.6}$$

Figure 10.8 shows a vertically displaced pile due to an axial compressive load, P, at the top of the pile and the relative vertical displacement, z, between the pile and the soil, at the location (nth node) where the skin friction force was evaluated. This relative movement is expressed as

$$z = z_1 - \Delta L \tag{10.7}$$

where, z_1 = the measured vertical settlement at the ground surface, and ΔL = the axial shortening of the pile between the first node at the ground surface and the nth node. Equation (10.7) can be rewritten in terms of the pile axial strain.

$$z = z_1 - \int \varepsilon_o d\bar{z} \tag{10.8}$$

The first derivative of the axial strain for Eq. (10.6) was approximated as the slope to a quadratic function that was obtained by a least squares curve fit through the axial strain data points. The number of nodes on each side of a particular location, n in Fig. 10.9, established whether a three-point or five-point curve fit for the quadratic function was selected. Since the first and last nodes along the pile did not have strain data available at adjacent nodes on both sides, the skin friction force was not evaluated at those nodes.

The integral of the axial strain for Eq. (10.8) was approximated as the area under the strain-depth diagram that was established by connecting the strain data points with straight lines. At the nth node, the integral expression is approximated by the cross hatched area on the axial strain-depth diagram shown in Fig. 10.9. The relative vertical displacement at the nth node was determined by Eq. (10.8).

Figures 10.11 and 10.12 were developed by applying the procedure mentioned above to the axial strains shown in Fig. 10.10. The values for f and z at each strain gage station have been connected by straight lines to illustrate the variation of these experimentally determined parameters along the pile length graphically. For clarity, only three curves have been shown; those corresponding to different magnitudes of the applied vertical load at the top of the pile. The axial strains shown in Fig. 10.10 were plotted to a depth of 34.5 ft. The deepest strain gage station, shown in Fig. 10.6 to be 37.5 ft below grade (2.5 ft above the pile tip), did not provide reliable strain measurements. Sixteen vertical loads were analyzed to determine the nonlinear behavior between f and z. Figures 10.13, 10.14, and 10.15 show the 16 experimentally

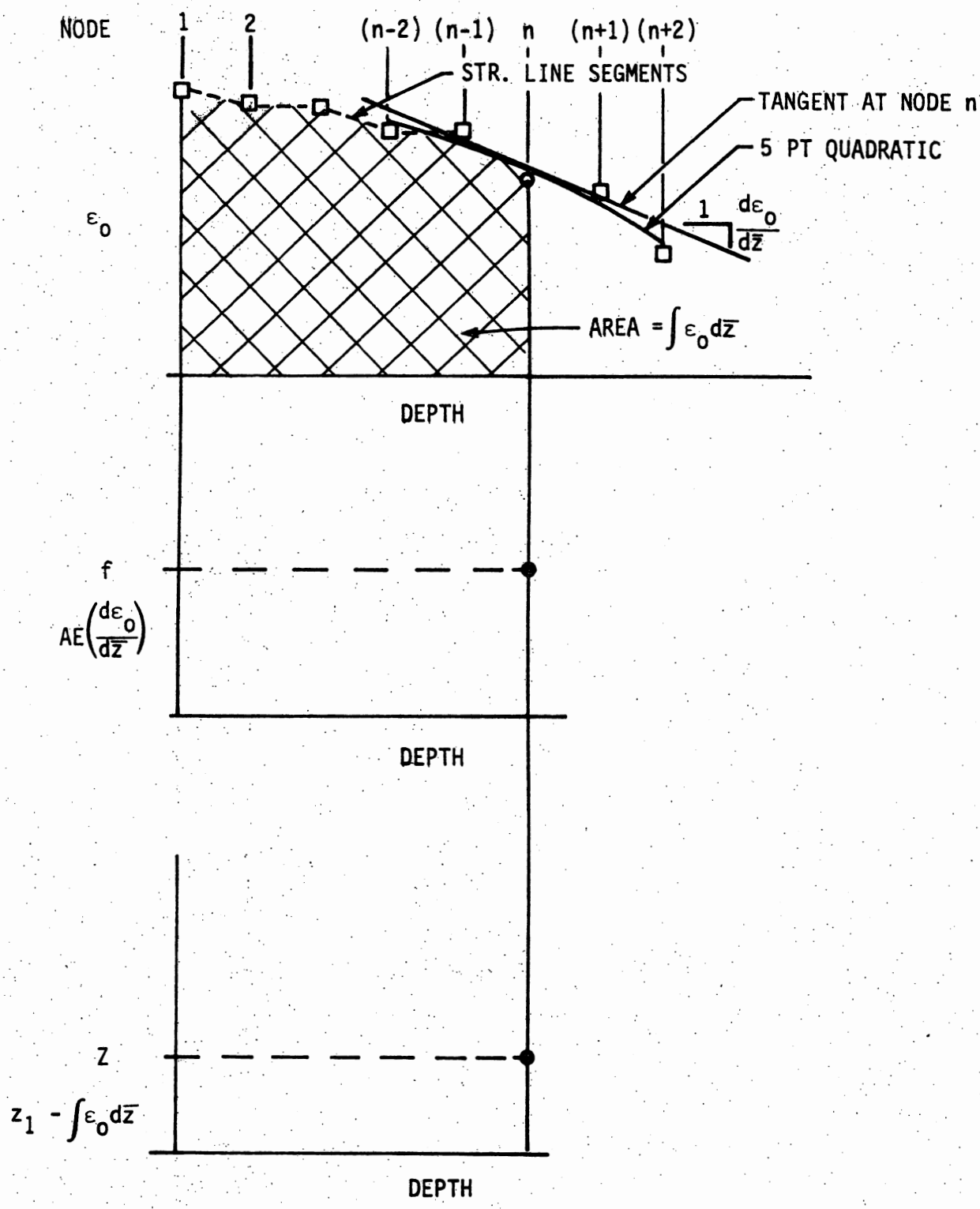

Figure 10.9. Development of f and z at nth node.

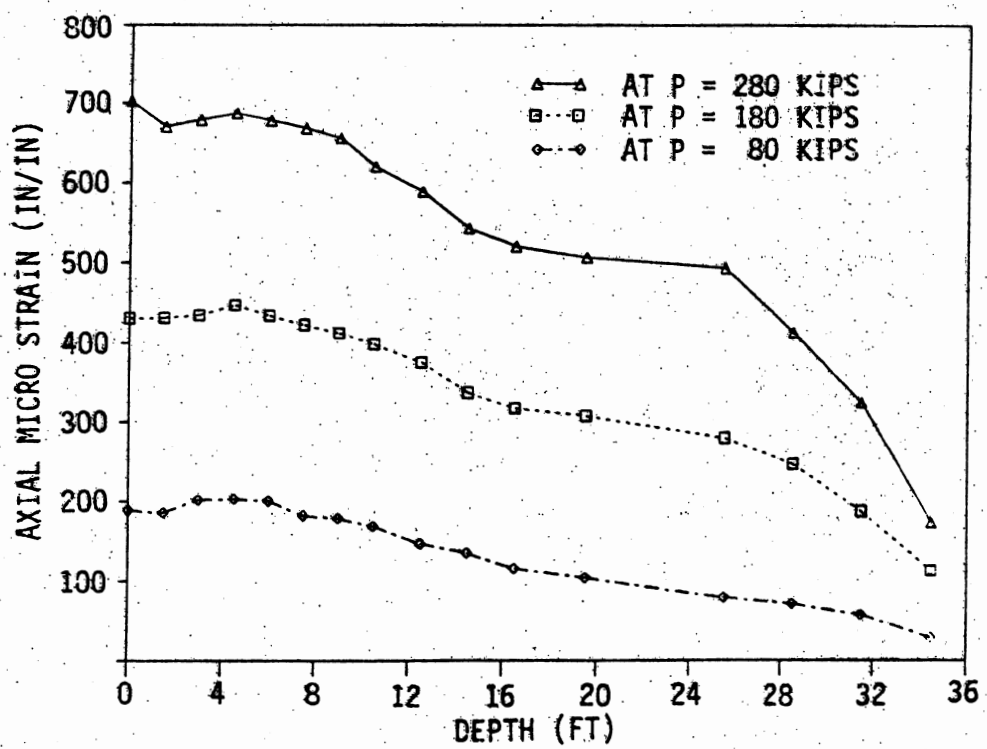

Figure 10.10. Axial strain, ε_o, distributions for vertical load test.

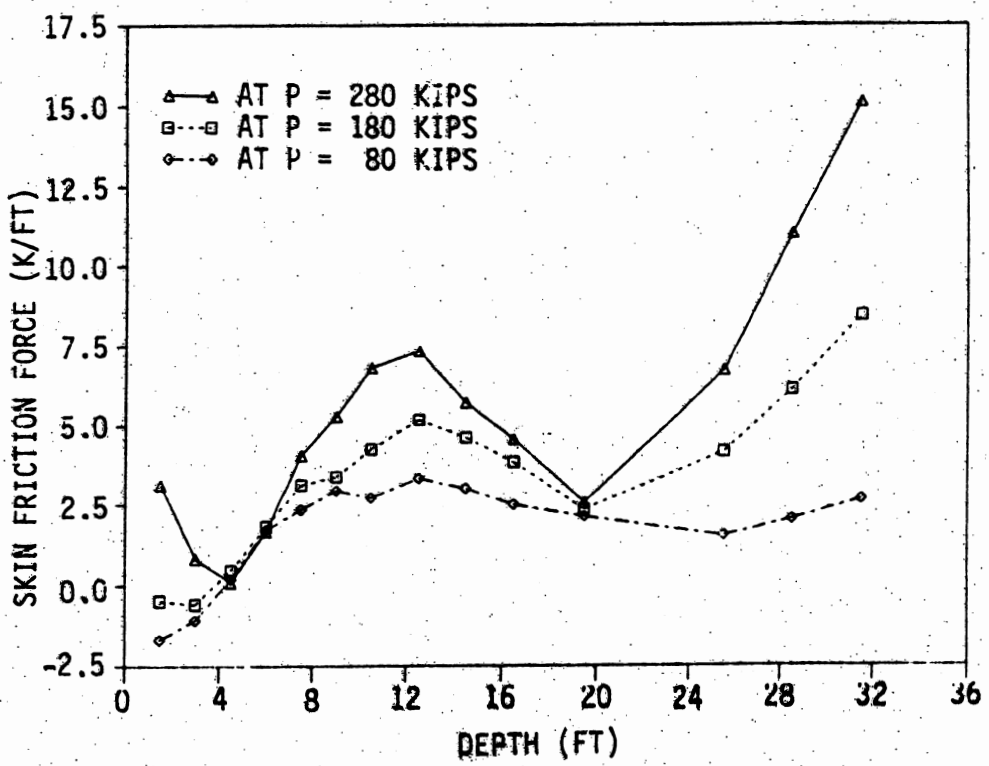

Figure 10.11. Skin friction force, f, distributions for vertical load test.

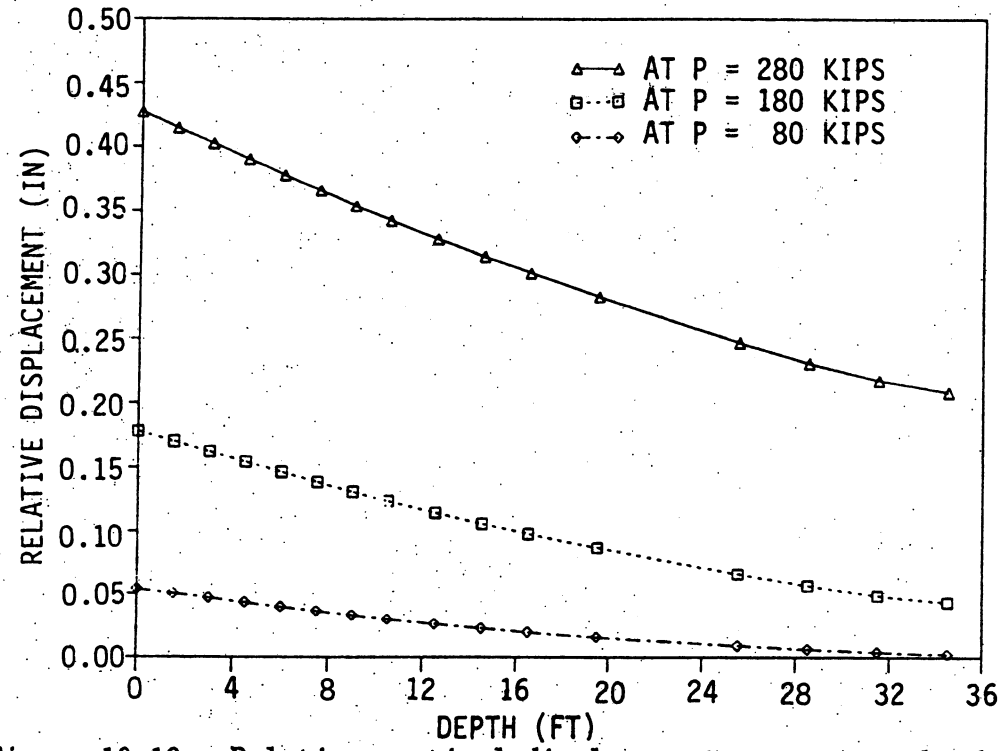

Figure 10.12. Relative vertical displacement, z, versus depth for vertical load test.

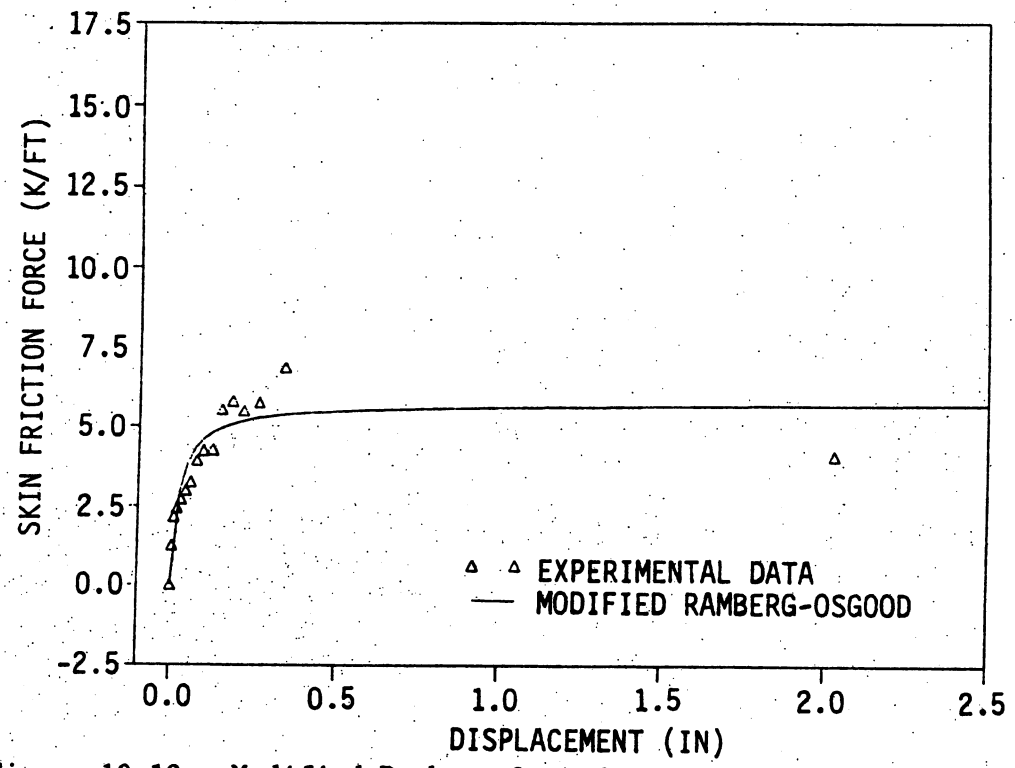

Figure 10.13. Modified Ramberg-Osgood f-z curve at 10.5 ft depth.

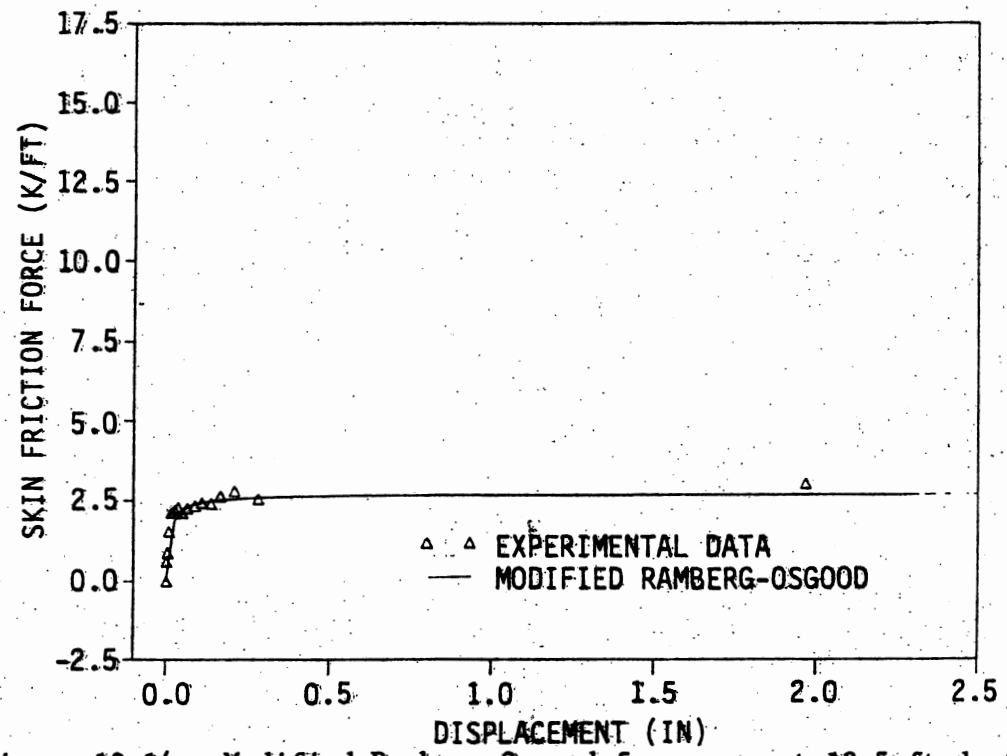

Figure 10.14. Modified Ramberg-Osgood f-z curve at 19.5 ft depth.

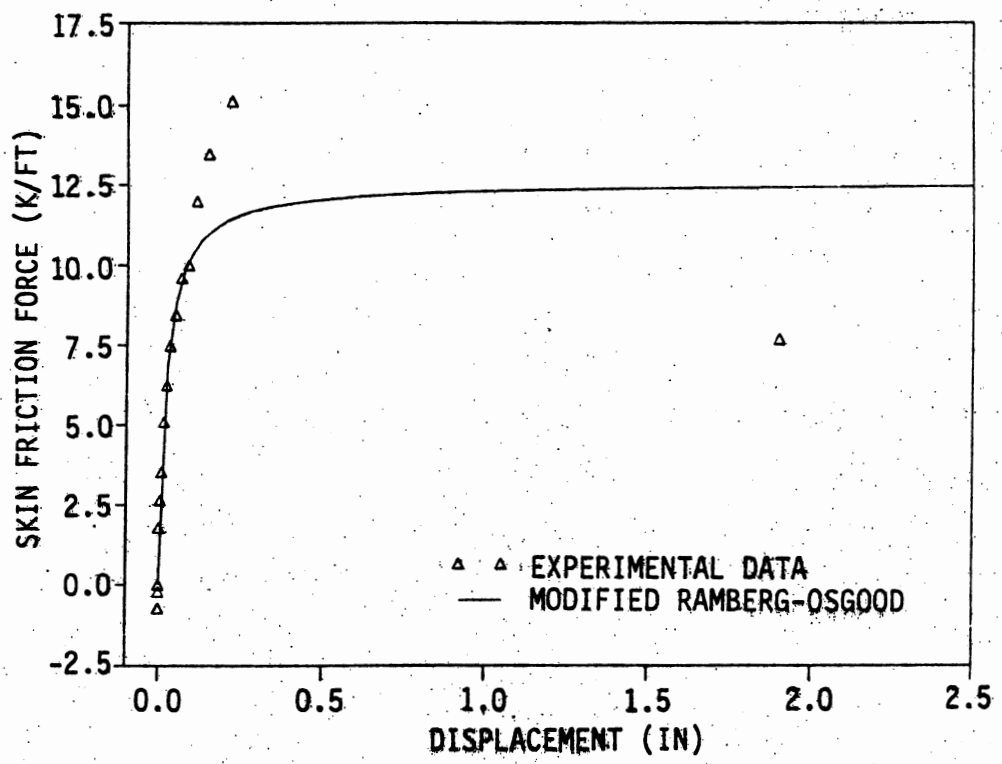

Figure 10.15. Modified Ramberg-Osgood f-z curve at 31.5 ft depth.

derived (f-z) coordinate data point pairs for the nodes at depths of 10.5, 19.5, and 31.5 ft, respectively.

A modified Ramberg-Osgood expression for f-z (Eq. 3.2 in Section 3.3.2) was established, by curve-fitting techniques involving the least squares method, to minimize the error between the data points and the function. From the least squares curve fit of the data at each gage station, with the shape function, n, equal to unity, the values for the maximum friction force, f_{max}, and the initial vertical stiffness, k_v, are shown in Figs. 10.16 and 10.17, respectively. The straight line segments shown in these figures were established, by visual inspection, to obtain linear variations for these soil parameters for all depths. The modified Ramberg-Osgood expressions for f-z for any soil depth were evaluated from Eq. (3.2), with n equal to unity and the two linearized soil parameters (f_{max} and k_v) obtained from Figs. 10.16 and 10.17.

10.3.3. Experimental q'-z' Curves

The soil resistance at the tip of a friction pile can be represented by a nonlinear relationship between the bearing stress, q, and the pile tip settlement, z. This soil behavioral characteristic can be expressed in the form of a modified Ramberg-Osgood q-z curve. The bearing stress at the bottom of the pile is given by

$$q = \frac{P - EA \int_L f dz}{A_e} \tag{10.9}$$

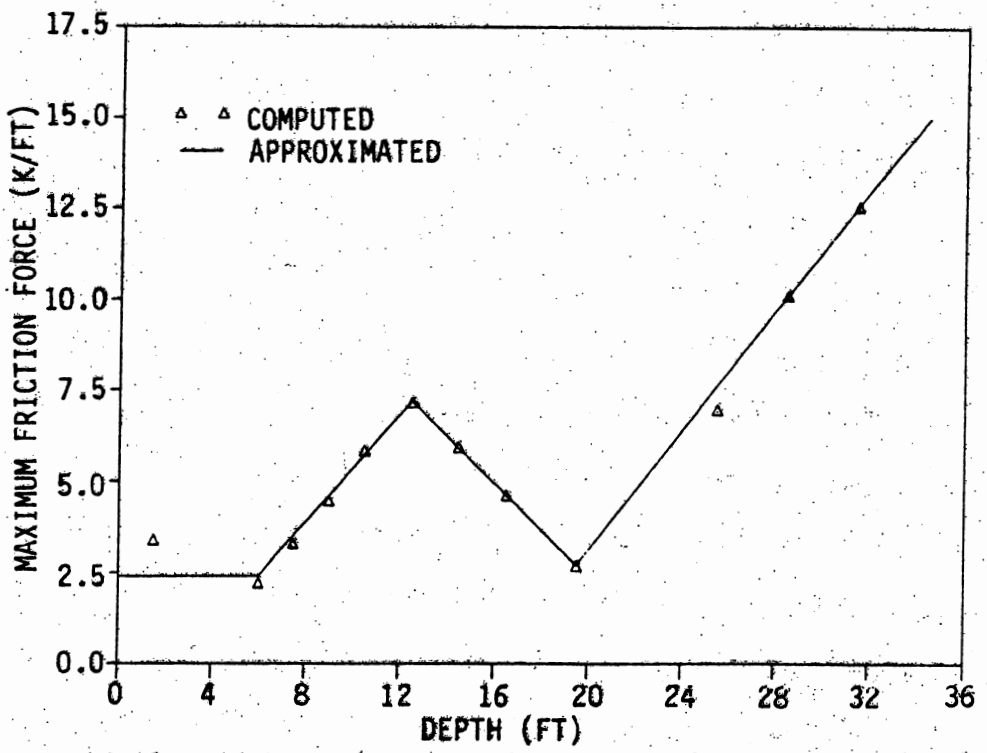

Figure 10.16. Maximum skin friction force, f_{max}, versus depth.

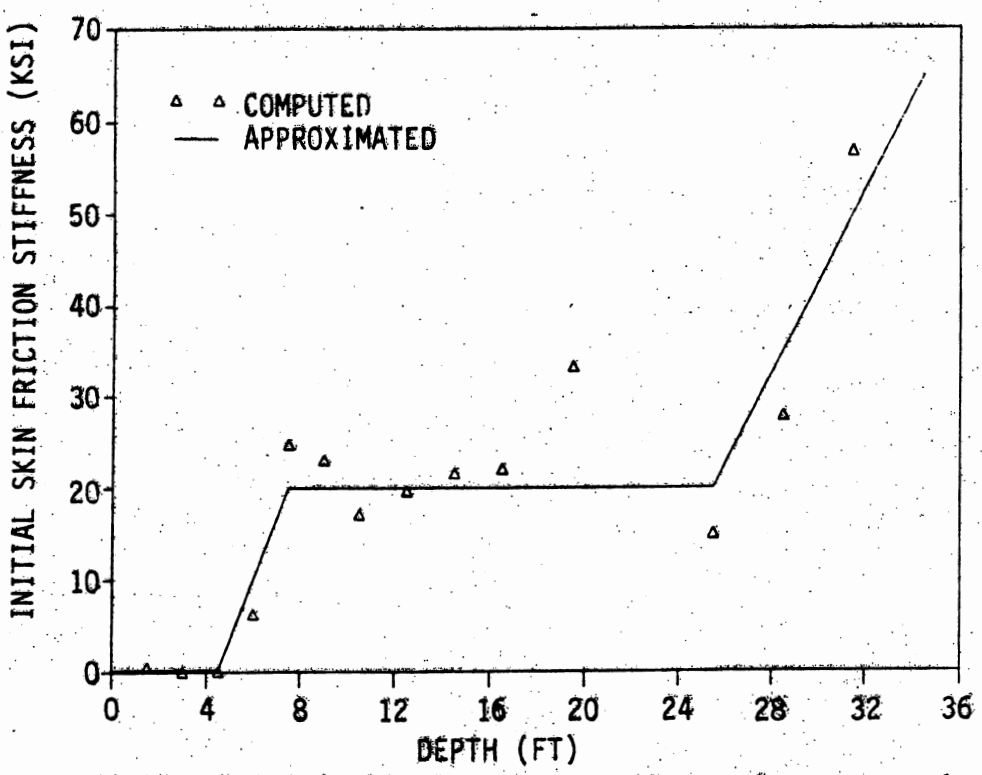

Figure 10.17. Initial skin friction stiffness, k_v, versus depth.

where, A_e = the effective bearing area (rectangular area whose dimensions are the pile cross section width and depth). Knowing the vertical displacement of the pile at the ground surface and the axial pile strain distribution, the tip settlement is expressed as

$$z = z_1 - \int_L \varepsilon_o dz \tag{10.10}$$

Mathematically, Eqs. (10.9) and (10.10) will provide the soil characteristics at the pile tip. However, the solution is sensitive to the accuracy of the computed axial strains. As shown in Fig. 10.10, the magnitudes of these strains decrease substantially with depth and are small at the last reliable gage station (at a depth of 34.5 ft). An extrapolation of the graphs to the pile tip does not provide realistic axial strains at the bottom of the pile. Therefore, rather than speculate on the pile behavior for the last 5.5 ft, a modified q-z relationship was developed at a depth of 34.5 ft. The soil resistance provided by the lower 5.5 ft of skin friction and bearing at the pile tip has been grouped together and denoted as the modified bearing stress, q'. The relative movement between the pile and the soil at a depth of 34.5 ft has been identified as the modified pile tip settlement, z'. Applying these modified soil parameters, Eqs. (10.9) and (10.10) can be rewritten as

$$q' = \frac{P - EA \int_o^{34.5} f dz}{A_e} \tag{10.11}$$

and

$$z' = z_1 - \int_{o}^{34.5} \varepsilon_o dz \tag{10.12}$$

Since reliable pile strains were obtained at a depth of 34.5 ft, Eq. (10.11) can be rewritten in terms of the axial strain, $\varepsilon_{o,34.5}$, at that depth.

$$q' = \frac{EA\ \varepsilon_{o,34.5}}{A_e} \tag{10.13}$$

Evaluating Eqs. (10.12) and (10.13) for each applied vertical load at the top of the pile, the 16 experimental data points shown in Fig. 10.18 were established. To provide a continuous expression describing this soil behavior, the modified Ramberg-Osgood function (Eq. (3.6) in Section 3.3.2), with the shape parameter, n, set equal to unity, was selected for the least squares curve fit. The curve fitting established the initial modified point stiffness, k'_q, and the maximum modified bearing stress, q'_{max}, as 20.4 k/in.^{3} and 135 ksf, respectively.

10.3.4. Experimental p-y Curves

The lateral load test, involving strong-axis bending of Test Pile P2, provided experimental results that were applied to determine the lateral soil resistance, p, and the corresponding lateral displacement, y, at various depths along the pile length, as shown in Fig. 10.19. These soil behavioral characteristics, which can be expressed in the form of modified Ramberg-Osgood p-y curves were obtained from the pile

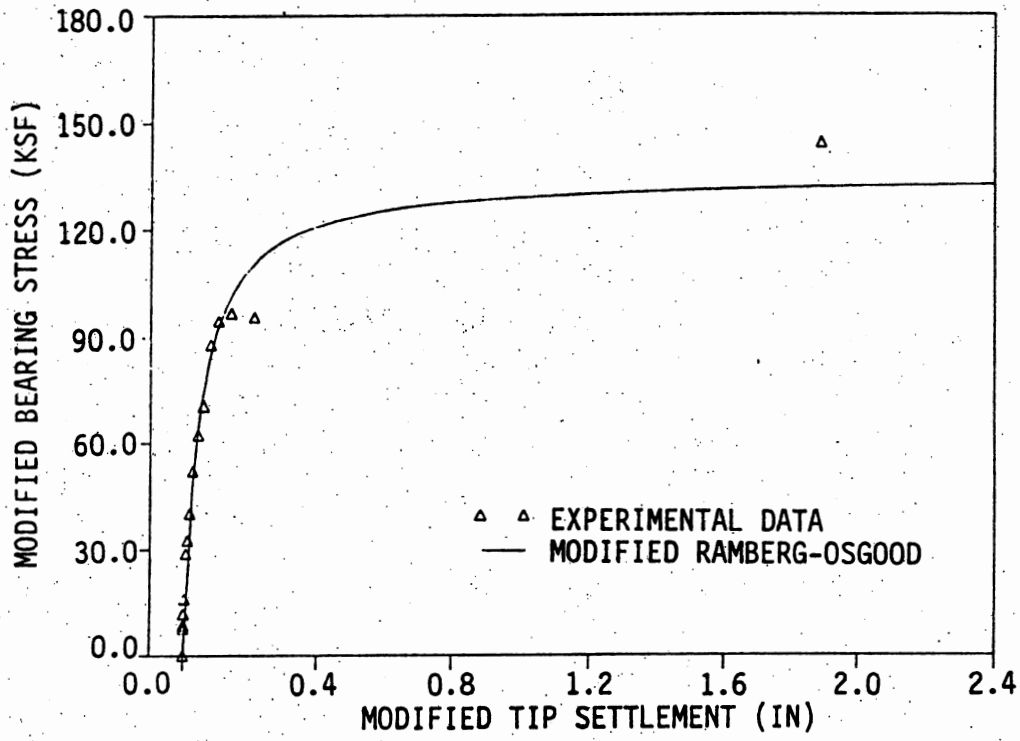

Figure 10.18. Modified Ramberg-Osgood q'-z' curve at 34.5 ft depth.

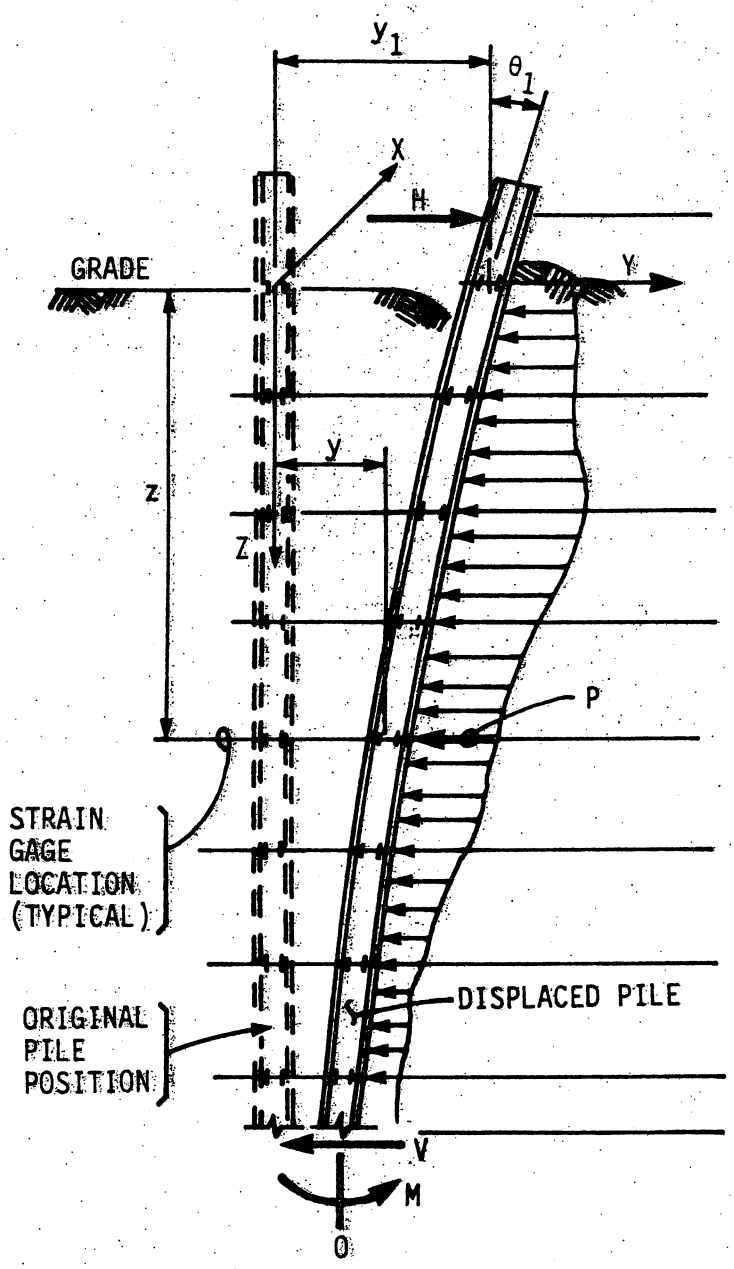

Figure 10.19. Forces acting on a segment of a laterally displaced pile.

strains, lateral displacement and rotation of the pile at specific locations.

From beam theory, the slope, θ; bending moment, M; shear force, V; and resistance, p, can be written as derivatives of the displacement, y, as shown in Eqs. (10.14) through (10.17), respectively.

$$\theta = \frac{dy}{dz} \tag{10.14}$$

$$M = EI \frac{d^2y}{dz^2} \tag{10.15}$$

$$V = EI \frac{d^3y}{dz^3} \tag{10.16}$$

$$p = EI \frac{d^4y}{dz^4} \tag{10.17}$$

Expressing the bending moment in terms of flexural strain, ε_{bx}, with respect to the x-axis, and solving for the lateral soil resistance and corresponding lateral displacement, Eqs. (10.18) and (10.19) were established.

$$p = \left(\frac{EI}{c}\right)\left(\frac{d^2\varepsilon_{bx}}{dz^2}\right) \tag{10.18}$$

$$y = \left(\frac{1}{c}\right) \int\int \varepsilon_{bx} dz \tag{10.19}$$

where, c = the distance from the neutral axis to the strain gage location.

For each lateral load, the bending strains were calculated from the measured total strains using the data reduction techniques discussed in Section 10.3.1. The distribution of these strong-axis bending strains is shown in Fig. 10.20 for three magnitudes of lateral load, H. The flexural strains were computed to a depth of 17 ft. Straight line segments were used to connect the computed strains at the strain gage stations or nodal points along the pile length to illustrate the variation in these strains.

The initial approach to evaluate the soil parameters, given by Eqs. (10.18) and (10.19), was to establish one continuous function for the bending strain that could be differentiated and integrated twice at any location along the entire pile length. Using the computed bending strains as data points, a single fifth-degree polynomial function was selected for curve fitting, involving a least squares approach. Other multi-degree polynomials were also attempted. All of the single continuous functions that provided good correlation with the computed bending strains experienced curvature errors, particularly within the top several feet of the pile length, resulting in negative lateral soil resistance for positive y values. Obvious lateral displacement errors occurred along the lower portion of the pile predicting that the pile tip moved several feet laterally.

To eliminate these problems associated with single function curve fits, an approach similar to the one described in Section 10.3.2 was selected. The lateral soil resistance at a particular depth was calculated as the second derivative to the least-squares quadratic function that was curve fit through a limited number of bending strain data

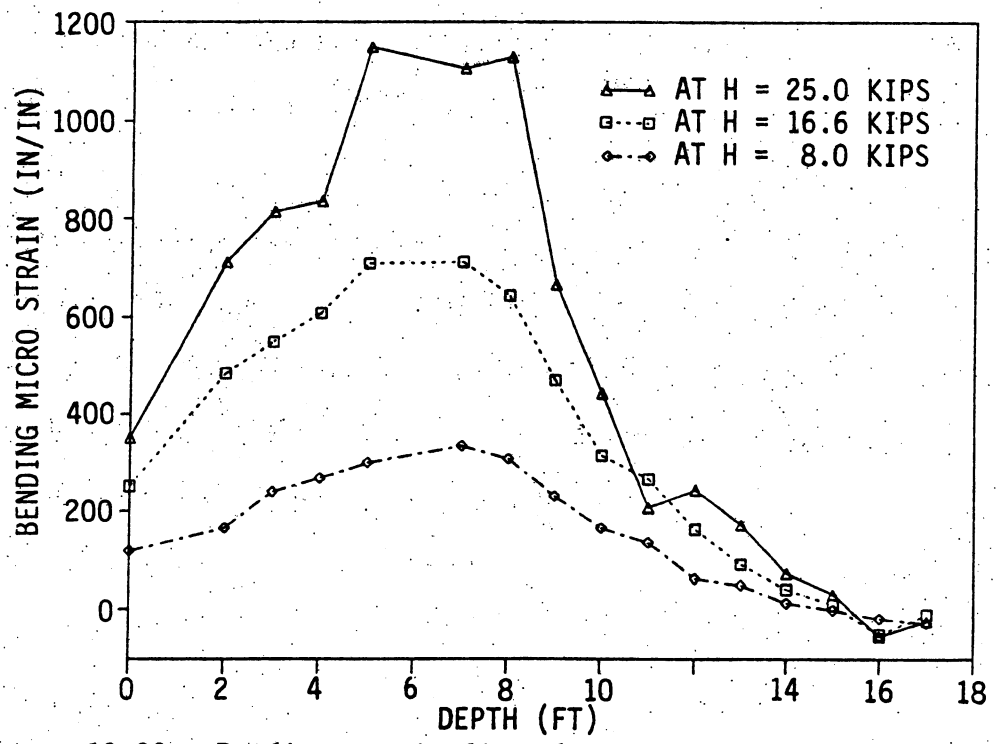

Figure 10.20. Bending strain distribution for the lateral load test.

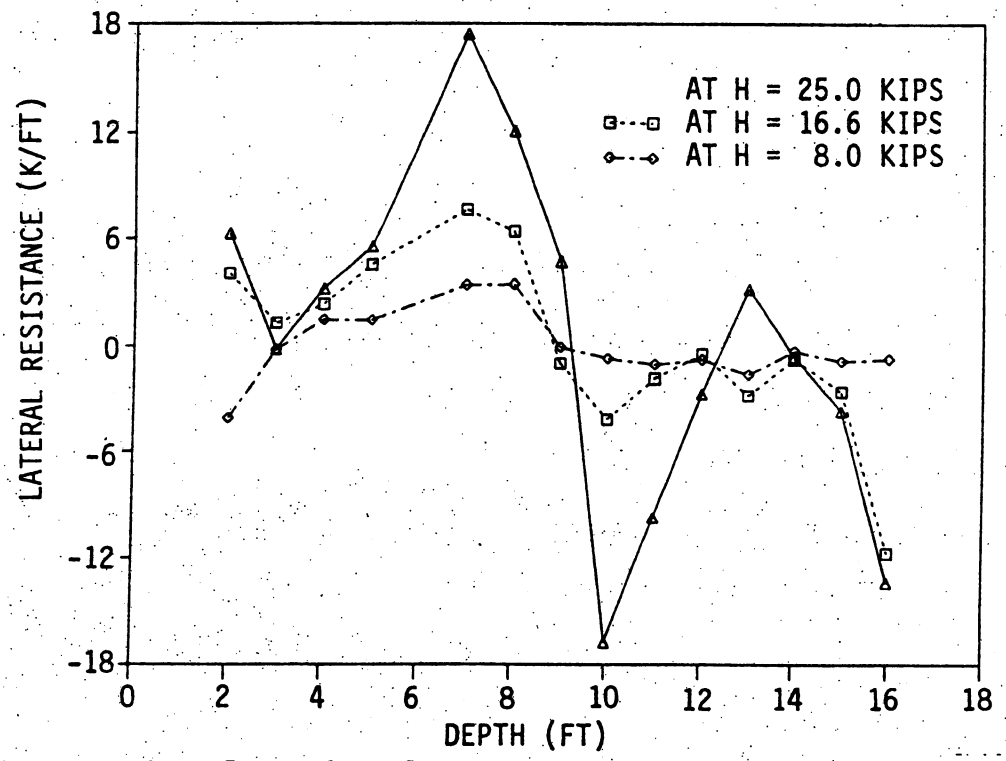

Figure 10.21. Lateral soil resistance, p, distribution for lateral load test.

points. Figure 10.21 shows the results of the data reduction for the lateral soil resistance at various depths for three values of lateral load that was applied at the top of the pile.

To obtain a continuous curve for the lateral displacement expressed by Eq. (10.19), a piecewise double integration procedure of the bending strain function (Fig. 10.20) was involved. A linear equation for the curvature of the elastic curve was assumed between two adjacent bending strain data points. Single integration of a linear segment produced a quadratic equation for the rotation of the pile over that segment. Single integration of this quadratic function produced a cubic equation for the lateral displacement of the pile in this same region.

The integration constants for the pile segment at the ground surface were the rotation and lateral movement of the pile at grade. For the other pile segments, continuity in the elastic curve was required between segments. An accurate measurement for the rotation at the top of the test pile was not obtained; therefore, another condition was selected to replace it. The displacement of the elastic curve was assumed to be zero at the depth where the lateral pressure equaled zero (9 ft from Fig. 10.21). This assumption, as presented in Ref. [41], ensured that p and y had the same sign. At the ground surface, displacement transducers provided an accurate measurement of the lateral displacement of the test pile; therefore, this displacement provided the other boundary condition. Figure 10.22 shows the final experimentally derived curves for the lateral displacement of the pile for three magnitudes of applied lateral load at the top of the test pile. Note that the curves predict a small amount of lateral movement at a depth of 17 ft.

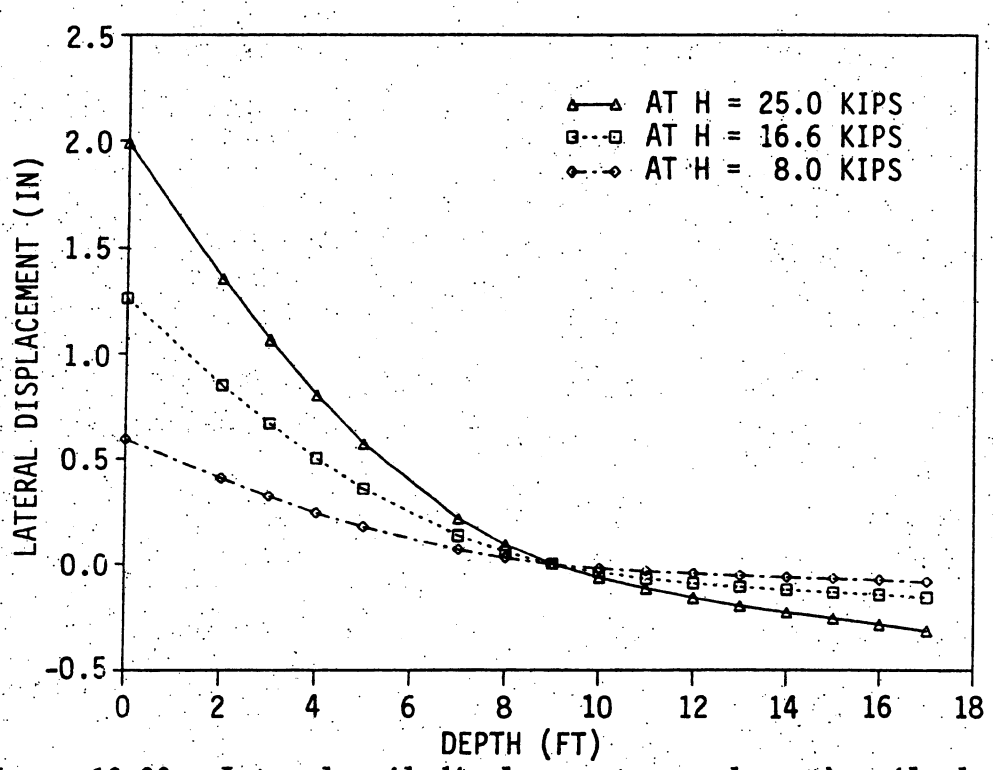

Figure 10.22. Lateral soil displacement, y, along the pile length for lateral load test.

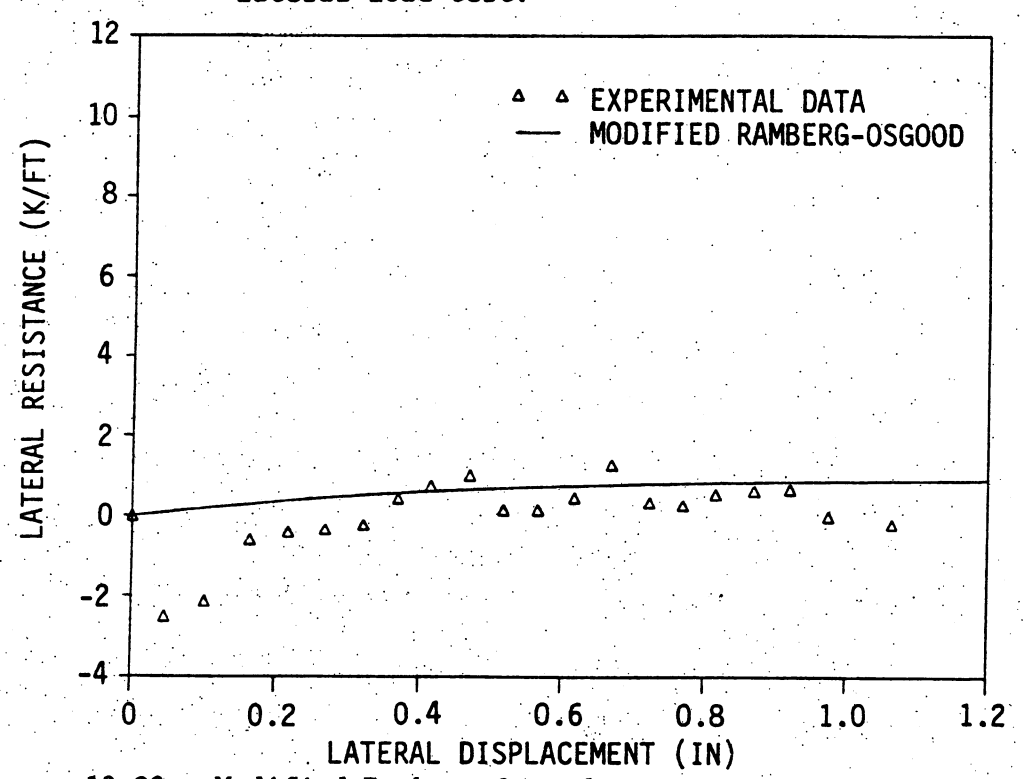

Figure 10.23. Modified Ramberg-Osgood p-y curve at 3.0 ft depth for lateral load test.

Since this motion probably did not occur, this calculated movement is an indication of the amount of experimental and/or data reduction error.

Twenty-one experimentally established p-y data point pairs at depths of 3, 4, and 5 ft are shown in Figs. 10.23-10.25, respectively. Each data point was developed for a different magnitude of lateral load applied at the top of the pile. Initially, at each strain gage station (except for the first and last stations), a least squares curve fit for the modified Ramberg-Osgood expression given by Eq. (3.8) in Section 3.3.3 was attempted. Since the lateral displacements induced during the lateral load test only partially developed the full lateral soil resistance response, the least squares curve-fitting technique produced unreasonable values for the maximum lateral soil resistance, p_u, and for the displacement, y_u, shown in Fig. 2.2. To develop a more realistic expression for the soil response, a visual curve-fitting approach for the modified Ramberg-Osgood curve was performed. The maximum soil resistance, p_u, the initial soil stiffness, k_h, and the shape parameter, n, establish the p-y soil response function. The effect of the shape parameter on the soil resistance and displacement behavior is given in Fig. 2.3. For n equal to two, reasonable correlation between the experimentally establshed p-y data points and the shape of the non-linear soil response curve resulted at the 3-, 4-, and 5-ft soil depths. The soil parameters p_u and k_h for each curve were established by successive trials to provide reasonable correlation with the available experimental data. The visual curve-fitting procedure established the values at the three selected depths (3, 4, and 5 ft) for p_u and k_h shown in Figs. 10.26 and 10.27 for the lateral load test. For the

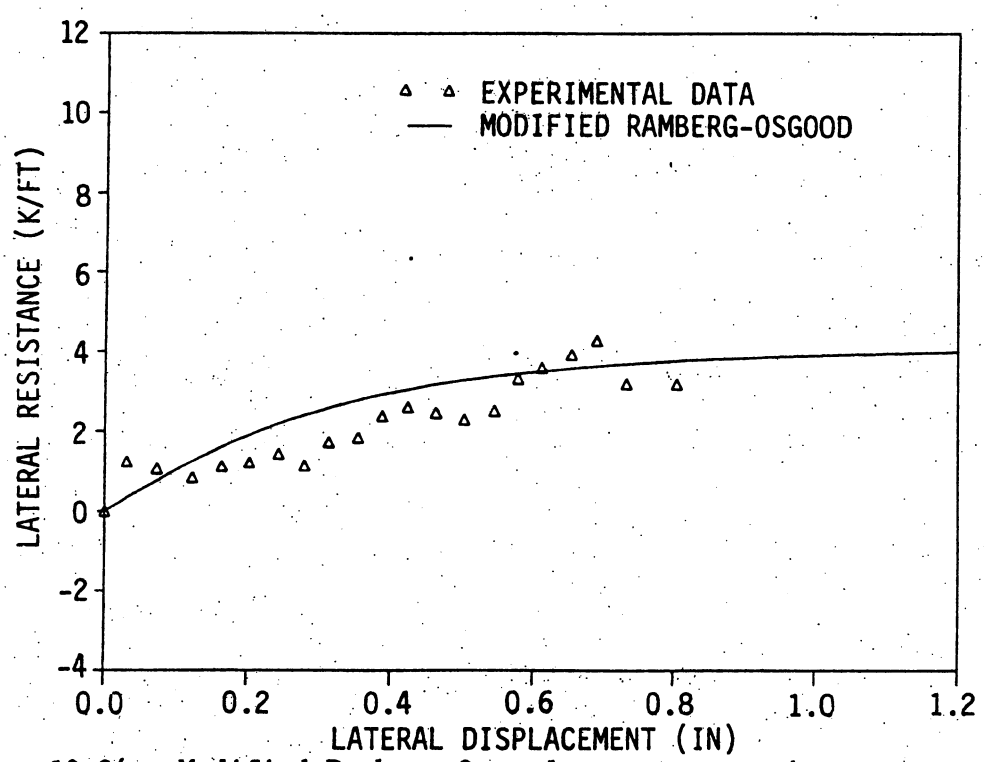

Figure 10.24. Modified Ramberg-Osgood p-y curve at 4.0 ft depth for lateral load test.

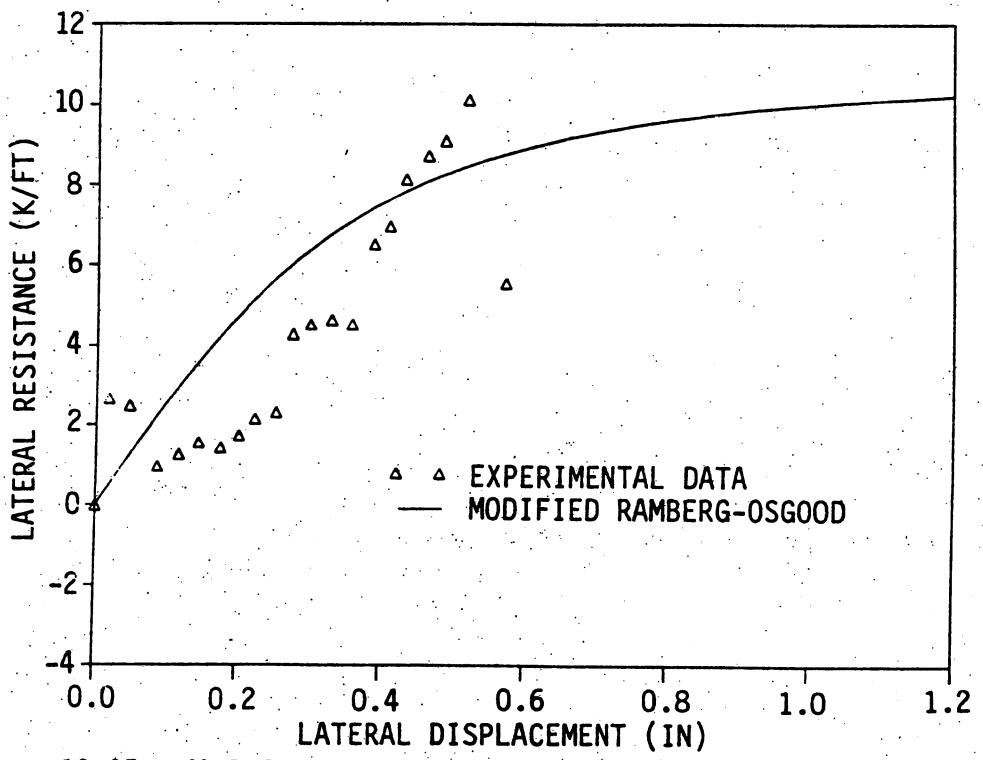

Figure 10.25. Modified Ramberg-Osgood p-y curve at 5.0 ft depth for lateral load test.

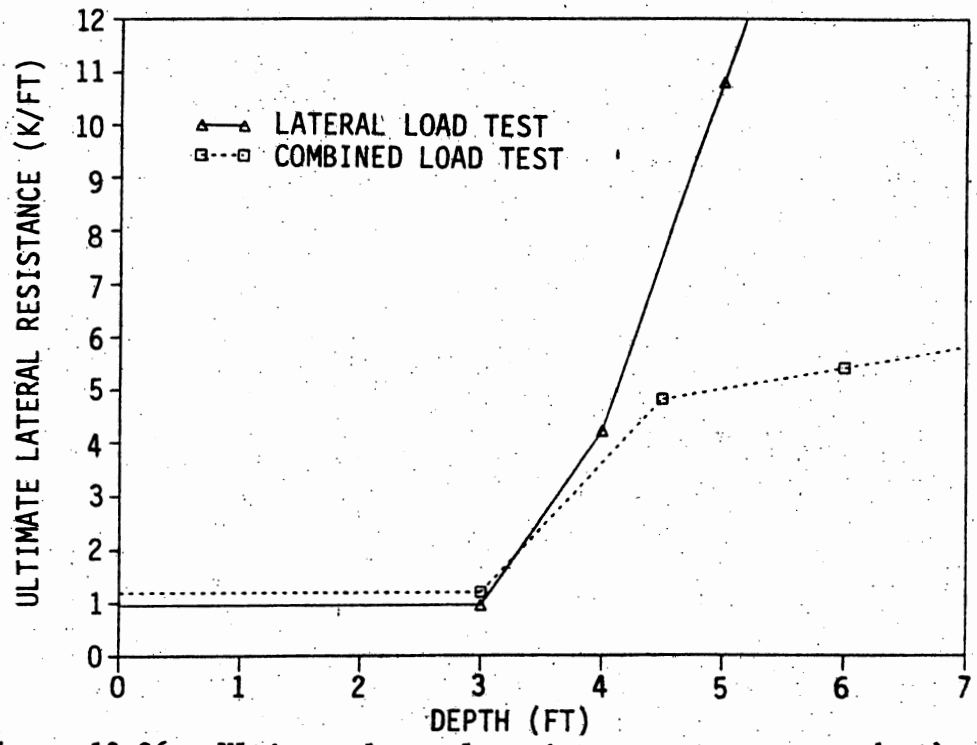

Figure 10.26. Ultimate lateral resistance, p_u, versus depth.

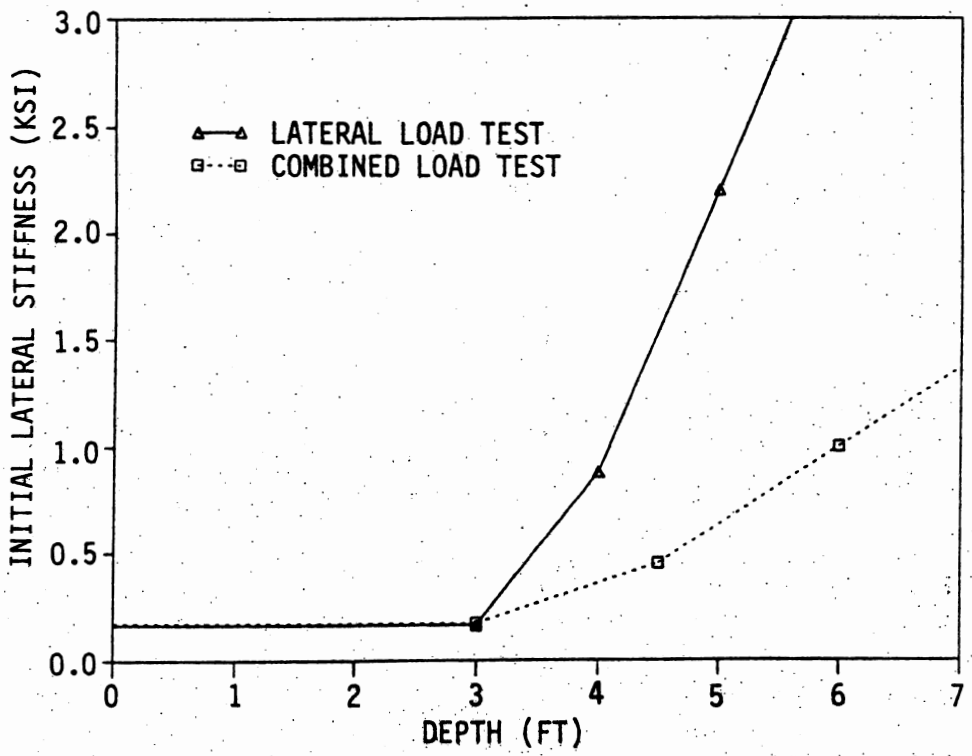

Figure 10.27. Initial lateral stiffness, k_h, versus depth.

first three feet of depth, these two soil parameters were considered to be constant. A linear variation in p_u and k_h was assumed to exist between the three specified depths. Between 5 ft and 10 ft depths, a linear extrapolation of the straight line beween the 4 ft and 5 ft depths was adopted to describe the soil initial stiffness and maximum resistance. Below a soil depth of 10 ft, p_u and k were asumed to be constant and equal to 43.8 k/ft and 8.80 ksi, respectively. Development of discrete experimentally derived soil behavior below a soil depth of 5 ft was not practical, since lateral soil displacements below that depth were small and dependent on an accurate location of the pile inflection point, as shown in Fig. 10.22. The correlation between the modified Ramberg-Osgood curves and the data points shown in Figs. 10.23-10.25 is probably as well as can be expected for results that involve double differentiation and double integration of functions established from curve-fitting techniques through experimentally obtained data.

An identical procedure was used to establish the p-y curves for the third field test with combined lateral and vertical loading. The resulting Ramberg-Osgood parameters p_u and k_h versus depth are illustrated in Figs. 10.26 and 10.27, respectively. The parameters are about the same as those for the lateral test within the first three feet below the surface. Beyond that depth, the strength and stiffness parameters for the combined load test are significantly below those of the lateral test, with maximum values for p_u and k_h at a depth of 10 ft established as 7.0 k/in. and 2.47 ksi, respectively. This difference is attributed to the direction that the pile is moving through the soil. In the combined load test, the pile was bent about its weak

axis. The edges of the flanges and only a portion of the web developed the passive soil pressure as the pile displaced laterally, since a gap between the pile and the soil developed along both sides of the web as the pile was driven. The existance of the steel shoes attached to the test piles to protect the strain gage conduits also reduced the amount of soil contact along the web. In the lateral load test, the test pile was bent about its strong axis, causing the entire face of the flange to develop the passive soil pressure as the pile was moved laterally. These observations suggest that the lateral strength and stiffness will be less for weak axis bending.

The soil resistance and displacement behavior at depths of 3 ft, 4-1/2 ft, and 6 ft for the combined load test are shown in Figs. 10.28, 10.29, and 10.30, respectively. These figures show the experimental p-y data points and the modified Ramberg-Osgood curves that were developed by the visual curve-fitting approach previously described. The first 12 data points were obtained from the lateral load phase of the combined load test. As discussed in Section 3.2.7, after completion of the lateral load sequence, a test malfunction caused a complete loss of lateral load. Data points 13 through 16 represent the soil behavior during reapplication of the lateral load. The effect on the soil resistance and displacement caused by the application of vertical load on the laterally displaced pile is illustrated by data points 16-32. Data point 32 correlates to the maximum applied vertical load of 280 kips. Vertical unloading of the test pile occurred between data points 32 and 36, and the lateral load was removed between data points 36 and 40.

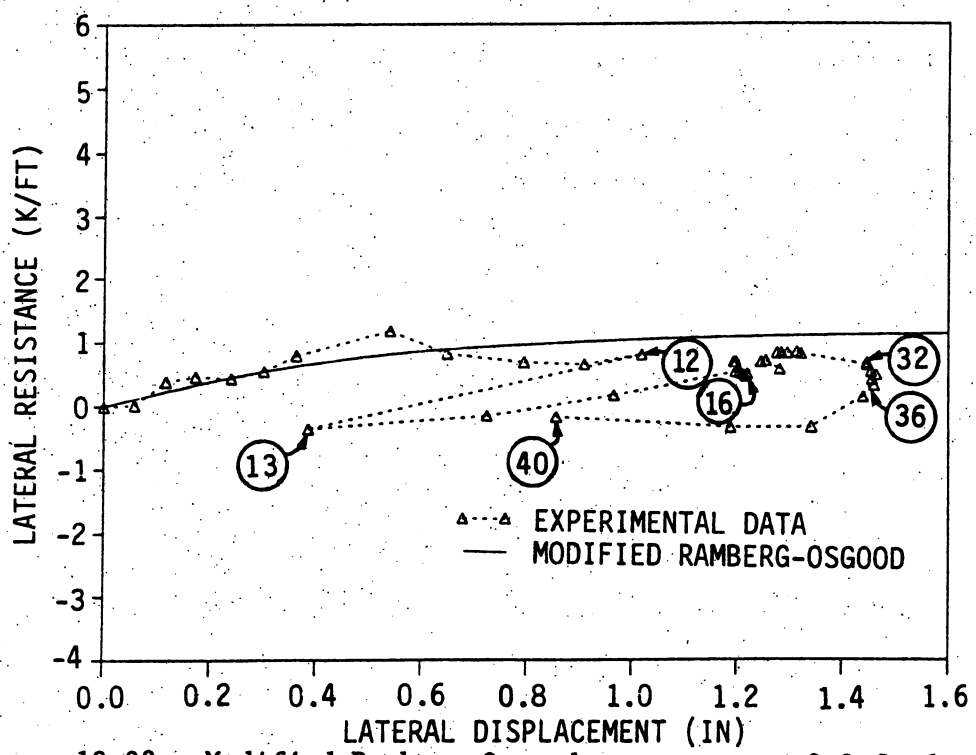

Figure 10.28. Modified Ramberg-Osgood p-y curve at 3.0 ft depth for combined load test.

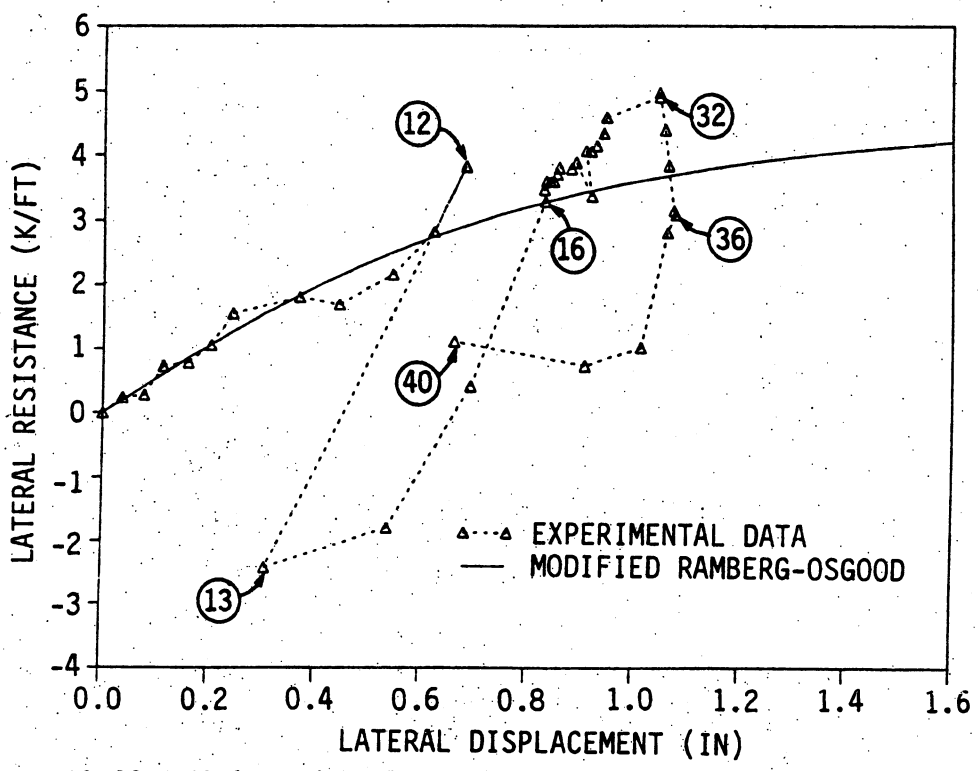

Figure 10.29. Modified Ramberg-Osgood p-y curve at 4.5 ft depth for combined load test.

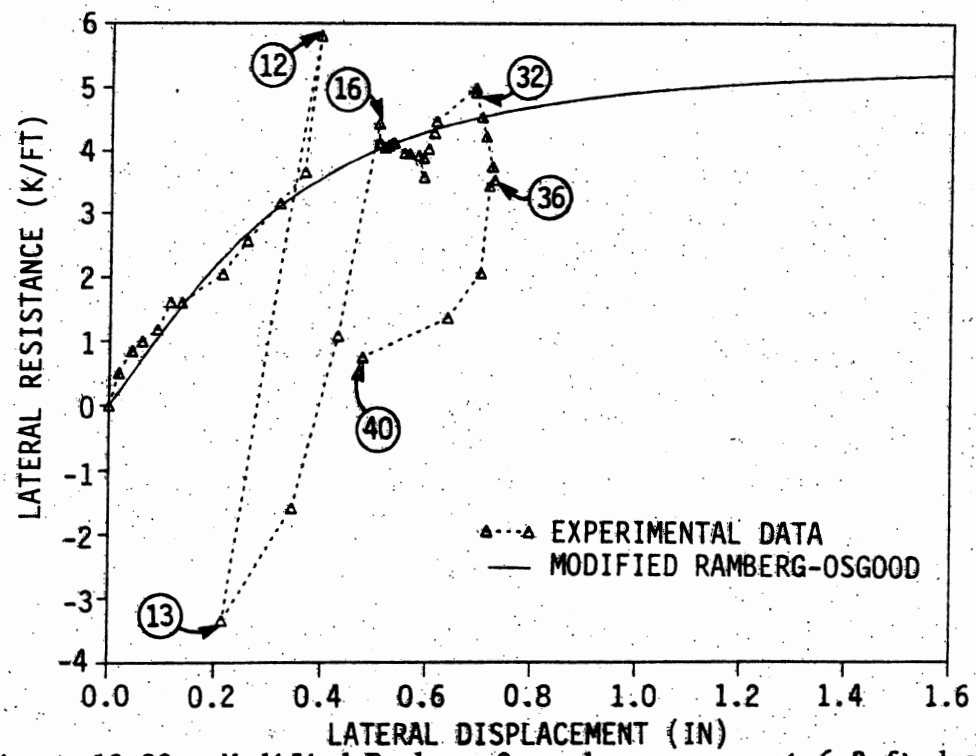

Figure 10.30. Modified Ramberg-Osgood p-y curve at 6.0 ft depth for combined load test.

11. APPENDIX B: MODEL PILE DEVELOPMENT AND TEST PROGRAM

11.1. Development

11.1.1. Model Scale and Components

Scaling of relevant model quantities for a static geotechnical system, in accordance with the Buckingham PI Theory [27,42,43], requires the selection of two independent quantities from which scaling relationships for all the other quantities can be derived. The two independent quantities normally selected are length and stress, with the scaling factor for stress normally set equal to one so that more direct comparisons can be made between a model and a prototype. In a static geotechnical system, time is not a relevant quantity. This condition would exist with rapidly dissipating or nonexistent soil pore pressures. When length and stress are the independent quantities, the scaling relationships of a static model that must be satisfied for complete similitude between a model and prototype are given in Table 11.1. All scaling factors, except the scaling factors for stress and strain that are equal to unity, can be expressed as powers of the length scale factor, K.

The most significant departure from the scaling relationships in the model involved the material densities. The density of all material in the model should have been increased by a factor of 1/K, that is, if the length scaling factor is equal to 1/10, the densities of the model components should be increased by a factor of ten. Density scaling is important since the in-situ vertical and lateral soil pressures are dependent upon the unit weight of the soil. Therefore, complete

similitude of a prototype soil would require increasing the unit weight of the model soil. If complete similitude is required in a model, a centrifuge is often utilized to artificially increase the unit weight of all materials [27].

The objective of a model test program determines whether complete similitude is necessary. The objective of the model tests in this research program was to study the relative behavior of a piling structure in a variety of soil mediums. The structural elements and soil mediums selected for the model were not intended to simulate any particular structure or soil condition. For the scaling relationships listed in Table 11.1, length, stress, and strain were selected as the primary quantities. The other quantities were considered to be secondary. Since model test results were compared with other model test results having the same scale, the effects of omitting density scaling will not be important. Also, model test results were compared with analytical studies that used actual geometric and material properties existing in the models. As long as the same parameters are used for all comparisons between experimental results and analytical models, exact similitude is not required.

A scaling factor equal to 1/10 was selected as a basis for development of the model components. The two most significant components of the scale model tests are the pile and the soil medium. A 1-in.-square by 60-in.-long tube was selected as the pile model. The prototype for the model was an HP10 × 42 that has a nominal flange width of 10 in. and a nominal depth of 10 in. The thickness of the tube was chosen with regard to strain sensitivity requirements for each test type

Table 11.1. Scaling relationships.

Scaled Quantity	Scale Factor
Length	K
Stress	1
Strain	1
Force	K^2
Area	K^2
Volume	K^3
Moment of inertia	K^4
Bending moment	K^3
Density	1/K

rather than to completely model the prototype. A tube wall thickness of 0.125 in. and 0.075 in. (14 gage) were used in the preliminary lateral load tests. These thicknesses allowed large lateral displacements without inducing yielding of the cross section. On subsequent vertical, lateral, and combined load tests, a tube wall thickness of 0.032 in. (21 gage) was used to improve the sensitivity of the axial and bending strains and yet to avoid local buckling of the cross section during vertical end bearing tests. The tube sections with 0.125 in. and 0.075 in. wall thicknesses had a yield stress of 36 ksi, while the 0.032 in. wall thickness tube sections had a yield stress of 75 ksi. The modulus of elasticity of steel was set equal to 29,000 ksi. To facilitate the connection between the test pile and the testing apparatus, a small 1-in.-thick square plate was welded to the top of the pile. For those model piles used in the end bearing tests, a plate was welded to the pile tip to distribute the reaction at the bottom of the test bin.

A fine, uniformly graded, masonry sand was selected for the model soil. A uniform soil was selected to minimize particle size segregation during sand placement. The gradation of the sand, shown in Fig. 11.1, indicates a maximum particle diameter of 1/16 in. The angle of internal friction, ϕ, determined by direct shear tests on dry sample of dense sand, was found to be equal to 34°. The instability of the loose sand soil structure prevented determination of the internal friction angle by conventional direct shear methods; therefore, ϕ could not be established for loose sand. In-situ soil densities were determined for each pile test as described in Section 11.1.2.

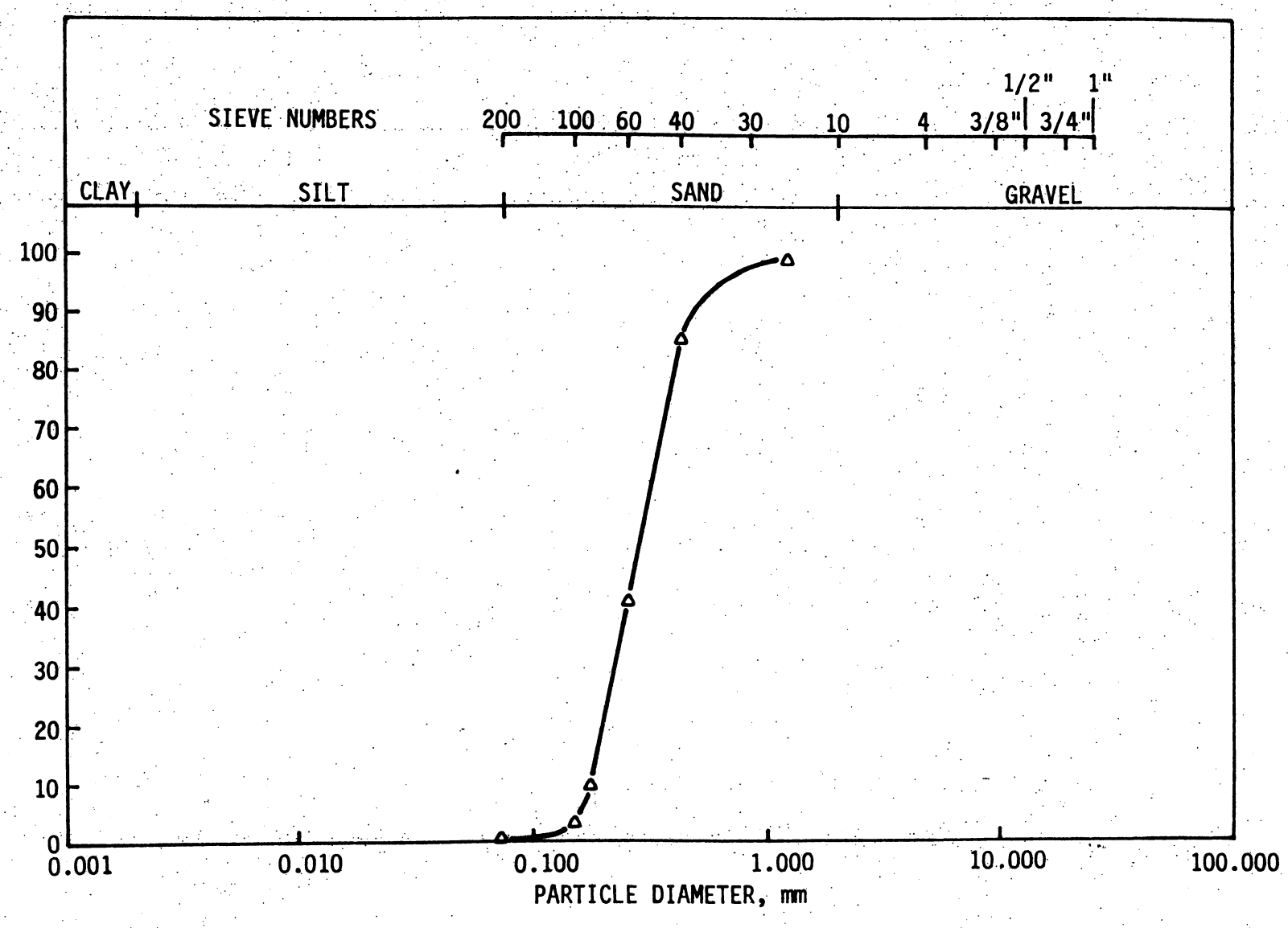

Figure 11.1. Partical size distribution curve for model pile tests.

The dimensions for the soil test bin were determined by preliminary model pile tests that investigated the influence of the soil bin sides and bottom on the behavior of the sand. This zone of soil movement was documented radiographically by Saglamer [44]. To establish the plan dimensions for the soil bin, observations of surface sand movements during lateral load pile tests were used to estimate the zone of influence of the pile. To determine the depth for the soil bin, vertical load pile tests were conducted. With the pile tip located at a specified distance above the bottom of the test bin, the pile was pushed 6 in. vertically through the sand medium. If the pile tip was located 15 in. above the bottom of the test bin, no noticeable increase in soil stiffness was detected as the pile was pushed downward. The size of the soil test bin was selected to provide 24 pile diameters clearance between the pile and the bin in the horizontal passive direction, 9 pile diameters clearance in the horizontal active direction, and 12 pile diameters clearance in the vertical direction beneath the tip of the friction piles. These dimensions were determined to be adequate to minimize the influence of the soil boundary on the behavior of the pile-soil model. Applying these clearances, the soil bin dimensions became 3-ft long, 1.5-ft wide, and 6-ft tall. The location of the pile in the soil bin is shown in Fig. 11.2.

The test set-up procedure consisted of positioning the pile in the empty soil bin and placing the soil medium around the pile. This procedure was adopted to avoid possible inconsistencies produced by driving or pushing the pile into the soil medium. The test program required the development of a soil placement technique that would provide

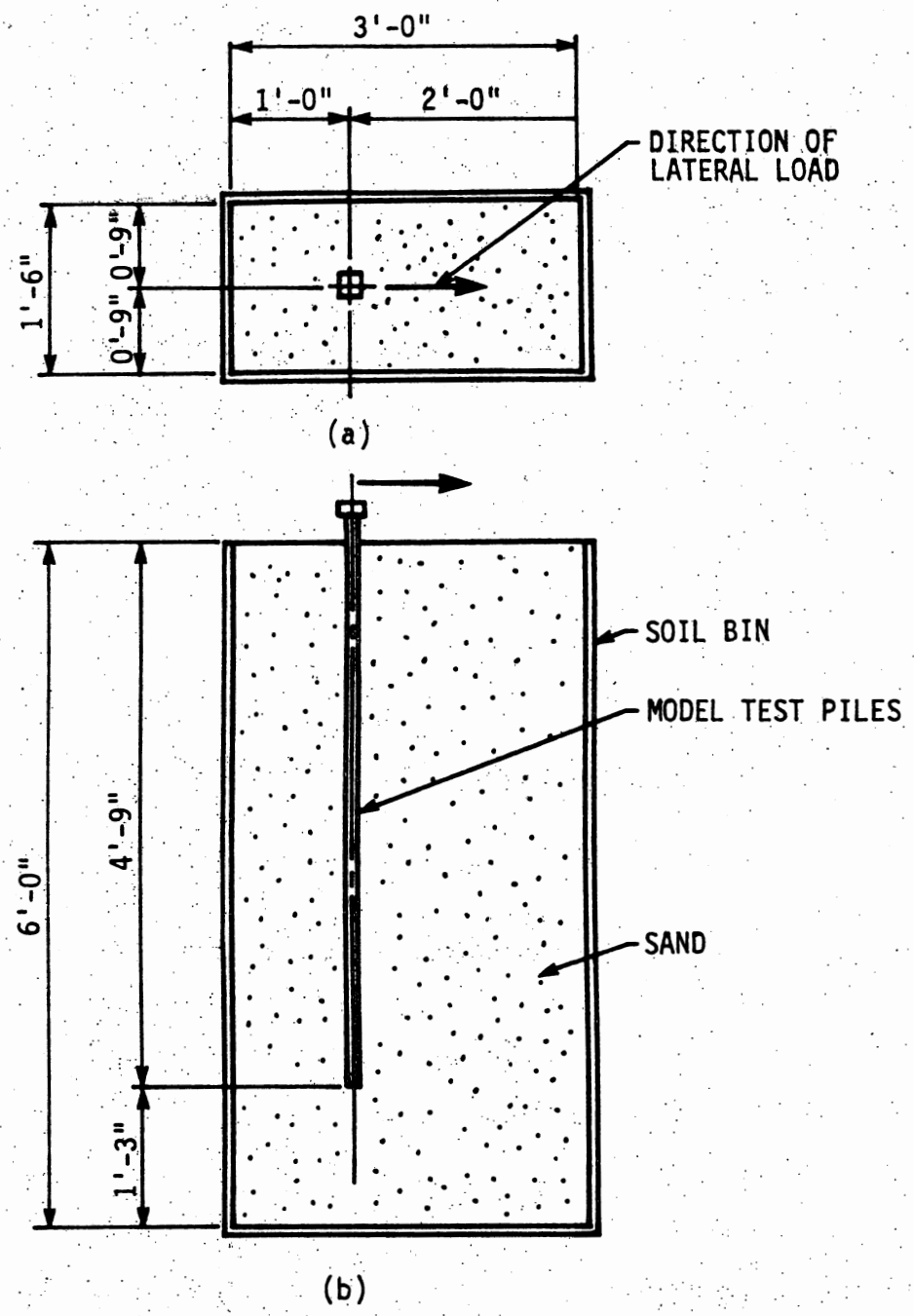

Figure 11.2. Model test pile location in the soil bin (a) plan view. (b) cross section.

a soil structure that could be duplicated without significant variation in soil density and soil friction angle within each soil layer for each test series. The soil structure was generated by utilizing a variation of the raining technique [27]: successively releasing a known quantity of sand, approximately 450 lbs, through a screen from a holding tank positioned on the top of the bin. The floor of the holding tank was hinged to provide a controlled deposition of each soil lift from a fixed position. After the sand fell into the bin, any surface irregularities were smoothed manually. Two opposite sides of the test bin contained windows that provided a view of the soil lift surface to assist the estimating of the soil density at six levels of the bin. The density for each 1 ft was based on an average soil height at the sides of the bin. The accuracy of any soil layer density was dependent upon the accuracy of the smoothing operation and the soil height markings on the window in the bin wall. Since the layer heights were typically between 10 in. and 12 in., a measuring error of 0.5 in. could result in a layer density error of ±5%. A loose sand density weighing between 90 pcf and 95 pcf was experimentally obtained with this approach.

A dense sand structure was formed when a concrete vibrator was placed against the outside face of the bin walls to vibrate the soil bin until the height of the lifts no longer decreased. By vibrating the bin, the sand consolidated fairly evenly with the surface of the sand dropping uniformly across the bin. A dense sand density weighing between 100 pcf and 105 pcf was obtained with this vibration technique.

11.1.2. Framework

The vertical load test framework, shown on the left half of Fig. 11.3, consisted of a self-contained structure constructed with structural angles and structural tubing. The framework was designed to apply vertical load at the top of each model test pile and to support the soil bin during soil dumping operations. Two double angle vertical legs supported the vertical load spreader beam and served as a tension tie to transfer the vertical load reaction to the support frame beneath the soil bin. Diagonal bracing stabilized these vertical uprights and limited lateral deformation of the soil bin occurred during the lateral load tests. Neoprene rubber pads were placed beneath the support framework to provide a flexible foundation for the soil bin when the bin was vibrated for consolidation and to provide a larger coefficient of sliding friction between the framework and the smooth concrete floor for the lateral load test. Lifting brackets mounted on the support framework were used to lift the frame and bin for dumping the soil into a transfer bin after a pile test was completed. A chute on the bottom bin was used to drain the sand from the test bin to the transfer bin.

The vertical load was applied to each model test pile by a screw mechanism, which was driven with a variable speed electric motor, acting through a torque multiplier. A schematic of the vertical load mechanism is shown in Fig. 11.3. The shaft transferring the load to the pile head was braced laterally to prevent any misalignment at the pile head. Bracing was also attached to the top of the test pile by the lateral load beam that was anchored to a lateral load frame. A roller assembly attached to the vertical frame uprights guided the test pile to prevent

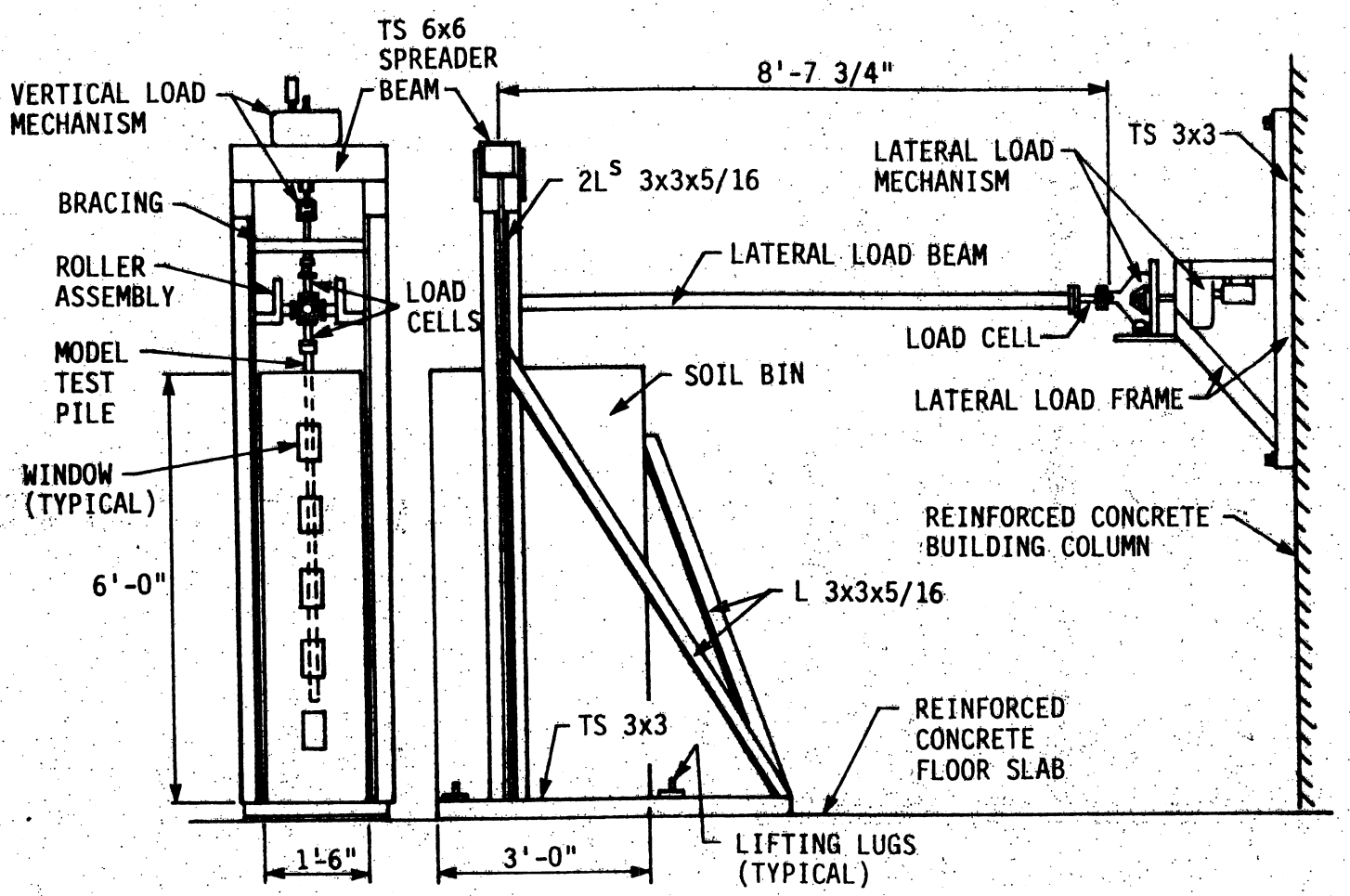

Figure 11.3. Vertical and lateral frameworks for model pile tests.

lateral movement of the pile transverse to the lateral load beam. The bracing system prevented lateral movement of the pile head and permitted relatively free vertical motion.

The lateral reaction frame, shown on the right half of Fig. 11.3, consisted of structural angles and structural tubing. The framework was mounted to a building column in a wall of the Structural Research Laboratory. The framework resisted the lateral load applied to the top of each model test pile and supported the lateral displacement drive mechanism. The framework was designed to be independent from the vertical framework and soil bin. A lateral load beam connected the drive mechanism to the pile head.

The lateral load beams were designed to provide rotational boundary conditions at the top of each test pile and to simulate a bridge superstructure. By applying lateral displacements and measuring the forces at the right end of the lateral load beam, the joint conditions at the pile head can be defined. The analytical model, IAB2D, was utilized to determine the moment of inertia of the lateral load beam that was required to simulate pile head rotations approaching a pinned-head or a fixed-head pile condition. A 1/2-in.-square bar was selected to approximate a pinned-head pile condition, and a standard 2-in.-diameter structural pipe was selected to approximate a fixed-head pile condition. Since the beams were loaded in tension during the lateral load pile tests, there was no need for lateral support to prevent buckling. The lateral load beams were bolted to the pile head using four 3/8-in.-diameter bolts that clamped the plate that was welded to the top of pile to a plate welded to the lateral load beams.

Static sliding friction forces between the vertical framework supporting the soil bin, the neoprene rubber pads, and the smooth concrete floor resisted the lateral load applied to the pile. Since the maximum lateral loads were approximately 250 lbs and the soil bin, and framework weighed approximately 3500 lbs, sliding or overturning of the soil bin was prevented.

The lateral load drive mechanism used to create the lateral displacements at the test pile head was the same mechanism used to generate vertical loads. The torque multiplier and electric drive motor, supported by the lateral load framework, turned a 1-in.-diameter threaded rod that was connected through a yoke device to the lateral load beam.

11.1.3. Pile Instrumentation

The model test piles were instrumented with electrical resistance strain gages along their length, as shown in Fig. 11.4, to record total strains induced by the applied test loads. Four different gage spacing patterns were used to obtain the distribution of the pile strains. Gage Pattern 1 was used for the preliminary model tests. The final vertical load, lateral load, and combined load tests were performed with Gage Pattern 2. The end-bearing pile tests were conducted with Gage Patterns 3 and 4 for the vertical load tests and combined load tests, respectively. The spacings of the gages for the laterally loaded piles were based on pile strain variations noted in the literature [44-48] and on the results obtained from analyses performed with IAB2D.

Strain gages were placed on two opposite, outside surfaces of the model piles with their electrical lead wires positioned inside the tube.

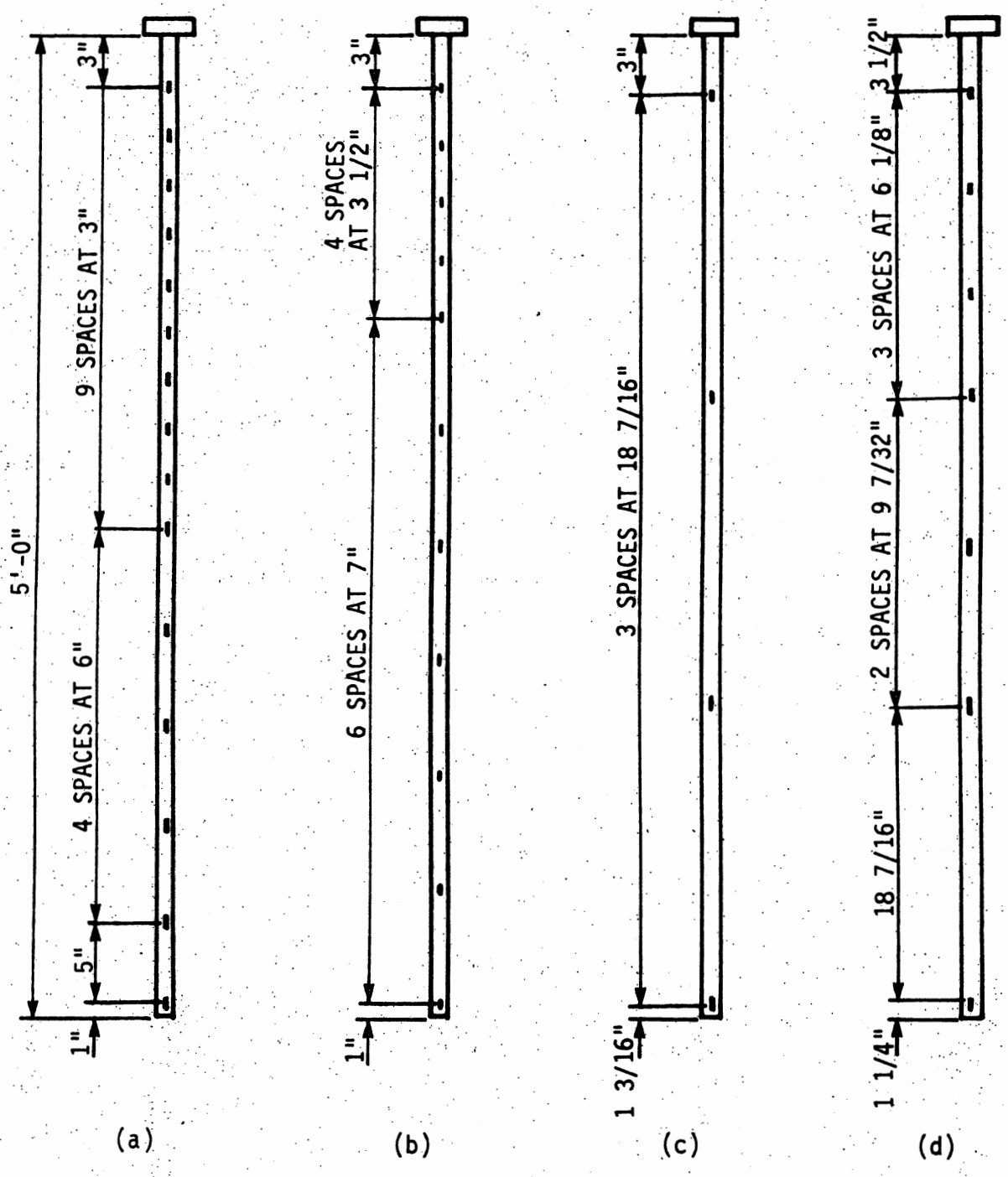

Figure 11.4. Strain gage locations for the model test piles: (a) gage pattern 1 (b) gage pattern 2 (c) gage pattern 3 (d) gage pattern 4.

Small diameter holes were drilled through the tube wall at each strain gage location to connect the gages to the lead wires. Since two gages were positioned on opposite sides of a cross section, bending moment and axial strains could be resolved from the strain information.

To protect the gages, an epoxy coating that cured to a hard smooth surface was used over each gage. The coatings covered an area approximately 1/4 in. by 1/2 in. and were typically 0.023-in. thick. The total coating area for all of the gages was approximately 2% of the total pile surface area exposed to the sand medium. The minimal effects of the protective gage coatings on the behavior of the pile were compensated for by using the same pile in all comparative tests.

A calibration test of each instrumented pile was conducted. Bending moments and axial loads were calculated from the pile strains using the elementary beam theory. These values were compared to the applied moments and axial loads. The calibration results revealed that the sight irregularities in the pile cross section and local stress concentrations at the lead wire holes did not produce significant errors in the calculated bending moments or axial loads at most of the strain gage locations. However, three gages on the combined load test model pile were adjusted by a calibration factor to match conventional beam theory.

11.2. Model Test Procedures

11.2.1. General Description

The scale model test program involved 40 pile tests. Eleven of these tests were analyzed and are reported herein, while the remaining tests established test apparatus design, testing procedures, soil and pile response, and geometric conditions. The objective of the test program was to determine experimentally the behavior of model test piles, subjected to vertical and/or lateral loads, in both loose and dense sands. The basic test parameters for the 11 reported model tests are given in Table 11.2. The test matrix contains four major parameter categories: (1) pile types (friction and end-bearing piles), (2) pile head types (fixed, pinned, abutment, and predrilled hole), (3) load types (vertical, lateral, combined, and lateral cyclic loads), and (4) soil types (loose and dense sand). Each row in Table 11.2 describes the parameters for each particular model test, for example, Test A-1 involved a pinned-head friction pile, embedded in loose sand, that was subjected to a vertically applied load. Seven test groups (A through G) were conducted and analyzed during the program. Test Type Nos. 1, 2, and 3 involved vertical load only, lateral load only, and combined loading, respectively. The combined load test contained two load phases. The first phase involved displacing the pile head laterally by applying a lateral load. The second phase, commencing after the pile head was displaced a specified amount, involved applying vertical load to the test pile while maintaining the lateral displacement at the pile head. The test matrix begins with pile models involving

Table 11.2. Test matrix for model piles.

Test Sequence		Pile Types		Pile Head Types				Load Types				Soil Types	
Test Group	Test Type	Friction Pile	End-Bearing Pile	Pinned Head	Fixed Head	Abutment	Predrilled Hole	Vertical Load	Lateral Load	Combined Load	Lateral Cyclic	Dense Sand	Loose Sand
A	1	x		x				x					x
	3	x		x						x			x
B	3	x			x					x		x	
C	2	x			x				x				x
	3	x			x					x			x
D	1	x			x		x	x				x	
	2	x			x		x		x			x	
	3	x			x		x			x		x	
E	3	x			x					x	x	x	
F	3	x			x	x				x		x	
G	3		x		x					x			x

simple head constraints and loading sequences and progresses toward more complex boundary conditions, such as the introduction of a predrilled hole or an abutment at the top of the pile. The pile head configurations for Test Groups A through E and G are shown in Fig. 11.5; and the configuration for Test F, involving the abutment, is shown in Fig. 11.6.

By minimizing, as much as possible, variations in soil properties due to soil placement procedures, the pile behavior induced by various load types could be investigated experimentally. The soil placement technique described in Section 11.1.1 was used to place the sand up to the elevation of the top strain gage. For the pile tests involving a predrilled hole (Test Sequence D), a 5-in.-diameter cylindrical tube was placed around the pile at the top to prevent soil contact along the upper eight inches of the length pile. For the pile tests involving an abutment (Test Sequence F), after the sand was placed up to the first strain gage station, the abutment and abutment wall assembly were mounted on the pile head and the back fill material, which was behind the abutment and wingwalls, was added by hand. A more thorough description of the test sequences is found in Sections 11.2.2 through 11.2.4.

11.2.2. Vertical Compression Tests

As shown in Fig. 11.7, vertical displacement of the pile head during the vertical load tests was measured with direct current displacement transducers (DCDTs) having a resolution of 0.001 in. Lateral movements of the pile head were minimized by bracing the top of the pile with the lateral load beam in one direction and with a bearing

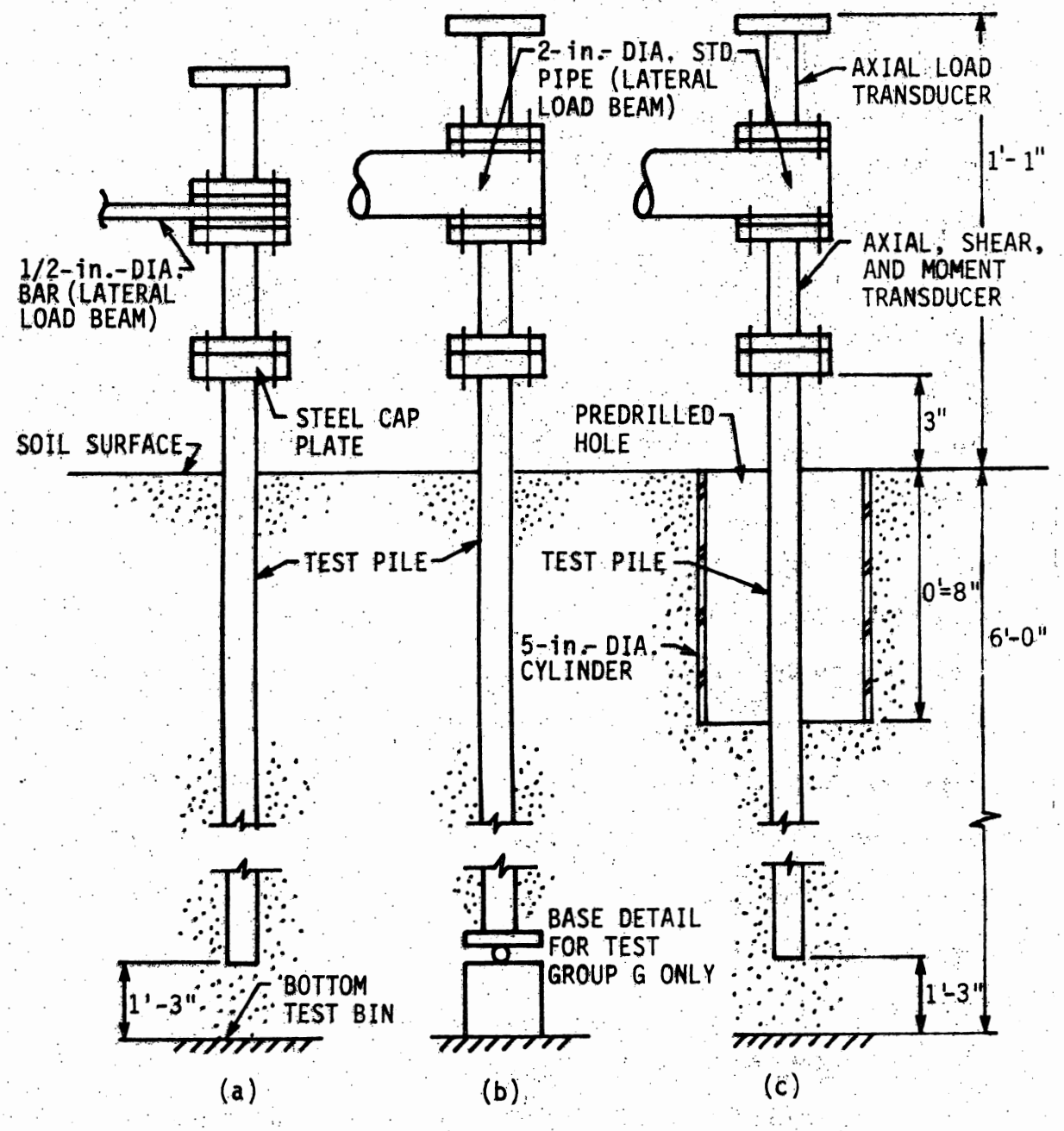

Figure 11.5. Pile head configurations for Test Groups A, B, C, D, E, and G: (a) test group A (b) test groups B, C, E, and G (c) test group D.

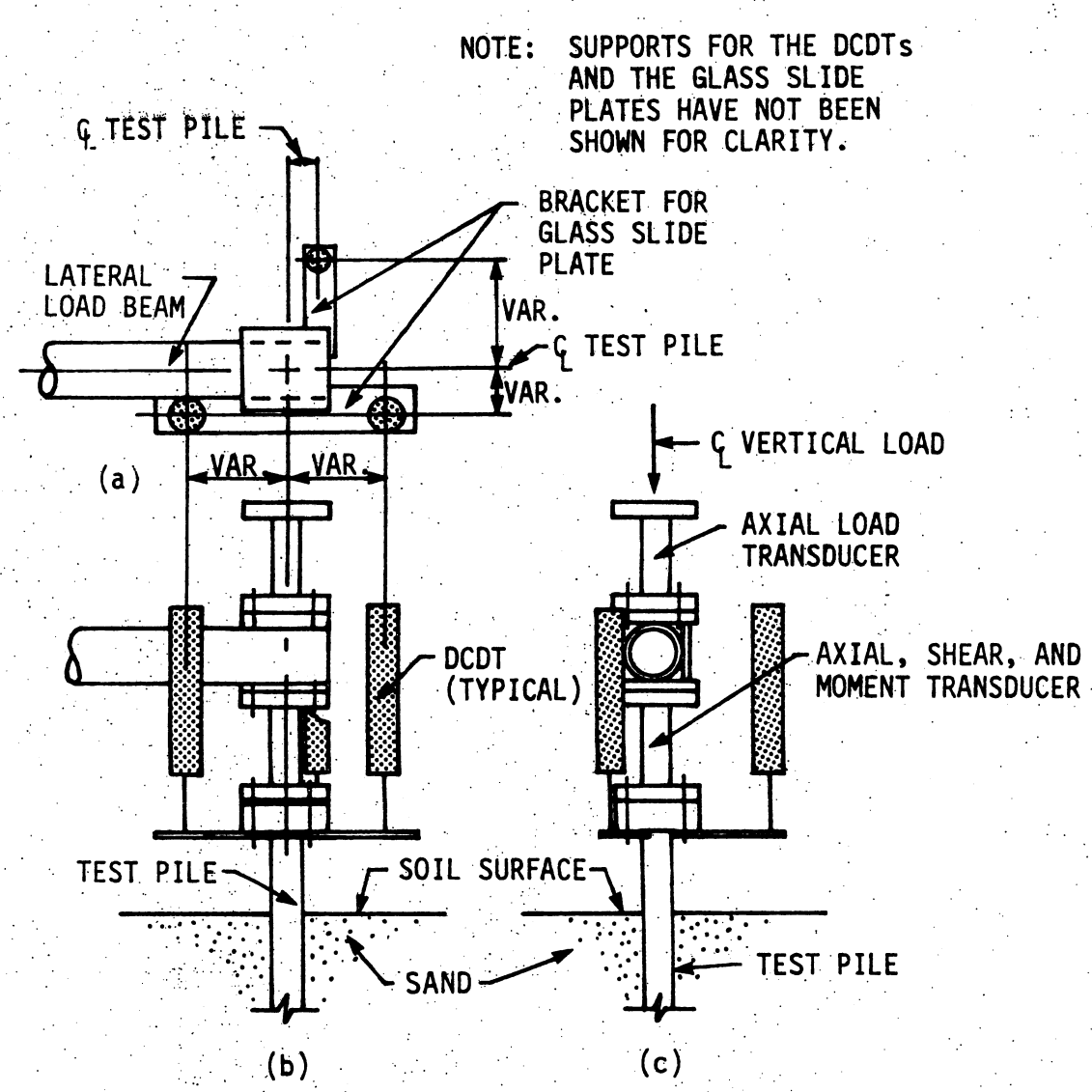

Figure 11.6. DCDT arrangement for vertical load tests: (a) plan view (b) side elevation (c) back elevation.

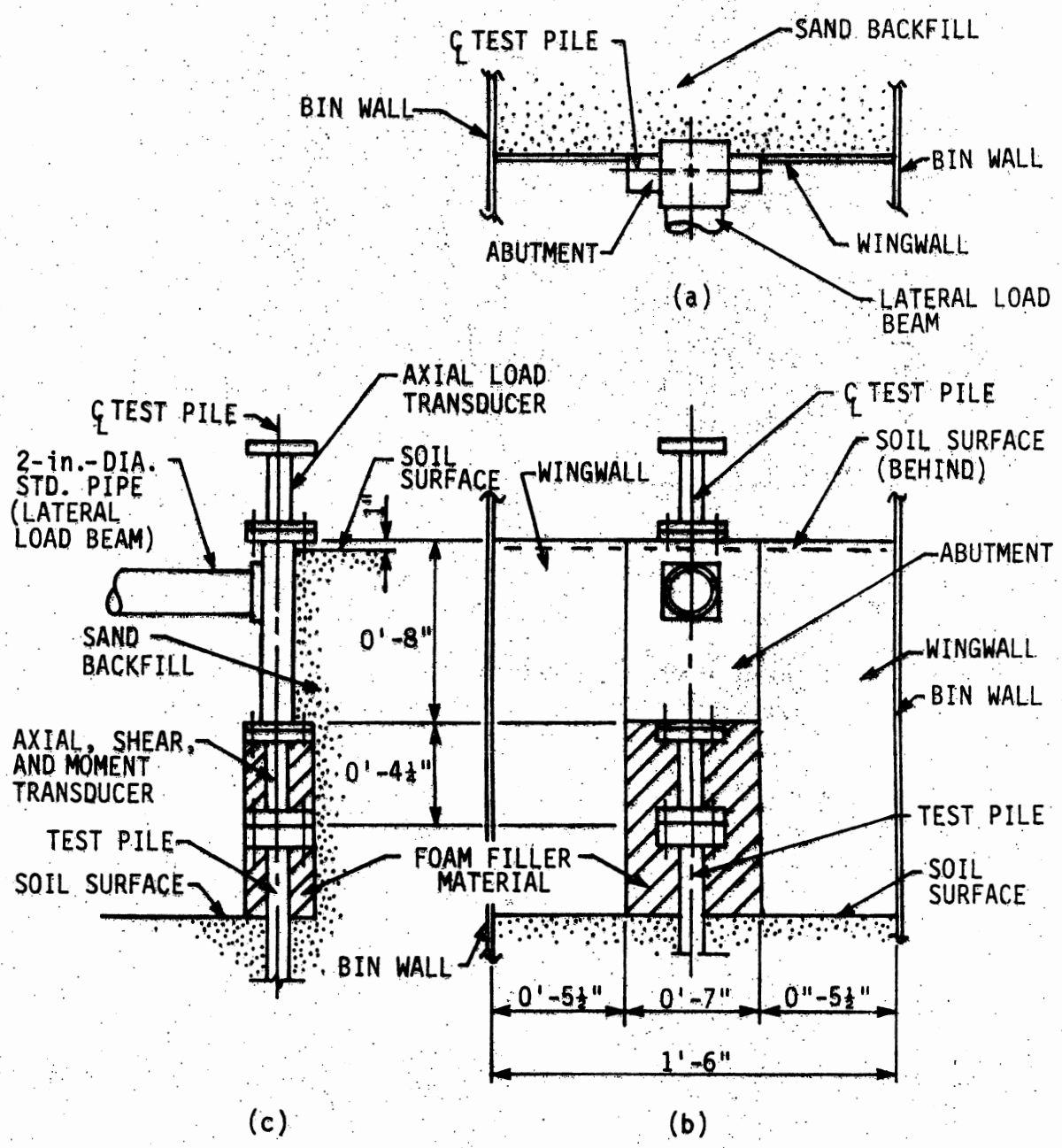

Figure 11.7. Pile head configuration for Test Group F: (a) plan view (b) front elevation (c) side elevation.

plate and roller assembly in the perpendicular direction, as shown in Fig. 11.3.

The vertical load was applied to the friction pile using a loading apparatus that provided a constant rate of vertical displacement. By using a mechanical displacement control loading mechanism rather than a load control device, test procedures would be more repeatable. The vertical displacement rate was established at 0.5 in./hr for all of the vertical load tests. The magnitude of the applied load was measured by a load transducer bolted to the plate at the top of the pile. The transducer was developed specifically for the model tests and had a sensitivity of ±2 lbs.

Data was recorded during the tests with a Hewlett-Packard Automatic Data Acquisition/Control System (DAS). The capabilities of this data acquisition system allowed the friction pile tests to be run continuously without stopping to record data. At a displacement rate of 0.5 in./hr, the DAS read all channels for a given displacement before the pile head had moved 0.006 in. The vertical load for the friction piles was applied until the load versus displacement plot for the test indicated that the ultimate capacity of the test pile was reached.

11.2.3. Lateral Load Tests

All of the lateral load tests were conducted using the same test procedures and test setup, except for the pile head conditions. The lateral displacement and rotation of the pile head were measured with displacement transducers. A bracket was mounted near the top of the pile to allow the transducers to monitor pile movement, with respect to the soil bin, at the soil surface. The arrangement of the transducers

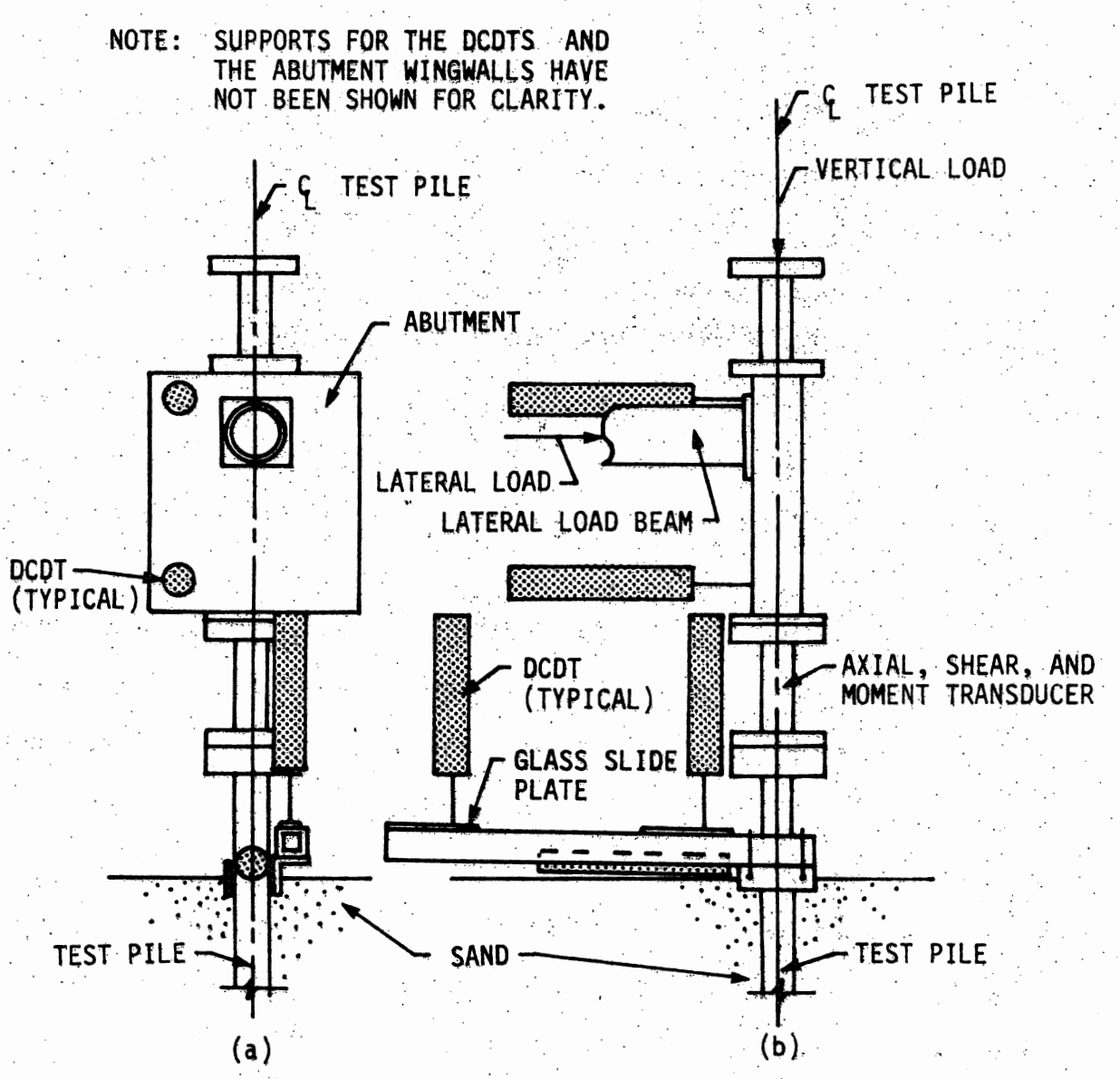

Figure 11.8. DCDT arrangement for pile test involving an abutment: (a) front elevation (b) side elevation.

for the lateral load tests is shown in Fig. 11.9. The lateral load required to induce the horizontal displacement of the pile head was measured by a load transducer located on the end of the lateral load beam next to the lateral load frame, as shown in Fig. 11.3. The load transducer measured the axial load, shear, and moment at the end of the lateral load beam next to the lateral load frame.

The lateral load tests were conducted under displacement control, rather than under load control; therefore, the pile head was displaced at a constant rate. The horizontal movement of the pile at the soil surface was measured with a displacement transducer. The displacement rate, established from preliminary tests, was approximately 1.0 in./hr for all of the lateral load tests. Preliminary tests conducted at other displacement rates of 0.5 in./hr and 2.0 in./hr and tests conducted with intermittant stops during these lateral load tests produced insignificant variations in pile behavior and capacity, suggesting that the displacement rate had a negligible effect on behavior. However, for consistency among the lateral load tests, a constant displacement rate was applied throughout the entire test.

The data collection control program for the data acquisition system was written to automatically collect and process the experimental data at predetermined displacement intervals. Except for the combined load tests, the model piles were displaced laterally until the maximum bending strains for the extreme fibers of the pile approached the yield strain. These lateral displacements permitted the measurement of pile strains to a maximum soil depth.

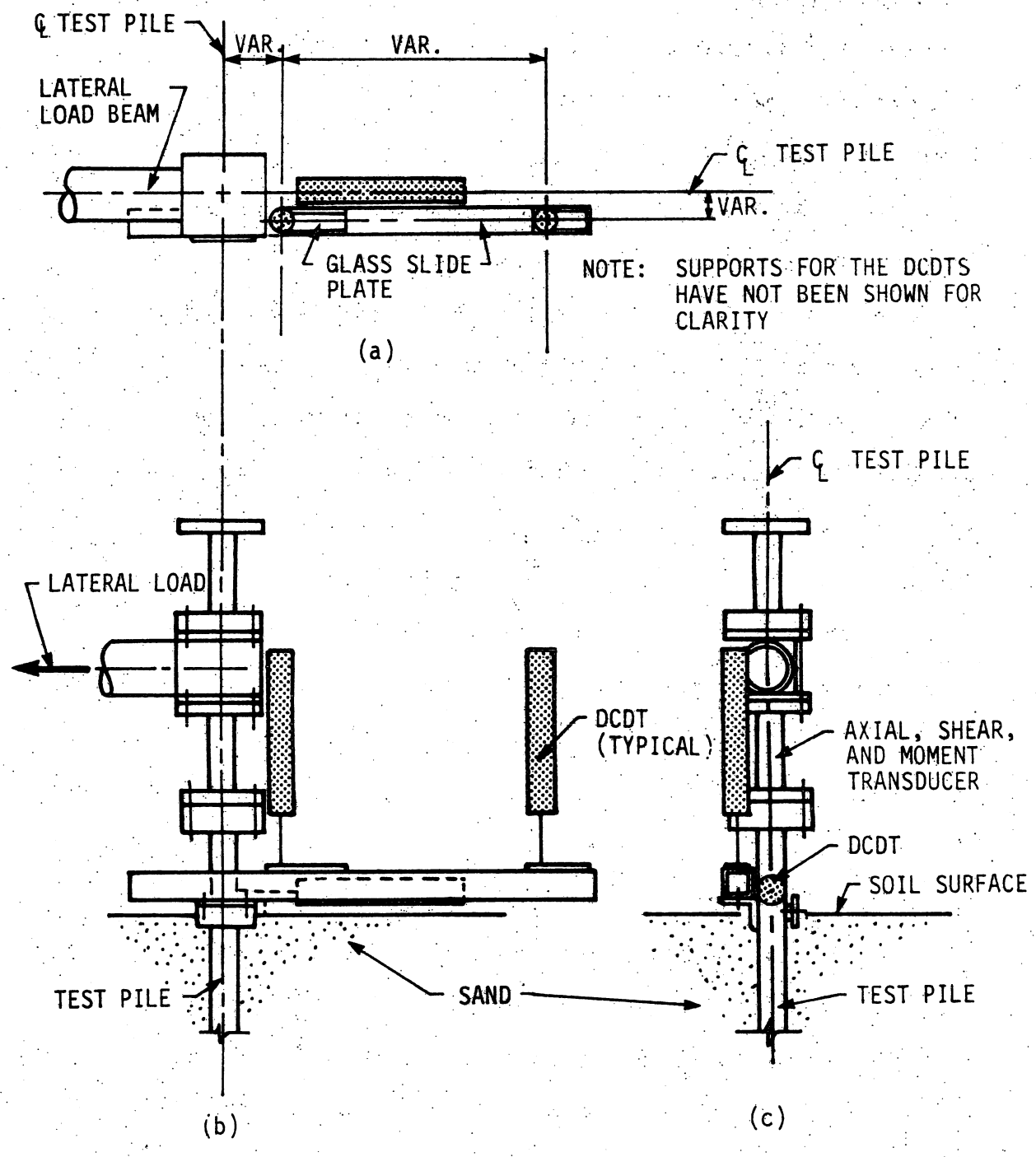

Figure 11.9. DCDT arrangement for lateral load tests: (a) plan view (b) side elevation (c) rear elevation.

For the lateral test involving a predrilled hole (Test Sequence D-2), the pile head displacement and rotation were measured at the location of the first pair of strain gages, rather than at the soil surface at the bottom of the predrilled hole. The test procedure for Test Sequence D-2 was the same as for the lateral load tests in Test Groups B and C.

11.2.4. Combined Load Tests

The combined load tests involved a lateral displacement phase and a vertical load phase. For consistency in the experimental program, the test preparation and loading procedures discussed in Section 11.2.3 for the lateral load tests were used for the first phase of the combined load tests. Before the vertical load was applied, the lateral displacement of the test pile head obtained at the completion of the lateral load phase was maintained by tightening a locking nut on the threaded rod at the lateral reaction frame (Fig. 11.3). The pile head was braced in the horizontal plane to provide proper alignment with the vertical load mechanism. A pin connection at the lateral load frame allowed the lateral load beam to rotate, as the test pile displaced vertically during the vertical load portion of these tests. A period of time elapsed between the two load phases, while the load mechanism was transferred from the lateral test frame to the vertical test frame. Previous preliminary tests conducted with a series of incremental displacements separated by time intervals indicated that the lateral load decreased by only a few pounds during the time intervals in which the lateral displacement was held constant. The vertical load was applied following the test procedures discussed in Section 11.2.2. The vertical load

phase of the combined load test was conducted until the ultimate pile capacity was obtained.

The lateral and vertical displacements and rotation of the pile head were monitored with displacement transducers. A combination of transducer arrangements that were used for the vertical load tests (Fig. 11.7) and lateral load tests (Fig. 11.9) was used in the combined load tests.

The preparation and testing for the first phase of the cyclic lateral load test (Test Sequence E-3) was conducted using the same procedures specified for Test Sequence B-2 with the exception that the lateral load was applied cyclically at a rate of 1.0 in./hr for both the loading and unloading portions of repeated load. The cyclic loading was terminated when a definite reduction in the lateral load resistance of the test pile, corresponding to the maximum lateral displacement, was observed. For this test, pile displacements, rotations, and strains were monitored at larger displacement intervals than for the other lateral tests, since the purpose for this test was to detect variations in pile capacity rather than to establish soil behavior characteristics. The lateral load beam, shown in Fig. 11.3, was braced against pile head movements perpendicular to the direction of the applied load to provide stability when the load beam was subjected to an axial compressive force.

Test Sequence F-3 involved combined loading of a fixed-headed test pile that had an abutment positioned on top of the pile. The abutment model was designed to represent a portion of a typical reinforced concrete bridge abutment containing one pile. Wingwalls were

placed on both sides of the abutment section to retain the backfill behind the abutment. A foam-rubber pad was placed at the bottom of the pile cap plate and abutment to prevent sand from flowing under the abutment and to minimize the amount of vertical load transferred in bearing between the abutment and the soil. Displacement instrumentation for this test consisted of DCDTs arranged to measure vertical settlement, lateral displacement, and rotation of the abutment and the pile head, as shown in Fig. 11.8. The movements of the pile head were measured at the soil surface. Load cells were positioned to measure the vertical and lateral load above the abutment. This test was conducted on the same test pile and soil medium that was used for Test Sequence F-1 (not reported herein), involving only axial loading. After the axial load test for the pile was completed, the instrumentation was reinitialized and the combined load test procedure was initiated. The test procedures for this test were similar to those used in the other combined load tests, except that for this test, a compressive force applied to the lateral load beam rather than a tension force. The abutment was displaced until the total lateral displacement at the pile head was approximately 0.5 in.. This lateral displacement was maintained as a vertical load was applied to the top of the abutment, directly above the test pile.

A vertical load test on a horizontally displaced end-bearing model test pile in loose sand was performed as Test Sequence G-3. Test Sequence G-3 differed from the friction pile tests in the following areas: (1) pile tip condition, (2) loading mechanism, and (3) test procedure. The end-bearing pile was positioned to bear directly against a

steel block and ball bearing spacer assembly that was inserted between the bottom of the pile and the floor of the test bin, as shown in Fig. 11.5. This pile tip condition was used to model an end-bearing pile condition. The lateral load phase of this combined load test was conducted with the testing procedures described for Test Sequences A-3 through E-3. The vertical load phase involved an application of vertical load by load control rather than by displacement control, since the end-bearing tests involved very small vertical displacements and relatively high loads. The load control test was conducted by applying increments of vertical load. For each load point, the load was held while all readings of displacement, load, and strain were recorded. The load was incremented until a significant change in the vertical displacement or rotation of the pile head was detected. Undamaged piles were used again, while damaged piles were either discarded or salvaged by cutting off the damaged areas and rewelding the bearing block to the pile tip. Vertical load increments of 400 lb were applied until the test pile buckled.

11.3. Model Test Data Reduction and Development of Soil Characteristics

11.3.1. Experimental Pile Strains

The model pile test experimental strain data, obtained from the electrical resistance strain gages, was analyzed using the data reduction techniques developed for the field test, as described in Section 10.3.1. An initial data censoring study was performed to verify the accuracy of the pile strains for all of the tests. The study involved

plotting the measured total pile strains versus pile depth for each magnitude of applied load at the pile head. Erratic or inconsistent strain measurements became evident and the associated gage was eliminated from the analysis. The second strain gage station from the top of the pile was determined to be unreliable; therefore, the strain data at this location was not included in the test evaluations.

The strain gages measured the total pile strain, ε, at the gage location. This strain included the axial strain, ε_o, induced by the applied axial load, and the bending strain, ε_b, caused by the applied bending moment. The strain gages were mounted on opposite pile faces and in the plane of uniaxial bending for the pile; therefore, the total strain at any point can be written as

$$\varepsilon = \varepsilon_o \pm \varepsilon_b \tag{11.1}$$

Since only two strain gages were placed at each specific location, the loss of any gage resulted in the loss of the entire strain gage station.

11.3.2. Experimental f-z Curves

Strain data from two vertical model pile tests and five combined tests provided experimental data to establish the relationship for the vertical skin friction force, f, and the relative vertical displacement, z, between the pile and the soil at various points along the pile lengths for each of the seven tests shown in Table 11.2. Data for the two tests involving only axial compressive loads (Test Sequences A-1 and D-1) were reduced utilizing the same procedures developed for the field test and described in Section 10.3.2.

The experimental data for the five combined load tests (Test Sequences A-3, B-3, C-3, D-3, and E-3) required additional censoring of the top six strain gage locations. The lateral displacement of the pile head in the first phase of the combined loading induced high bending strains in the top portion of the test pile. The algebric sum of the strains for the two gages implied that a significant axial force existed in the pile when vertical loads had not, in fact, been applied. This occurred because the total pile strains were large and primarily bending. Hence, a small error in the measured strain produced a small error in the computed bending strain but, unfortunately, a large error in the computed axial strain. The measured strain data could not be corrected for the upper portion of the model pile. Below a depth of about 35 in., where the bending strains were low, the axial strains could be accurately determined from the total measured strains. Therefore, the strain gages in the upper portion of the pile were not used to evaluate the f-z soil behavior.

Figure 11.10 shows the axial force in the test pile at the soil surface and at several depths at and below 35 in. for the vertical load phase of the five combined load tests. The axial force at the soil surface was calculated as the difference between two load cell measurements. The first load cell which was used to monitor the vertically applied loads was located above the lateral load beam, as shown in Fig. 11.3. The reaction at the end of the lateral load beam was measured by the second load cell. The axial pile forces in the lower portion of the pile length were computed from the measured strains. As illustrated in Fig. 11.10, the difference between the calculated

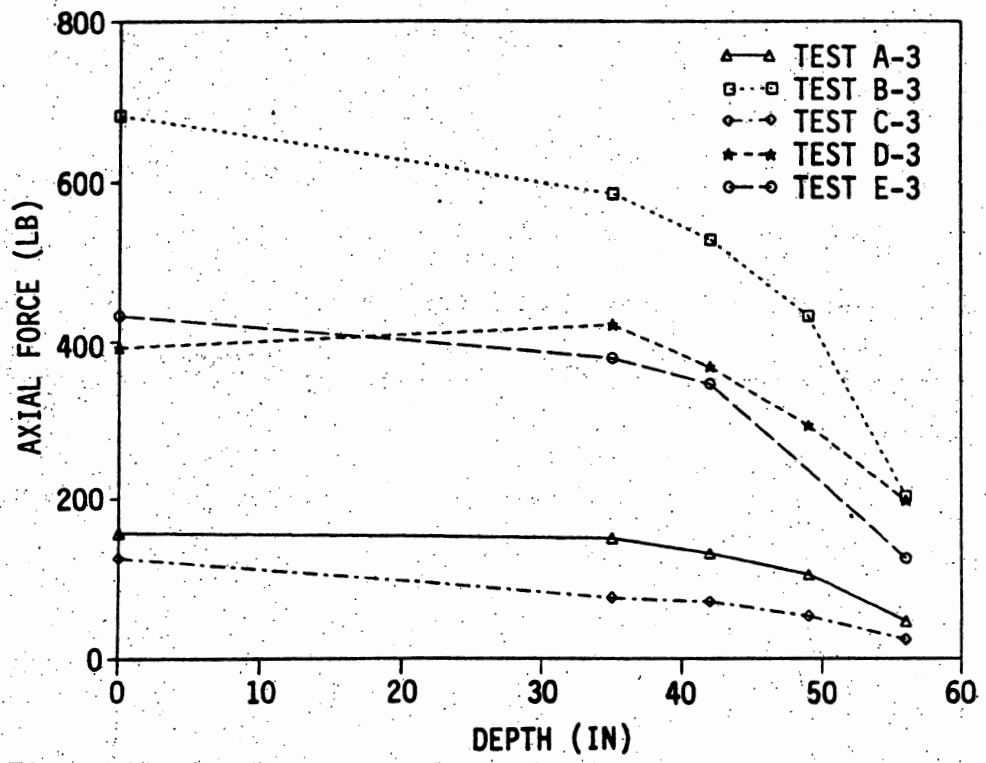

Figure 11.10. Experimental axial force in pile for combined load pile tests.

axial pile force at the soil surface and at a depth of 35 in. was less than 15 lb for four of the five combined load tests, indicating that only a small amount of load was transferred to the soil for the upper 35 in. of the test pile. Therefore, the vertical frictional resistance for the upper portion of the test pile was small, since the model pile was initially displaced laterally during the first phase of the combined load test.

A five point curve fitting technique, involving the least squares method, was used to determine the variation of frictional force along the pile. Quadratic functions provided the best curve fit through each set of five experimentally obtained axial pile strain data points, two on each side of a particular gage station, except at the second gage location from the ends of the test pile, where only three data points were used for the curve fit. Each quadratic expression for the axial pile strains was differentiated once and the resulting expression was evaluated and substituted into Eq. (10.6) to obtain the vertical skin friction resistance. The relative vertical displacement at each particular gage location was established from Eq. (10.8), where the integral of the axial pile strain function was approximated as the area under the curve formed by connecting the strain data points with straight line segments.

The resulting f-z data point pairs were plotted for each strain gage location. Figure 11.11 shows the results for the vertical soil resistance and relative vertical displacement at four selected depth locations for the second phase of Test Sequence A-3. The data points have been connected with straight lines to graphically illustrate the

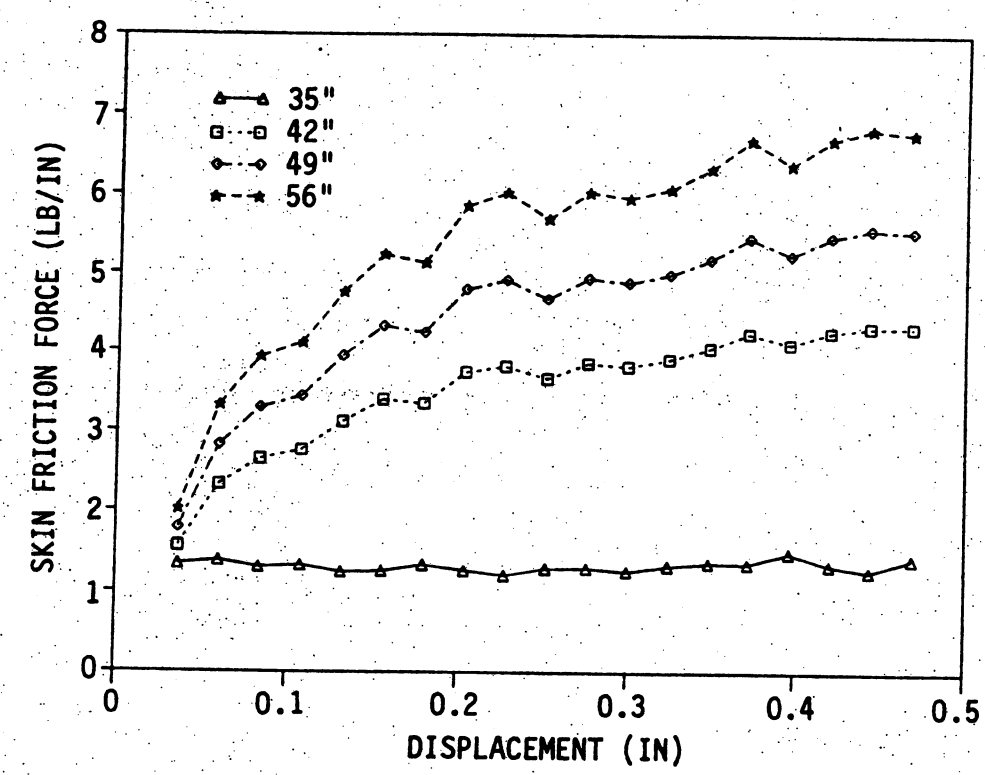

Figure 11.11. Several f-z curves for the vertical load phase of Test Sequence A-3.

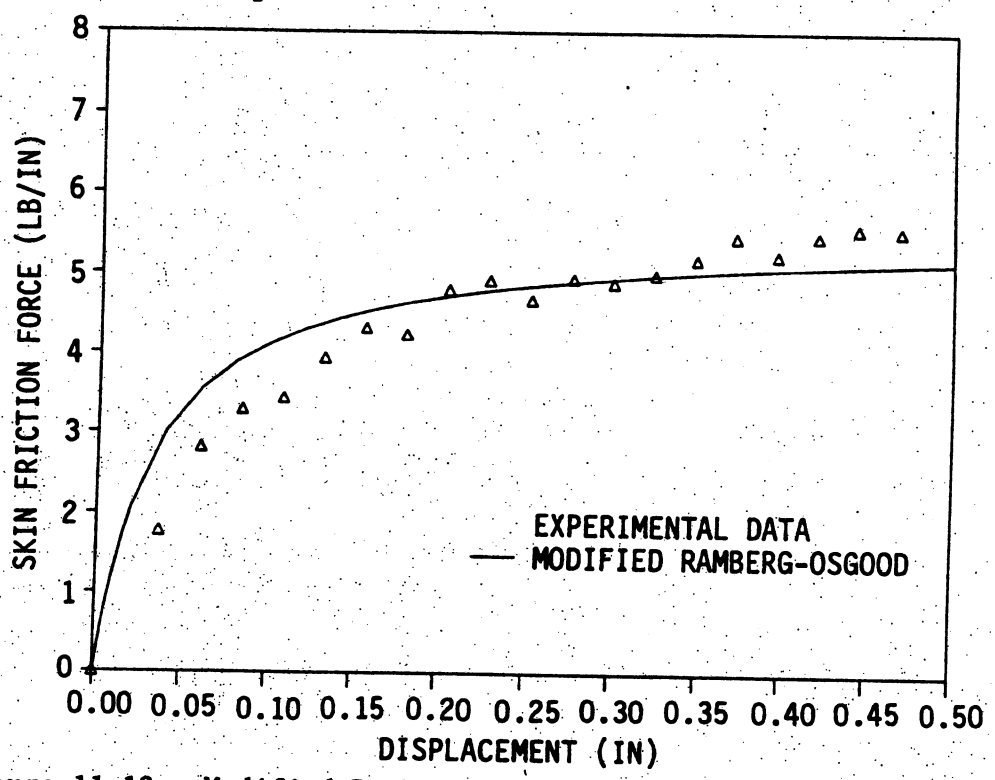

Figure 11.12. Modified Ramberg-Osgood f-z curve at 49 in. depth for the vertical load phase of Test Sequence A-3.

variation in the experimental data. For each of the monitored depths a modified Ramberg-Osgood expression (Eq. (3.2)), having a shape parameter, n, equal to unity was selected by a visual fit of the f-z data point pairs. Figure 11.12 shows the modified Ramberg-Osgood curve established for the gage station at 49 in. below the soil surface for the second phase of Test Sequence A-3. The curve parameters describing the maximum friction force, f_{max}, and initial vertical stiffness, k_v, were established at each appropriate strain gage station. The magnitudes of f_{max} and k_v are shown in Figs. 11.13 and 11.14, respectively, for Test Sequences A-1, A-3, and C-3 that were conducted in loose sand, while Figs. 11.15 and 11.16 show the magnitudes of these parameters for Test Sequences B-3, D-3, and E-3 that were conducted in dense sand. The magnitudes of Test Sequence D-1 are not shown because n was assumed equal to 0.75 instead of 1.0. The straight line segments shown in Figs. 11.13 through 11.16 represent a visual, best fit, multi-linear relationship for f_{max} and k_v versus soil depth. These linearized soil parameters were required to model the soil behavior for the analytical model, IAB2D.

11.3.3. Experimental q-z Curves

The development of the nonlinear soil response describing the relationship between bearing stress, q, and the pile tip settlement, z, involved a much simpler technique than the approach required for the field test data. The pile strains near the tip of the model test piles were available in the laboratory tests; therefore, the pile axial force at approximately 1 in. from the pile tip was known for each magnitude of applied axial load at the top of the pile. Assuming that the axial force at the last strain gage station equaled the bearing force

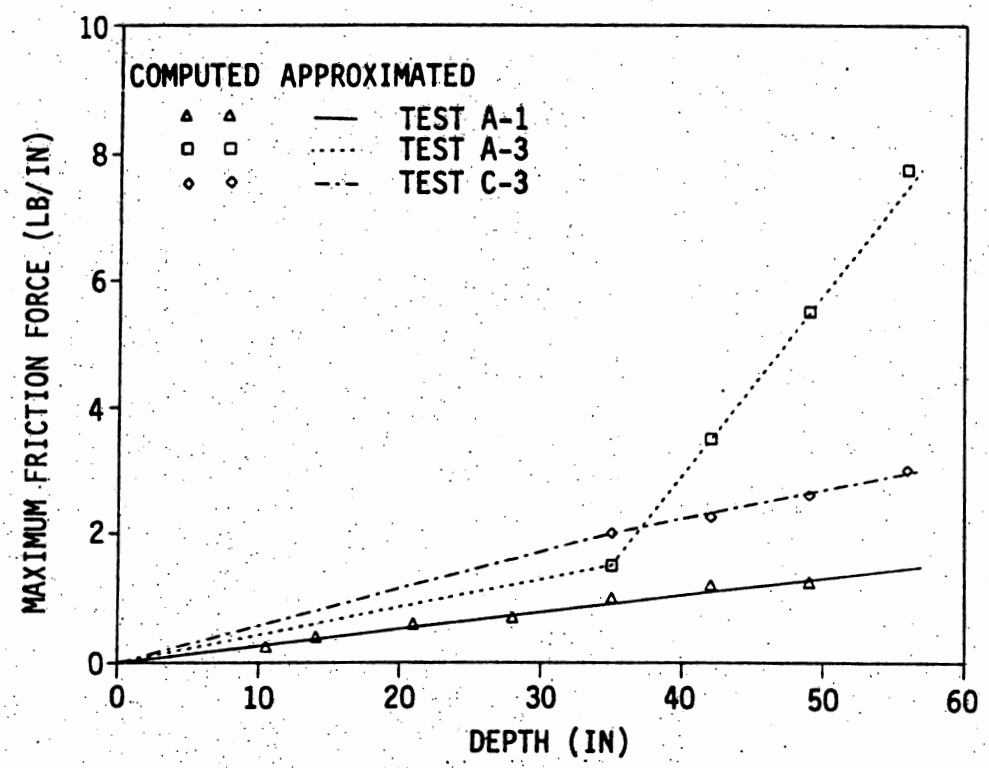

Figure 11.13. Maximum skin friction force, f_{max}, versus depth for vertical load tests in loose sand.

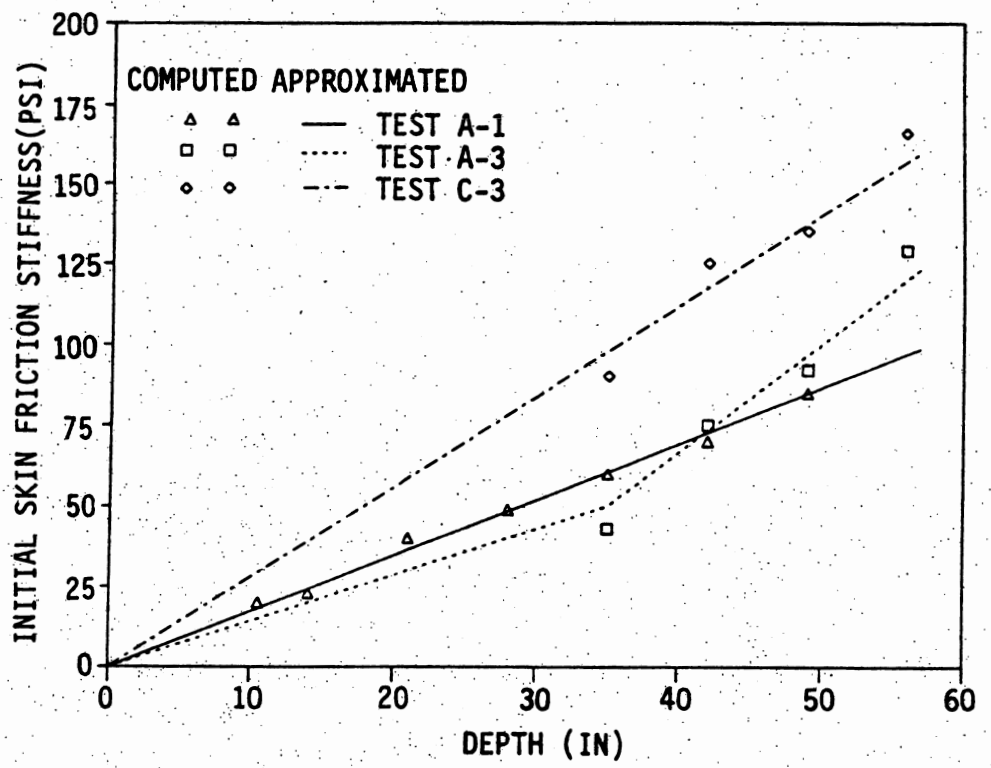

Figure 11.14. Initial skin friction stiffness, k_v, versus depth for vertical load tests in loose sand.

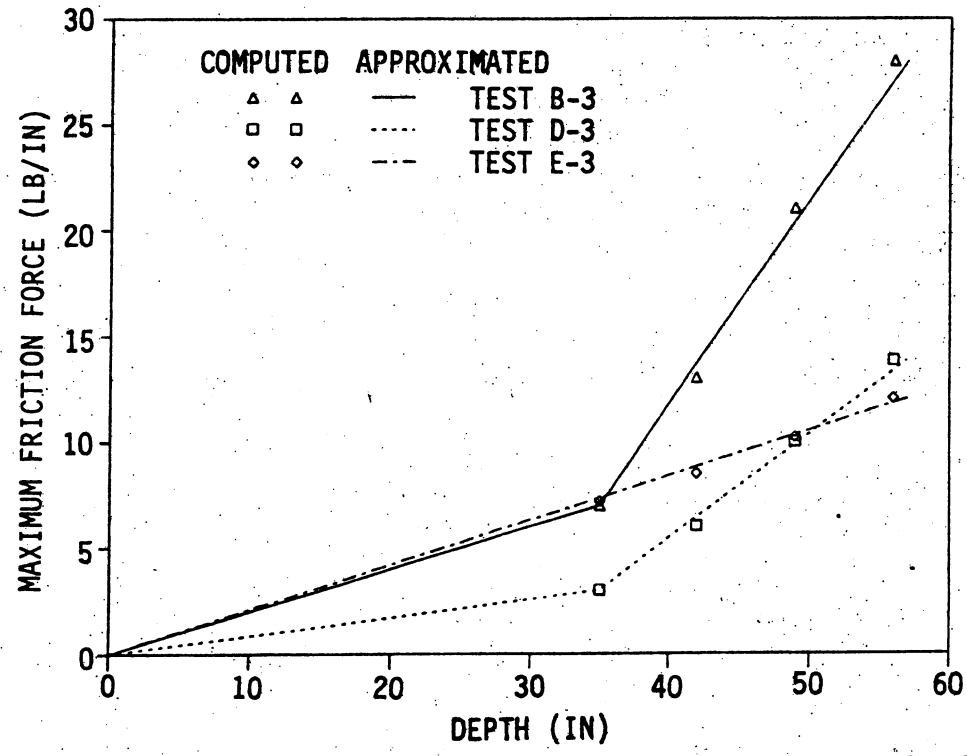

Figure 11.15. Maximum skin friction force, f_{max}, versus depth for vertical load tests in dense sand.

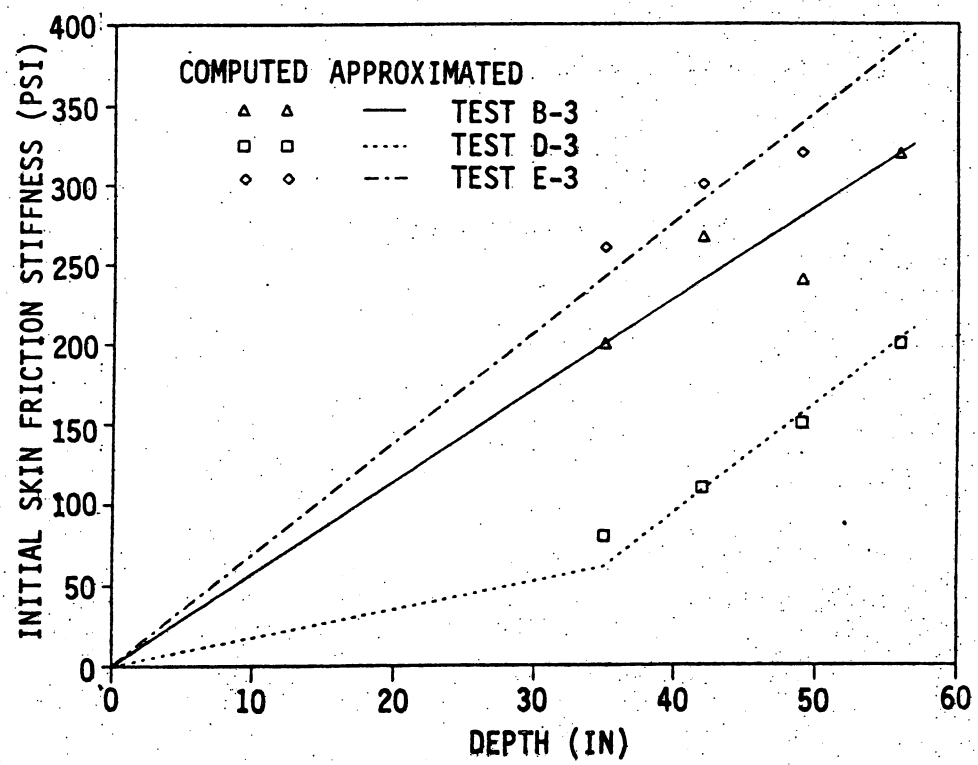

Figure 11.16. Initial skin friction stiffness, k_v, versus depth for vertical load tests in dense sand.

at the pile tip and knowing the axial strain distribution along the pile length, the bearing stress and pile tip displacement were determined. A representative q-z response (Test Sequence C-3) is shown in Fig. 11.17. The modified Ramberg-Osgood curve (Eq. (3.4)) shown was obtained by curve fitting techniques. For the seven test sequences conducted, a summary of the calculated soil parameters for the maximum bearing stress, q_{max}, initial point stiffness, k_q, and shape parameter, n, is given in Table 11.3. The parameters listed for Test Sequence F-3 were based on Test Sequence B-3, which involved dense sand also. Test Sequence G-3 pile tip soi parameters were selected to represent the large stiffness provided by the bottom of the test bin.

11.3.4. Experimental p-y Curves

The model pile tests involving lateral displacements (lateral load and combined load tests) were conducted to establish the relationship between the lateral soil resistance, p, and the corresponding lateral displacement, y, required to analytically model the soil response. Preliminary lateral load tests (not reported herein) examined the sensitivity of the lateral pile behavior and soil resistance and displacement relationships. These preliminary tests established the background for conducting the lateral displacement phases of the seven test sequences given in Table 11.2. For the combined load tests, the strain gage stations above a soil depth of 35 in. that were eliminated for the f-z development were considered for the p-y development, since the bending strains were not nearly as sensitive as the axial strains for these tests.

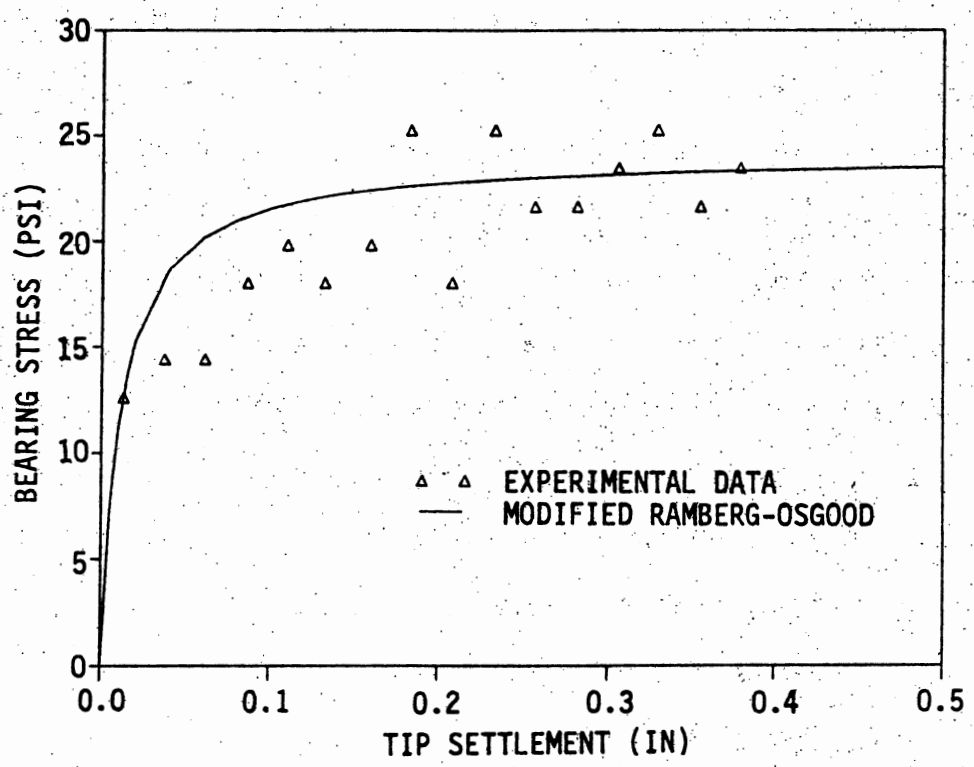

Figure 11.17. Modified Ramberg-Osgood q-z curve at 56 in. depth for the vertical load phase of Test Sequence C-3.

Table 11.3. Summary of soil parameters n, q_{max}, and k_q.

Test Sequence	Soil Type	n	q_{max}	K_q
A-1	loose	1.00	60.0	6,000
A-3	loose	1.00	47.5	6,500
B-3	dense	1.00	200.0	2,000
C-3	loose	1.00	24.0	2,100
D-1	dense	0.75	100.0	1,590
D-3	dense	1.00	220.0	2,200
E-3	dense	1.00	115.0	5,400
F-3	dense	1.00	200.0[a]	2,000[a]
G-3	loose	1.00	40,000	10,000

[a]From Test Sequence B-3.

The techniques used to develop the p-y response for the laboratory tests were similar to the approach described in Section 10.3.4 for the field tests. The difference involved the degree of curve for the function used to approximate the pile bending strains, obtained from the experimentally measured total strains. For the laboratory model tests, a cubic function, rather than a quadratic function, was curve fitted to five consecutive bending strain data points, by a least squares formulation. Large variations of the bending strains along the pile length and a coarse strain gage spacing caused an inaccurate curve fit of the strain values with a quadratic function. The second degree function tended to smooth out the variations in the strain data, resulting in an under-estimation of the lateral soil pressures. An equilibrium check of the forces acting on the pile using the derived lateral soil pressures and the applied lateral load revealed that the derived soil pressures were too small when a quadratic function was assumed. A study with different degrees of curves showed that a third-degree curve was adequate to produce representative lateral soil pressure; however, the lateral resistance of the soil was still slightly underestimated.

Double differentiation and double integration of the bending strain functions were performed as described in Section 10.3.4 to obtain the terms needed to evaluate the lateral soil resistance (Eq. (10.18)) and corresponding lateral displacement (Eq. (10.19)), respectively. After establishing p-y data point pairs corresponding to various magnitudes of applied lateral load for each strain gage location, except the top and bottom gage, a modified Ramberg-Osgood expression (Eq. (3.8)) was selected to provide the best visual curve fit to the data points. The

shape parameter, n, for the curves was established to be equal to unity for the model pile tests in loose sand and one-third for the tests in dense sand.

Each modified Ramberg-Osgood curve has the characteristic soil parameters of maximum soil resistance, p_u, and initial soil stiffness, k_h. The values for these parameters vary with soil depth, z, and soil density. Figures 11.18 and 11.19 show the calculated p_u versus depth and k_h versus depth data point pairs, respectively, for the model pile tests conducted in loose sand, while Figs. 11.20 and 11.21 show the same soil parmeters for the dense sand pile tests. With the complex interaction of soil/abutment/wingwall and pile in Test Sequence F-3, no p-y information was obtained. Also, no p-y parameters are presented for Test Sequence G-3, but they can be approximated by the loose sand in Test Sequence C-3. The variation in p_u and k_h with soil depth have been approximated by the visually established straight lines shown in these figures. These linear functions were used to establish values for p_u and k_h required to analytically model the soil behavior in the computer model, IAB2D.

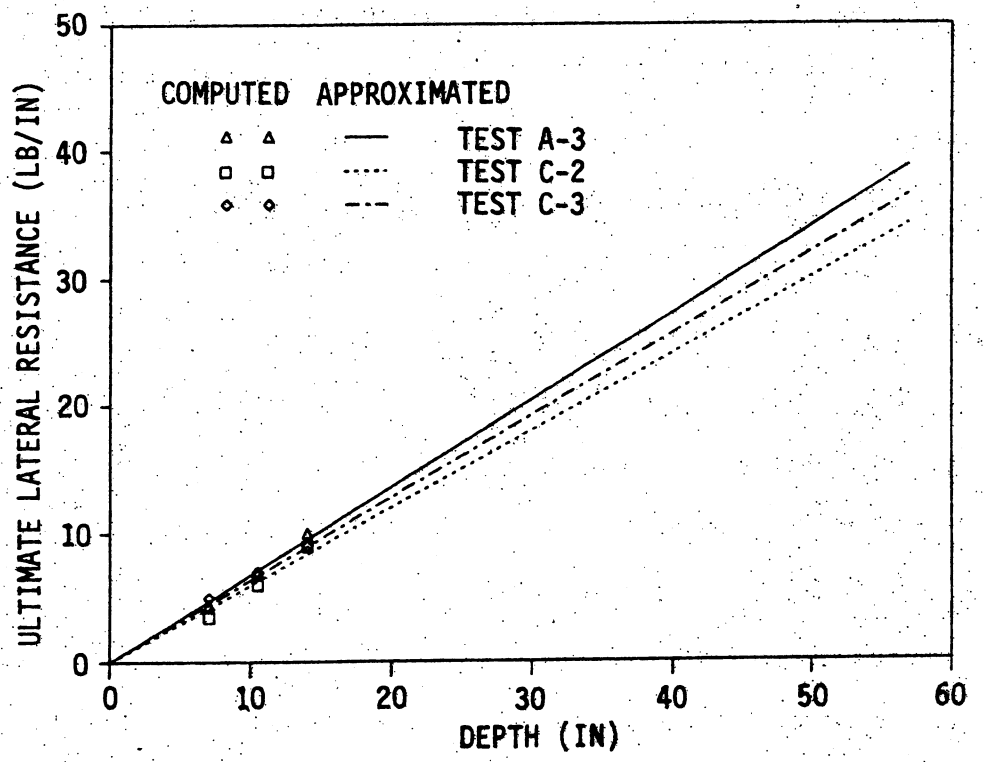

Figure 11.18. Ultimate lateral resistance, p_u, versus depth for lateral load tests in loose sand.

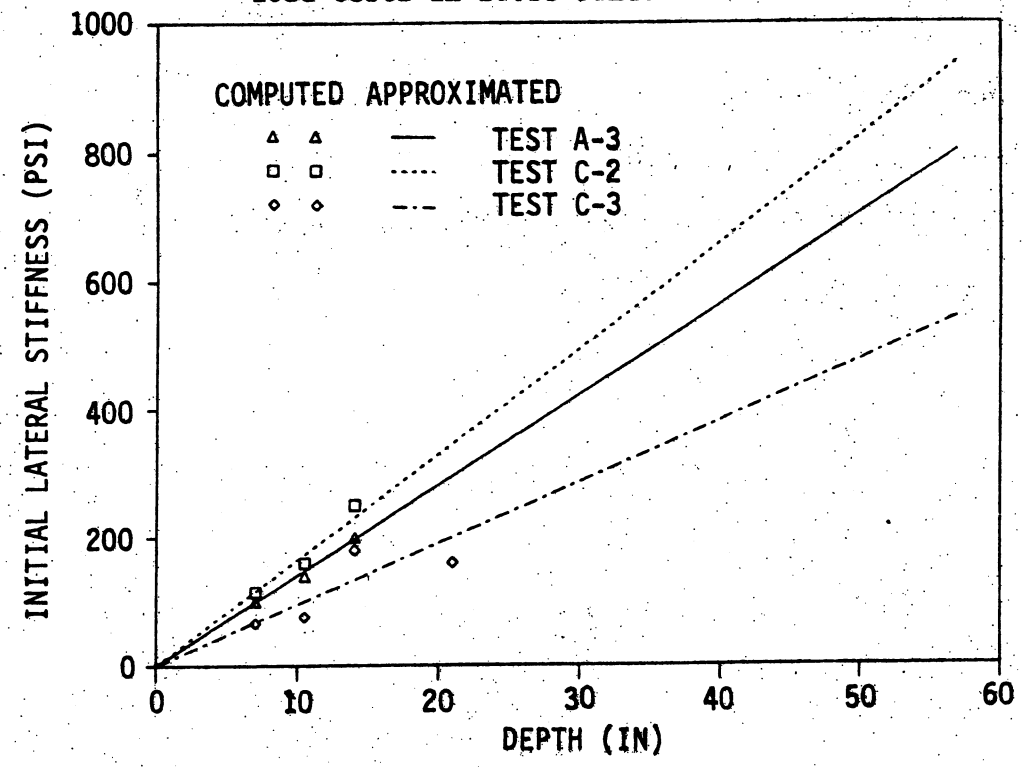

Figure 11.19. Initial lateral stiffness, k_h, versus depth for lateral load tests in loose sand.

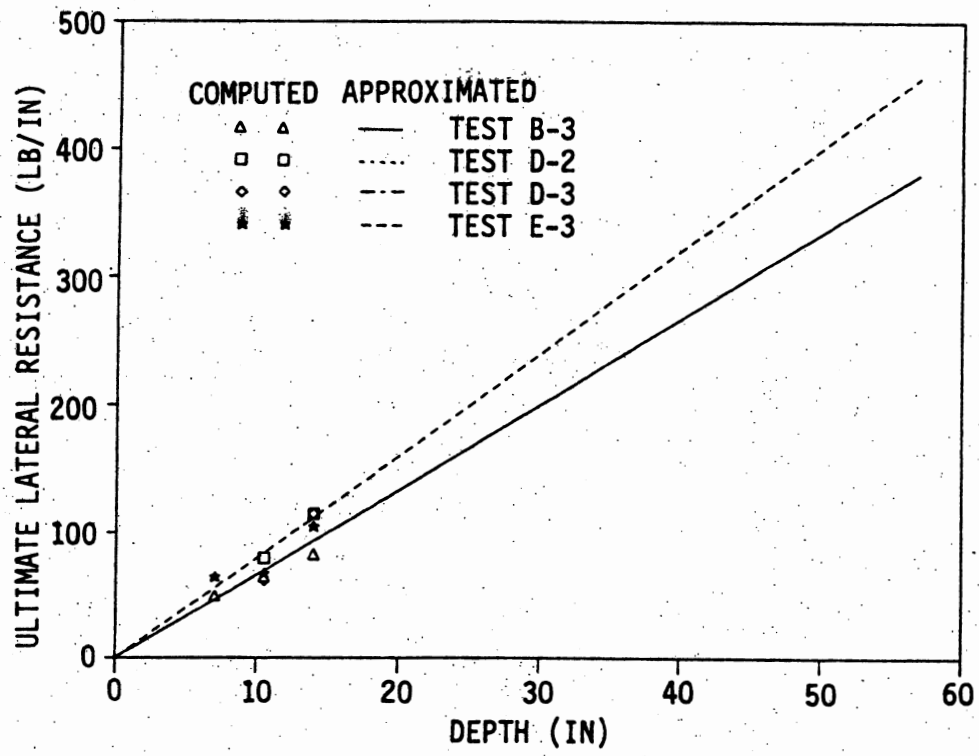

Figure 11.20. Ultimate lateral resistance, p_u, versus depth for lateral load tests in dense sand.

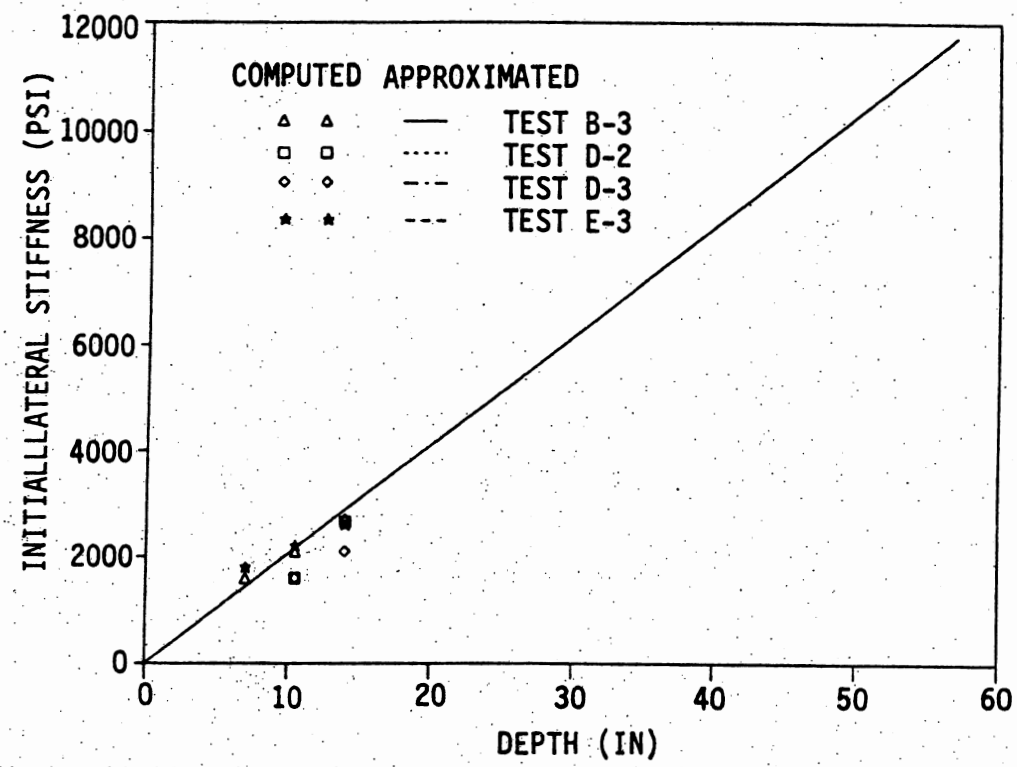

Figure 11.21. Initial lateral stiffness, k_h, versus depth for lateral load tests in dense sand.

12. APPENDIX C: DEVELOPMENT OF EQUIVALENT LENGTHS

Since the pile is being analyzed as an equivalent cantilever, the correct equivalency must be used in determining the length of the cantilever. In this appendix three different equivalencies will be used to develop equations for calculating this length: (1) horizontal stiffness, (2) maximum bending moment, and (3) elastic buckling load. Equations will be developed for fixed-head and pinned-head piles embedded in a uniform soil and in a graded soil. For this development, the piles are assumed to remain elastic.

12.1. Fixed-Head Pile in a Uniform Soil

For a fixed-head pile embedded in a uniform soil the equivalent length for determining the horizontal load required to produce a specified horizontal displacement is determined by equating the horizontal stiffness of the actual pile and the equivalent cantilever, that is, equal horizontal load at the head of the pile for a unit horizontal displacement as shown in Fig. 5.1.

For a pile longer than its critical length (Eq. (5.5)) the deflection, Δ_g, and rotation, θ_g, at the soil surface due to an applied horizontal load, H, and moment, M_g, at the soil surface, are given by [5]

$$\Delta_g = \sqrt{2}\,\frac{H}{k_h}\left(\frac{\ell_c}{4}\right)^{-1} + \frac{M_g}{k_h}\left(\frac{\ell_c}{4}\right)^{-2} \tag{12.1}$$

$$\theta_g = \frac{H}{k_h}\left(\frac{\ell_c}{4}\right)^{-2} + \sqrt{2}\,\frac{M_g}{k_h}\left(\frac{\ell_c}{4}\right)^{-3} \tag{12.2}$$

For the soil-pile system shown in Fig. 12.1 the moment at the soil surface is

$$M_g = M + H\ell_u \tag{12.3}$$

where M is the moment at the head of the pile. Substitution into Eqs. (12.1) and (12.2) gives the displacement and rotation at the ground surface. Adding the displacements of the portion above the surface, the displacement and rotation at the head will be, respectively,

$$\Delta = \Delta_g + \theta_g \ell_u + \frac{H\ell_u^{\,3}}{3EI} + \frac{M\ell_u^{\,2}}{2EI} \tag{12.4}$$

$$\theta = \theta_g + \frac{H\ell_u^{\,2}}{2EI} + \frac{M\ell_u}{EI} \tag{12.5}$$

Equations (12.4) and (12.5) are functions of only H and M. Setting the rotation at the head of the pile equal to zero (fixed), Eq. (12.5) can be solved to obtain the moment at the head as a function of the horizontal load, H. Substituting this equation for moment into Eq. (12.4), the following is obtained

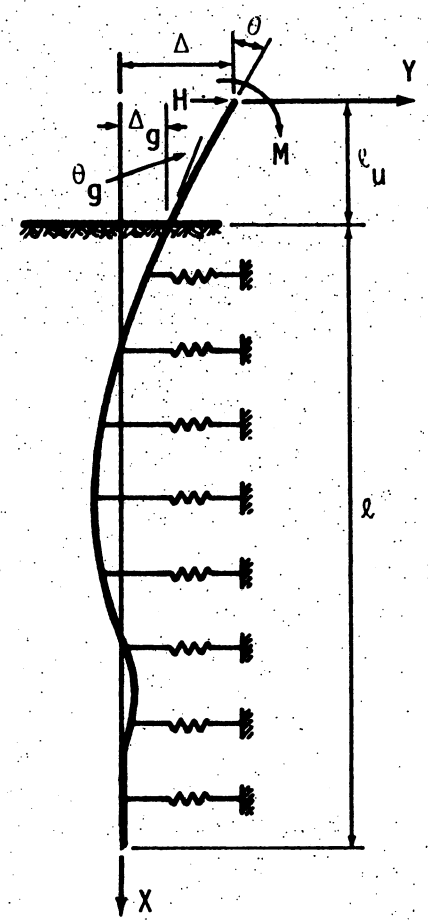

Figure 12.1. Winkler model of soil-pile system with applied horizontal load, H, and moment, M.

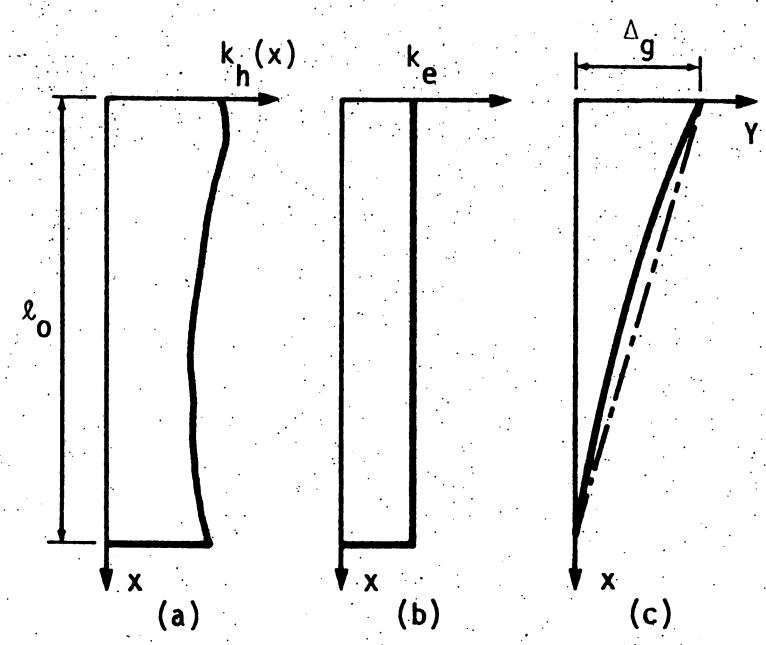

Figure 12.2. Piles in nonuniform soil: (a) actual variation of stiffness (b) equivalent uniform stiffness (c) assumed displaced shape.

$$\frac{H}{\Delta} = \frac{\dfrac{\ell_u}{EI} + \dfrac{\sqrt{2}}{k_h}\left(\dfrac{4}{\ell_c}\right)^3}{\dfrac{\ell_u^4}{12(EI)^2} + \dfrac{\sqrt{2}\,\ell_u^3}{3k_hEI}\left(\dfrac{4}{\ell_c}\right)^3 + \dfrac{\ell_u^2}{k_hEI}\left(\dfrac{4}{\ell_c}\right)^2 + \dfrac{\sqrt{2}\,\ell_u}{k_hEI}\left(\dfrac{4}{\ell_c}\right) + \dfrac{1}{k_h^2}\left(\dfrac{4}{\ell_c}\right)^4} \tag{12.6}$$

For the case of the equivalent cantilever with no rotation at the head (Fig. 5.1a) and a horizontal displacement Δ, the horizontal stiffness is given by

$$\frac{H}{\Delta} = \frac{12\ EI}{\left(\ell_u + \ell_e\right)^3} \tag{12.7}$$

By setting Eq. (12.7) equal to Eq. (12.6) and simplifying, the ratio of the equivalent embedded length to the critical length is given by

$$\frac{\ell_e}{\ell_c} = \sqrt[3]{\frac{256\left(\dfrac{\ell_u}{\ell_c}\right)^4 + 256\sqrt{2}\left(\dfrac{\ell_u}{\ell_c}\right)^3 + 192\left(\dfrac{\ell_u}{\ell_c}\right)^2 + 48\sqrt{2}\left(\dfrac{\ell_u}{\ell_c}\right) + 12}{256\left(\dfrac{\ell_u}{\ell_c}\right) + 64\sqrt{2}}} - \frac{\ell_u}{\ell_c} \tag{12.8}$$

Equation (12.8) is plotted in Fig. 5.2. As discussed, this equivalent length is only valid for determining the horizontal stiffness of a fixed-head pile.

For a fixed-head pile embedded in a uniform soil, an equivalent length will be developed such that the maximum moment in the equivalent cantilever system is equal to the maximum moment in the actual system

for a given horizontal displacement. The maximum moment occurs at the head of the pile for both systems. Setting the rotation at the head equal to zero in Eq. (12.5), the horizontal load can now be determined as a function of the moment, M. Substituting this horizontal load into Eq. (12.4) produces

$$\frac{M}{\Delta} = \frac{-\left[\frac{\sqrt{2}\,\ell_u}{k_h}\left(\frac{4}{\ell_c}\right)^3 + \frac{1}{k_h}\left(\frac{4}{\ell_c}\right)^2 + \frac{\ell_u^{\,2}}{2EI}\right]}{\frac{\ell_u^{\,4}}{12(EI)^2} + \frac{\sqrt{2}\,\ell_u^{\,3}}{3k_hEI}\left(\frac{4}{\ell_c}\right)^3 + \frac{\ell_u^{\,2}}{k_hEI}\left(\frac{4}{\ell_c}\right)^2 + \frac{\sqrt{2}\,\ell_u}{k_hEI}\left(\frac{4}{\ell_c}\right) + \frac{1}{k_h^{\,2}}\left(\frac{4}{\ell_c}\right)^4} \tag{12.9}$$

For the equivalent cantilever with no rotation at the top the ratio of moment to displacement is given by

$$\frac{M}{\Delta} = -\frac{6EI}{\left(\ell_u + \ell_e\right)^2} \tag{12.10}$$

(The negative sign corresponds to the sign convention used in Fig. 12.1.) Setting Eq. (12.10) equal to Eq. (12.9) and simplifying, the following equation relating the equivalent embedded length ℓ_e to the pile critical length ℓ_c is obtained

$$\frac{\ell_e}{\ell_c} = \sqrt{\frac{128\left(\frac{\ell_u}{\ell_c}\right)^4 + 128\sqrt{2}\left(\frac{\ell_u}{\ell_c}\right)^3 + 96\left(\frac{\ell_u}{\ell_c}\right)^2 + 24\sqrt{2}\left(\frac{\ell_u}{\ell_c}\right) + 6}{128\left(\frac{\ell_u}{\ell_c}\right)^2 + 64\sqrt{2}\left(\frac{\ell_u}{\ell_c}\right) + 16}} - \frac{\ell_u}{\ell_c} \tag{12.11}$$

The above dimensionless equation is plotted in Fig. 5.2.

An equivalent cantilever is now selected for a fixed-head pile embedded in a uniform soil such that its elastic buckling load is equal to the elastic buckling load for the actual soil-pile system. Deflection and rotation at the pile head are assumed to be zero during buckling. Appendix D shows that the elastic buckling load for an initially curved column is the same as for an initially straight column. Buckling is usually confined to within the critical length (Eq. (5.5)). For practical purposes the variation in axial load over this length conservatively can be ignored [5]. Buckling of a pile will generally only be a problem where a very soft soil overlies a stronger foundation material.

Stability of a partially embedded pile has been studied by Granholm [29]. The study was conducted assuming the pile to be infinitely long and the head of the pile either fixed or pinned. No horizontal translation of the pile head was permitted, and the pile was assumed to be embedded in a uniform medium. For the portion of the pile embedded in the soil the differential equation is

$$\frac{d^4y}{dx^4} + \beta_e^2 \frac{d^2y}{dx^2} - \alpha^4 y = 0 \tag{12.12}$$

and the differential equation for the unembedded portion is

$$\frac{d^4y}{dx^4} + \beta_e^2 \frac{d^2y}{dx^2} = 0 \tag{12.13}$$

where β_e is equal to $\sqrt{P/EI}$, and α is equal to $\sqrt{k_h/EI}$. Integrating Eqs. (12.12) and (12.13) and satisfying the terminal conditions, the solution for elastic buckling obtained by Granholm [29] is

$$\beta_e \ell_u \sin \beta_e \ell_u \left\{1 - \left(\frac{\beta_e \ell_u}{\alpha \ell_u}\right)^2 - \frac{1}{\alpha \ell_u}\left[1 + \left(\frac{\beta_e \ell_u}{\alpha \ell_u}\right)^2\right]\sqrt{2 - \left(\frac{\beta_e \ell_u}{\alpha \ell_u}\right)^2}\right\}$$
$$+ \cos \beta_e \ell_u \left\{2 - \left(\frac{\beta_e \ell_u}{\alpha \ell_u}\right)^4 + \alpha \ell_u \left(\frac{\beta_e \ell_u}{\alpha \ell_u}\right)^2 \sqrt{2 - \left(\frac{\beta_e \ell_u}{\alpha \ell_u}\right)^2}\right\} - 2 = 0 \tag{12.14}$$

The factor for buckling, $\beta_e \ell_u$, has been determined from Eq. (12.14) by Granholm for various values of $\alpha \ell_u$ (Note: $\alpha \ell_u$ is equal to $4\ \ell_u/\ell_c$). The elastic buckling load for the pile is found by

$$P_e = \beta_e^2\ EI \tag{12.15}$$

The elastic buckling load for the equivalent cantilever with a fixed-head is

$$P_e = \frac{\pi^2 EI}{\left[0.5(\ell_u + \ell_e)\right]^2} \tag{12.16}$$

where the 0.5 represents the effective length factor. Setting Eq. (12.16) equal to Eq. (12.15) and simplifying gives

$$\frac{\ell_e}{\ell_c} = \left(\frac{2\pi}{\beta_e \ell_u} - 1\right)\frac{\ell_u}{\ell_c} \tag{12.17}$$

Introducing the solution from Ref. [29] for $\beta_e \ell_u$, the ratio of the equivalent cantilever length to the critical length is plotted in Fig. 5.2.

From Refs. [1] and [49], the theoretically correct elastic buckling load for a fixed-headed pile entirely embedded in a uniform soil is equal to $2.5\sqrt{k_h EI}$. The solution presented here gives the critical load reduced to $2.0\sqrt{k_h EI}$ (ℓ_u equal zero and ℓ_e equal 1.11 ℓ_c in Eq. (12.16)). Thus, the above solution is conservative when considering piles entirely embedded.

The displacement along the length of a pile embedded in a uniform soil from Poulos and Davis [6] is

$$y(x) = \frac{8H}{\sqrt{2}\ell_c k_h} K_{YH}(x) + \frac{16M_g}{\ell_c^2 k_h} K_{YM}(x) \tag{12.18}$$

where

$$K_{YH}(x) = \frac{\sinh \xi \cos \xi \left(\frac{x}{\ell}\right) \cosh \xi \left(1 - \frac{x}{\ell}\right) - \sin \xi \cosh \xi \left(\frac{x}{\ell}\right) \cos \xi \left(1 - \frac{x}{\ell}\right)}{\sinh^2 \xi - \sin^2 \xi} \tag{12.19}$$

$$K_{YM}(x) = \frac{\sinh \xi \left[\cosh \xi \left(1 - \frac{x}{\ell}\right) \sin \xi \left(\frac{x}{\ell}\right) - \sinh \xi \left(1 - \frac{x}{\ell}\right) \cos \xi \left(\frac{x}{\ell}\right)\right]}{\sinh^2 \xi - \sin^2 \xi} + \frac{\sin \xi \left[\sinh \xi \left(\frac{x}{\ell}\right) \cos \xi \left(1 - \frac{x}{\ell}\right) - \cosh \xi \left(\frac{x}{\ell}\right) \sin \xi \left(1 - \frac{x}{\ell}\right)\right]}{\sinh^2 \xi - \sin^2 \xi} \tag{12.20}$$

$$\xi = \frac{4\ell}{\sqrt{2\ell_c}} \tag{12.21}$$

Since most piles are longer than their critical length, the solution for displacement will be determined for flexible piles, that is, $\ell = \ell_c$.

Using the sign convention from Fig. 12.1 for a pile with an unsupported length, ℓ_u, above the ground, the horizontal force at the head of the pile is given by Eq. (12.7) and the moment is given by Eq. (12.10). By applying Eq. (12.3), the moment at the ground surface is

$$M_g = \frac{6EI\Delta}{\left(\ell_{em} + \ell_u\right)^2} - \frac{12EI\Delta\ell_u}{\left(\ell_{eh} + \ell_u\right)^3} \tag{12.22}$$

where ℓ_{eh} and ℓ_{em} are the equivalent embedded lengths for horizontal load (Eq. (12.8)) and maximum moment (Eq. (12.11)), respectively. Substituting Eqs. (12.7) and (12.22) into Eq. (12.18), the ratio of displacement along the length of the pile to the horizontal displacement at the pile head is given by

$$\frac{y(x)}{\Delta} = \frac{3K_{YH}(x)}{8\sqrt{2}\left(\frac{\ell_{eh}}{\ell_c} + \frac{\ell_u}{\ell_c}\right)^3} + \frac{K_{YM}(x)}{8}\left[\frac{3}{\left(\frac{\ell_{em}}{\ell_c} + \frac{\ell_u}{\ell_c}\right)^2} - \frac{6}{\left(\frac{\ell_{eh}}{\ell_c} + \frac{\ell_u}{\ell_c}\right)^3}\left(\frac{\ell_u}{\ell_c}\right)\right] \tag{12.23}$$

As described in Section 5.3, the frictional capacity at the soil-pile interface should be neglected if y(x) is greater than some limit, y_{max}. The depth at which this occurs is defined as ℓ_n, that is,

$$\frac{y(\ell_n)}{\Delta} = \frac{y_{max}}{\Delta} \tag{12.24}$$

The length ℓ_n should be subtracted from the total pile length when the friction capacity of the pile is evaluated. It is obtained by substituting Eq. (12.23) (with x equal ℓ_n) into Eq. (12.24) and solving for ℓ_n. The resulting ℓ_n/ℓ_c is plotted in Fig. 5.13 versus ℓ_u/ℓ_c for y_{max}/Δ values of 0.05, 0.1, 0.2, and 0.3.

12.2. Pinned-Head Pile in a Uniform Soil

For a pinned-head pile embedded in a uniform soil, the equivalent cantilever development is similar to the development of the fixed-head pile. The ratio of the horizontal load displacement to the horizontal displacement is

$$\frac{H}{\Delta} = \frac{3EI}{\left(\ell_u + \ell_e\right)^3} \tag{12.25}$$

Proceeding in a manner similar to the fixed-head case (M equal to zero instead of θ equal to zero at the pile head), the following equation is obtained.

$$\frac{\ell_e}{\ell_c} = \sqrt[3]{\left(\frac{\ell_u}{\ell_c}\right)^3 + \frac{3}{4}\left(\frac{\ell_u}{\ell_c}\right)^2 + \frac{3}{8}\left(\frac{\ell_u}{\ell_c}\right) - \frac{\ell_u}{\ell_c}} \tag{12.26}$$

The above equation is plotted in dimensionless terms in Fig. 5.3.

The maximum moment in a pinned-head pile embedded in a uniform soil occurs at some location along the length of the pile. The maximum moment in the equivalent cantilever will occur at the base and is equal to the maximum in the actual system. From Poulos and Davis [6] the moment along the length of the pile is

$$M(x) = -\frac{H\ell_c}{2\sqrt{2}}\left[K_{MH}(x) - 2\sqrt{2}\left(\frac{\ell_u}{\ell_c}\right)K_{MM}(x)\right] \tag{12.27}$$

where

$$K_{MH}(x) = \frac{\sin\xi\,\sin\xi\left(\frac{x}{\ell}\right)\sinh\xi\left(1-\frac{x}{\ell}\right) - \sin\xi\,\sinh\xi\left(\frac{x}{\ell}\right)\sin\xi\left(1-\frac{x}{\ell}\right)}{\sinh^2\xi - \sin^2\xi} \tag{12.28}$$

$$K_{MM}(x) = \frac{\sinh\xi\left[\sinh\xi\left(1-\frac{x}{\ell}\right)\cos\xi\left(\frac{x}{\ell}\right) + \cosh\xi\left(1-\frac{x}{\ell}\right)\sin\xi\left(\frac{x}{\ell}\right)\right]}{\sinh^2\xi - \sin^2\xi} - \frac{\sin\xi\left[\sinh\xi\left(\frac{x}{\ell}\right)\cos\xi\left(1-\frac{x}{\ell}\right) + \cosh\xi\left(\frac{x}{\ell}\right)\sin\xi\left(1-\frac{x}{\ell}\right)\right]}{\sinh^2\xi - \sin^2\xi} \tag{12.29}$$

and ξ is given by Eq. (12.21). Since most piles are longer than their critical length, the solution for the moment will be determined for flexible piles, that is, $\ell = \ell_c$. The expressions for the displacement and rotation at the soil surface and the displacement at the pile head are given by Eqs. (12.1), (12.2), and (12.4) (with M set equal to zero), respectively. The ratio of the moment to the pile head displacement is

$$\frac{M(x)}{\Delta} = - \frac{\left[k_h \ell_c \quad K_{MH}(x) - 2\sqrt{2} \left(\frac{\ell_u}{\ell_c}\right) K_{MM}(x) \right]}{2\sqrt{2} \left[\sqrt{2} \left(\frac{4}{\ell_c}\right) + 2\ell_u \left(\frac{4}{\ell_c}\right)^2 + \sqrt{2}\, \ell_u^2 \left(\frac{4}{\ell_c}\right)^3 + \frac{\ell_u^3 k_h}{3EI} \right]} \tag{12.30}$$

For the moment to be a maximum, the numerator in Eq. (12.30) must be a maximum. Letting

$$Q_M(x) = K_{MH}(x) - 2\sqrt{2} \left(\frac{\ell_u}{\ell_c}\right) K_{MM}(x) \tag{12.31}$$

the value of $Q_M(x)$ along the length of the pile can be examined and the maximum, $(Q_M)_{max}$, selected. The maximum moment occurring at the base of the equivalent pinned cantilever divided by the pile head displacement is

$$\frac{M}{\Delta} = - \frac{3EI}{\left(\ell_u + \ell_e\right)^2} \tag{12.32}$$

The negative sign corresponds to the sign convention used in Fig. 12.1. Setting Eq. (12.32) equal to Eq. (12.30) and simplifying, we obtain the following equation, which is plotted in Fig. 5.3.

$$\frac{\ell_e}{\ell_c} = \sqrt{\frac{3}{16\,(Q_M)_{max}} \left[1 + \frac{8}{\sqrt{2}} \left(\frac{\ell_u}{\ell_c}\right) + 16 \left(\frac{\ell_u}{\ell_c}\right)^2 + \frac{32\sqrt{2}}{3} \left(\frac{\ell_u}{\ell_c}\right)^3 \right]} - \frac{\ell_u}{\ell_c} \tag{12.33}$$

The development of the equation for elastic buckling of a pinned-head pile embedded in a uniform soil is similar to the fixed-head case. The solution for the elastic buckling load obtained by Granholm [29] is

$$\frac{\tan \beta_e \ell_u}{\beta_e \ell_u} = \frac{1 - \left(\frac{\beta_e \ell_u}{\alpha \ell_u}\right)^2 - \frac{1}{\alpha \ell_u}\left(\frac{\beta_e \ell_u}{\alpha \ell_u}\right)^2 \sqrt{2 - \left(\frac{\beta_e \ell_u}{\alpha \ell_u}\right)^2}}{1 + \left(\frac{\beta_e \ell_u}{\alpha \ell_u}\right)^2 - \left(\frac{\beta_e \ell_u}{\alpha \ell_u}\right)^4 + \alpha \ell_u \left(\frac{\beta_e \ell_u}{\alpha \ell_u}\right)^2 \sqrt{2 - \left(\frac{\beta_e \ell_u}{\alpha \ell_u}\right)^2}} \tag{12.34}$$

The factor for buckling, $\beta_e \ell_u$, has been determined from Eq. (12.34) by Granholm for various values of $\alpha \ell_u$. (Note: $\alpha \ell_u$ is eual to $4\ \ell_u/\ell_c$.) The elastic buckling load for the equivalent cantilever is given by

$$P_e = \frac{\pi^2\ EI}{\left[0.7\ (\ell_u + \ell_e)\right]^2} \tag{12.35}$$

where 0.7 is the effective length factor for the pinned-head pile. Setting Eq. (12.35) equal to Eq. (12.15) and simplifying yields

$$\frac{\ell_e}{\ell_c} = \left(\frac{\pi}{0.7\ \beta_e \ell_u} - 1\right) \frac{\ell_u}{\ell_c} \tag{12.36}$$

Using the solution from Ref. [29] for $\beta_e \ell_u$, the various values of $\alpha \ell_u$ for the ratio of the equivalent cantilever length to the critical length are plotted then in Fig. 5.3. The elastic buckling load presented here for an equivalent pinned-head pile entirely embedded in a uniform soil is the same as the load given in Refs. [1,49], that is, $2.0\sqrt{k_h EI}$.

The displacement along the length of a pinned-head pile is given by Eq. (12.18). Setting the sign convention from Fig. 12.1 and Eqs. (12.3) and (12.25), with the moment at the pile head, M, equal to zero, the moment at the ground surface is

$$M_g = -\frac{3EI\Delta}{\left(\ell_u + \ell_{eh}\right)^3} \tag{12.37}$$

where ℓ_{eh} is the equivalent embedded length for the horizontal load (Eq. (12.25)). When Eqs. (12.25) and (12.37) are substituted into Eq. (12.18), the ratio of displacement along the length of the pile to the horizontal displacement at the pile head is given by

$$\frac{y(x)}{\Delta} = \frac{3}{\left(\frac{\ell_{eh}}{\ell_c} + \frac{\ell_u}{\ell_c}\right)^3}\left[\frac{1}{32\sqrt{2}}K_{YH}(x) - \frac{1}{16}\left(\frac{\ell_u}{\ell_c}\right)K_{YM}(x)\right] \tag{12.38}$$

where $K_{YH}(x)$ and $K_{YM}(x)$ are given by Eqs. (12.19) and (12.20), respectively. By setting $y(\ell_n)$ equal to y_{max}, Fig. 5.14 was produced in a manner similar to Fig. 5.13.

12.3. Piles in a Nonuniform Soil

For a pile embedded in a soil with a nonuniform stiffness, $k_h(x)$, an equivalent uniform soil stiffness, k_e, will be determined as shown in Fig. 12.2. With the equivalent uniform stiffness the critical pile

length, ℓ_c, can be determined by Eq. (5.5). The equivalent cantilever lengths (Section 5.2.1) and the length, ℓ_n, to be neglected when calculating the frictional resistance (Section 5.3), can then be determined.

Setting the work of the equivalent uniform soil equal to the work of the actual non-uniform soil over a length, ℓ_o, gives

$$\int_o^{\ell_o} \frac{k_e y^2}{2}\, dx = \int_o^{\ell_o} \frac{k_h(x) y^2}{2}\, dx \tag{12.39}$$

The length, ℓ_o, is the active length of the pile in bending, which is taken here as one-quarter of the deflected wave shape, that is, approximately $\ell_c/2$, or

$$\ell_o = 2 \sqrt[4]{\frac{EI}{k_e}} \tag{12.40}$$

The displaced shape is approximated by the straight line as shown in Fig. 12.2c

$$y = \Delta_g \left(1 - \frac{x}{\ell_o}\right) \tag{12.41}$$

Substituting Eq. (12.41) into Eq. (12.39) gives

$$\frac{k_e \ell_o^3}{3} = \int_o^{\ell_o} k_h(x)\, (\ell_o - x)^2\, dx \tag{12.42}$$

which is the second moment of the area of the $k_h(x)$ diagram taken about a line at depth ℓ_o. Thus, when the actual soil stiffness distribution,

$k_h(x)$ is known, Eq. (12.42) can be solved for the effective uniform stiffness k_e.

For a soil stiffness which varies linearly, the exact solution is known [5]. Consider the case in which the stiffness varies from zero at the ground surface to k_1 at the depth ℓ_o. Then, $k_h(x)$ is equal to $n_h x$ where

$$n_h = \frac{k_1}{\ell_o} = \frac{k_1}{2}\sqrt[4]{\frac{k_e}{EI}} \tag{12.43}$$

Since the integral, I_k, on the right-hand side of Eq. (12.42) represents the second moment of the area of the $k_h(x)$ diagram about ℓ_o,

$$I_k = \frac{k_1 \ell_o^3}{12} \tag{12.44}$$

which, when used in Eq. (12.42), yields

$$k_e = \frac{k_1}{4} \tag{12.45}$$

To evaluate the approximation involved in k_e, the pile flexibilities obtained by using Eq. (12.45) will be compared to the exact theory. The displacements for the equivalent uniform soil are given by Eqs. (12.1) and (12.2) with k_h equal k_e. The exact displacements [5] for the linearly varying stiffness case are

$$\Delta_g = 2.43 \frac{H}{n_h} \left(\frac{\ell_c'}{4}\right)^{-2} + 1.62 \frac{M_g}{n_h} \left(\frac{\ell_c'}{4}\right)^{-3} \tag{12.46}$$

$$\theta_g = 1.62 \frac{H}{n_h} \left(\frac{\ell_c'}{4}\right)^{-3} + 1.73 \frac{M_g}{n_h} \left(\frac{\ell_c'}{4}\right)^{-4} \tag{12.47}$$

in which

$$\ell_c' = 4 \sqrt[5]{\frac{EI}{n_h}} \tag{12.48}$$

The equivalent uniform case will give the same results as Eqs. (12.46) and (12.47), if the corresponding flexibility coefficients are equal. Identifying the flexibility coefficients by

$$\begin{Bmatrix} \Delta_g \\ \theta_g \end{Bmatrix} = \begin{bmatrix} f_{11} & f_{12} \\ f_{21} & f_{22} \end{bmatrix} \begin{Bmatrix} H \\ M_g \end{Bmatrix} \tag{12.49}$$

will occur if k_e is equal to 0.204 k_1, 0.151 k_1 or 0.186 k_1 for the flexibility coefficients f_{11}, f_{12}, and f_{22}, respectively. The value of k_e equal $0.25k_1$, from the work equivalency (Eq. (12.45)), is sufficiently close to this and is recommended for determining an equivalent uniform soil stiffness.

In general the following procedures can be followed for determining the equivalent uniform stiffness:

Step 1. Guess k_e

Step 2. Calculate $\ell_o = 2 \sqrt[4]{EI/k_e}$

Step 3. Calculate I_k (use Fig. 12.3)

Step 4. Determine new $k_e = 3I_k/\ell_o^3$

Step 5. Return to Step 2 until convergence

As an example of this procedure for a layered soil, the equivalent stiffness, k_e, from Fig. 12.4 will be determined. Let EI equal 14440 k-ft^2.

Step 1. Guess k_e = 100 ksf

Step 2. Calculate $\ell_o = 2\sqrt[4]{\frac{14440 \text{ k-ft}}{100 \text{ ksf}}} = 6.93$ ft

Step 3. Now ℓ_2 = 2.93 ft, so from Fig. 12.3, the second moment of the area of the $k_h(x)$ disribution about ℓ_o can be found as

$$I_k = 72 \text{ ksf} \left[\frac{4 \text{ ft}^3}{12} + 4(2.93 \text{ ft} + 2 \text{ ft})^2\right]$$

$$+ 580 \text{ ksf} \quad \frac{2.93 \text{ ft}^3}{3} = 12247 \text{ k-ft}$$

Step 4. Determine $k_e = \left[\frac{3(12247 \text{ k-ft})}{(6.93 \text{ ft})^3}\right] = 110$ ksf

Step 2. (Second Iteration) $\ell_o = 2\sqrt[4]{\frac{14440 \text{ k-ft}}{110 \text{ ksf}}} = 6.77$ ft

Step 3. (Second Iteration) ℓ_2 = 2.79 ft

I_k = 11492 k-ft

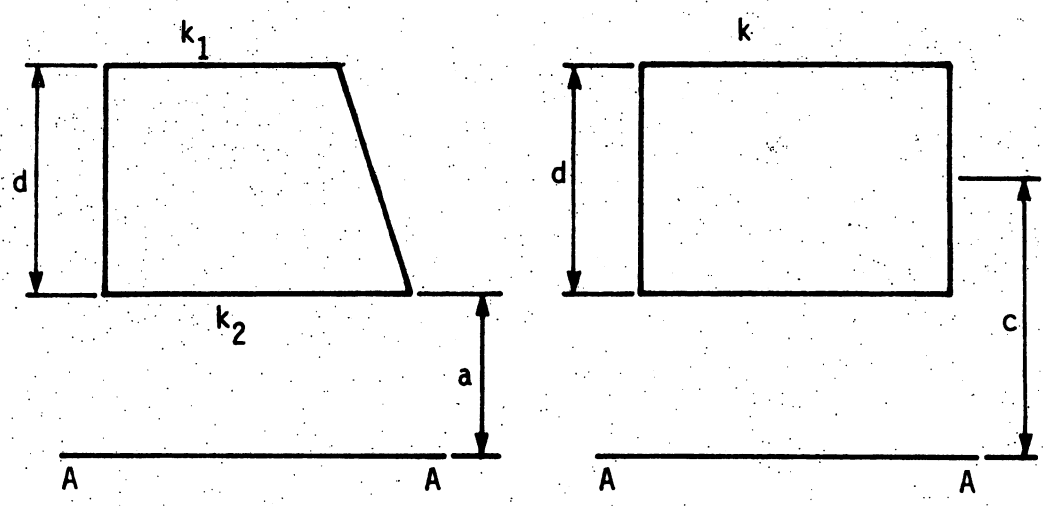

$$I_k = k_1\left[\frac{d^3}{36} + \frac{d}{2}\left(a + \frac{2d}{3}\right)^2\right] + k_2\left[\frac{d^3}{36} + \frac{d}{2}\left(a + \frac{d}{3}\right)^2\right]$$

$$I_k = k\left[\frac{d^3}{12} + dc^2\right]$$

Figure 12.3. Second moment of area about line A - A.

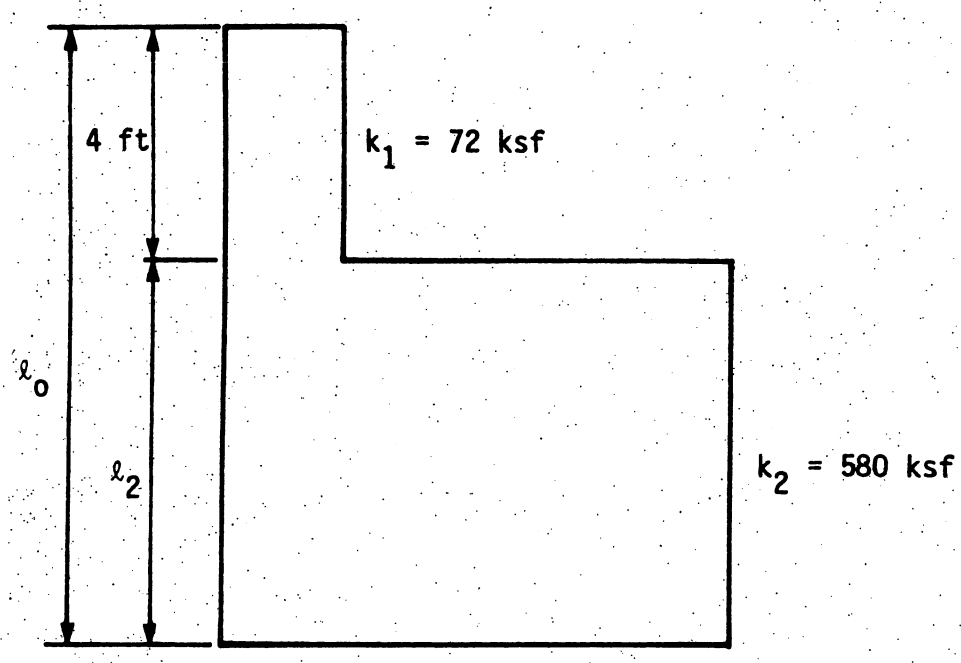

Figure 12.4. Layered soil system for example of determining k_e.

Step 4. (Second Iteration) $k_e = 111$ ksf $\cong 110$ ksf

Step 5. The converged solution is $k_e = 111$ ksf

13. APPENDIX D: MOMENT AMPLIFICATION IN EQUIVALENT CANTILEVERS

In this appendix the moment amplification in fixed (Fig. 13.1) and pinned (Fig. 13.2) head beam-columns (equivalent cantilevers) with a horizontal displacement applied to the head is investigated. First, a beam-column that has been stressed by displacing its head a distance Δ from an initially straight position (Alternative One in Section 5.2.3.1) will be studied. Secondly, the beam-column will be assumed to be unstressed with a Δ displacement at its head (Alternative Two in Section 5.2.3.2).

13.1. Initially Straight Columns

The straight fixed-head column, shown in Fig. 13.1, is investigated by initially giving the column a horizontal displacement that produces the initial end moments of

$$M_i = \frac{6\ EI\Delta}{L^2} \tag{13.1}$$

Then, the axial load, P, is applied to the column. From Fig. 13.1a the horizontal reaction is given by

$$H = \frac{M_1 - M_2 - P\Delta}{L} \tag{13.2}$$

Summing moments in Fig. 13.1b and applying elementary beam theory,

$$M = -\ EI\ \frac{d^2y}{dx^2} \tag{13.3}$$

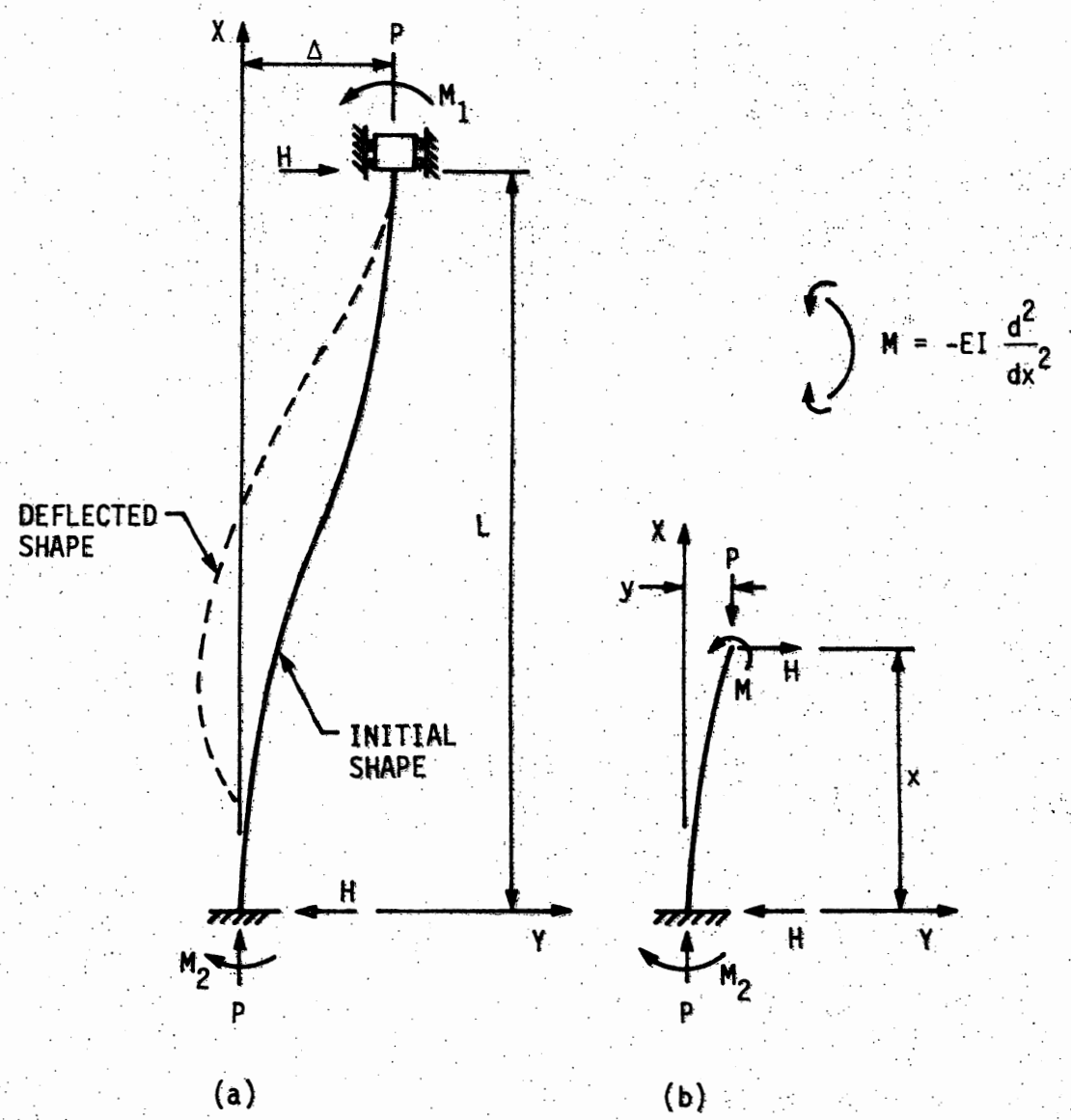

Figure 13.1. Initially straight fixed-head column: (a) displaced location (stressed in this position before the vertical load is applied) (b) free body diagram for determining the differential equation.

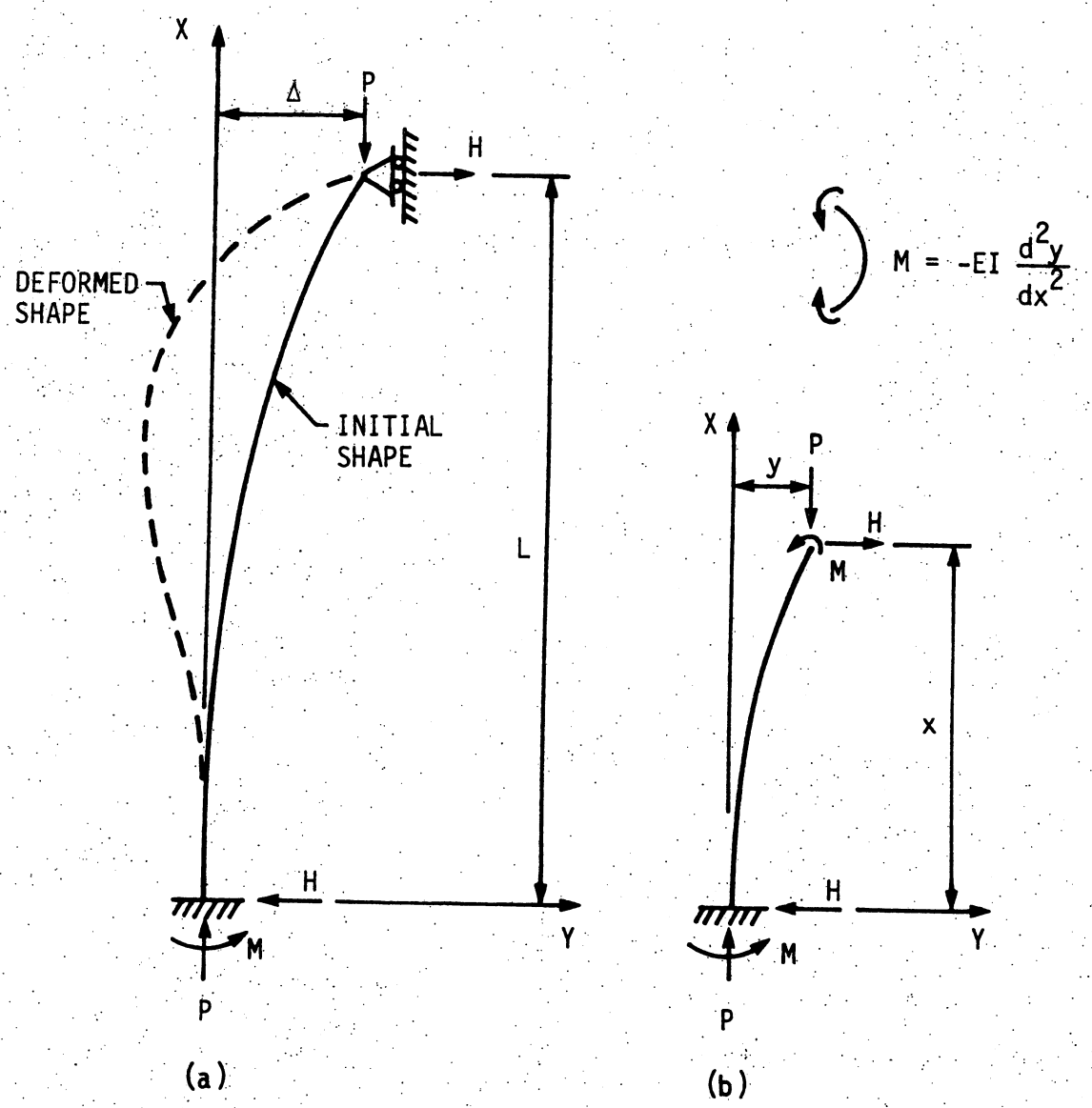

Figure 13.2. Initially straight pinned-head column: (a) displaced location (stressed in this position before the vertical load is applied) (b) free body diagram for determining the differential equation.

the resulting differential equation for this beam-column is

$$\frac{d^2y}{dx^2} + k^2y = -\frac{M_2}{EI} - \left(\frac{M_1 - M_2 - P\Delta}{EIL}\right) x \tag{13.4}$$

where

$$k^2 = \frac{P}{EI} \tag{13.5}$$

Using the boundary conditions of zero displacement and rotation at the base of the column and a displacement of Δ at the head, the differential equation can be solved. This produces two equations, which are functions of M_1 and M_2. These equations can be solved simultaneously producing the following equations for the end moments:

$$M_1 = \frac{P\Delta\ (1 - \cos kL)}{2(1 - \cos kL) - kL \sin kL} \tag{13.6}$$

$$M_2 = \frac{P\Delta\ (\cos kL - 1)}{2(1 - \cos kL) - kL \sin kL} \tag{13.7}$$

Since these equations show that M_2 equals $-M_1$, the beam-column deforms in an anti-symmetric mode similar to its initial shape.

To force the weaker symmetric buckling mode, the principle of superposition is used to add a small initial symmetric imperfection. The solution of a non-stressed column with this imperfection will be added to the above solution. The small initial symmetric imperfection is

$$y_i = -\frac{\varepsilon}{2}\left(1 - \cos\frac{2\pi x}{L}\right) \tag{13.8}$$

where ε is the maximum offset from the straight position. Proceeding in a manner similar to the first differential equation and defining y_2 to be the incremental displacement caused by the initial imperfection y_i, the following differential equation is determined:

$$\frac{d^2y_2}{dx^2} + k^2y_2 = -k^2\left[\frac{\varepsilon}{2}\left(1 - \cos\frac{2\pi x}{L}\right)\right] - \left(\frac{M_A - M_B}{EIL}\right)x - \frac{M_B}{EI} \tag{13.9}$$

where M_A and M_B are the moments at the head and base, respectively (corresponding to M_1 and M_2). Solving Eq. (13.9) for the boundary conditions of zero displacement and rotation at the support points, two equations that are functions of M_A and M_B are determined.

$$M_A(1 - \cos kL) + M_B(\cos kL - 1) = \left[\frac{1}{\left(\frac{4\pi^2}{(kL)^2} - 1\right)} + 1\right]\frac{\varepsilon P}{2}\,kL\sin kL \tag{13.10}$$

$$M_A\left(\frac{\sin kL}{kL} - \cos kL\right) + M_B\left(\frac{\sin kL}{kL} - 1\right) = \left[\frac{1}{\left(\frac{4\pi^2}{(kL)^2} - 1\right)} + 1\right]\frac{\varepsilon P}{2}(1 - \cos kL) \tag{13.11}$$

Equations (13.10) and (13.11) can be solved simultaneously giving expressions for M_A and M_B that are added to M_1 and M_2 from Eqs. (13.6) and (13.7) to give the results shown in Fig. 13.3. This figure shows the total head, base, and mid-height moment, M, in terms of the amplification factor, A_m, defined as

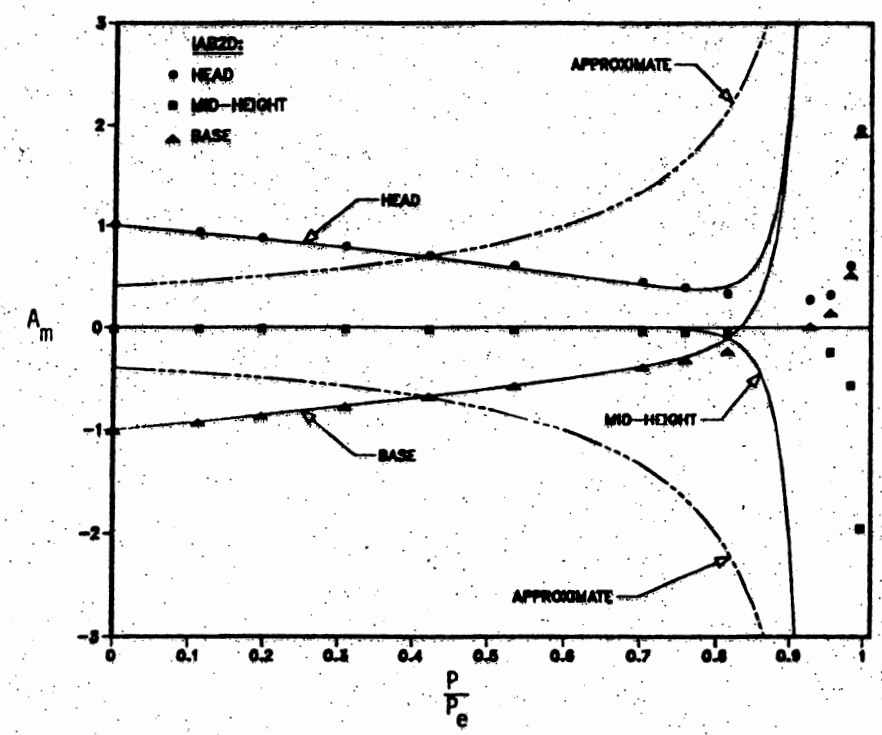

Figure 13.3. Moment amplification for an initially straight fixed-head column with a horizontal head displacement, Δ.

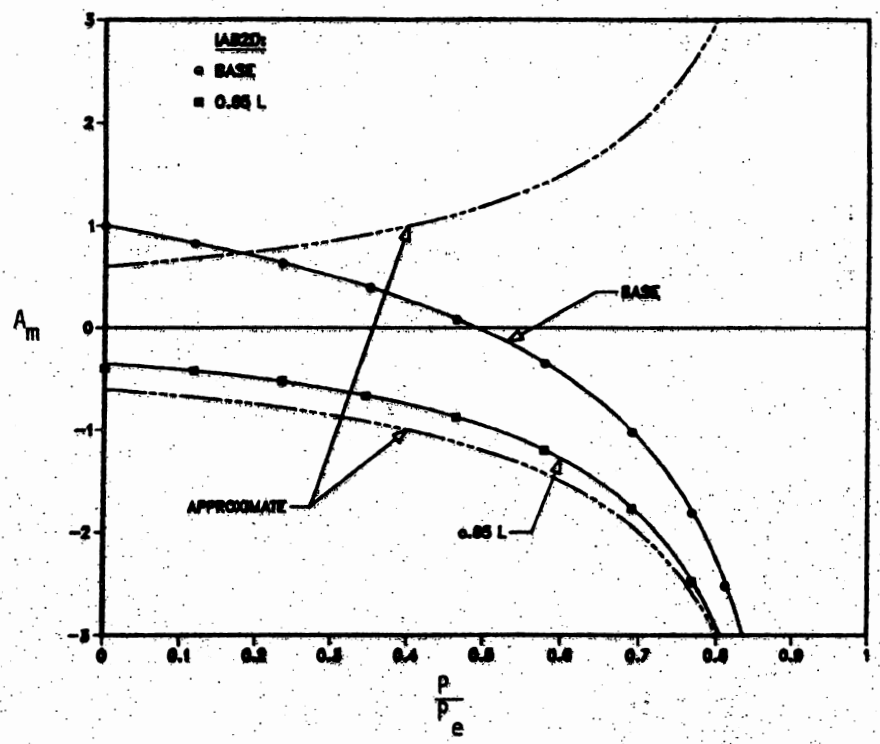

Figure 13.4. Moment amplification for an initially straight pinned-head column with a horizontal head displacement, Δ.

$$A_m = \frac{M}{M_i} \tag{13.12}$$

in which M_i is the maximum primary bending moment given by Eq. (13.1). The abscissa is the ratio of the applied axial load, P, to the critical axial load, P_e, given by

$$P_e = \frac{\pi^2 EI}{(0.5\ L)^2} \tag{13.13}$$

which is the elastic buckling load for a straight fixed-head column. Also shown in this figure are the finite element results at the above locations and the approximate amplification factor, which is used in the design equations (Eqs. (5.1) and (5.3)), defined as

$$A_m = \frac{C_m}{1 - \frac{P}{P_e}} \tag{13.14}$$

where C_m, applicable for no lateral load or joint translation and defined in Section 5.1, is used to establish an equivalent uniform moment for the equivalent cantilever.

This column is initially bent in double curvature, with the maximum moments occurring at the ends of the column. Such columns generally have a sudden type of failure, one of "unwinding" through double curvature to single curvature [28]. A similar type of failure is shown by both the differential equation and the finite element results (Fig. 13.3). Close to the buckling load, the moment at the base reverses direction and the column fails. Although the deformed shape is not in single

curvature, the failure is sudden as the column snaps through to the symmetric mode. The differential equation solution does not quite pass through the finite element results near P/P_e equal to one, since both solutions are sensitive to the amount of imperfection added. The finite element results also depend on the number of elements used in the solution. The elastic buckling load is shown to be that of a straight column, since the asymptote is located at P/P_e equal to one.

Both the stability equation, Eq. (5.1) or (5.3), and the yield equation, Eq. (5.2) or (5.4), are to be checked using the initial end moment, M_i, Eq. (13.1). Figure 13.3 shows that the approximate amplification factor used in the stability equation is conservative, that is, it bounds the head, base, and mid-height moments for axial loads greater than about 0.4 P_e. For axial loads less than about 0.6 P_e, the yield equation will give conservative results because it uses the unamplified end moment, that is, A_m equals one in Fig. 13.3. Thus, by checking both the stability equation and the yield equation, the design will be conservative for the entire range of P/P_e. The recently published Load and Resistance Factor Design Manual [38] from the American Institute of Steel Construction [38,50] has made simplifications and clarifications for the beam-column interaction equations. In this manual there is only one equation to be checked. The same amplification factor is used, but it is limited to the values greater than or equal to one. This is similar to checking both the yield and stability equations as discussed above. Also, the 0.4 lower limit on C_m is removed as discussed both in Chapter H of the LRFD Commentary and in a recently published paper [50].

The coordinate system for a straight pinned-head column is shown in Fig. 13.2. After a horizontal displacement is imposed at the top of the column, the initial elastic moment at the column base is

$$M_i = \frac{3EI\Delta}{L^2} \tag{13.15}$$

when an axial load is applied at the top of the displaced column, the differential equation for this system is

$$\frac{d^2y}{dx^2} + k^2y = \frac{M}{EI} - \left(\frac{M - P\Delta}{EIL}\right)x \tag{13.16}$$

Since the column is not geometrically symmetric, an initial column alignment imperfection is not required to produce the minimum buckling mode. The boundary conditions for the solution of this differential equation are zero displacement and rotation at the base of the column and a displacement equal to Δ at the head of the column. A fourth boundary condition of zero moment at the column head was used in deriving Eq. (13.16). The solution of the differential equation for the base moment, M, is

$$M = \frac{P\Delta\left(\frac{\sin kL}{kL}\right)}{\left(\frac{\sin kL}{\cos kL} - \cos kL\right)} \tag{13.17}$$

The moment amplification factor, A_m, defined by Eq. (13.12), is

$$A_m = \frac{kL \sin kL}{3\left(\frac{\sin kL}{kL} - \cos kL\right)} \tag{13.18}$$

The expressions for the amplification factor at the column base and at x equal to 0.65 L, the maximum moment location in the buckled shape, are shown in Fig. 13.4. The solution shows that the moment at the base reduces and changes direction as the ratio of P/P_e increases from zero to 1.0. As with the fixed-head case, previously developed, both the stability equation, Eq. (5.1) or (5.3), and the yield equation, Eq. (5.2) or (5.4), must be checked for a proper design. Since the asymptote is located at P/P_e equal to one, the elastic buckling load for this case is the same as a straight pinned-head column and is given by

$$P_e = \frac{\pi^2 EI}{(0.7L)^2} \tag{13.19}$$

13.2. Initially Curved Columns

For Alternative Two, the initial shape for the fixed-head column shown in Fig. 13.1 is assumed to be stress-free and given by

$$y_i = \frac{\Delta}{2}\left(1 - \cos\frac{\pi x}{2L}\right) \tag{13.20}$$

Proceeding in a manner similar to that in Section 13.1, the differential equation for this beam-column is similar to Eq. 13.4 and is given by

$$\frac{d^2y_2}{dx^2} + k^2y_2 = \frac{k^2\Delta}{2}\left(1 - \cos\frac{\pi x}{L}\right) - \frac{M_2}{EI} - \frac{(M_1 - M_2 - P\Delta)}{EIL}\,x \tag{13.21}$$

where y_2 is the incremental horizontal displacement caused by the axial load, and k is from Eq. (13.5). The boundary conditions are zero incremental displacement and rotation at the column ends. The solution of the differential equation provided two equations that are functions of the anti-symmetric end moments,

$$M_1 \left(\frac{\sin kL}{kL} - \cos kL\right) - M_2 \left(\frac{\sin kL}{kL} - 1\right) = P\Delta \left(\frac{\sin kL}{kL}\right) - \frac{P\Delta}{2} \left[\frac{1}{\left(\frac{\pi^2}{(kL)^2} - 1\right)} + 1\right] (\cos kL + 1) \tag{13.22}$$

$$M_1 \left(1 - \frac{kL \sin kL}{\cos kL - 1}\right) - M_2 = \frac{P\Delta}{2} \left[\frac{1}{\left(\frac{\pi^2}{(kL)^2} - 1\right)} + 1\right] \frac{kL \sin kL}{\cos kL - 1} \tag{13.23}$$

To induce the weaker symmetric buckling mode, the small initial symmetric imperfection shown in Eq. (13.8) was added. The solution in terms of an amplification factor, A_m, given by

$$A_m = \frac{M}{P\Delta/2} \tag{13.24}$$

is shown in Fig. 13.5. The amplification factor has been defined as the ratio of the total moment at either the head, base, or mid-height to the moment in Alternative Two (Section 5.2.3.2).

The same type of buckling behavior established for the fixed-head case in Section 13.1 was determined for this case, that is, a sudden type

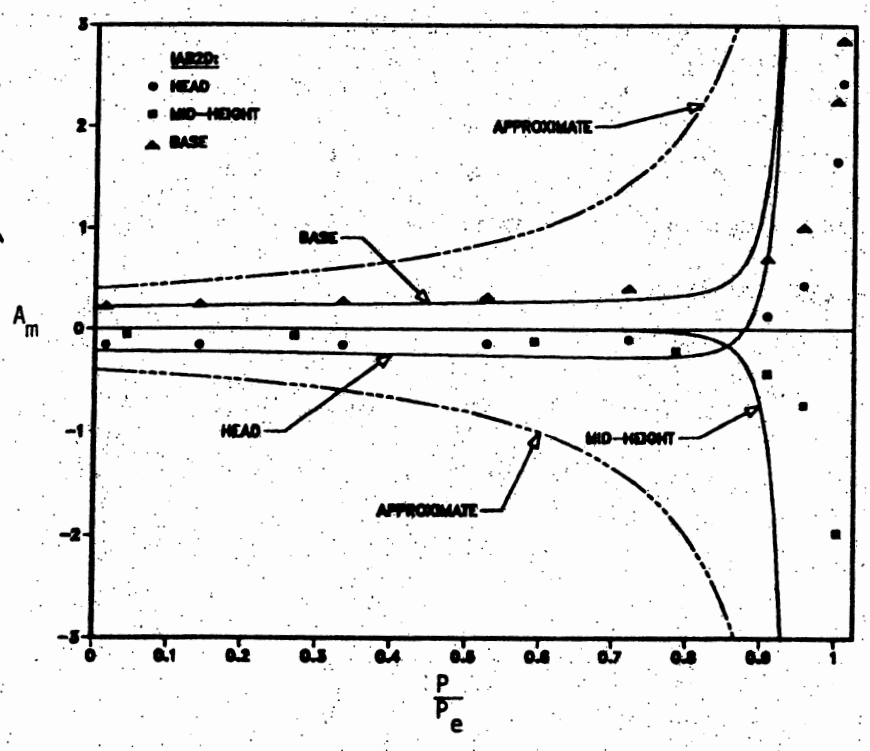

Figure 13.5. Moment amplification for an initially curved fixed-head column with a horizontal head displacement, Δ.

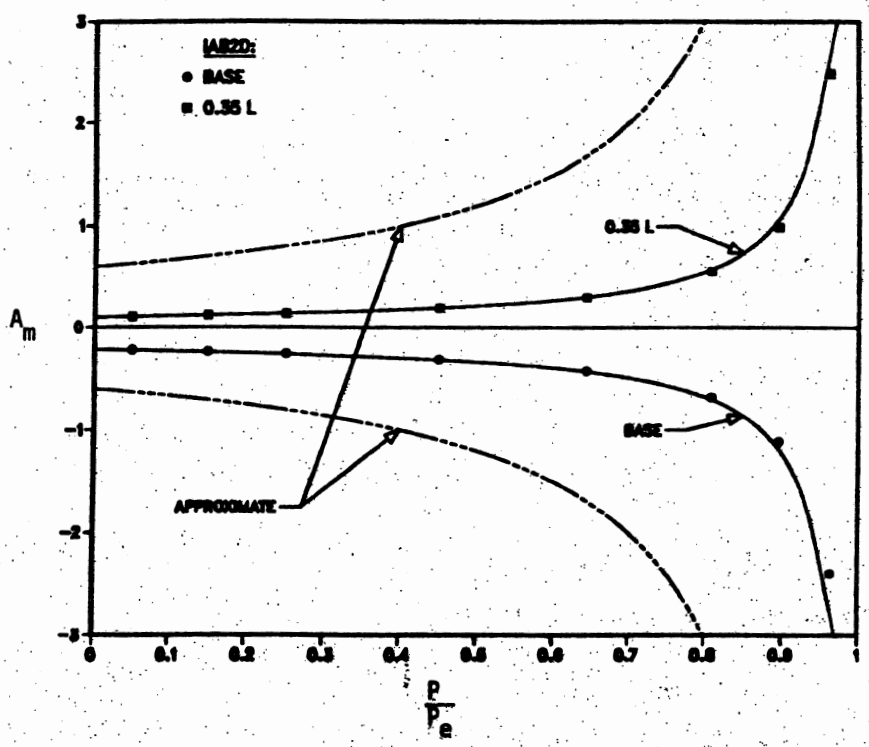

Figure 13.6. Moment amplification for an initially curved pinned-head column with a horizontal head displacement, Δ.

of "snap through" failure occurs as the head moment direction reverses. Again, the elastic buckling load is given by Eq. (13.13), since the asymptote occurred at P/P_e equal to one. The approximate amplification factor given by Eq. (13.14) is shown to be conservative over the entire range of P/P_e.

For Alternative Two, the initial shape of the pinned-head column shown in Fig. 13.2 is assumed to be stress-free and given by

$$y_i = \Delta \left(1 - \cos \frac{\pi x}{2L}\right) \tag{13.25}$$

The governing differential equation is

$$\frac{d^2 y_2}{dx^2} + k^2 y_2 = k^2 \Delta \left(1 - \cos \frac{\pi x}{2L}\right) + \frac{M}{EI} - \frac{(M - P\Delta)}{EIL} x \tag{13.26}$$

Since the column is not geometrically symmetric, an initial displacement imperfection is not required to induce the weakest buckling mode. The boundary conditions used for solving the differential equation are zero incremental displacement at the column head and zero displacement and rotation at the base of the column. A fourth boundary condition, which was used to derive Eq. (13.26), is that the moment at the column head is equal to zero. Solving the differential equation established the moment at the column base as

$$M = \frac{P\Delta}{\left[\frac{\pi^2}{4(kL)^2} - 1\right]\left(1 - \frac{\tan kL}{kL}\right)} + P\Delta \tag{13.27}$$

The amplification factor is defined as the ratio of either the moment at the base or at 0.35 L from the top to the moment for Alternative Two ($P\Delta$)

$$A_m = \frac{M}{P\Delta} \tag{13.28}$$

The resulting expressions are shown in Fig. 13.6. The approximate amplification factor given by Eq. (13.14) is shown to be conservative for the entire range of P/P_e. The results for both the finite element solution and the differential equation solution show that the column base moment is opposite to the direction assumed and that the elastic buckling load is given by Eq. (13.19), since the asymptote occurs at P/P_e equal to one.